2012

Structure and Organization of Nuclear Pore Proteins

Claire Atkinson

STRUCTURE AND ORGANIZATION OF NUCLEAR PORE PROTEINS STUDIED BY FLUORESCENCE POLARIZATION MICROSCOPY

A Thesis Presented to the Faculty of

The Rockefeller University

in Partial Fulfillment of the Requirements for

the degree of Doctor of Philosophy

by

Claire Atkinson

June 2012

STRUCTURE AND ORGANIZATION OF NUCLEAR PORE PROTEINS STUDIED BY FLUORESCENCE POLARIZATION MICROSCOPY

Claire Atkinson, Ph.D.

The Rockefeller University 2012

The nuclear pore complex (NPC) is a large macromolecular assembly that controls the flow of molecules between the nucleus and the cytoplasm. Elucidating the structure and organization of this complex will be crucial to understanding the mechanism of nucleocytoplasmic transport, but due to its size, the NPC presents a challenge to structure determination. There are electron microscopy (EM) structures of the entire NPC, and high resolution crystal structures of some of the individual components have been solved, but the arrangement of proteins within the overall complex remains unknown. An approach to solving structures of macromolecular complexes is to fit high resolution structures into an EM map, but the resolution of the EM structures of the NPC is too low to do so accurately. Additionally, approximately one third of the proteins making up the NPC contain unstructured regions that are not amenable to traditional structural techniques. These proteins (the FG nups) contain multiple phenylanine-glycine repeats, which bind cargo and transport it through the pore. Although many conflicting models for transport have been proposed, the mechanism still remains unclear.

Polarization fluorescence microscopy can be used to determine the orientation, mobility, and proximity of molecules. In this work, polarization microscopy techniques were developed to study aspects of the structure and organization of the NPC in live cells.

In the first part of this project, structural proteins were tagged with GFP in a defined position and their orientation within the NPC was determined. This showed that Nic96 is arranged in a head-to-tail ring around the perimeter of the NPC lumen and that the Y-shaped Nup107/160 complex is oriented with its long axis parallel to the plane of the nuclear envelope. This orientation technique can be used to help bridge the gap between EM and crystal structures of the NPC and its constituent parts.

In the second part of this work, the FG nups were tagged with GFP and polarization microscopy was used to determine their organization within the NPC. This showed that some of the FG nups adopted an ordered conformation which was unpredicted in any models for transport. FG nups which are located in center of the NPC lumen were more ordered than those at the periphery. This order was conserved between mammalian and yeast homologues of the same protein, suggesting functional relevance.

Factors which affect the ordering of the FG domains were investigated. Domain swapping experiments showed that relocating the FG domains of the central nups to the cytoplasmic side caused them to become disordered, suggesting a role for local interactions in their organization. Removal of the FG repeats had no effect on the behavior of Nup62, only a limited effect on Nup54, and prevented Nup98 from localizing to the pore, indicating that FG-FG interactions are not dominant in determining order. Ameliorating active transport, and disassociation of cargo from the NPC had no effect on the behavior of the FG domains. Taken together, these data led to development of a model for nematic ordering of the FG domains, in which dense packing and alignment of these domains within the NPC lumen leads to organizational, but not positional, order.

For my parents

With love and thanks

ACKNOWLEDGEMENTS

I would like to express my gratitude to everyone who has helped and supported me throughout my time at Rockefeller University: mentors, collaborators, colleagues and friends.

First and foremost, I thank my mentor and advisor Dr. Sandy Simon. I am incredibly indebted to Sandy, not just for teaching me about cell biology, but for teaching me how to think about doing science. He gave me the freedom to pursue my own ideas, but was always there with support and suggestions when I needed it, and always had my back. I will miss our discussions, his enthusiasm, and most of all his humor.

Many thanks to Dr. Günter Blobel and Dr. Rod Mackinnon, for their guidance while serving on my Faculty Advisory Committee, and to Dr. David Piston, for being the external member of my thesis committee.

This project was begun in collaboration with two people: Dr. Alexa Mattheyses and Dr. Martin Kampmann. It was a truly enjoyable experience to work with both of them, and I am grateful for their insight, suggestions for experiments, and for teaching me so much. Especial thanks to Alexa for teaching me microscopy, being an excellent mentor, and an even better friend. Parts of this thesis were adapted from papers written with Alexa, Martin and Sandy.

I am grateful to the members of the Simon lab for advice, help with reagents, and for making the lab such an enjoyable place to work. Laura Macro provided many informative discussions and has been an amazing source of support; I am lucky to have

worked with her. Dr. Marina Fix helped me with many technical and scientific questions, for which I am extremely grateful. Marcello Im provided help and administrative support. Especial thanks go to Dr. Cameron Bess, Dr. Patrick Bhola, Dr. Dan Johnson, Trilly Gregg, Dr. Barrie Rich, Dr. Josh Honeyman, Tom McDonagh, and Rachel Belote for stimulating conversations.

I must also acknowledge the members of the Blobel lab who provided me with reagents. Dr. Elias Coutavas was always very helpful answering my questions and providing me with plasmids. Dr. Sozanne Solmaz helped me with the Ran purification protocol. Dr. Ivo Melčák provided me with plasmids.

I also thank the David Rockefeller Graduate Program and the Dean's Office for their help and support along the way. I thank Kristen Cullen, Marta Delgardo, and Cristian Rosario for their commitment to graduate students.

Disan Davis and Alexa Mattheyses provided critical comments on parts of this thesis, for which I am truly grateful.

My family- Lary, Giles, Kate, Rachel and Hannah- for their love and encouragement. My New York family- Disan Davis, Illya Bomash, Birthe Meineke, Simon Elsässer, Joe Osmundson, and Amelia Greer, with whom I could not have done without. Joe, Disan, Illya: I owe you more than I can say. The friends back home who supported me, despite being across the ocean- Vanessa Garden, Helen Taylor, Anna Goodhand, George Anstey, Hannah Daley, Steph Southall, Roxanne Ransome, Felicity Burling, Felicity Long, and Dr. Gregory Lim. Many thanks to everybody else who lent me support or made me smile.

TABLE OF CONTENTS

LIST OF FIGURES

CHAPTER 1: Introduction

CHAPTER 2: Microscope Set-up and Theory

CHAPTER 3: Determining the Orientation of NPC Proteins

CHAPTER 4: Polarization Microscopy of FG Proteins

LIST OF TABLES

LIST OF ABBREVIATIONS

AG	Alanine glycine (motif/repeat)
ATP	Adenosine triphosphate
DTT	Dithiothreitol
EM	Electron microscopy
ER	Endoplasmic reticulum
FG	Phenylalanine glycine (motif/repeat/nup)
FRET	Förster resonant energy transfer
GAP	GTPase-activating protein
GDP	Guanine diphosphate
GFP	Green fluorescent protein
GTP	Guanine triphosphate
HEPES	4-(2-hydroxyethyl)-1-piperazineethanesulphonicacid
Kap	Karyopherin
NA	Numerical aperture
NE	Nuclear envelope
NES	Nuclear exit sequence
NLS	Nuclear localization sequence
NPC	Nuclear pore complex
Nup	Nucleoporin
PCR	Polymerase chain reaction
m/r/tRNA	Messenger/ribosomal/transfer ribonucleic acid
SEM	Standard error of the mean
TIR/ TIR-FM	Total internal reflection/ total internal reflection fluorescence microscopy
WGA	Wheat germ agglutinin

Introduction

In eukaryotic cells, cellular functions are compartmentalized into membrane bound organelles. The genetic material of the cell is contained within the nucleus. Communication between the nucleus and the cytoplasm occurs through the nuclear pore complex (NPC), a large multi-protein assembly which is embedded in pores in the nuclear envelope (NE) created by fusion of the inner and outer nuclear membranes (Ryan and Wente, 2000).

A wide range of molecules involved in basic cellular processes are transported through the NPC, including proteins, RNA, and ribosomal subunits. This transport is highly regulated and the determination of which molecules can traverse the nuclear envelope is governed by their interactions with the NPC. This transport is specific; molecules over ~40kD undergo selective transport while smaller molecules can passively diffuse. Therefore, nucleocytoplasmic transport can be a point of regulation for access to the genetic material, and this access is controlled by a substrate's ability to interact with the NPC.

Structure and Composition of the NPC

The NPC has a total mass of ~50 MDa in budding yeast and ~120 MDa in vertebrates (Rout et al., 2000; Cronshaw et al., 2002). It is composed of ~30 distinct proteins, termed nucleoporins. Structures of the overall shape and symmetry of the complex have been determined using electron microscopy (EM) (Gall, 1967; Akey and

Goldfarb, 1989; Akey and Radermacher, 1993; Yang et al., 1998), and cryo-electron tomography has been used to generate structures at a resolution beyond 6 nm (Beck et al., 2004; 2007). These structures show that the NPC has eightfold symmetry about the nucleocytoplasmic axis; its central core displays dyad symmetry about a perpendicular axis within the NE plane. Outside of the central core, the NPC is asymmetric, with 8 filaments projecting from the cytoplasmic face of the channel, while the nuclear side of the channel is decorated with a basket-like structure comprised of 8 filaments joined to a distal ring (Stoffler et al., 2003).

Some data have suggested that the central core of the NPC may be flexible (Stoffler et al., 1999; Wang and Clapham, 1999; Liashkovich et al., 2011). EM of individual complexes has shown large scale shape changes (Akey, 1990; 1995), and a model for modulation of the ring diameter has been proposed on the basis of crystallographic studies (Melčák et al., 2007; Solmaz et al., 2011). The NPC can transport cargo of up to 39 nm in diameter (Panté and Kann, 2002); it has been proposed that the diameter of the pore may enlarge to accommodate these large cargoes. Additionally, while the majority of NPCs are 8 fold symmetric, a small number of NPCs with 9 or 10 fold symmetry have been observed (Hinshaw and Milligan, 2003).

The structure of the central core of the NPC can be considered as layers of proteins (nucleoporins or nups) arranged as concentric cylinders (Hoelz et al., 2011). These proteins fall broadly into four categories, building up from the membrane to the center of the complex. The first layer is comprised of integral membrane proteins which anchor the NPC to the membrane (Antonin et al., 2005; Madrid et al., 2006; Miao et al., 2006; Stavru et al., 2006; Chadrin et al., 2010). The next two layers contain structural

proteins which have an architectural function: first a layer of coat proteins which line the membrane, followed by a layer of adaptor proteins. The adaptor proteins link the coat to the innermost layer of the NPC, containing the transporter proteins which line a central channel of 40-50nm diameter. These make up approximately one third of the nucleoporins and consist of a folded domain which anchors the protein in the NPC and a natively unstructured domain that contains multiple repeats of a phenylalanine-glycine motif (FG nups) (Wente et al., 1992). It is these proteins which engage the cargo and its chaperones (Figure 1).

Due to the 8 fold symmetry of the NPC, nucleoporins are present in 8, 16, 32 or 64 copies (Rout et al., 2000; Cronshaw et al., 2002). The relative stoichiometry of these proteins has been estimated using quantitative Western blotting. However, the proteins of the NPC turn over at different rates, with some peripheral proteins having residence times on the second timescale (Daigle et al., 2001; Griffis et al., 2002; Rabut et al., 2004) whereas some of the core components remain permanently assembled in cells which have exited the cell cycle (D'Angelo et al., 2009). Therefore, at any one time a single pore may vary in the exact number of each nucleoporin present.

Strategies for Determining the Structure of Macromolecular Complexes

Determining the structure of macromolecular complexes such as the NPC is crucial for understanding their function, but these complexes present a challenge: often the size of the entire assembly is too large to make it amenable to high-resolution techniques. X-ray crystallography can typically be applied only to individual proteins or

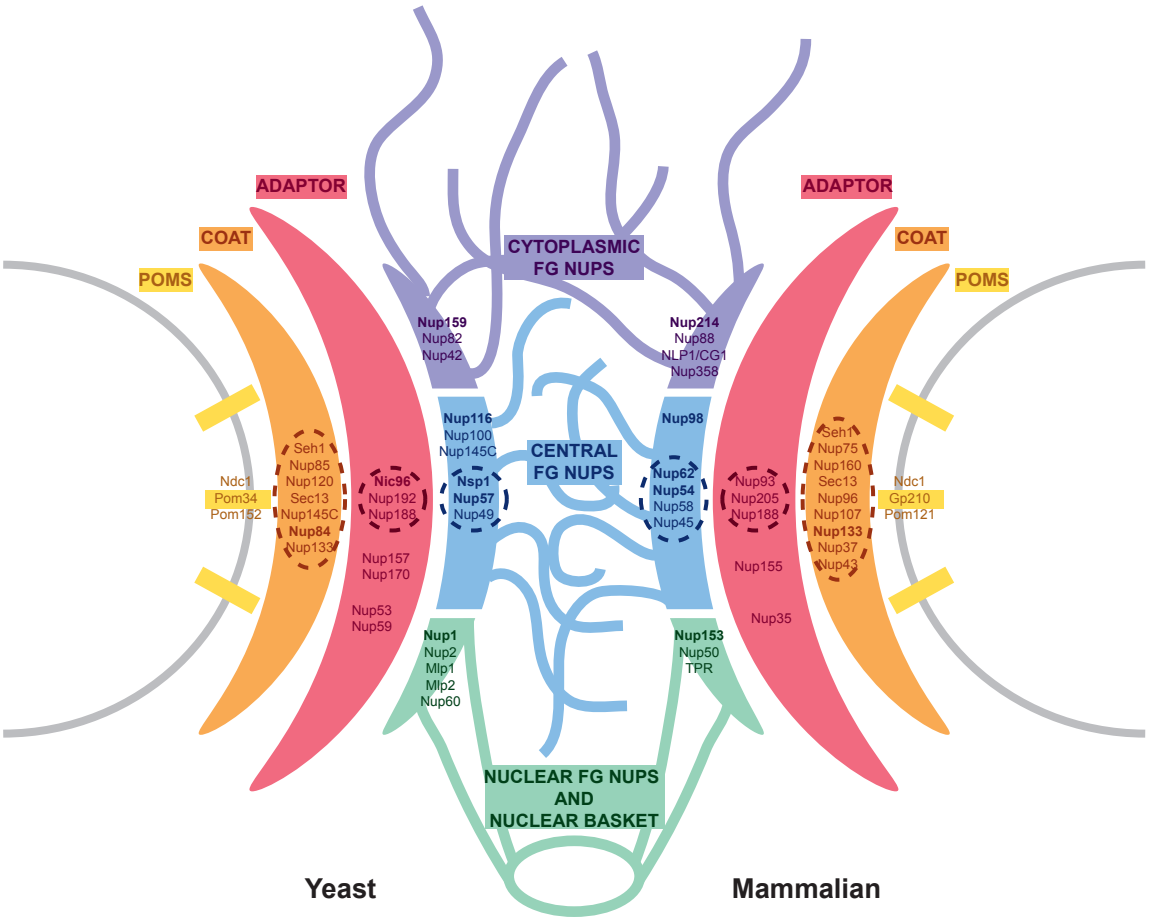

Figure 1: Structure and Composition of the NPC. The nuclear envelope is shown in grey; transmembrane proteins are shown in yellow; coating nups are shown in orange; adaptor nups are shown in pink; central FG nups are shown in blue; cytoplasmic FG nups are shown in purple; nuclear FG nups are shown in green. Yeast proteins are shown on the left; mammalian proteins are shown on the right. Protein subcomplexes are shown within dashed lines. Proteins used in this study are highlighted in bold.

smaller subcomplexes, while techniques that are suitable for the study of the entire assembly, such as electron microscopy (EM), are limited in their resolution. This is referred to as the "resolution gap problem". Additionally, the inherent flexibility of many large complexes presents challenges in obtaining high resolution EM data, and/or crystal structures of all the components. One approach to solving the structures of large complexes is to integrate information obtained from different techniques (Alber et al., 2007; Elad et al., 2009). However, this can be challenging when the resolution gap between different types of structures is wide, as is the case for the NPC.

A coarse model for NPC architecture has been generated computationally, based mainly on low-resolution immuno-EM and protein-protein interaction data. However, this model lacks information regarding the orientation and shape of NPC building blocks, which would be required to place crystal structures into the overall map.

Several individual NPC proteins, as well as binary and tertiary complexes, have been characterized at high resolution using X-ray crystallography (Hodel et al., 2002; Berke et al., 2004; Hsia et al., 2007; Jeudy and Schwartz, 2007; Napetschnig et al., 2007; Boehmer et al., 2008; Brohawn and Schwartz, 2009b; Leksa et al., 2009). These structures, together with predictions based on protein sequence, suggest that the majority of nucleoporins are constructed from a small set of fold classes (Devos et al., 2006). The FG nups contain both unstructured FG domains as well as folded domains which are predominantly coiled coils. The structural nucleoporins contain α-solenoids, β propellers, or both.

Many of the nucleoporins are present as part of larger subcomplexes. These subcomplexes remain assembled during disassembly of the NPC during metazoan mitosis

(Belgareh et al., 2001). Several subcomplexes have been characterized biochemically, and are stable enough that they can be purified in an intact form from yeast (Siniossoglou et al., 2000) or reconstituted from proteins recombinantly expressed in *E.coli* (Schlaich et al., 1997). The structure of some of these subcomplexes has been determined using single particle EM (Lutzmann et al., 2002).

An experimental approach to bridging the resolution gap in NPC structural biology is three-dimensional EM of NPC subcomplexes, followed by docking of crystal structures into the EM (Kampmann and Blobel, 2009). This strategy elucidated the arrangement of seven nucleoporins within the Y-shaped Nup84 complex. However, this approach has not resolved the higher-order arrangement of the subcomplexes within the NPC. Components of two of these complexes- the Y-shaped complex and Nic96 in the Nsp1 complex- are discussed in more detail below.

Y-Shaped Subcomplex

One of the best characterized subcomplexes is the metazoan Nup107/160 complex and its yeast homolog, the Nup84 complex. The yeast complex contains 7 proteins: Nup84, Nup85, Nup120, Nup133, Nup145C, Seh1, and Sec13 (Figure 2A). The mammalian complex contains homologs of each of these proteins as well as two additional members: Nup160 (homologous to yeast Nup120), Nup107 (Nup84), Nup96 (Nup145C), Nup75 (Nup85), Sec13, Seh1, Nup37, and Nup43. Single particle EM of the yeast Nup84 complex shows that it is Y-shaped with two flexible hinge regions (Kampmann and Blobel, 2009). Protein-protein interaction mapping and 2-dimensional

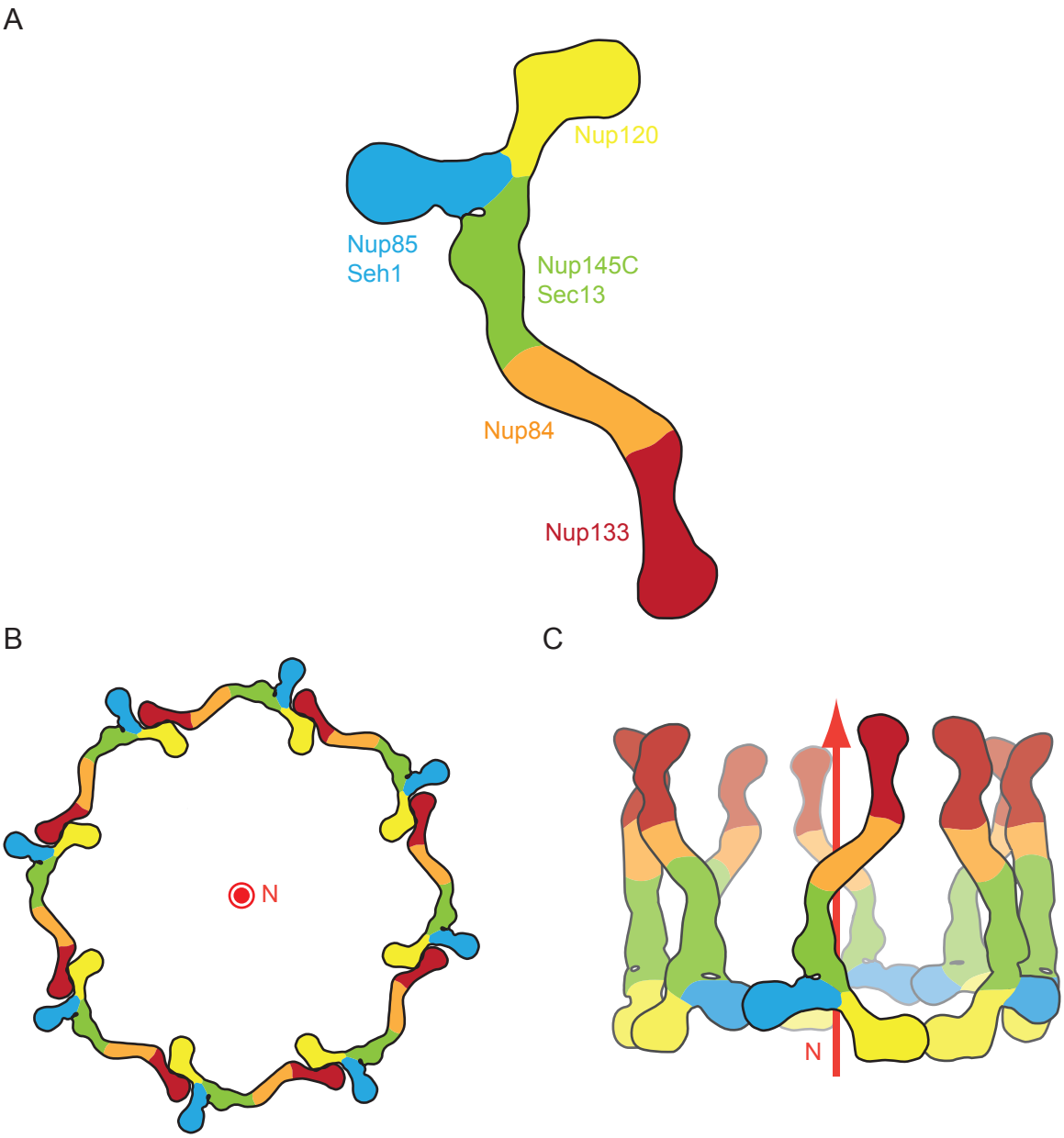

Figure 2: Models for the Orientation of the Y Shaped Complex. A) Schematic of yeast Y shaped complex. B) "Head-to-tail ring" model for Y-shaped complex orientation in the NPC, viewed down the nucleocytoplasmic axis. C) "Lattice model" of Y-shaped complex orientation in the NPC, viewed side on.

EM have determined the position of several of the proteins within the complex, which allowed crystal structures of yeast Seh1/Nup85, yeast Sec13/Nup145C/Nup84 (N terminal domain), human Nup107 (C terminal domain)/ Nup133 (C terminal domain) and human Nup133 (C terminal domain) to be docked into the higher resolution structure. However, crystal structures have not been solved for all the protein domains for the nucleoporins making up this complex, making completion of a high resolution model of this complex unavailable.

The Y-shaped complex is localized close to the pore membrane, as part of the layer of coat proteins. Several of the proteins in the complex contain predicted membrane-curvature sensing domains (Drin et al., 2007), consistent with the complex playing a role in stabilization of the highly curved pore membrane. Indeed, this complex is one of the first to be recruited during NPC formation, and is required for NPC assembly (Doye and Hurt, 1997; Harel et al., 2003; Walther et al., 2003).

The individual components of this complex have been defined, and its overall position within the NPC is known. However, the arrangement of the Y-shaped complex within the overall NPC architecture has been a source of controversy. Two mutually exclusive models for possible arrangements have been proposed. In the "head-to-tail ring" model, Nup84 complexes lie with their long axis parallel to the nuclear envelope plane and form a ring through interaction of the end of the stem of the "Y" with the short arms of the neighboring "Y" (Debler et al., 2008; Nagy et al., 2009) (Figure 2B). According to the "lattice model", the Nup84 complexes interact via their short arms, with their long axes parallel to the nucleocytoplasmic axis (Brohawn et al., 2008; Brohawn and Schwartz, 2009a) (Figure 2C).

Thus, the predicted orientation of the subcomplex differs within the NPC by 90° between these two models. More generally, knowledge of the orientation of individual nucleoporins within the NPC will be essential for the elucidation of NPC architecture at high resolution by docking of high-resolution nucleoporin structures into lower-resolution NPC maps.

Nic96/Nup93

Nic96 in yeast, and its mammalian homolog Nup93 (Grandi et al., 1997), are proteins which link the inner coat layer of the NPC to the FG nups. Nic 96 is an essential protein (Zabel et al., 1996; Gomez-Ospina et al., 2000). Nic96 binds to the structural nucleoporins Nup188 and Nup192 (Nup188 and Nup205 in mammalian cells; additionally Nup93 interacts with the mammalian homolog of yeast Nup53) (Nehrbass et al., 1996; Zabel et al., 1996; Theerthagiri et al., 2010). These interactions take place through the C terminal portion of Nic96 (Schrader et al., 2008b).

Nic96 is also a component of the FG nup containing Nsp1complex, thereby linking the structural components to the inner transport machinery (Grandi et al., 1993; Fahrenkrog et al., 1998). The Nsp1 complex contains three FG nups: Nsp1, Nup49 and Nup57 (Nup62, Nup45, Nup58 and Nup 54 in mammalian cells). Nic96 participates in the Nsp1 complex via its N terminus, which is predicted to form a coiled coil helix bundle with helices from Nsp1, Nup57 and Nup49 (Figure 3).

Nic96 without the N terminal domain has been crystallized, and folds into an α-helical structure which deviates from the classical α-solenoid fold (Jeudy and Schwartz,

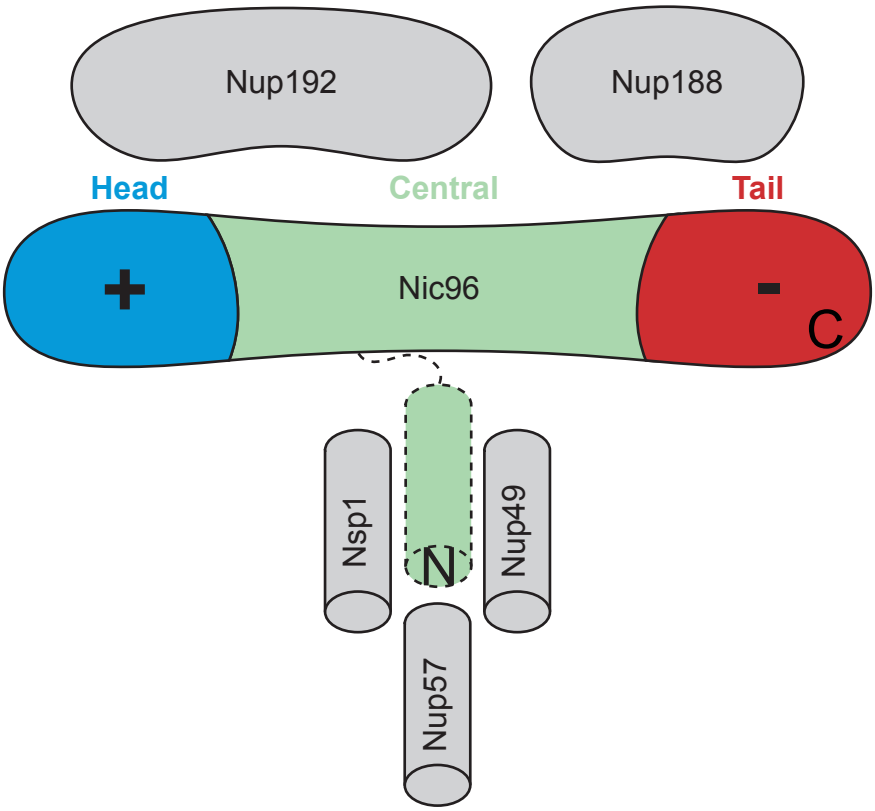

Figure 3: Nic96 Domain Organization. The C terminal portion forms an extended rod-like structure. The 'head' domain bears an overall postive electrostatic potential, whereas the tail domain bears and overall negative electrostatic potential. The N terminal domain of Nic96 has not been crystallized but is proposed to be α-helical. The C terminal domains interact with Nup188 and Nup192; the N terminal domain interacts with Nsp1, Nup49, and Nup57.

2007). The overall shape of the domain is an elongated rod. While the arrangement and orientation of Nic96 in the NPC has not previously been determined, a model has been proposed on the basis of structural and biochemical data. The head of the rod is positively charged while the tail domain bears an overall negative charge. Surface point mutations of Nic96 which change the charge of residues at the head of the Nic96 rod are synthetic lethal with Nup188 disruption. On the basis of these data, it was suggested that Nic96 could form an head-to-tail octameric ring, in which the long axis of Nic96 is perpendicular to the nucleocytoplasmic axis (Schrader et al., 2008b). However, this model needs to be further validated in vivo to fit Nic96 into the overall NPC architecture.

Cargo Transport through the NPC

FG domains are crucial for the transport function of the NPC. They fill the central channel, extending into the nucleus and cytoplasm, and act as barrier to nonspecific molecules. This barrier excludes molecules larger than 40 kDa from diffusing passively between the nucleus and cytoplasm, while simultaneously allowing receptor-mediated transport of much larger cargo molecules, such as ribosomal subunits.

Imported cargo molecules contain a nuclear localization sequence (NLS) (Dingwall et al., 1982; Dingwall and Laskey, 1991; Görlich et al., 1995) which binds karyopherins in the cytoplasm (Adam and Gerace, 1991; Görlich et al., 1994; Moore and Blobel, 1994). Karyopherins provide an adaptor function, as they interact with both cargo molecules and the NPC, allowing transit (Rexach and Blobel, 1995; Radu et al., 1995a; 1995b). In the nucleus the karyopherin and cargo are dissociated both from the NPC and

from each other by the small GTPase Ran (Melchior et al., 1993; Moore and Blobel, 1993; Melchior et al., 1995; Moroianu et al., 1996). The predominant form of Ran in the nucleus is RanGTP; it is this form which dissociates import cargo. GTP loading is stimulated by RCC1 (Prp20p in yeast), which is localized to the nucleus through interactions with chromatin and the nuclear basket (Ohtsubo et al., 1989; Bischoff and Ponstingl, 1991; Klebe et al., 1995).

Protein cargo with a nuclear export sequence (NES) can bind karyopherins in complex with RanGTP and is transported to the cytoplasm, where RanGAP (rna1p in yeast) stimulates the hydrolysis of GTP and dissociates the Ran-cargo-karyopherin complex (Bischoff et al., 1994; Moroianu and Blobel, 1995). RanGDP is recycled back to the nucleus by the transport receptor NTF2 (Corbett and Silver, 1996; Bayliss et al., 1999). The asymmetric locations of RanGAP and RCC1 set up gradients of RanGTP and RanGDP across the NE, with RanGTP concentrated in the nucleus and RanGDP in the cytoplasm (Figure 4) (Akhtar et al., 2001).

Binding to the NPC and directional movement are separate steps in the transport process (Richardson et al., 1988). In permeabilized cells, cargo complexed with karyopherin can bind at the NE in the absence of Ran, but Ran is required for the active import of the cargo (Moore and Blobel, 1992). It has been shown that reversing the gradient of RanGTP: RanGDP causes a reversal of the direction of transport (Nachury and Weis, 1999). Thus, GTP hydrolysis is not required for the mechanical movement of cargo through the pore, but is required for directionality (Izaurralde et al., 1997; Schwoebel et al., 1998).

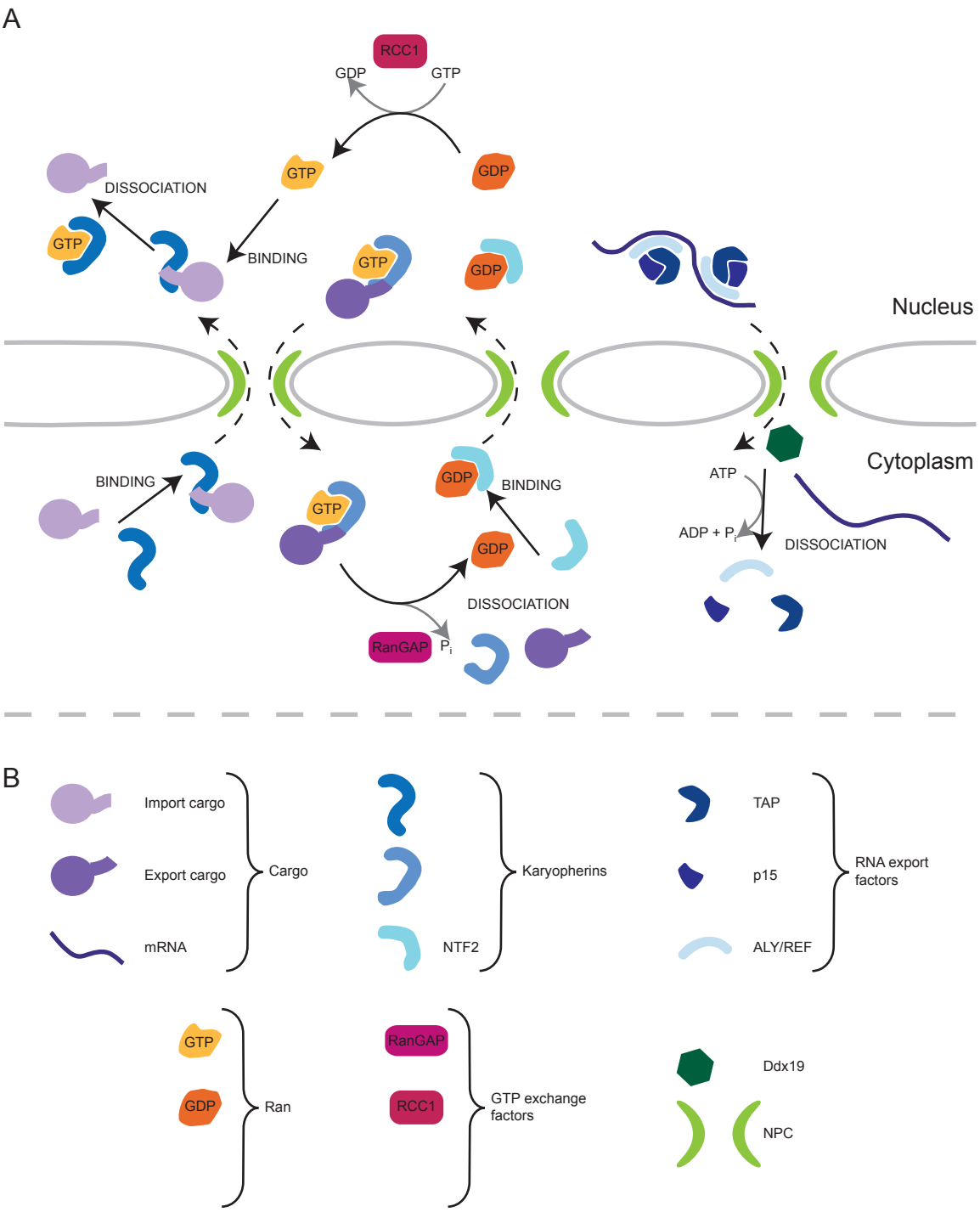

Figure 4: Schematic of Ran GTP:GDP Cycle. A) Ran GTP:GDP cycle. Import and export processes are indicated by black dashed arrows. Left to right: Ran dependent import; Ran dependent export; Ran import by NTF2; Ran independent mRNA export. B) Key to molecules depicted in (A).

While protein import, protein export, and some RNA export processes (notably those of tRNA and rRNA) depend on binding to karyopherins and the RanGTP: GDP cycle (Arts et al., 1998; Zemp and Kutay, 2007), the bulk export of mRNA is Ran independent (Clouse et al., 2001). Export is mediated by non-karyopherin protein factors associated with the mRNA. For most mRNA, the pathway is dependent on TAP (Mex67 in yeast) for interaction with the NPC (Kadowaki et al., 1994; Segref et al., 1997; Grüter et al., 1998; Moreno et al., 1998; Kang and Cullen, 1999; Katahira et al., 1999). During the export process, the mRNA undergoes a cycle of docking, transport, and release on the cytoplasmic side of the NPC, where the DEAD box helicase Ddx19 (Dbp5 in yeast) is involved in disassembly of the mRNA export complex (Snay-Hodge et al., 1998; Tseng et al., 1998; Lund and Guthrie, 2005). Ddx19 is localized to the cytoplasmic face of the NPC via interaction with Nup214 (Moeller and Basquin, 2009; Napetschnig et al., 2009). This remodeling by Ddx19 acts as a Brownian ratchet mechanism to impose directionality on mRNA export (Stewart, 2007) (Figure 4).

The interaction between a karyopherin and cargo is crucial for determining the selectivity of transport. Each karyopherin recognizes a specific repertoire of cargo; some karyopherins such as CRM1 and karyopherin α are able to bind a wide spectrum of target molecules while others such as CAS have a single known substrate (Fornerod et al., 1997; Kutay et al., 1997; Stade et al., 1997; Hood and Silver, 1998; Conti and Kuriyan, 2000; Goldfarb et al., 2004). Recognition depends on the presence of an NES or NLS in the cargo, however there are no specific consensus sequences for these signals. Classical NLSs recognized by karyopherin α contain either one or two clusters of basic residues (Kalderon et al., 1984; Robbins et al., 1991; Lange et al., 2007) although many other

diverse sequences are recognized by karyopherins (Pollard et al., 1996; Jäkel and Görlich, 1998). Similarly, while the classical NES recognized by CRM1 is characterized by the presence of 4 hydrophobic residues (Dong et al., 2009), there are many different NESs present on a wide range of substrates (Fischer et al., 1995). In this way, the karyopherins act as an adaptor by in allowing molecules with varied properties to enter the NPC.

As well as interacting with cargo, the karyopherins interact with the NPC through the FG repeats. Different karyopherins bind different sets of FG nucleoporins, suggesting there are some specific transport pathways through the NPC (Damelin and Silver, 2000; Allen et al., 2001; Terry and Wente, 2007). However, there is redundancy in the FG domains, as many can be deleted with no detriment to cargo import (Strawn et al., 2004). The interaction of cargo with the FG nups depends on the FG repeats themselves: point mutations in the FG binding regions of karyopherinβ/importinβ or NTF2 decrease their ability to translocate cargo, and mutation of the FG motif to AG prevents karyopherin binding (Bayliss et al., 1999; 2000). Crystal structures have been solved of Nsp1 FG repeats in complex with karyopherin β1. These structures show hydrophobic interactions between the phenylalanine residue of the FG and residues of the binding pocket of the transport receptor. Additionally, in this structure a single karyopherin molecule is bound to multiple FG repeats, but there is no structure for Nsp1 outside of the FG binding pockets, making it unclear how the karyopherin interacts with the remainder of the FG domain. It also cannot be determined whether the FG repeats present in the structure originate from a single FG domain or multiple domains. (Bayliss et al., 2000).

FG Nups

The FG nups are anchored in the NPC by their structured domains; immuno-EM of these domains has shown that some are located in the center of the NPC, while others localize either to the nuclear or cytoplasmic side. The asymmetrically located FG nups are completely dispensable for transport (Walther et al., 2002; Strawn et al., 2004). In EM structures of the NPC the FG domains appear as unstructured density in the pore lumen (Feldherr and Akin, 1997), which is consistent with *in vitro* studies using circular dichroism and gel filtration that show these domains to have an extended, unfolded conformation (Denning et al., 2003). Immuno-EM has been used to demonstrate that the FG domains of some of the FG nups are present on both sides of the pore, suggesting they can extend away from the site of the anchored domain, and are potentially moving from one side of the NPC to the other (Paulillo et al., 2005; Chatel et al., 2012).

The "linker" portions of the FG domains between the FG repeats show little conservation of sequence, although they contain a high proportion of disorder-promoting amino acids (Denning and Rexach, 2007). The amino acid sequences surrounding the repeats vary, with some FG motifs appearing in longer repetitive motifs such as FxFG or SxFG (Terry and Wente, 2009). There is redundancy in function between some FG nups; in yeast up to 50% of the total mass of the FG nups can be deleted while maintaining the integrity of transport (Strawn et al., 2004). However, the type of FG repeat present is important, as either one of the GLFG containing proteins Nup116 and Nup100 could be deleted, but removal of both was lethal.

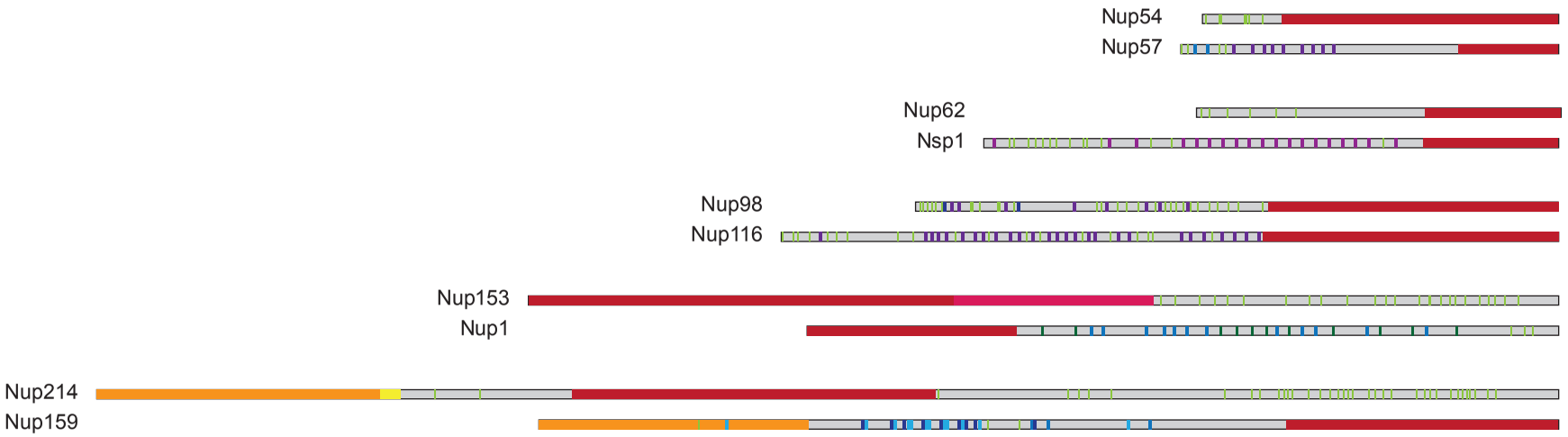

Figure 5: Diagram of FG Nucleoporins. Mammalian and yeast homologues of the same protein are shown in pairs. Folded/structured domains are shown in red; β propellers are shown in orange with C terminal extensions in yellow; Zn finger domains are shown in pink. FG domains are shown in grey, with FG repeats depicted as follows: FG, green; FXFG, blue; GLFG, purple; FSFG, magenta; SXFG, dark blue; PXFG, light blue; FXF, dark green.

It is therefore proposed that the lumen of the NPC is filled with these unstructured domains, creating a barrier to non specific transport while allowing passage of cargo via interaction with the FG repeats. The FG nucleoporins used in this study are schematized in Figure 5.

Nup54

Nup54 is a centrally located FG nup with an N terminal FG domain and a C terminal folded domain (Guan et al., 1995; Melčák et al., 2007; Solmaz et al., 2011). It forms a subcomplex with Nup62, Nup58, and Nup54 that is anchored to the NPC via interactions with Nup93 (Hu et al., 1996). It contains 7 FG repeats, located close to the N terminus of the FG domain, and is modified with O-linked glycosyl groups (Holt et al., 1987; Snow et al., 1987). It is estimated that Nup54 is present in 32-48 copies per NPC (Cronshaw et al., 2002). The yeast homolog of Nup57 is Nup54, which has 15 GLFG repeats, and an estimated abundance of 16 copies per NPC (Rout et al., 2000).

Nup62

Nup62 is a component of the same subcomplex as Nup54, and therefore is centrally located (Schwarz-Herion et al., 2007). It has a C terminal coiled coil domain and an N terminal FG domain, containing 6 FXFG repeats. It is O-glycosylated at an estimated 10 glycosylation sites, the majority of which are predicted to be in a serine/threonine rich region located on the FG domain in between the FG repeats and the

coiled coil domain (Holt et al., 1987; Lubas et al., 1995). Nup62 is estimated to be present in 16 copies per NPC (Cronshaw et al., 2002). The yeast homolog of Nup62 is Nsp1. Nsp1 is essential and contains 12 FG repeats and 22 FXFG repeats. It is estimated to be present in 32 copies per NPC (Rout et al., 2000).

Nup98

Nup98 is centrally located in the NPC, and contains 39 FG repeats (Chatel et al., 2012); it is the only mammalian nucleoporin which contains GLFG motifs. It is essential for mouse gastrulation and Nup98 knock out cells display defects in NPC assembly (Wu et al., 2001). It has an N terminal FG domain and a C terminal folded domain which is autoproteolytically processed (Fontoura et al., 1999; Rosenblum and Blobel, 1999; Hodel et al., 2002). Both the FG domain and the folded domain are necessary for Nup98 localization to the NPC (Griffis et al., 2002). Nup98 is dynamically associated with the NPC, and also has roles in transcription, although it is unclear whether the Nup98 populations involved in nuclear transport and transcription are the same (Capelson et al., 2010). It is estimated to be present in 8 copies per NPC and contain 2 O-glycosylation sites (Holt et al., 1987; Cronshaw et al., 2002).

Nup98 has two yeast homologues, Nup100 and Nup116. Nup116 contains 9 FG repeats and 40 GLFG repeats. Simultaneous removal of both the Nup100 and Nup116 GLFG repeats is lethal, as is removal of the entire Nup116 FG domain (Strawn et al., 2004). Knock-out of Nup116 results in a temperature sensitive phenotype which is lethal at 37°C due to formation of a nuclear envelope seal over the NPC (Wente and Blobel,

1993). Nup116 is located in the central channel of the NPC with a bias towards the cytoplasmic face (Ho et al., 2000). It is estimated that it has an abundance of 8 copies per NPC. (Rout et al., 2000)

Nup153

Nup153 is located on the nucleoplasmic face of the NPC where it is a component of the nuclear basket (Cordes et al., 1993; Sukegawa and Blobel, 1993; Panté et al., 1994). It is estimated that there are 8 copies of Nup153 per NPC (Cronshaw et al., 2002). It has an N terminal folded domain which anchors it to the NPC, a central domain containing four zinc finger motifs, and a C terminal FG domain, which has 25 FxFG repeats. The zinc finger domain is able to bind Ran, suggesting that it may act as a sink for RanGTP, concentrating it at the nuclear side of the NPC where it is in a position to dissociate cargo from the pore (Schrader et al., 2008a). Nup153 plays a role in many export processes, both of protein and RNA (Ullman et al., 1999; Walther et al., 2001). It is one of the most mobile nucleoporins (Rabut et al., 2004).

The yeast homologue of Nup153 is Nup1, which is also a component of the nuclear basket. It has 22FxFG repeats, and is present in an estimated 8 copies per NPC (Rout et al., 2000).

Nup214

Nup214 is located on the cytoplasmic side of the NPC where it is part of the cytoplasmic filaments and interacts with components of the RNA export machinery (Kraemer et al., 1994). It has a N terminal domain containing a β propeller which interacts with the DEAD box helicase Ddx19, a centrally located coiled coil domain, and a C terminal FG domain which contains 35 FG repeats (Schmitt et al., 1999; Napetschnig et al., 2009). It is glycosylated and has an estimated abundance of 8 copies per NPC (Cronshaw et al., 2002).

The yeast homolog of Nup214 is Nup159, which has a slightly different domain arrangement (Kraemer et al., 1995). It has an N terminal β propeller domain which binds the Ddx19 homolog Dbp5, a central FG domain containing 25 FG repeats, and a C terminal coiled coil domain. Like Nup214 it forms part of the cytoplasmic filaments and is present in an estimated 8 copies per NPC (Rout et al., 2000.)

Models for Transport

Even though the protein components involved have been determined, the mechanism by which the FG domains move cargo through the NPC remains unclear. Several models have been proposed for transport, and these models predict widely different behaviors for the FG nups and their interactions with cargo (Figure 6) (Peters, 2009).

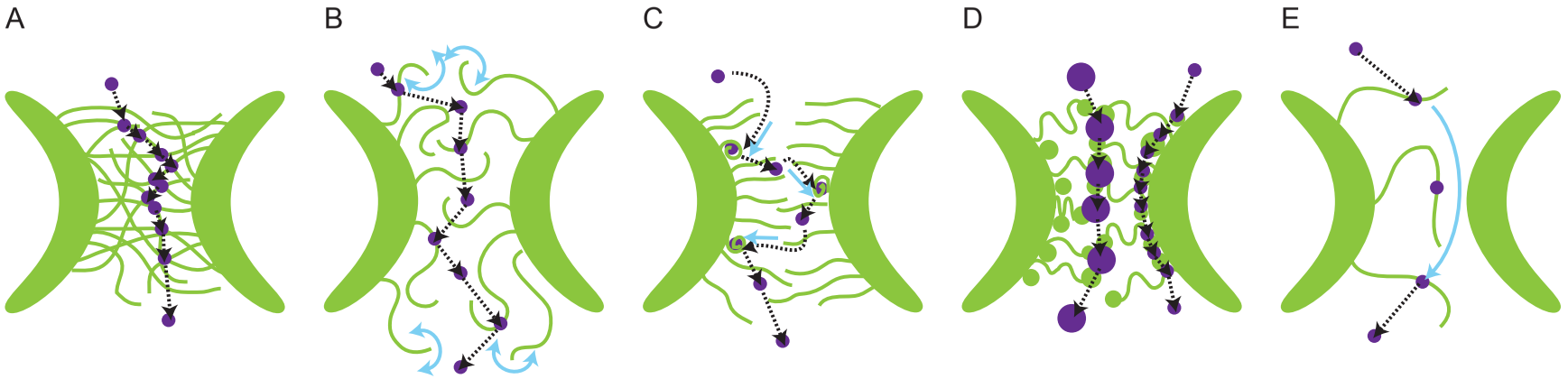

Figure 6: Models for Nucleocytoplasmic Transport. A) Hydrophobic gel model. B) Entropic exclusion model. C) Collapse model. D) Forest model. E) Brownian ratchet model. FG Nups are shown in green; cargo is shown in purple; cargo binding and unbinding is shown with black dashed arrows; movement of the FG domains is shown with blue solid arrows.

The hydrophobic gel model is based on the observation that exogenously purified FG nups can be treated to form a gel. This depends on the FG repeats, as when the FG repeats of Nsp1 were mutated to SG, the gel did not form. Karyopherin bound cargo was able to diffuse into these gels at a faster rate than a non-specific molecule of similar size. The model therefore hypothesizes that the NPC contains a saturated network of hydrophobic FG-FG interactions linking the FG nups, and that cargo can "melt" through this network by temporarily binding to and breaking a FG-FG node before diffusing on to the next (Figure 6A). However, in order to form the gel a pH shift to ~11 was required, raising questions about the possibility of such gels forming in a physiological context (Frey et al., 2006; Frey and Görlich, 2007; 2009). Additionally, these experiments showed that the network of FG-FG interactions must be saturated in order to account for specificity, which is hard to reconcile with experiments that show that 50% of the FG domains can be deleted while maintaining the integrity of transport (Strawn et al, 2004).

In contrast, the virtual gate model proposes that the FG nups are dynamic and form an entropic barrier to non specific molecules entering the pore (Figure 6B). This model is based on the unstructured nature of these domains and computational simulation of diffusion in an array of wells of energy potential which represent cargo binding events. It proposes that cargo which can bind the FG repeats can overcome the entropic barrier to enter the pore space (Rout et al., 2000; 2003). However, this model remains largely theoretical has not been directly tested *in vivo*.

A further modification of this model suggests that the presence of cargo within the pore also helps prevent non-specific molecules from entering the pore (Timney et al., 2006; Zilman et al., 2007; 2010). This was tested using an artificial nanopore lined with

the FG domain from Nsp1. In these experiments, non specific cargo was prevented from transiting the nanopore only in the presence of transported cargo, which was selectively favored. These experiments were notable in attempting to recapitulate the geometry of the NPC; however the increase in selectivity was dependent on the diameter and height of the nanopore used, highlighting the importance of considering the *in vivo* parameters of the NPC (Jovanovic-Talisman et al., 2009) .

Atomic force microscopy of purified FG domains attached to a surface suggested that these domains form a polymer brush-like structure. Upon the addition of cargo, the FG domains collapsed down to the surface. This lead to the development of the "collapse" model, in which cargo binding causes the FG domain to retract, pulling the molecule into the NPC (Lim et al., 2006; 2007a; 2007b) (Figure 6C). However, these experiments only tested a single nup, Nup153, which is a component of the nuclear basket and may not be representative of the central and cytoplasmic nups. Additionally, the geometry and density of these domains when tethered to gold nanodots on a flat surface may impose the observed polymer brush-like behavior, which may not be recapitulated in the NPC *in vivo*.

The dual gate model attempts to reconcile the polymer gel and virtual gate models, and is based on data showing that in a bead binding assay only a subset of the FG nups were able to bind each other via FG-FG interactions (Patel et al., 2007). In this model, the FG nups in the center of the pore form a cross-linked gel, while those at the periphery form an entropic gate. Again, this model is based only on *in vitro* observations and has not been tested *in vivo*.

The “forest” model also invokes different behaviors of FG nups depending on the level of “cohesion” of their FG repeats, and is based on determination of the hydrodynamic radii of purified FG nups, as well as mutational analyses of the FG repeats and their surrounding regions. This model proposes that some “cohesive” FG nups exhibit inter-molecular FG-FG interactions and adopt a collapsed coil structure. This coiled structure can either line the wall of the pore as a “shrub” or can be at the end of relaxed or extended coil structures, filling the center the pore as a “tree” (Figure 6D). “Non-cohesive” FG domains can also form collapsed coils and relaxed or extended coils, but these structures are not dependent on FG-FG interactions. This model suggests that large cargoes use the FG repeats of “trees” to move through the central channel of the NPC, while smaller cargoes interact with the “shrubs” at the periphery of the pore (Yamada et al., 2010). Like the entropic exclusion and hydrophobic gel models, it is not clear how this model would account for directionality, as cargo that is able to unbind from and diffuse between FG repeats within the pore would also be able to diffuse out of the pore with equal probability on each side.

The “reduction of dimensionality” model is a simpler version of the “forest” model, in that it also proposes that the FG domains are lining the walls of the pore lumen, and is based on observed cargo transit rates and immune-EM localization of the FG domains. In this model the FG domains provide a hydrophobic lining to the lumen of the NPC, along which cargo can diffuse in a two dimensional search to reach the other side (Peters, 2005).

The Brownian ratchet model places importance on the cargo-FG domain interaction. This model is based on computational exploration of the NPC parameter

space, and suggests that once a cargo molecule binds an FG repeat, it remains bound, traversing the pore while still complexed with the FG domain until it is dissociated by RanGTP in the nucleus (Mincer and Simon, 2011) (Figure 6E).

Few of these models attempt to reconcile the data from previous studies with results recorded in a different system, and do not account for all the experimental observations. However, since the techniques used involved different experimental conditions and methodology, this may account for incompatible results. Careful evaluation of previous data is necessary in proposing a model for nucleocytoplasmic transport.

These models differ in the behavior they predict for the FG nups in several areas: the dynamic versus static behavior of the domains; the interactions between the FG repeats of the domains; whether the different nups are behaving homogenously to one another; how cargo binding affects the structure of the domains; how long a cargo molecule must remain bound to an FG repeat in order to transit the pore. The dynamic behavior predicted for the FG domains in the entropic exclusion model is in opposition to that predicted by the hydrophobic gel model, in which the FG domains are static. The majority of transport models do not differentiate between the FG nups, but the forest model and the dual gate model both suggest that the FG domains of different nucleoporins may have different properties.

While many of these models predict differing behavior for the cargo, they both invoke rapid binding and unbinding of cargo molecules from the FG repeats during transit. In contrast, the Brownian ratchet model predicts only a single, or a few, binding steps per transit, and the collapse model predicts that a single FG domain makes many

contacts with a karyopherin Different affinities between karyopherins and FG domains have been measured experimentally, with K_D values ranging from 0.4 ±0.02 nM to ≥4μM, depending on which technique was used and which nucleoporin and cargo molecule were studied (Bayliss et al., 1999; Ben-Efraim and Gerace, 2001; Ribbeck and Görlich, 2001; Pyhtila and Rexach, 2003; Terenbaum-Novatt et al., 2012). While a K_{off} value of $\geq 3.3 \times 10^{-2}$ has been measured between Kap95 and Nup1 in vitro, a systematic study of K_{off} values in vivo would help determine how long cargo molecules may remain bound to NPC components (Pyhtila and Rexach, 2003). One was in which these processes could be studied is by using FCS; this technique has been used to distinguish between karyopherin-mediated transport and passive diffusion, however these studies did not address the kinetics of cargo unbinding from FG repeats (Cardarelli and Gratton, 2010; Cardarelli et al., 2011).

These models are often based on the behavior of exogenously expressed FG domains in *in vitro* assays, or on computational modeling. However, in a cell the arrangement and density of the FG domains are very different than in many of the *in vitro* assays. It is unclear how the circular geometry of the NPC and the extremely high local concentration of FG repeats affect the behavior of these domains *in vivo*. Studying these proteins in their native context in live cells in therefore crucial for differentiating between the models for transport and determining the mechanism by which cargo moves through the NPC.

Fluorescence Anisotropy

Fluorescence anisotropy is a powerful tool that can be used to probe a protein's environment, determine the size or mobility of molecules, reveal the rotational diffusion of membrane proteins, and quantify the proximity or interactions between proteins with Förster resonance energy transfer (FRET) measurements (Axelrod, 1979; Velez and Axelrod, 1988; Yuan and Axelrod, 1995; Gautier et al., 2001; Mattheyses et al., 2004). Combining these measurements with microscopy allows the determination of spatial variations in fluorescence anisotropy.

Principles of Anisotropy Measurements

This section outline the principles involved in making anisotropy measurements of fluorescent molecules; for more details, see textbooks of biophysical chemistry (Cantor and Schimmel, 1980).

When a fluorophore absorbs a photon of light, it can transition from the ground electronic state to an excited state. From the excited state, some energy is rapidly dissipated through vibrational relaxation, following which there are different processes by which the molecule can return to the ground state: non radiative processes; non radiative transfer of energy to another molecule via FRET, which causes excitation of the acceptor molecule; intersystem crossing to a triplet state; emission of a photon (i.e., fluorescence). The transitions between the electronic states of a molecule are associated

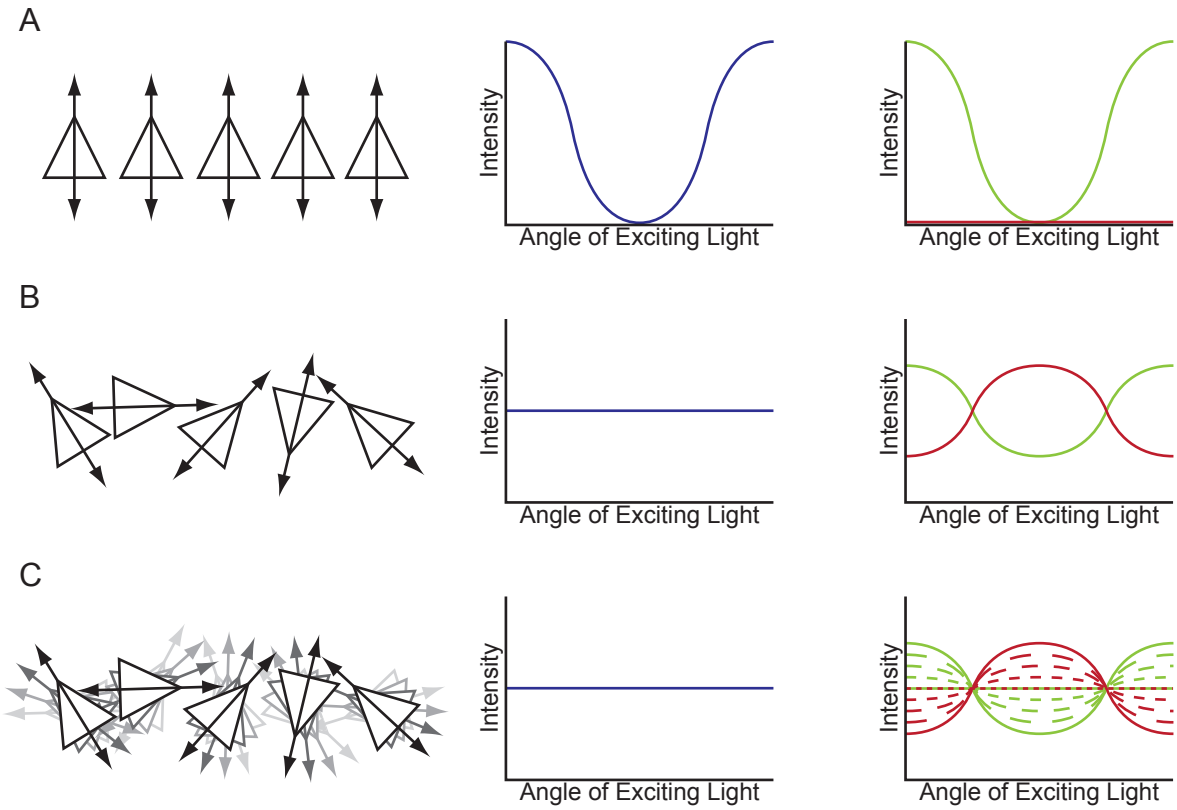

Figure 7: Emission from Aligned and Randomly Oriented Fluorophores. The first column shows the orientation of the fluorophores; the second column shows the total light emitted after excitation with light of different polarizations; the third column shows the emitted light split into vertical (green) and horizontal (red) components. A) Immobile fluorophores aligned in a single orientation are maximally excited by light polarized parallel to their dipoles and emit light of a single polarization. B) Immobile fluorophores with a random distribution of orientations emit the same total intensity of light for all excitation orientations and emit light polarized parallel to the excitation polarization. C) Mobile fluorophores with a random distribution of orientations emit the same total intensity of light for all excitation orientations; the emitted light is more depolarized the more mobile the fluorophore is.

with transition dipole moments for the absorption and emission of light, these are the absorption dipole and emission dipole, respectively. When exposed to linearly polarized light, the orientation of the excitation dipole with respect to the electric vector of the excitation light determines the probability of absorption. This probability *p* is:

$$p \propto \cos^2\theta, \qquad [1]$$

Where θ is the angle between the absorption dipole and the electric vector of the exciting light. Therefore, fluorophores with absorption dipoles parallel to the polarization of the exciting light will be preferentially excited, while fluorophores with perpendicular absorption dipoles will not be excited (Figure 7A). Within a population of randomly oriented fluorophores, a selected subset of fluorophores will be excited (Figure 7B).

When an excited fluorophore emits light, the light will be polarized parallel to the emission dipole. The emitted light can be split into components parallel ($I_{/\!/}$) and perpendicular ($I_{\perp}$) to that of the exciting light using polarized filters (Figure 7). This forms the basis for anisotropy (*r*), which is a quantification of the extent to which the polarization of the exciting light is maintained, and is defined by

$$r = (I_{/\!/} - I_{\perp}) / (I_{/\!/} + 2I_{\perp}) \qquad [2]$$

Where the denominator, ($I_{/\!/} + 2I_{\perp}$), represents the total light intensity. This consists of the component collected in the parallel channel ($I_{/\!/}$), the component collected in the perpendicular channel, ($I_{\perp}$) and a component in the vertical *z* which is not collected but assumed to be equal to ($I_{\perp}$).

The polarization of fluorescence is affected by several factors. The first is the orientation of the fluorophore with respect to the exciting light. When fluorophores with

dipoles that are not parallel to the excitation light are excited, they emit light of a different polarization. Second, the absorption and emission dipoles of a fluorophore are not necessarily parallel, and therefore the polarization of light may be changed in the absorption/emission process. Third, there is a delay between the absorption of a photon and the emission of light- the fluorescence lifetime- the length of which is a property of the fluorophore. The mobility of a fluorophore will therefore affect depolarization, because if it rotates during this time, the initial polarization will be lost. Factors affecting the mobility of the fluorophore therefore affect anisotropy; these include viscosity, temperature, and the size of the molecule (Swaminathan et al., 1997). Additionally, the longer the fluorescence lifetime, the more time the molecule has to move before emission. The final factor which causes depolarization is non radiative energy transfer between fluorophores (i.e. FRET). This occurs when the emission spectrum of the donor fluorophore overlaps with the absorption spectrum of the acceptor fluorophore. The efficiency of this process is dependent on the distance between the fluorophores and the relative orientation of their dipoles.

The anisotropy value of a fluorophore or a population of fluorophores therefore contains information about three parameters: the orientation of the fluorophore, its mobility, and its proximity to other fluorophores (Figure 8). Fluorophores which are more mobile, less oriented, and closer together will have lower anisotropy than those which are immobile, aligned to the exciting light, or sparsely distributed.

The values of anisotropy recorded will also depend on the properties of the fluorophore itself. GFP is a 26.9kDa protein with an average fluorescence lifetime of 3ns (Volkmer et al., 2000). The absorption and emission dipoles of GFP have been estimated

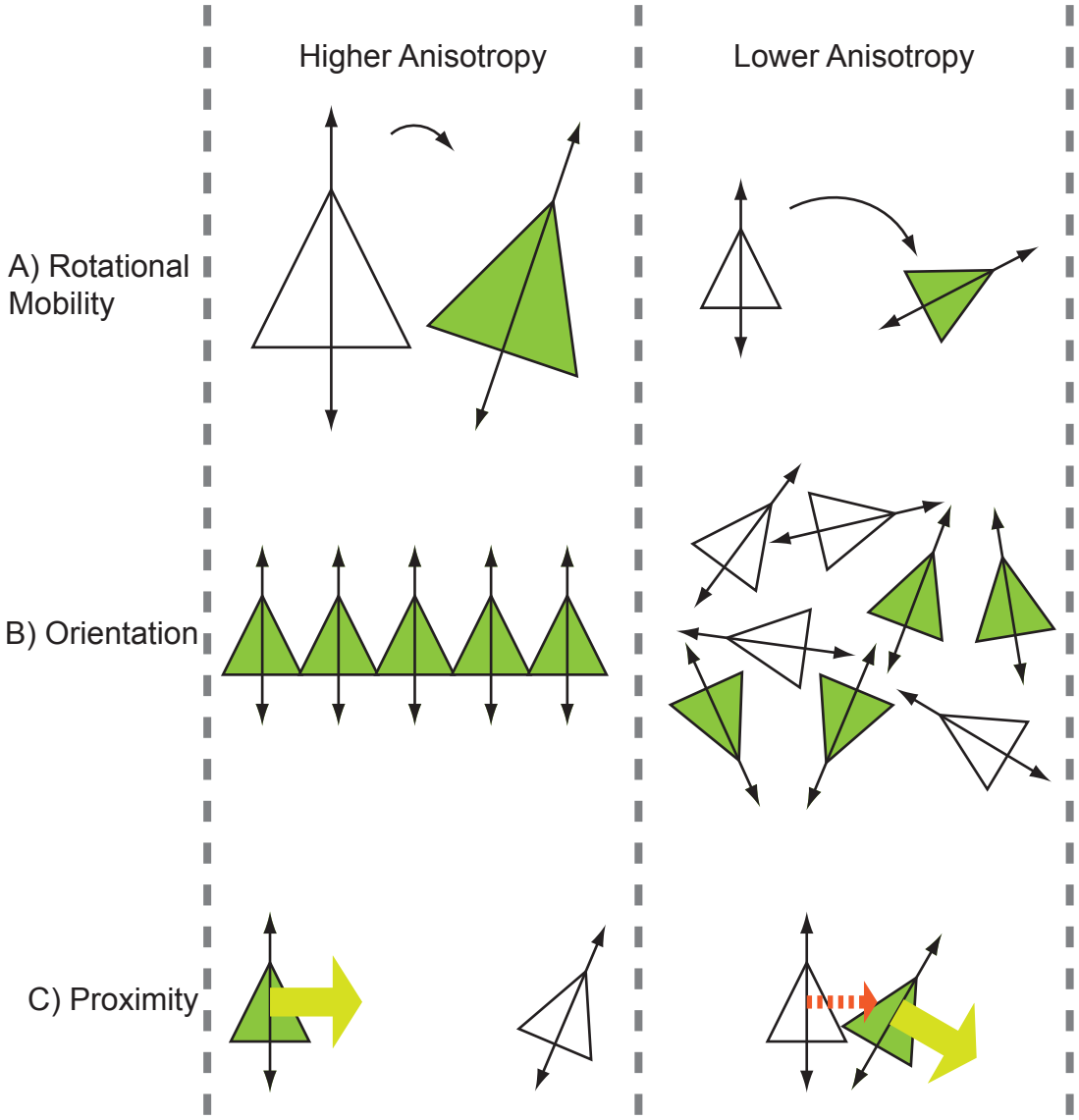

Figure 8: Information from Anisotropy. The first column shows factors that will lead to a higher measured anisotropy, the second column shows factors that will lead to a lower measured anisotropy. A) Rotational mobility: larger molecules will move less during the fluorescence lifetime and will have a higher anisotropy than smaller molecules. B) Orientation: fluorophores oriented in the same direction and parallel to the excitation light will have a higher anisotropy than those which are randomly oriented. C) Proximity: sparsely distributed fluorophores will have a higher anisotropy that fluorophore which are close enough in space for FRET to occur.

to be within 5° of each other; therefore if the GFP is immobile and aligned to the exciting light, the polarization of the exciting light will be maintained (Inoué et al., 2002; Rosell and Boxer, 2003).

Given these parameters, theoretical anisotropy values for GFP under different conditions can be calculated. If GFP is free to rotate in solution, the anisotropy will be 0.32. If GFP is randomly oriented but not mobile, the anisotropy will be 0.4. If GFP is rigidly held in a defined orientation, the anisotropy will vary depending on the orientation of GFP relative to the polarization of the exciting light. Theoretically, the maximum achievable anisotropy is 1, if the dipole is oriented exactly parallel to the exciting light, whereas the minimum anisotropy for a perpendicular orientation is -0.5 (Cantor and Schimmel, 1980).

Anisotropy Measurements in Biological Systems

Anisotropy allows the detailed study of higher-order organization in biological systems. The orientation of fluorophores embedded in a biological membrane has been revealed by fluorescence polarization microscopy (Blackman et al,, 1996; Sund et al., 1999). On the basis of these types of measurements, polarization techniques have been used to monitor changes of membrane orientation during exocytosis (Anantharam et al., 2010).

Anisotropy has also been used to probe the relative degree of order and disorder of different protein domains within the MHC complex. In this study, GFP was placed

either at the C terminal end of the MHC molecule H2L or within the sequence of the protein itself. Polarized fluorescence measurements of the GFP within the protein sequence showed that it was oriented relative to the membrane, revealing a rigid attachment to the target molecule. This allowed the determination of FRET homotransfer that showed the clustering state of the molecule differs following peptide loading and export from the ER. In contrast the GFP at the C terminus was shown to be disordered relative to the membrane (Rocheleau et al., 2003).

The arrangement and symmetry of yeast septin proteins during septation have also been studied using polarization microscopy. Here, the GFP was orientationally constrained by fusing it to the septins using a rigid helical linker. This allowed the determination of the average direction of a septin filament, and it was shown that the septins undergo a 90° change in orientation during the transition from an hourglass to a ring structure during septation (Vrabioiu and Mitchison, 2006; 2007).

In each of these studies, anisotropy established the organization of a fluorophore relative to a greater structure (i.e. the plasma membrane, and the septin hourglass and ring structures). Anisotropy microscopy allows the measurement of the order and dynamics of membrane-bound or macromolecular structures, which are otherwise difficult to study. This thesis will describe the application of these techniques to the nuclear pore complex; and demonstrate their utility in determining protein orientation and the organization of unstructured domains in a macromolecular complex.

Chapter 2: Microscope Set-up and Theory

Microscope Set-up and Calibration

In order to measure anisotropy, a microscope system had to be modified to deliver linearly polarized light to the sample and record the emission in parallel and perpendicular channels. The sample was excited using a 488nm argon laser; this was polarized at the source, but to clean up the polarization of the light a polarizing filter was placed in the light path. In the microscope co-ordinate system ***xyz***, ***z*** is the optical axis and ***xy*** is the imaging plane. To control the axis along which the incoming light was polarized, a half wave plate was used, allowing for fine alignment. Fluorescence emission was split based on polarization into two channels aligned parallel and perpendicular to the excitation polarization. A clean-up polarizer was placed in the light path of each channel, and they were imaged simultaneously side by side. $I_{\parallel}$ is the light collected in the parallel channel, and $I_{\perp}$ is the light collected in the perpendicular channel.

Light of different polarizations is differentially transmitted through the system. In order to determine an accurate anisotropy value, this has to be corrected for. To do so, a fluorescent solution with a theoretical anisotropy of 0 was imaged. This allowed the determination of a system dependent factor, *G*, accounting for differences in sensitivity in the detection channels $I_{\parallel}$ and $I_{\perp}$. A deep-well solution of dilute fluorescein was imaged with light polarized both in ***x*** and ***y*** (i.e. two polarizations of the exciting light which are perpendicular to each other), and averaged to give *G*.

In these experiments, the excitation light used was ***y***-polarized, and in an ideal system $I_{/\!/} = I_y$ and $I_{\perp} = I_x$. In our experimental system the sample was observed with a high numerical aperture (NA) objective lens (NA=1.45), which causes a mixing of polarization since at high angles of collection there is a "***z***" polarization component mixed in to both $I_{/\!/}$ and $I_{\perp}$ (Axelrod, 1979). With the ***z***-axis corresponding to the optical axis and imaging the ***xy*** plane, the observed intensities are given by:

$$I_{\parallel} = K_a I_z + K_b I_y + K_c I_x \; ; \; I_{\perp} = K_a I_z + K_c I_y + K_b I_x \qquad [3.1, 3.2]$$

Where I_x, I_y, and I_z are the intensities which would be observed with a polarizer oriented along the ***x***, ***y***, or ***z*** axis as detected by a small aperture, and correspond to the theoretical unmixed light intensities. I_x and I_y are the corrected $I_{/\!/}$ and $I_{\perp}$, and can be calculated from this equation using weighing factors derived for our system: K_a =0.385, K_b =1.006, K_c =0.030, and the simplifying assumption $I_x = I_z$ as in a randomly oriented system.

The system was calibrated by measuring steady-state anisotropies for small inorganic dyes in dilute solution as well as monomeric GFP expressed in the cytoplasm of living cells. These vary in their fluorescence lifetimes and rotational diffusion and therefore will yield a range of anisotropy values. The anisotropy of these fluorophores was measured with both ***x*** and ***y*** excitation polarizations. Following correction, these values were not sensitive to whether the exciting light was polarized in ***x*** or in ***y***. The fluorescent dyes used, their lifetimes (τ) and measured anisotropy were: Rose Bengal (τ = 76ps; r = 0.28±0.01), Erythrosin B (τ = 75ps r = 0.27±0.004), $Ru(Bipy)_3$ (τ = 5.21µs, r = 1.85^{-6}), and fluorescein (τ = 4ns r = 0.019±0.002). For monomeric GFP expressed in the

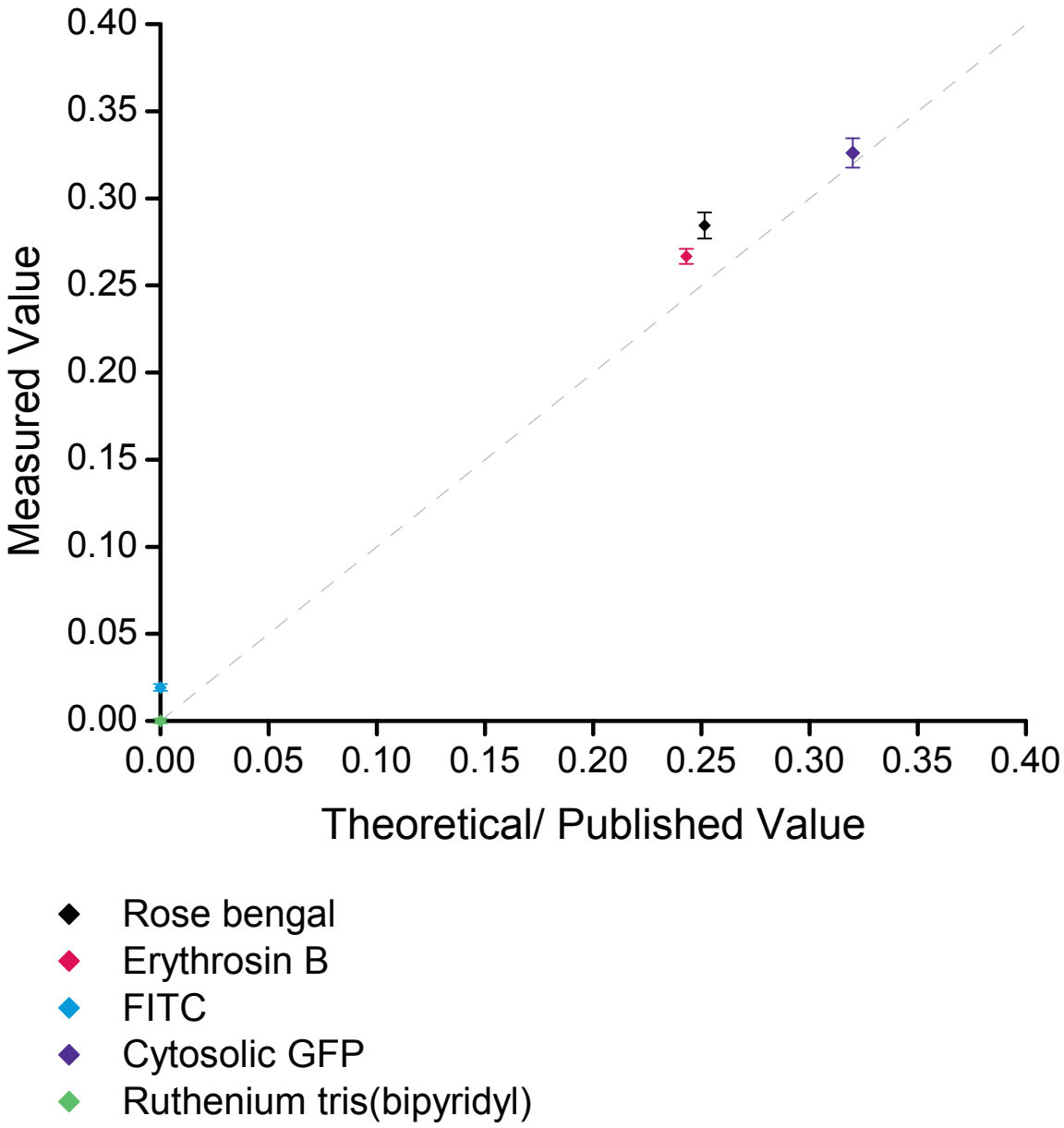

Figure 9: Calibration of Microscope with Fluorescent Standards. Comparison of expected and measures anisotropy values for five fluorescent molecules. Error bars show standard deviation.

cytosol of HeLa cells $r = 0.326 \pm 0.008$. These measurements all agree with previously published values (Figure 9) (Clayton et al., 2002; Thompson et al., 2002). This demonstrates that the microscope set up and corrections for transmission differences and high NA yield accurate anisotropy measurements.

Theory of Dipoles in the NPC

A theoretical framework was created for studying proteins tagged with GFP in the NPC using polarization microscopy. This framework took into account the angle between the absorption and emission dipoles, the orientation of GFP within the NPC, the organization of the NPC within the NE, and the number of copies of the nup within the NPC.

The NPC has eightfold symmetry around its nucleocytoplasmic axis and the central core has a two-fold dyad symmetry across the NE. In budding yeast, the diameter of the NPC is ~100 nm, the diameter of the central channel is ~40 nm, and its length along the nucleocytoplasmic axis is ~30 nm. One NPC can have 8, 16, or 32 copies of a given protein.

The coordinate system ***xyz*** was defined with respect to the microscope where ***z*** is the optical axis, the ***xy*** plane is the imaging plane, and ***y*** is the direction of the electric field dipole of the polarized excitation light. The nuclear cross-section which is imaged lies in the ***xy*** plane. ***N***, the nucleocytoplasmic axis, lies in the ***xy*** plane and is always normal to the NE. The position of an individual NPC in the NE is described by the angle γ between ***N*** and ***y*** (Figure 10A).

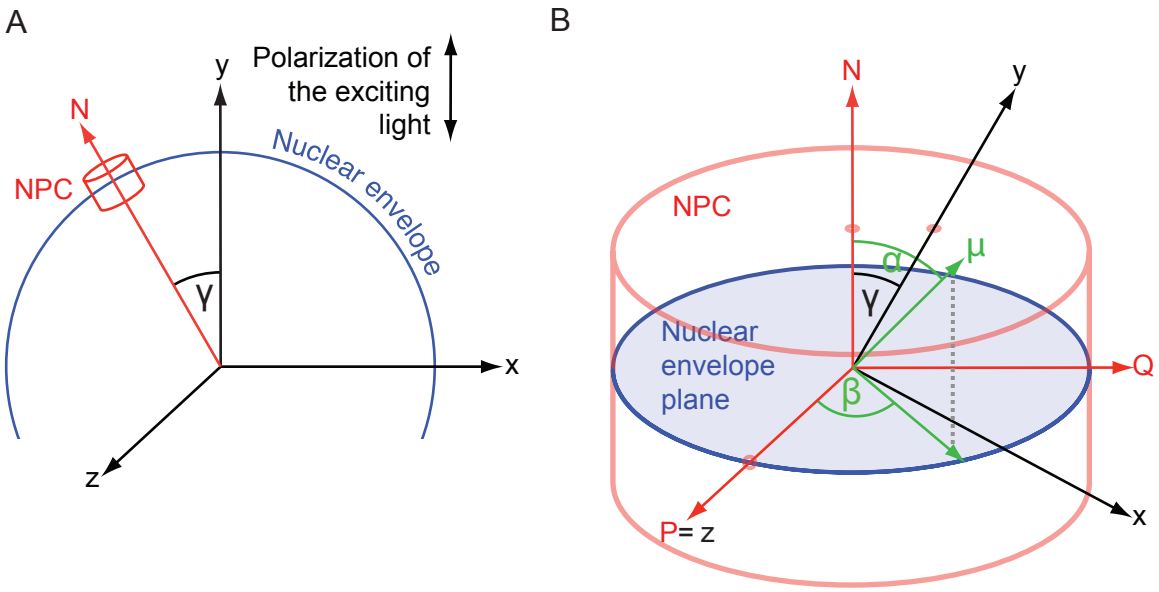

Figure 10: NPC Coordinate System. Nuclear envelope is shown in blue; nuclear pore complex is shown in red. A) Microscope coordinate system: ***z*** is the optical axis; ***xy*** is the imaging plane, and the excitation light is polarized in ***y***; ***N*** is the nucleocytoplasmic axis and lies in the ***xy*** plane, normal to the NE; γ relates ***N*** and ***y***. B) NPC coordinate system: ***N*** is the nucleocytoplasmic axis; ***PQ*** is the plane of the NE, ***P*** is parallel to ***z***; ***μ*** is the dipole of a fluorophore and is defined by α, the polar angle between ***N*** and ***μ***, and β, the azimuthal angle.

The coordinate system ***NPQ*** was defined with respect to the NPC. ***P*** is parallel to ***z*** and ***Q*** lies in the ***xy*** plane. ***PQ*** is the plane of the NE. The excitation and emission dipoles of a fluorophore can be defined in either the ***NPQ*** or ***xyz*** coordinate system. The dipole $\boldsymbol{\mu}$ of a fluorophore rigidly attached to the NPC is defined by two angles: α, the polar angle between $\boldsymbol{\mu}$ and ***N***, and β, the azimuthal angle, describing the orientation in the NE plane (Figure 10B). Due to the symmetry constraints of the NPC, GFP molecules attached to nucleoporins will be present in eight or sixteen copies per NPC.

In these experiments, the focal plane is a slice through the mid-plane of the nuclear envelope. Since **N** is perpendicular to the NE, individual NPCs are oriented at different angles relative to the single excitation polarization depending on the orientation of the NE. Therefore, in a single exposure, spatially separated NPCs oriented at 0°-360° to the exciting light are imaged simultaneously. This allows for measurements of many NPC orientations to be made in a single cell.

If a fluorophore is rigidly attached to an NPC protein, all the fluorophores will be held in the same orientation with respect to the NPC. The orientation of the NPC to the electric field dipole of the exciting light will change depending on the orientation of the NE, and therefore so will the orientation of the dipole. This will result in modulation of the anisotropy value depending on the angle γ.

In contrast, if the fluorophore is able to adopt a random orientation with respect to the protein, or is mobile, each of the copies of the fluorophore will have a different value for α and β. Therefore, the fluorophores will not be oriented with respect to the NPC, and the anisotropy measured will be independent of NE orientation and will be a single value. Theoretically, the technique can be used to distinguish between a domain that is

disordered and rigidly held (which will have an anisotropy of 0.4) and one that is disordered and flexible (which will have an anisotropy of 0.32 if it is completely free to rotate). In practice, the absolute anisotropy measured will be affected by experimental factors such as the cellular background (discussed below) which makes it more difficult to distinguish between these two possibilities experimentally. However, polarization microscopy of the NE can be used to easily distinguish between a population of GFP which is randomly oriented and one in which GFP is held in a specific orientation within the NPC.

Determination of the Orientation of Fluorophores in the NPC

Eight fluorophores held in a specific orientation in the NPC will differ in their position around $\boldsymbol{N}$ (as indicated by angle β), but should all share the same α. If there are sixteen symmetrical nups, one ring of eight is related to the other by a rotation of 180° around an axis within the plane of the NE. $\boldsymbol{\mu}$ is invariant with respect to rotation by 180°($\alpha = \alpha$+180), and therefore the anisotropy will not be affected by whether there is 8 or 16 copies.

For fluorophores in a specific orientation, the anisotropy as a function of nuclear envelope orientation can be calculated:

$$r(\gamma) = (K_2 - K_1)\frac{I_y - I_z}{(K_1+2K_2)I_x+(K_2+2K_1)I_y+3K_3I_z} \qquad [4]$$

where

$$I_x = \frac{1}{2}a^2c^2 + a^2d^2 + \frac{3}{8}b^2c^2 + \frac{1}{2}b^2d^2 - 2abcd \quad [5]$$

$$I_y = a^4 + 3a^2b^2 + \frac{3}{8}b^4 \quad [6]$$

$$I_z = \frac{1}{2}a^2 \sin^2\alpha + \frac{1}{8}b^2 \sin^2\alpha \quad [7]$$

with $a = \cos\alpha \cdot \cos\gamma$, $b = \sin\alpha \cdot \sin\gamma$, $c = \sin\alpha \cdot \cos\gamma$ and $d = \cos\alpha \cdot \sin\gamma$.

K_1, K_2 and K_3 are correction factors for high numerical aperture observation (discussed above). The derivation of these equations is given in Kampmann 2009.

The predicted anisotropy for any α value can be plotted as a function of position around the NE. Solving this equation over all possible α angles shows how the variance in anisotropy as a function of NE orientation depends on the fluorophore orientation (Figure 11A). For all fixed fluorophore orientations there is a modulated anisotropy function $r(\gamma)$. As expected from the symmetry of the NPC / NE system, $r(\gamma)$ has a periodicity of 180º and displays mirror symmetry around the axes γ = 90º, γ = 180º and γ = 270º in all cases. Three types of anisotropy patterns are predicted: Type I, displaying maxima for γ = 0º and 180º and minima for γ = 90º and 270º (Figure 11A, blue curve), Type II, displaying minima for γ = 0º, 90º, 180º, and 270º alternating with maxima (green curve), and Type III, with minima for γ = 0º and 180º and maxima for γ = 90º and 270º (yellow curve).

The extremes of these patterns can be illustrated with three examples. In the first, α = 0° (Figure 12A). All eight GFP dipoles are parallel to ***N.*** The NPC at the top of the NE is positioned at γ = 0. In this position, all eight dipoles are parallel to the excitation polarization. As γ increases, the efficiency of excitation is modulated by a factor of

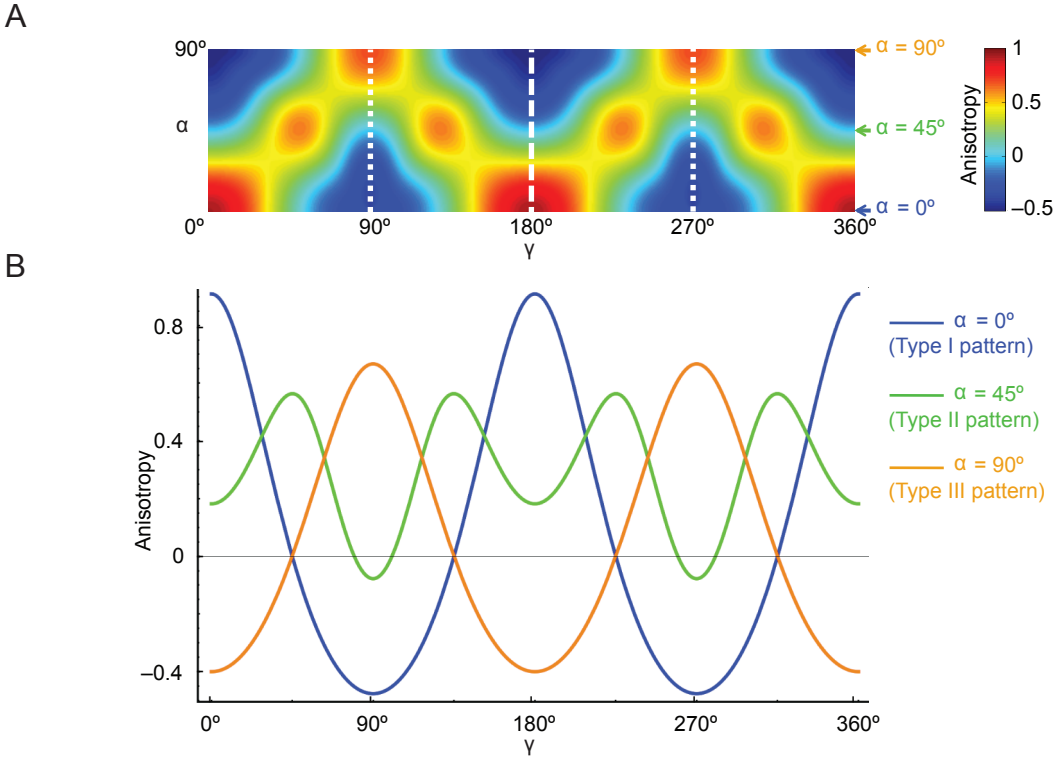

Figure 11: Predicted Anisotropy Values. A) For a fluorophore with any orientation given by the angle α, the anisotropy r can be predicted as a funtion of the nuclear envelope orientation γ. All predicted functions $r(\gamma)$ have a period of 180° (indicated by dashed line) and have mirror symmetry (dotted lines). B) Examples of three predicted pattern types. Anisotropy values for three different values of α are shown as a function of NE position.

$\cos^2(\gamma)$. The polarization of the emitted light also changes, decreasing the anisotropy. When $\gamma = 90°$, as shown with the NPC on the side of the NE, the dipoles are perpendicular to the excitation polarization and will not be excited. This gives a curve which has maxima at $\gamma = 0°$ and minima at $\gamma = 90°$: i.e. Type I.

In the second case, $\alpha = 45°$ (Figure 12B). The GFP dipoles are arranged with equal components parallel and perpendicular to ***N***. When determining the orientation of these dipoles with respect to both the NE and excitation polarization, there are more factors to consider. Any component of the dipoles in ***z*** remains in ***z*** regardless of position on the NE, while those in the ***xy*** plane have different excitation probabilities depending γ. This results in a more complex theoretical plot, which is nonetheless similar to the first cases in that anisotropy is characterized by a modulation with respect to NE position. This plot is a Type II pattern.

In the final example, $\alpha = 90°$ (Figure 12C). Each dipole is perpendicular to ***N***, and two different orientations for the GFP dipoles are illustrated: either pointing into the NPC, like spokes of a wheel, or tangential to the perimeter of the NPC, arranged in a ring. The two arrangements differ in the angle β, but the predicted anisotropy is the same for these arrangements because the anisotropy measurement is macroscopic and insensitive to the internal organization of these dipoles. The dipoles for an individual NPC in either case can be rearranged within the NE plane, without altering their orientation, to form the distribution shown the other case. This illustrates how β does not contribute to the anisotropy.

For $\alpha = 90°$, at $\gamma = 0°$ none of the dipoles are aligned with the excitation polarization. Half are parallel to ***z*** and will not contribute to the fluorescence signal; the

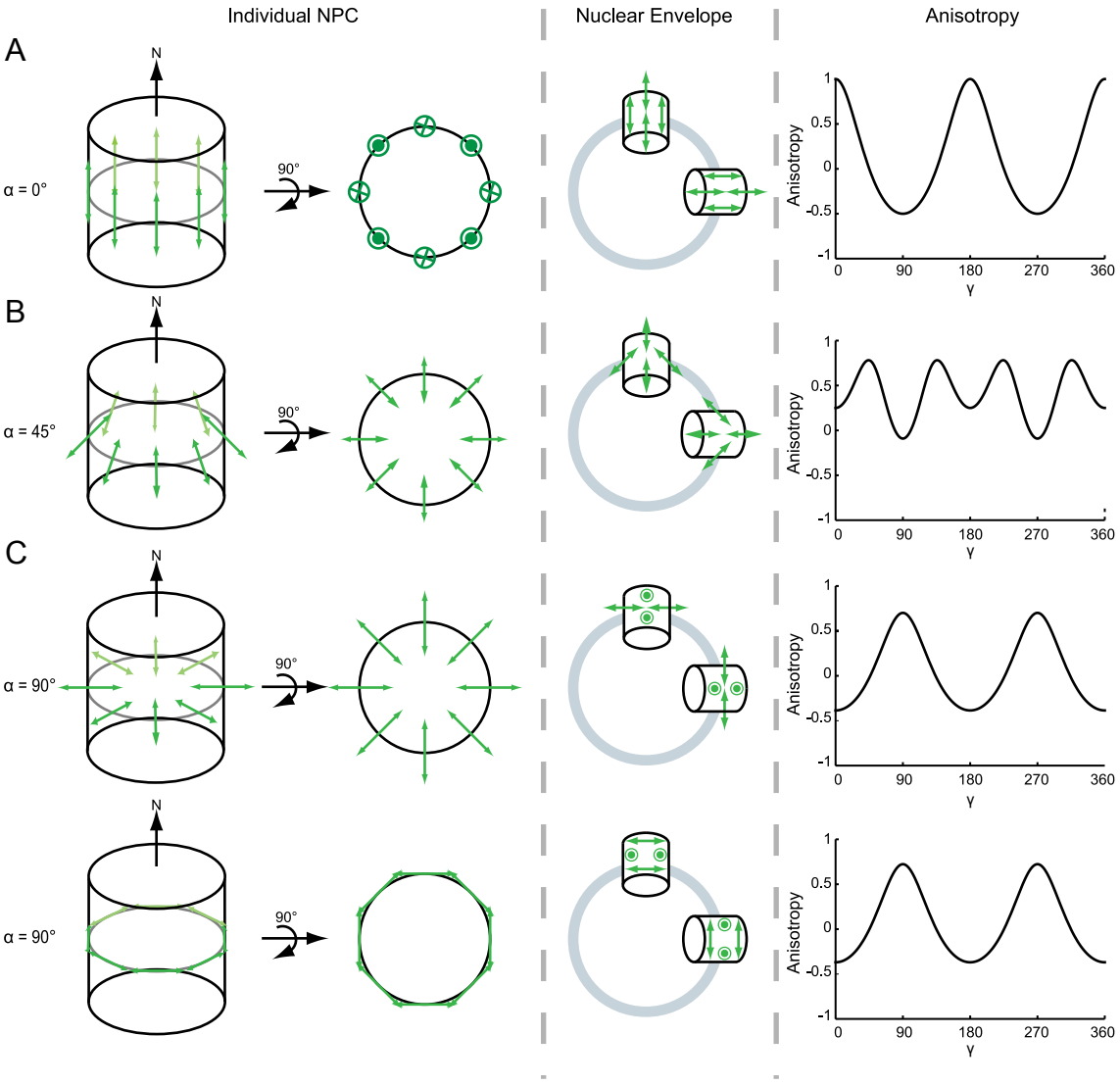

Figure 12: Examples of Dipole Orientations in the NPC. Excitation light is polarized in the vertical direction; 0º is parallel to the polarization of light. A) $\alpha = 0º$; Dipoles oriented parallel to the nucleocytoplasmix axis (***N***). There is maximum anisotropy when $\gamma = 0°, 180°, 360°$ and minimum anisotropy when $\gamma = 90°, 270°$ (Type I). B) $\alpha = 45°$; Dipoles oriented at 45° to ***N***. The curve has maxima at $\gamma = 45°, 135°, 225°, 315°$ and minima at $\gamma = 0°, 90°, 180°, 270°, 360°$ (Type II). C) $\alpha = 90°$; Dipoles are oriented perpendicular to ***N***. The dipoles can be arranged two different ways inside the NPC and yield the same anisotropy because anisotropy is insensitive to β. The anisotropy has maxima at $\gamma = 90°, 270°$ and minima at $\gamma = 0°, 180°, 360°$ (Type III).

remainders are parallel to ***x*** and cannot be excited. As γ increases, the component of the dipoles which is in ***x*** is rotated in the ***xy*** plane and the excitation probability increases. The projections in ***z*** do not change with γ. At γ = 90° the dipoles are maximally aligned to the excitation polarization. This gives a curve which has maxima at γ = 90° and minima at γ = 0°, which is a Type III pattern.

The above examples illustrate the three possible pattern types. However, they show the extremes of these patterns. Additionally, the amplitude of $r(\gamma)$ within one pattern type changes monotonically with α. Theoretically, every possible orientation of α corresponds to a unique anisotropy pattern and the amplitude and the shape of the measured curve can be used to determine the orientation of the GFP dipole in the NPC.

In practice, experimentally measured anisotropy values will differ from the theoretical values due to the following factors: averaging of light from NPCs with slightly different orientations within the curved nucleus, because of the finite z-resolution of the microscope; corrections applied due to imaging through a high NA objective; photobleaching; binning of anisotropy values according to position around the nuclear envelope at the analysis stage; potential flexibility of the GFP-tagged nucleoporin domain; different orientations for multiple copies of the same protein.

The resolution of our microscope in the ***z*** direction for light emitted from GFP (~525 nm) is 525 nm$\cdot n/\mathrm{NA}^2 \approx$ 380 nm. The yeast nucleus has a radius of ~1000 nm, and the mammalian nucleus has a radius of ~4000nm. Even if the nuclear cross-section of the nucleus is perfectly in focus, some light from nuclear envelope regions above and below the focal plane will be collected, leading to weighted averaging of light from NPCs with different γ values (within a range of ~ ±10º for yeast; mammalian nuclei are bigger and

will have less curvature in the focal plane). Due to the spherical symmetry of the nucleus, this is equivalent to a convolution of $r_\alpha(\gamma)$ with a function that describes the decay of the focal field around the focal plane, leading to a decreased amplitude of the anisotropy pattern.

As discussed above, the polarization of the observed fluorescence is distorted by collection with a high NA objective, and correction factors were applied to all data. This is an important step for recovering anisotropy values from isotropically distributed fluorophores, and was necessary to achieve accurate anisotropy measurements during calibration. However, this correction assumes equal fluorescence in the two perpendicular channels I_x and I_z, which is correct for isotropically oriented fluorophores but not for those which are have a distinct orientation. Therefore, the corrections applied are not necessarily accurate for ordered fluorophores in the NPC.

To test the effect applying these corrections has on ordered data, theoretically observed $I_{/\!/}$ and $I_\perp$ images were calculated by combining the high NA correction factors and known intensities of I_x, I_y, and I_z. The correction for "un-mixing" (using the NA correction factors for an isotropic distribution of fluorophores), was then applied to the theoretical data. This generated computational curves that do not vary in shape, and vary only slightly in amplitude, from the data before un-mixing. We therefore concluded that assuming an isotropic distribution has only a small effect on the anisotropy values recorded (Figure 13).

Furthermore, if the corrections applied are appropriate, the anisotropy of a structured GFP in the NPC should change in phase, but not amplitude, when excited with light of different polarizations. This was tested using Nic96 tagged with GFP at its C

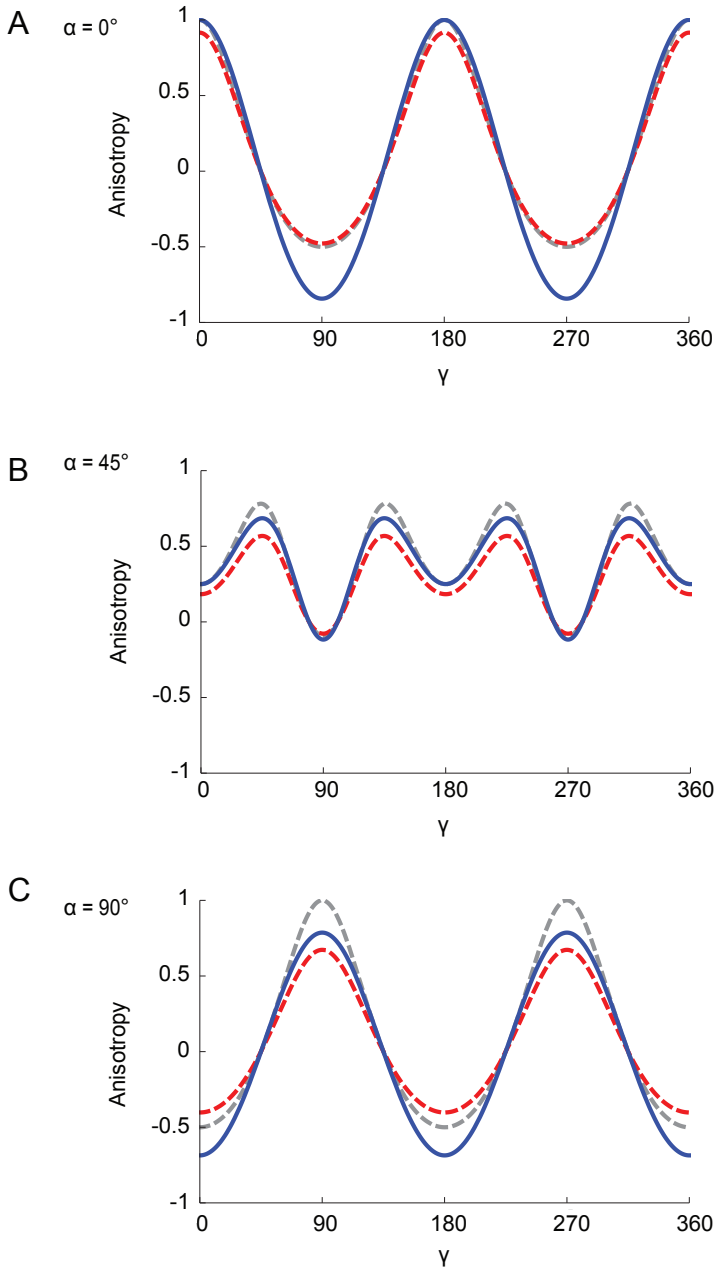

Figure 13: Corrections for High NA Observation of Polarized Light. Theoretical calculations of anisotropy as a function of nuclear envelope position with three different assumptions. A) $\alpha = 0°$, B) $\alpha = 45°$, C) $\alpha = 90°$. The ideal theoretical curve (grey dashed). Polarizations mixed as they are through the microscope (red dashed). The high NA correction applied to the mixed polarizations (blue). The blue line most closely resembles the actual processing of the data.

terminus. Figure 14 shows that when the exciting light is rotated through 90°, the amplitude of the anisotropy curve does not change.

A general concern with polarization microscopy is that photobleaching, like excitation, depends on the orientation of fluorophores with respect to the polarized light direction. Fluorophores oriented with their dipoles parallel to exciting light are photobleached more efficiently than fluorophores oriented with their dipoles perpendicular to the exciting light. As a consequence, NE regions with high anisotropy values would be most affected by photobleaching. If significant photobleaching occurs during the exposure, the amplitude of the anisotropy pattern will be decreased. The extent of photobleaching occurring during the 2000 ms exposure time was tested, and minimal photobleaching was detected, and this did not have a significant effect on anisotropy.

During the automated extraction of anisotropy curves from the microscopic images (discussed further in the section below), average anisotropy values are calculated for image sectors that cover γ values in 11.5º increments (for yeast nuclei) or 10º increments (for mammalian nuclei). This corresponds to convolution of $r_\alpha(\gamma)$ with a top-hat function that is 11.5º or 10º wide, respectively. Again, this will decrease the amplitude of the anisotropy pattern.

If a nucleoporin is somewhat flexible, there would be deviations from a single value of α. In the simplest case, each construct will have one average α value corresponding to an energy minimum, and display a distribution of α values around it. This situation would lead to convolution of $r(\alpha, \gamma)$ with this distribution function in the α direction. This would decrease the amplitude of the measured anisotropy curve, and depending on the flexibility of the protein, may prevent determination of its orientation. However, for a

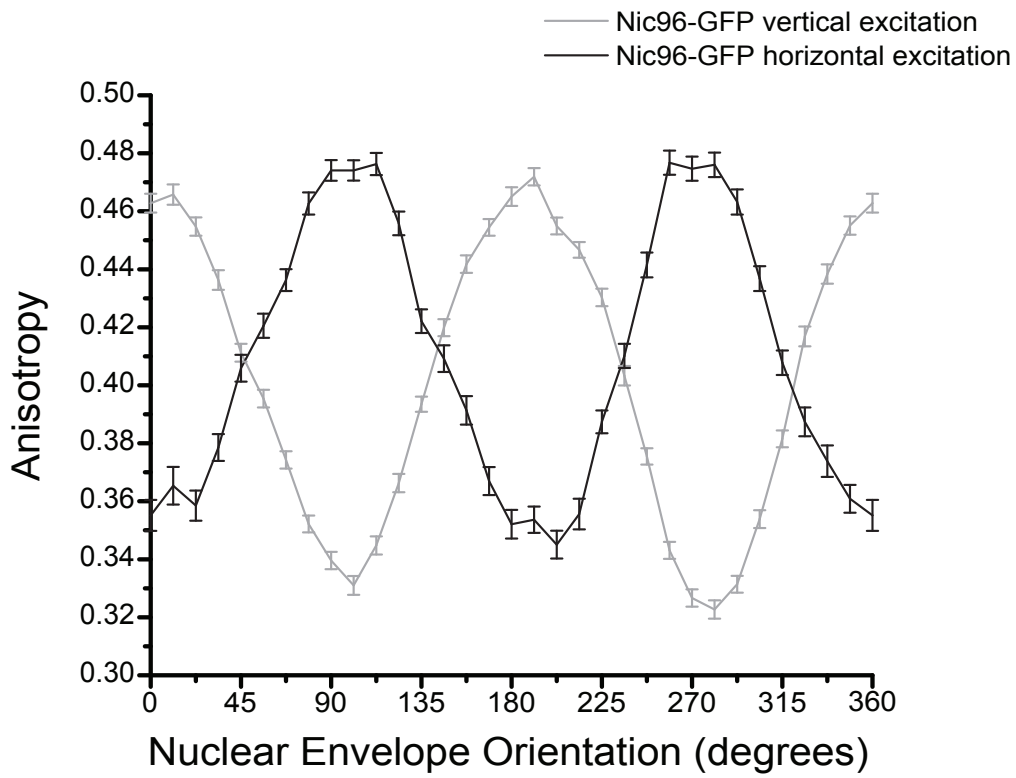

Figure 14: Rotation of Excitation Polarization. Anisotropy of Nic96-GFP when excited with either vertically polarized light (grey) or horizontally polarized light (black). The curves are of comparable amplitude but shifted in phase through 90°.

protein with a small degree of flexibility, it is still be possible to determine the average orientation.

One further complicating factor is the potential existence of multiple orientations for an individual nucleoporin molecule, which would prevent the determination of a single orientation. For example, it is possible that a nucleoporin could have distinct conformations that correlate with functional states of the NPC. Furthermore, while nucleoporins present in eight or sixteen copies per NPC must have the same orientation with respect to the nucleocytoplasmic axis, as dictated by the eightfold and dyad symmetry axes of the NPC, nucleoporins present in thirty-two (or more) copies per NPC may occur in two (or more) distinct orientations. In these cases, the measured anisotropy would therefore reflect the vector sum of these orientations. It is difficult to exclude such a scenario on the basis of polarized fluorescence microscopy alone. However, if a robust anisotropy curve of a high amplitude is measured, the orientations of the different copies with respect to the nucleocytoplasmic axis should be similar or identical.

Each of these effects will change the amplitude, and possibly the shape, of the anisotropy curve measured. The extent of these changes may have only a slight effect, but could potentially affect the conclusions drawn from the data. The effect of these factors on anisotropy patterns was investigated using simulation. While the exact combined effect of these factors on the anisotropy pattern will depend on the experimental parameters of microscope, sample, and computational data analysis, the summed effect was approximated by convoluting $r(\alpha, \gamma)$ with a two-dimensional Gaussian. Even for very wide Gaussians, the overall pattern of the anisotropy function is similar, albeit flattened

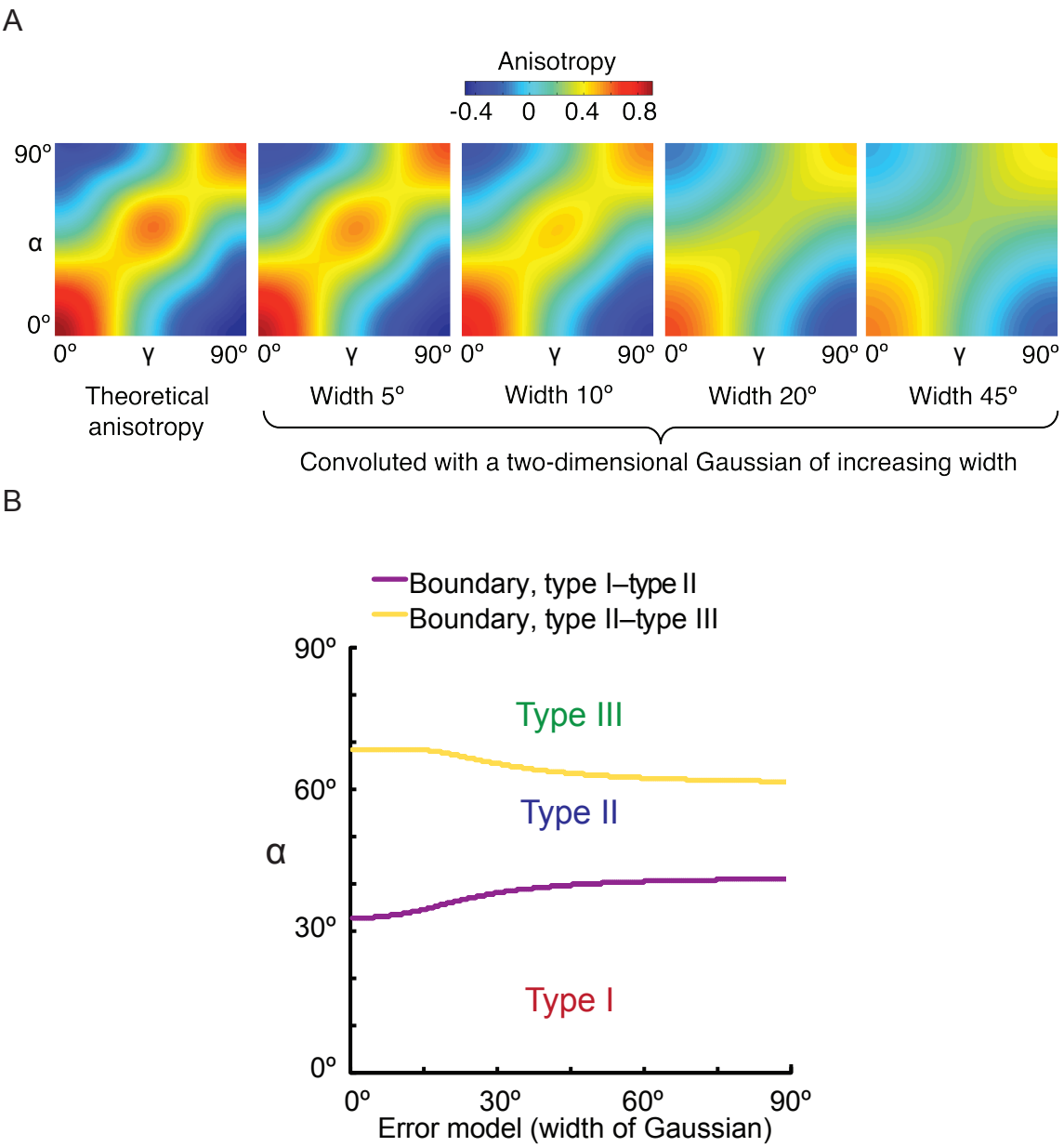

Figure 15: Effect of Experimental Factors on Anisotropy Patterns. To simulate the effect of experimental factors on the anisotropy curve shape, the theoretical anisotropy pattern was convolved with two dimensional Gaussians of increasing width. A) Left panel: theoretical anisotropy for all α values as a function of γ. Panels left to right: convolution with Gaussians of increasing width. B) Effect of Gaussian convolution on the values of α at which transitions between pattern types occur.

(Figure 15A). Therefore, determining the pattern type can be used to place limits on the orientation of the protein.

To examine for which α values the transitions between pattern types I, II and III occur, the roots of $dr/d\alpha$ for $\gamma = 0^{\circ}$ (Type I-to-Type II transition) and for $\gamma = 90^{\circ}$ (Type II-to-Type III transition) were determined. For the theoretical anisotropy pattern, the transitions occur for $\alpha \approx 33^{\circ}$ (Type I-to-Type II) and $\alpha \approx 68^{\circ}$ (Type II-to-Type III). When the anisotropy pattern is convoluted with Gaussians of increasing width, the boundaries shift to larger values of α (Type I-to-Type II) or smaller values of α (Type II-to-Type III). However, the boundaries are relatively robust over a wide range of Gaussian widths (Figure 15B).

For convolution with a 90º-wide Gaussian, which is a much more dramatic flattening of the anisotropy curves than can be expected from experimental factors, the Type I-to-Type II transition occurs for $\alpha \approx 41^{\circ}$, and the Type II-to-Type III transition occurs for $\alpha \approx 61^{\circ}$. Since the exact magnitude of anisotropy flattening due to experimental factors is unknown, we adopted the very conservative assumption that Type I patterns occur for $0^{\circ} \leq \alpha < 42^{\circ}$, Type II for $33 \leq \alpha \leq 68^{\circ}$, and Type III patterns for $60^{\circ} < \alpha \leq 90^{\circ}$ (Figure 15B).

Therefore, the pattern type should correspond directly to a range of possible orientations for the fluorophore. The amplitude of the pattern cannot be used to directly measure α, but the amplitude of different patterns can be compared as both will have been convoluted with the same factors.

Analysis of Anisotropy Data

In these experiments, nucleoporins were tagged with GFP and imaged using polarized light. Images were acquired simultaneously in the $I_{//}$ and $I_{\perp}$ channels and automated analysis routines were developed to allow accurate calculation of the anisotropy values as a function of the orientation of the nuclear envelope. Since the signal is noisy for a single cell and it may be difficult to assign an orientation for all the portions of its NE, it was necessary to analyze multiple cells and create an average, which increases the signal: noise and ensures that all of the orientations of the NE are represented. Development of automated analysis routines allowed for unbiased selection of pixels for analysis, assignment of NE orientation, and easy collation of data from multiple cells (Figure 16).

The first stage of the analysis routine was corrections for media background fluorescence and differences in transmission of light through the system which were applied to the entire image. An image of only medium (I_{medium}) acquired with the same parameters as the sample was subtracted, and the image was corrected for transmission differences and spatial differences using an average of several fluorescein images (G):

$$I = \frac{I' - I_{medium}}{\left(\frac{G}{Max(G)}\right)} \qquad [8]$$

Individual cells were identified for further analysis allowing exclusion of cells not in focus, sick cells, or cells with aberrantly shaped nuclei. A rough overlay of $I_{//}$ and $I_{\perp}$ was achieved with standard *x-y* shift values. However, correct registration is critical in

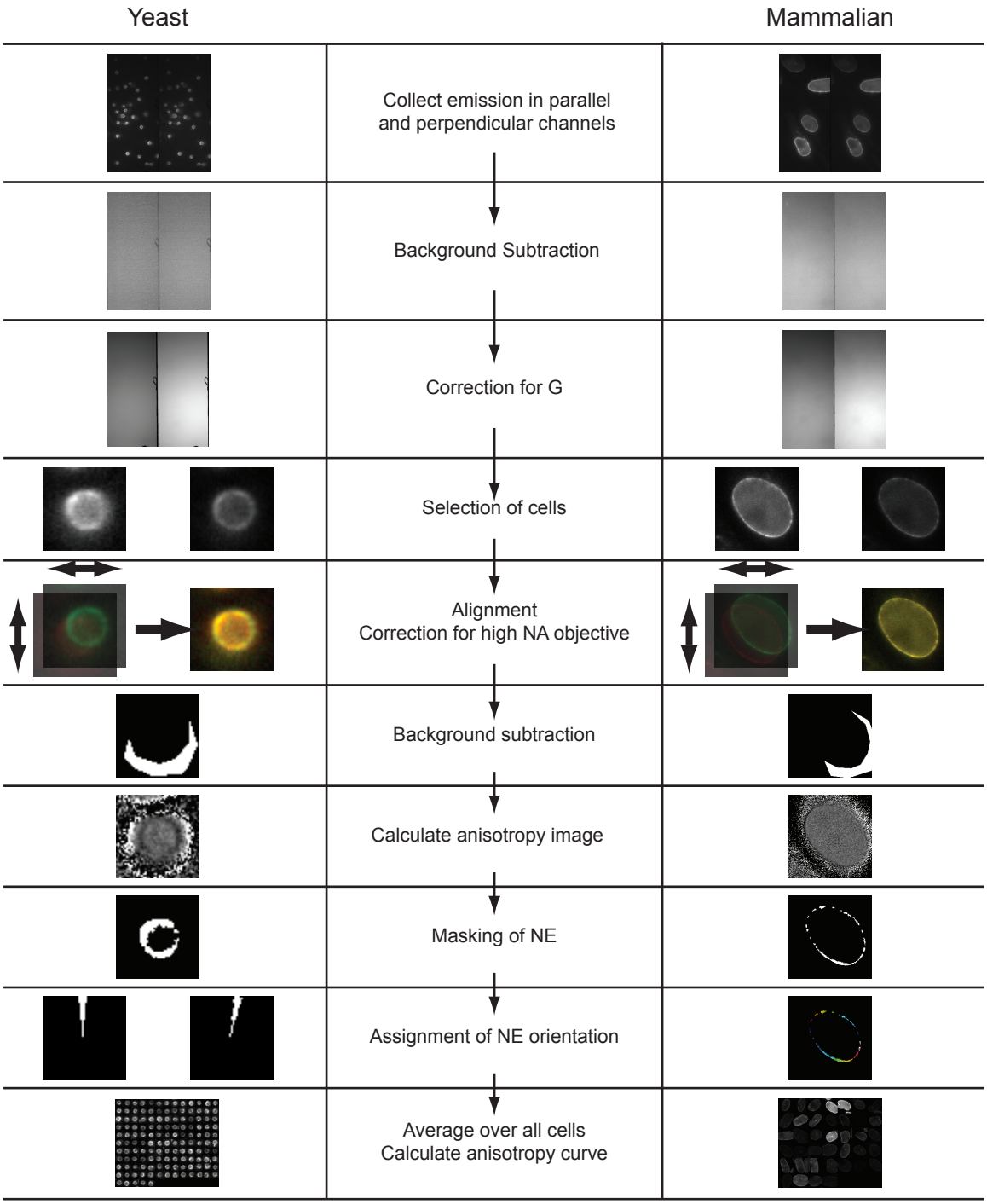

Figure 16: Schematic of Analysis. Flowchart showing analysis steps. Left side, yeast cells; right side, mammalian cells.

ratio techniques. To calculate accurate anisotropy values pixel-by-pixel, precise alignment of the $I_{/\!/}$ and $I_{\perp}$ images was necessary, especially since the NE signal was only few pixels wide. Global alignment of the $I_{/\!/}$ and $I_{\perp}$ halves of the micrograph did not give satisfactory results for all cells. Instead, image pairs of individual nuclei were cropped from the micrographs and aligned automatically with sub-pixel accuracy based on cross-correlation. Following alignment, corrections for the high NA objective were applied.

The number of GFPs is limited by the number of nup copies per NPC. One major hurdle in data analysis arose from the low fluorescence signal at the NE and a high, variable background fluorescence from the cytoplasm. The level of background fluorescence was kept as low as possible by optimizing the yeast growth conditions and using low fluorescence media for both yeast and mammalian cells. However, the cytosolic background varied significantly between different yeast strains and mammalian constructs, as well as between individual cells (Figure 17).

The effect of background fluorescence from the cell cytoplasm on anisotropy calculations was examined using the test nucleoporin Nup57 in yeast. For these experiments two constructs were tested, one with the GFP on the N terminus at the end of the FG domain (Nup57-GFPtip) and the other with GFP on the C terminus proximal to the coiled coil domain (Nup57-GFPfolded). The anisotropy values for the same set of cells with and without background subtraction were compared. If background was not subtracted (Figure 18 A and C, blue lines), both the anisotropy values and the amplitude of the anisotropy pattern were lower, on average, than the values after background subtraction for both constructs (Figure 18A and C, red lines). Therefore, the amount of background is affecting the measured anisotropy.

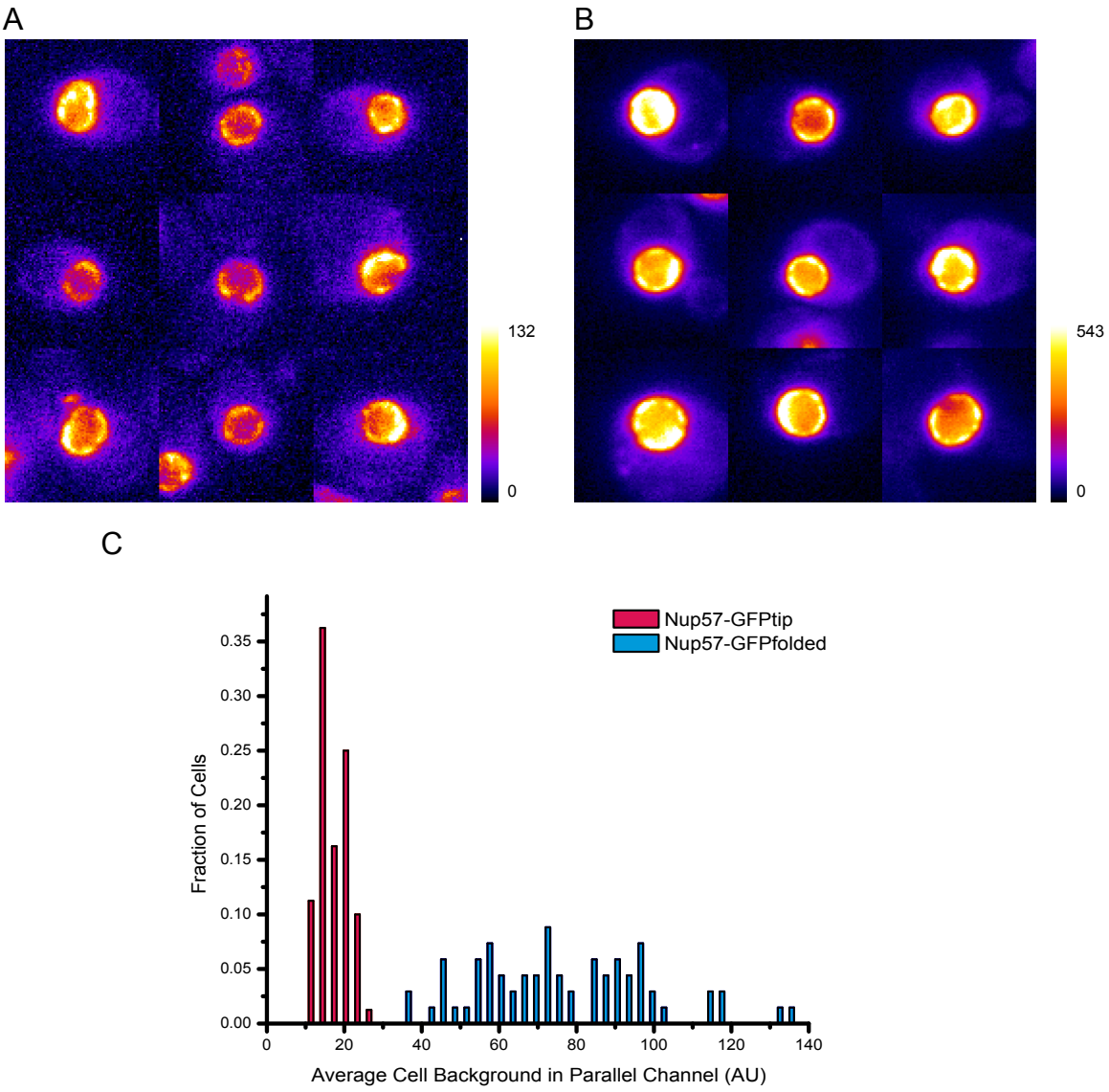

Figure 17: Background Fluorescence Varies Between Cells and Between Yeast Strains. A) Individual Nup57-GFPtip cells as imaged in $I_{\parallel}$. The intensity is displayed on a pseudocolor scale so it is possible to see both the GFP fluorescence on the nuclear envelope and the background fluorescence in the cytosol. B) Individual Nup57-GFPfolded cells as imaged in $I_{\parallel}$ displayed with a pseudocolor scale. C) Histogram of average background calculated for a population of Nup57-GFPtip (red) and Nup57-GFPfolded (blue) cells. There is a spread of background values within each individual strain. The background levels between strains is very different.

To investigate this further, a computer simulation was created in which artificial $I_{\parallel}$ and $I_{\perp}$ images were generated with either anisotropy modulation around the perimeter of the NE or a constant anisotropy. A background similar to that found in the experimental strain was added. Before calculation of anisotropy, a "background" value was subtracted from each channel. The values subtracted corresponded to no background, the correct background, or twice the correct background. The theoretical anisotropies have the same characteristics as the experimental anisotropies. A correct background subtraction increases the anisotropy and the amplitude of the modulation over no background subtraction (Figure 18 B and D, blue lines compared to red lines). If too much background is subtracted, the anisotropy value is even higher and the curve modulation larger (Figure 18 B and D, green lines). While the exact contribution from cytoplasmic and out-of-focus fluorescence to the NE pixels is unknown, and the background subtraction changes the absolute value of the anisotropy measured, the subtraction does not affect whether or not a curve is modulated. Thus, the conclusions drawn from the data regarding whether a fluorophore is ordered or disordered remain valid regardless of background subtraction.

Cell-by-cell background corrections were incorporated into the analysis. A cytoplasmic region was selected manually and its average intensity was taken as the cell background; this was calculated for both $I_{\parallel}$ and $I_{\perp}$. While there will also be a contribution from out-of-focus fluorescence within the nucleus, this was more constant between cells, and so should have the same effect on each curve. Additionally, the anisotropy in the cytoplasm is lower and will therefore have a larger blurring effect. This individualized cytoplasmic background subtraction improved the robustness of the analysis, with the

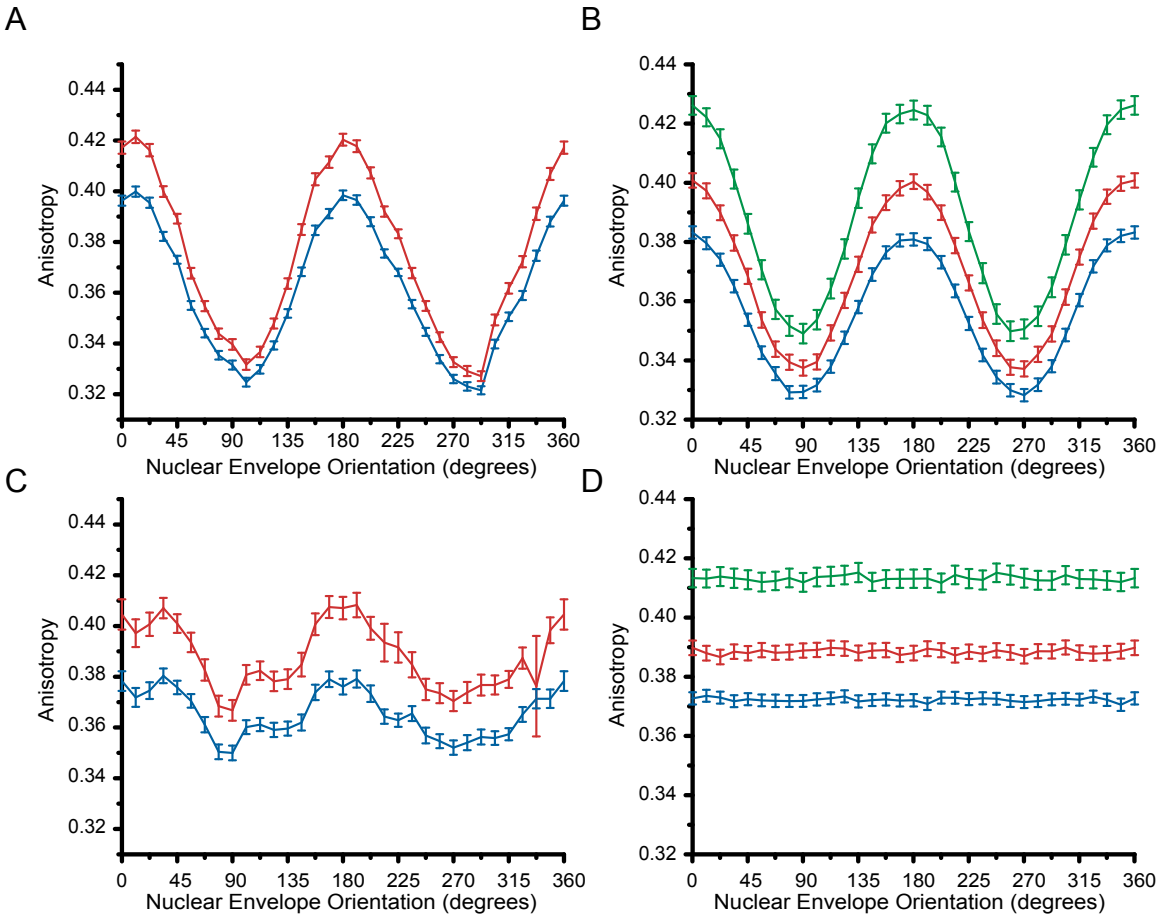

Figure 18: Effect of Background Subtraction on Anisotropy. Experimental and theroretical effects of different background subtractions. Blue is no background subtracted; red is the correct background subtracted; green is twice the correct background subtracted. A) Experimental data: background subtraction from Nup57-GFPfolded. B) Theoretical data: Ordered GFP. C) Experimental data: background subtraction from Nup57-GFPtip. D) Theoretical data: randomly oriented GFP.

average anisotropy reproducibly converging on a single value in experiments on the same strains on successive days.

To determine the anisotropy, an image was calculated from the corrected $I_{/\!/}$ and $I_{\perp}$ images in which each pixel value corresponds to its anisotropy. However, only the pixels corresponding to the nuclear envelope are relevant. To select these pixels for analysis, intensity based thresholding was used on an image which reconstituted the total intensity of the cropped images (i.e. $I_{/\!/}+2I_{\perp}$). This allowed determination of the NE by selection of the brightest pixels. The selection of which pixels to analyze is an important consideration; if too a large number of pixels is chosen, cytoplasmic and out-of-focus nuclear pixels will be selected and these will contribute to the anisotropy measured, making the measurement less accurate. However, if too few pixels are selected, more noise will be introduced into the analysis. As a test, different percentages of pixels were selected to determine the optimum number to analyze. This resulted in the selection of an area of the NE corresponding to the top 200 pixels (10% of the cropped image size) in yeast cells and the top 1000 pixels (2.5% of the image size) in mammalian cells. This threshold slightly undersamples the NE pixels, ensuring that only NE fluorescence is included in the analysis. These pixels were used to create a mask which was applied to the anisotropy image.

The next challenge in the analysis was to determine the orientation of the NE. Yeast nuclei are circular, and therefore the angle γ corresponds directly to the position around the NE. The nucleus was divided into sectors corresponding to NE position. Sectors of different sizes will contain different numbers of pixels. In determining the most appropriate sector size to use, there are two factors to consider. A smaller sector

size will contain fewer pixels, so the sector must be big enough to collect a reasonable amount of pixels per orientation. However, the larger the sector, the more of the NE it encompasses, and therefore bigger sectors contain a wider range of orientations which will be binned together to create a single value. Not analyzing enough pixels per orientation will decrease signal: noise, while binning too many orientations together will decrease the amplitude of the curve. The same data was analyzed with sector sizes of 1/4, 1/8, 1/16, 1/32 and 1/64 of a circle; this analysis showed that 32 sectors gave the optimal balance. Notably, 1/32 of a circle gives a sector with a central angle (θ) close to 10°, for which $\sin\theta \approx \theta$ and $\cos\theta \approx 1$.

A mask of these individual sectors of a circle, $I_{sector\ j}$ (j = 1-32), was created and applied to the anisotropy image. Pixels falling both within $I_{sector\ j}$ and the NE mask were assigned to sector j. The sector mask was then rotated by 11.25° and the routine repeated. This was carried out for each individual nucleus, generating an anisotropy list of pixels from all cells for each sector j. Each pixel is given equal weight, regardless of how many other pixels are present in the segment in which it originated. All the pixels belonging to the same segment orientation were averaged and the mean and standard error of the mean (SEM) of these values were assigned to the sector position and plotted.

Mammalian nuclei have a more irregular shape, and therefore using circular segmentation would not give an accurate measure of NE orientation. Two methods for determining the orientation of the NE were developed. In the first, sections of the NE were cropped out, masked based on their intensity, and their orientation was determined by cross-correlation with a line of a known orientation. However, this involved time-consuming manual selection of regions to crop out for analysis, and since all the pixels in

a cropped section were assigned the same value, only completely straight sections of the NE could be analyzed. Additionally, the anisotropy of all the pixels within the cropped sections was averaged before binning and averaging over all segments of the same orientation, meaning that not all individual pixels carried the same weight in the final average.

A second analysis routine was therefore created, in which each of the pixels in the NE mask was assigned an orientation individually. A section of NE centered around each pixel was cropped and positions of the all the NE pixels within this section were plotted. A straight line was fitted to this plot and its slope determined. The NE mask was then rotated through 90° and the analysis was repeated for the same pixel. Pixels which could be fitted to slopes which were compatible with each other after the 90° rotation were assigned the appropriate NE orientation. Pixels were binned in 10° increments and averaged, giving each pixel equal weight.

These analysis routines allowed determination of the average anisotropy as a function of NE orientation. The anisotropy was plotted as $r(\gamma)$, and these curves have three important parameters: the phase, which gives information about the orientation of the fluorophore; the amplitude, which contains information about both the mobility of the fluorophore and its orientation; the absolute anisotropy values (for disordered fluorophores), which depend on mobility.

Effects of Homo-FRET

Homo-FRET is a non-radiative transfer of energy between two like fluorophores. The efficiency of homo-FRET depends on physical parameters of the fluorophores, the distance between the fluorophores, and their relative orientations. One concern with these experiments is that homo-FRET between GFP attached to nucleoporins could decrease the anisotropy and prevent discrimination between curve shapes.

To investigate to what extent homo-FRET could influence measured anisotropy, two extreme situations were theoretically examined: either the GFPs are ordered in a fixed orientation, or they are adopt multiple orientations at random.

FRET efficiency is given by:

$$E = \frac{1}{1+(R/R_0)^6} \qquad [9]$$

where R is the distance between the fluorophores and R_0 is the Förster radius (Förster, 1948). R_0 depends on physical parameters including the refractive index of the medium, the overlap integral, and the dipole orientations, described by κ^2.

First, fluorophores that are attached to structural nups and oriented with respect to the NPC are considered. The smallest possible distance R between two GFPs in one ring based on the geometry of the NPC (assuming central channel r = 20 nm) is R = 153 Å. The probability of energy transfer is dependent on the orientation of GFP within the NPC. In the most favorable orientation for energy transfer, $\alpha = 0$ and $\kappa^2 = 1$, the efficiency of homo-FRET is 0.1%. However, in this configuration, FRET will not lead to depolarization because the dipoles share the same orientation, and therefore the emission polarization will be the same with or without energy transfer. As the angle between the

dipoles increases, the depolarization increases while the efficiency of homo-FRET decreases. For an ordered system, the effects of homo-FRET on anisotropy patterns measured from oriented fluorophores are negligible.

Second, fluorophores that do not show a fixed orientation with respect to the NPC were analyzed. There are two possible scenarios: GFP attached to the folded domain and localized to a specific location in the barrel of the NPC, or GFP attached to the unstructured FG domain and occupying the central channel. The minimum distance R between GFPs in one ring is R = 153 Å, as calculated above. In a randomly oriented system, κ^2 = 2/3 and R_0 = 47 Å, the Förster radius for GFP. In this case, a negligible FRET efficiency, E = 0.8%, is predicted. If there are more than 8 copies of the protein and therefore multiple rings, the homo-FRET efficiency will depend on the distance between the rings and their register.

For GFP attached to the tip of the flexible domain, the simplifying assumption that the GFPs are randomly and isotropically distributed in the central channel was used. Under these conditions, the concentration of GFP calculated according to copy number is: 0.035 mM (8 copies); 0.7 mM (16 copies); 1.4 mM (32 copies). This is a reasonable assumption considering the volume of the pore lumen, and the length and flexibility of the FG protein domains, and is conservative for some FG domains which have been shown to extend beyond the central channel into the nucleoplasm or cytoplasm thereby decreasing their effective concentration and thus the homo-FRET efficiency. The critical concentration at which E = 50% is 3.8 mM. If a GFP-tagged nup is present in 16 or 32 copies, depolarization due to homo-FRET is possible.

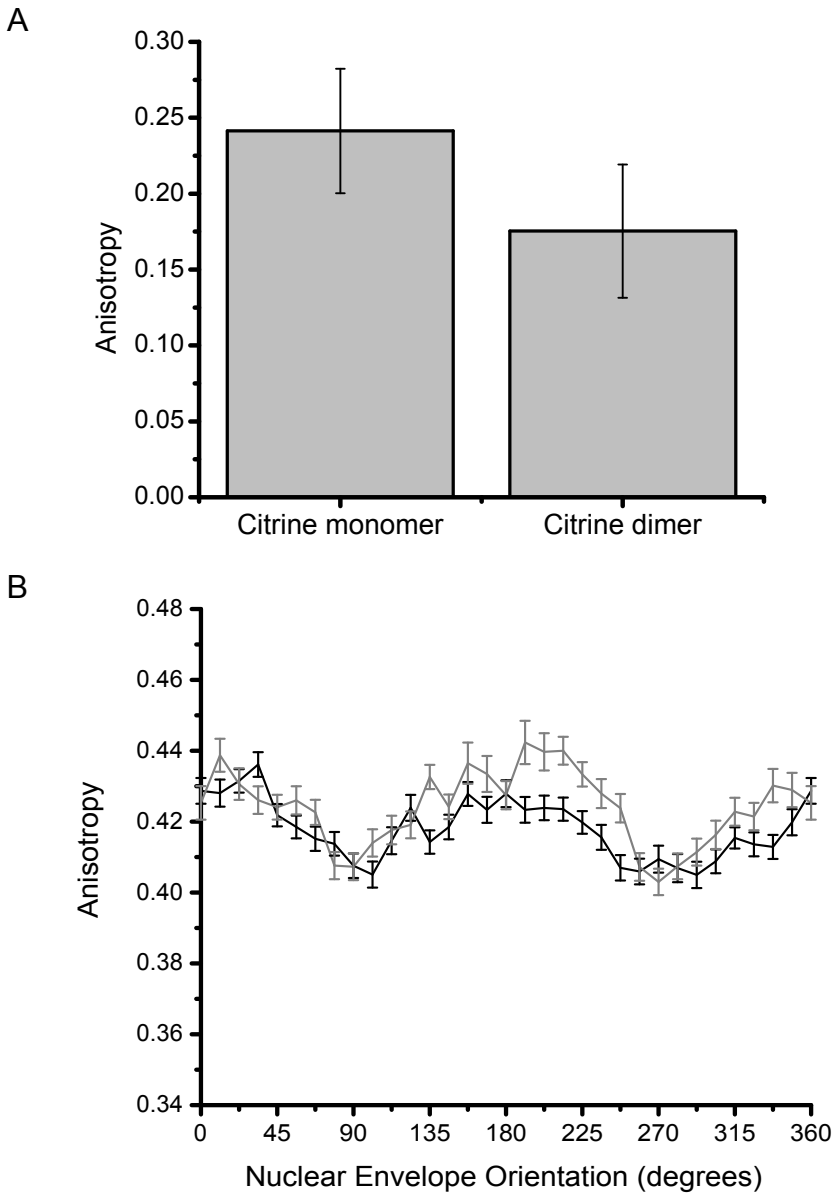

Figure 19: Tests for Homo-FRET. A) Anisotropy of cytosolic citrine monomers or dimers in yeast cells. B) Test for homoFRET between GFP at the tips of FG domains. Varying percentage of labeled Nup57-GFPtip. Black curve shows 100% labeling (haploid cells); grey curve shows 50% labeling (diploid cells, one copy tagged).

To determine if homo-FRET could be detected in solution, the fluorescent protein mCitrine was expressed in the cytosol of yeast cells, either as a monomer or as a dimer of two citrine molecules joined by a short linker. The anisotropy of the cytosolic fluorescence in yeast expressing these constructs was calculated. For the monomer, the anisotropy was 0.241 whereas for the dimer it was 0.175, indicating loss of polarization due to homo-FRET (Figure 19A).

As described above, it is possible that homo-FRET could occur if GFP is at the tip of the FG domain. To determine experimentally if this homo-FRET was occurring between tagged FG domains, Nup57-GFPtip was used as a test. The concentration of GFP molecules in the NPC lumen was altered by utilizing haploid and diploid yeast: in the haploid, there is only one copy of the Nup57 gene and this is tagged with GFP, so that every copy of the Nup57 protein will be labeled; in the diploid there are two copies of the Nup57 gene of which only one is labeled, leading to only 50% of the Nup57 protein being labeled on average. It would be expected that if homo-FRET were occurring, the amplitude of the haploid curve would be decreased relative to that of the diploid. However, the curves had the same shape, indicating that homo-FRET is not taking place (Figure 19B).

One further way to test for homo-FRET would be to measure the anisotropy, then bleach 50% of the signal using unpolarized light, before taking a second reading of the anisotropy. If there was no change between the two anisotropy readings, it would mean that no FRET was occurring. This would be a way to test for homo-FRET in mammalian cells, where the labeling density is unknown.

Chapter 3: Determining the Orientation of NPC Proteins

This section covers how the orientation of a GFP tagged structural protein within the NPC can be determined. In this process, three factors must be considered: the orientation of a fluorophore within the NPC, which is determined from anisotropy; the orientation of the fluorophore relative to the protein, which must be fixed, and the orientation of the protein in the NPC, which is unknown. The information from the first two factors is combined to recover protein orientation. The two proteins for which orientations were determined are Nic96 in yeast cells, and Nup133 in mammalian cells.

Relationship of Fluorophore Orientation to Protein Orientation

As described in Chapter 2, the orientation of the GFP dipole relative to the NPC can be determined based on the anisotropy as a function of the orientation of the nuclear envelope. In order to relate this to the arrangement of a protein within the NPC, the GFP must be attached to the protein by a rigid linker in a defined orientation, so that the orientation of its dipole relative to the protein of interest is known.

To obtain rigid fluorophore-nucleoporin fusion constructs with known geometry, a previously published approach was adapted. GFP contains a short N terminal α-helix, which can be fused directly to a C terminal α-helix in a protein of interest. Thus, the two proteins will be joined by a continuous α-helix which provides a rigid linker (Vrabioiu and Mitchison, 2006). Changing the number of amino acids in this linker helix will rotate GFP around the linker helix axis by angles dictated by α-helical geometry (i.e. 103° for

each amino acid removed). Each fusion construct is described by two numbers, (*–p*/*–q*), which define the number of amino acids omitted from the C-terminus of the nucleoporin (*p*) and the number of amino acids omitted from the N-terminus of GFP (*q*). Different constructs for which the sum of *p* and *q* is the same have a linker helix of the same length.

The orientation of GFP within the NPC will change for each construct in a series with different helix lengths. The orientation of each GFP can then be determined based on the anisotropy values. This orientation will be compatible with only a certain range of orientations for the protein of interest in each case. Since it is assumed that the protein must have the same orientation within the NPC regardless of linker helix length, for a series of constructs the possible orientations of each can be combined to determine values which are compatible with all of them.

A coordinate system was set up to describe the orientation of GFP relative to the protein. Two perpendicular axes, ***u*** and ***v***, were defined within the nucleoporin. ω and θ are the angles between the fluorophore transition dipole ***μ*** and the nucleoporin axes ***u*** and ***v***, respectively (Figure 20A). The orientation of the GFP fluorescence transition dipole relative to its crystal structure has been previously determined and is at ~80° to the rigid helical linker (Inoué et al., 2002; Rosell and Boxer, 2003). For each construct the nucleoporin was modeled fused to GFP with a rigid helix of the appropriate length, to determine the angles ω and θ. The orientation of the nucleoporin within the NPC is characterized by two angles: ψ, the angle between ***u*** and the nucleocytoplasmic axis ***N***, and φ, describing rotation of the ***v*** around **u** (Figure 20B).

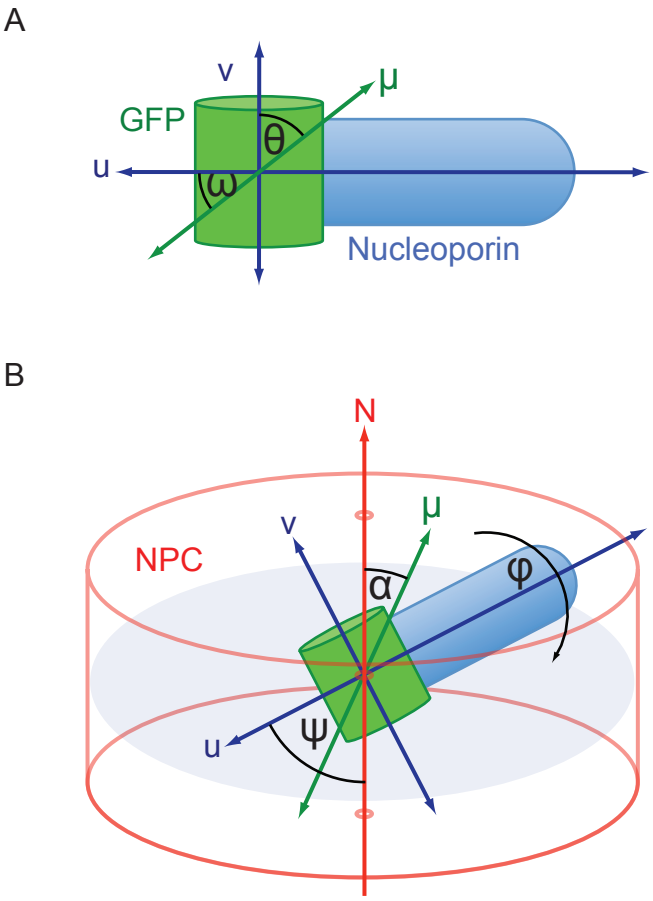

Figure 20: Protein Coordinate System. A) Two perpendicular axes, ***v*** and ***u***, are arbitrarily defined within the protein. These are related to the fluorophore dipole ***μ*** by the angles ω (between ***u*** and ***μ***) and θ (between ***v*** and ***μ***). B) Orientation of the protein in the NPC. The fluorophore dipole ***μ*** is related to the nucleocytoplasmic axis ***N*** by the angle α. The orientation of the protein relative to the NPC is defined by two angles: ψ (between ***u*** and ***N***) and φ (rotation around ***v***).

Orientation of Nic96

The first nucleoporin that was examined was yeast Nic96, since a model has been proposed for its orientation in the NPC. This model places Nic96 in a head-to-tail octameric ring around the perimeter of the NPC, an arrangement which this method can be used to test. Nic96 contains C terminal α-helices, and crystal structures for its C terminal domain have been solved (Jeudy and Schwartz, 2007; Schrader et al., 2008), which allowed generation of molecular models for Nic96-GFP fusion constructs.

Molecular models for some nucleoporin-GFP fusion constructs contain internal steric clashes between the nucleoporin and GFP moieties and therefore cannot exist in the modeled conformations. Since Nic96 is an essential protein in yeast, it was assayed whether a given Nic96-GFP construct was functional by comparing the growth of haploid wild-type Nic96 strains with the growth of haploid Nic96-GFP siblings after tetrad dissection of heterozygous diploids. When the constructs that were predicted to contain steric clashes were transfected into yeast, they had reduced or no function as assayed by tetrad analysis (Figure 21) and the GFP fluorescence lacked a clear nuclear localization. This suggested that these constructs were unable to localize correctly to the NPC (Figure 22). Some of the constructs which did not show a steric clash also had reduced Nic96 function, and/or reduced nuclear envelope staining. This may be due to steric clashes with other proteins of the NPC. Any constructs with reduced Nic96 function and/or reduced nuclear-envelope staining were excluded from further analysis for this reason. The six Nic96-GFP constructs that passed all tests were (–5/–4), (–6/–4), (–5/–5),

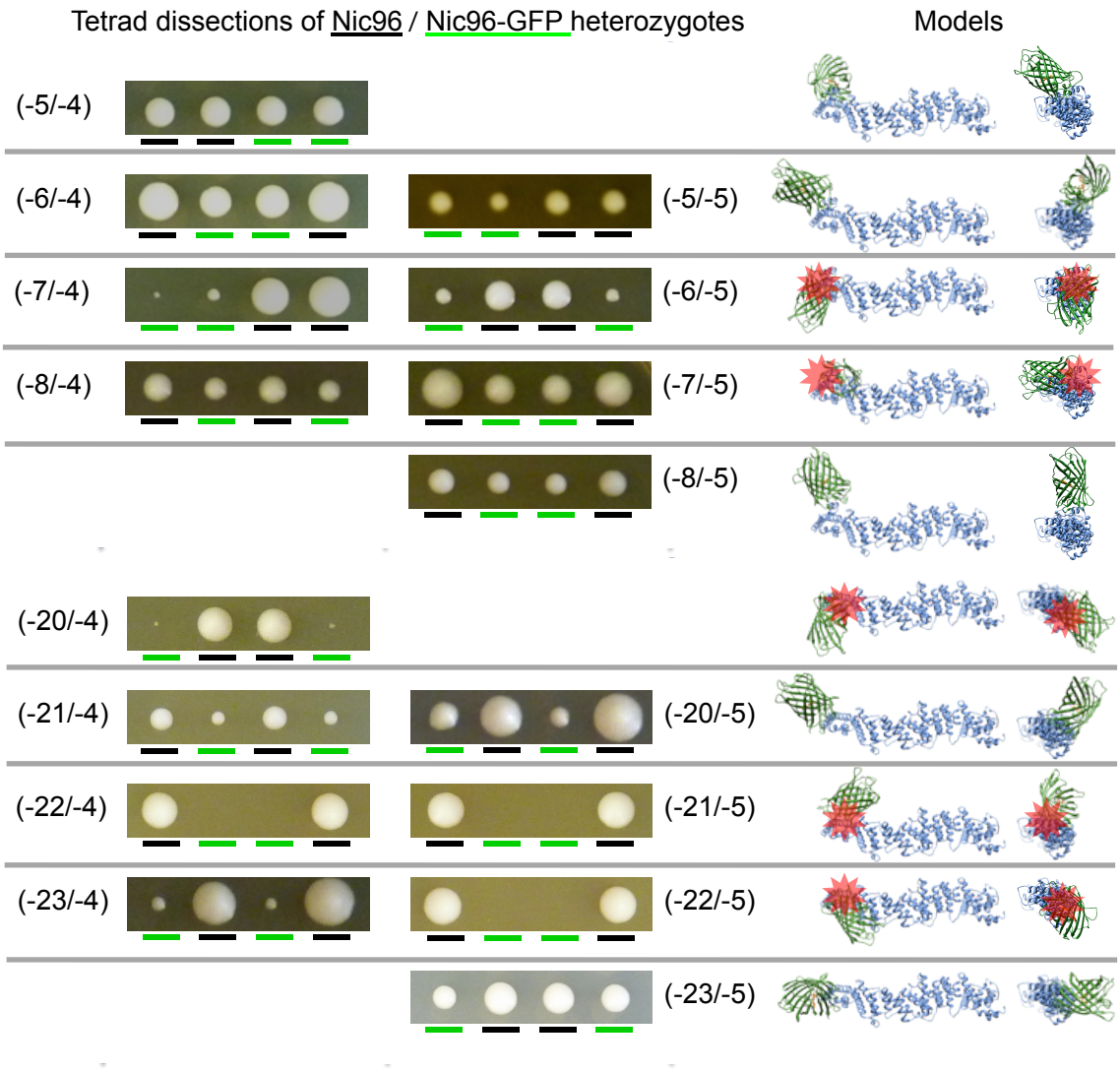

Figure 21: Viability of Nic96-GFP Constructs. Nic96 was fused to GFP with linker helices of varying length (numbers of amino acids removed shown in parentheses) using genomic tagging. Constructs with the same linker helix length are shown in the same row. The functionality of the GFP tagged Nic96 was assayed using tetrad dissection, shown in the left hand columns. Haploids bearing the GFP tagged copy of Nic96 are indicated by the green bars; wild type haploids are shown by black bars. The right hand columns show molecular models of the tagged constructs; where there is a steric clash between Nic96 (blue) and GFP (green) it is indicated with a red star.

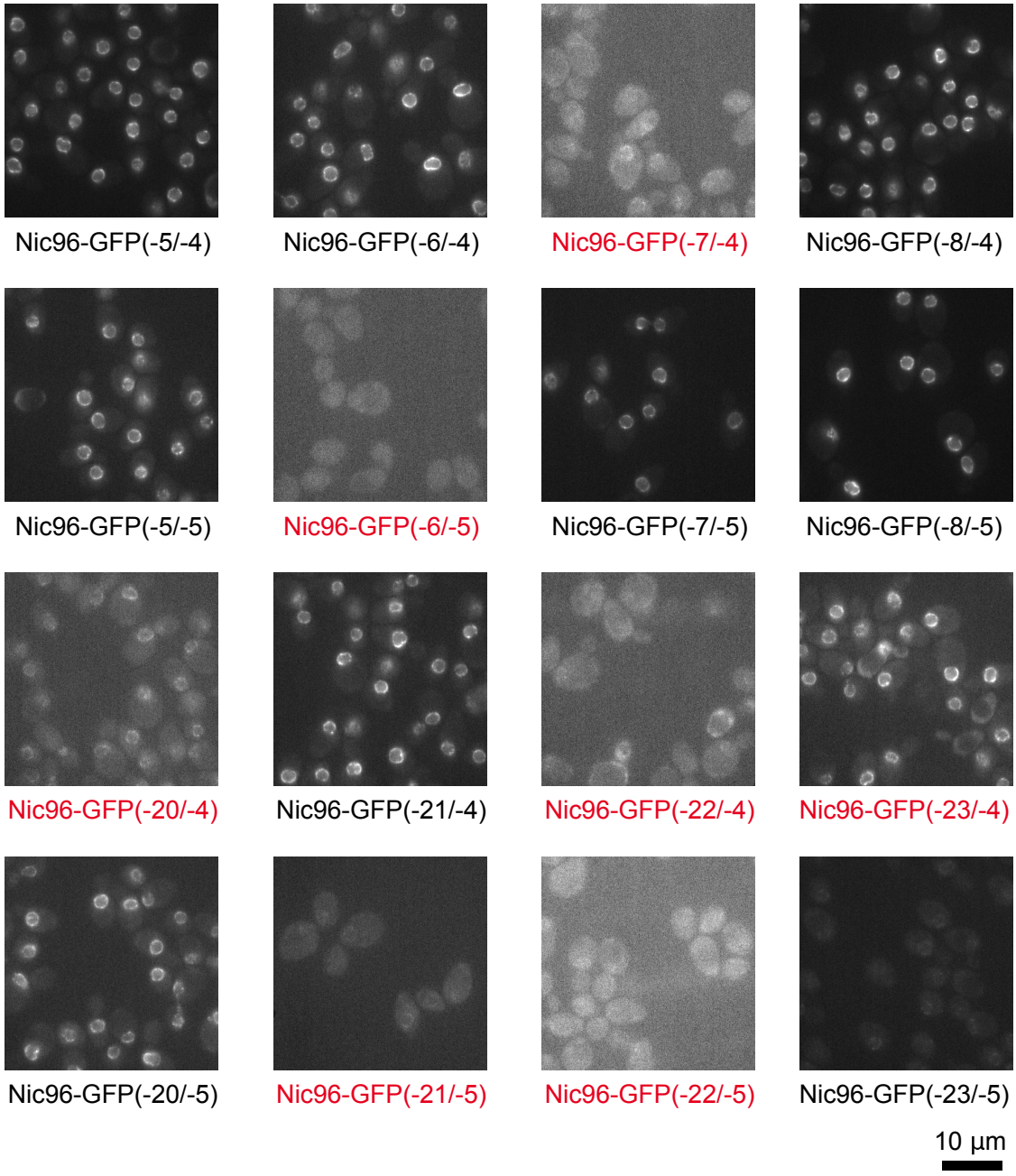

Figure 22: Fluorescence of Nic96-GFP Constructs. Images of a field of cells in the $I_{||}$ channel for each construct. There are differences in the expression levels and subcellular locations of the constructs. Helix lengths that resulted in a predicted steric clash are indicated in red.

(–8/–5), (–21/–4) and (–20/–5). These constructs represent 4 unique linker helix lengths (Figure 23).

The 6 Nic96-GFP expressing yeast strains were imaged and the anisotropy as a function of NE orientation was calculated. All 6 constructs showed a modulated anisotropy pattern, indicating the protein has a defined orientation within the NPC (Figure 24). All patterns were Type I (maxima for $\gamma = 0^{o}$ and 180^{o}), but the amplitudes of the (–5/–4) and (–8/–5) patterns (purple and red lines) were higher than those of the other patterns. The curves with the same linker helix length are shown on the same plots; the anisotropy is consistent for these constructs (blue and green lines).

To interpret the anisotropy measurements for Nic96-GFP constructs, axes ***u*** and ***v*** were defined within Nic96. ***u*** corresponds to the long axis of the crystallized Nic96 domain (Figure 25A). Since constructs (–6/–4) and (–5/–5) have the same linker helix length, as do constructs (–21/–4) and (–20/–5), four distinct molecular models were generated for the six constructs. The angles θ and ω were determined from each model. For a given pair of θ and ω, there is a range of possible α values that will depend on the orientation of the protein in the NPC. The expected value of α was calculated for every combination of ψ and φ in each construct (Figure 25B).

These construct-specific plots of α as a function of ψ and φ were then used to identify the range of ψ and φ values that was compatible with the anisotropy patterns which had been experimentally observed. As described above, our conservative assumption is that type I anisotropy patterns occur for constructs with $\alpha < 42^{o}$. Since type I patterns were observed for all constructs, the space of possible ψ and φ combinations in each plot could be restricted to those values that correspond to $\alpha < 42^{o}$.

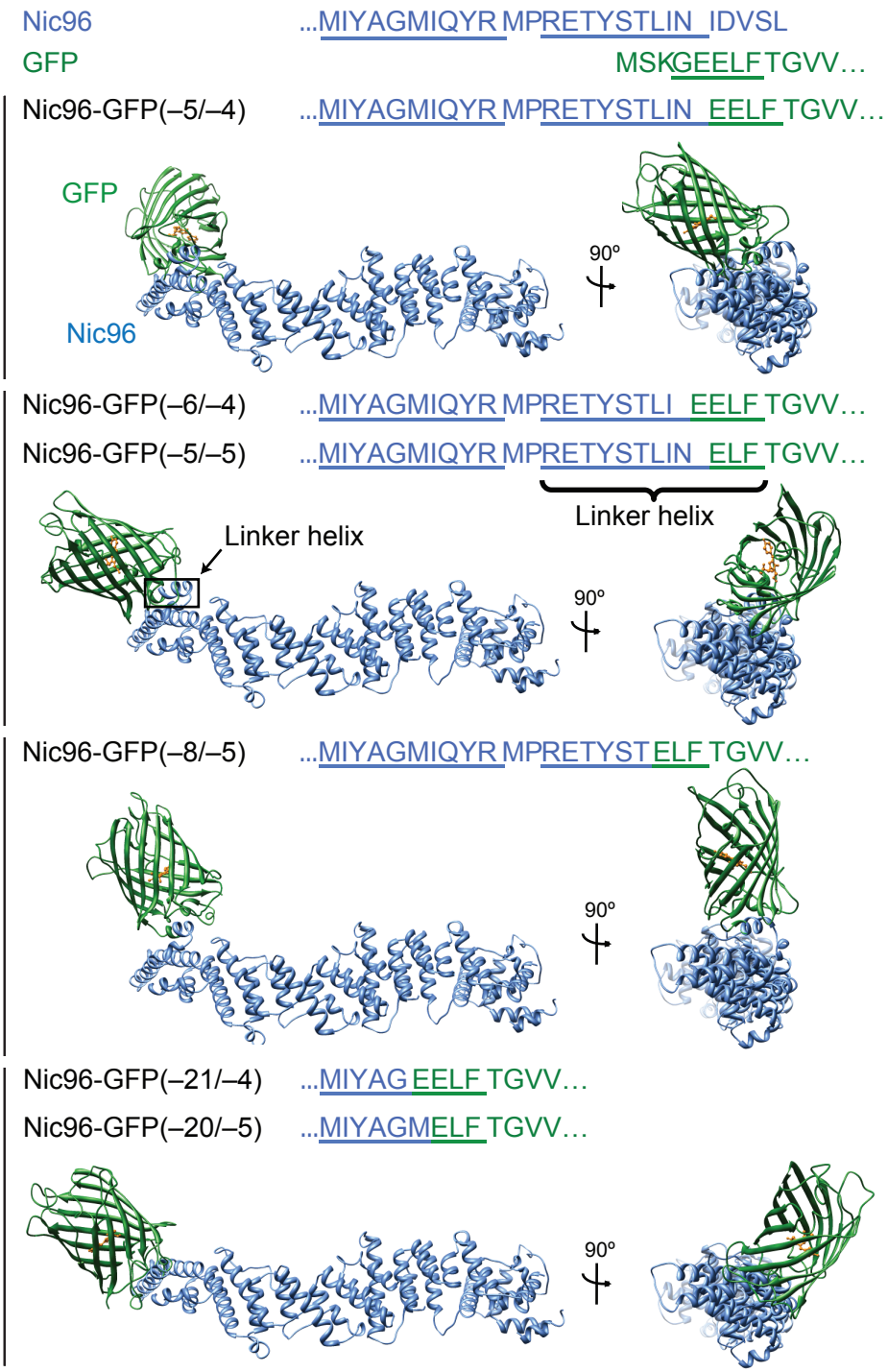

Figure 23: Nic96 Models. Molecular models of the Nic96-GFP constructs used in this study. Nic96 is blue, GFP is green. The amino acid sequences of Nic96 C terminus and GFP N terminus are shown at the top; helices are underlined. The sequence of the linker helix for each construct is shown underlined above the model.

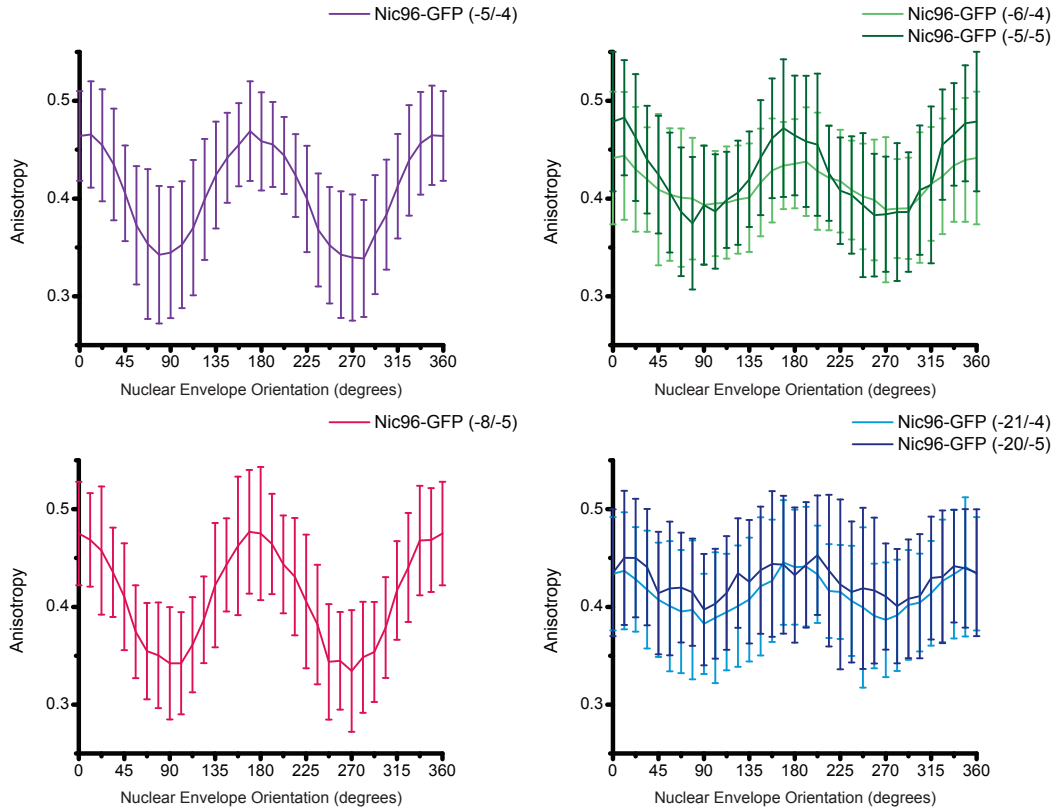

Figure 24: Nic96 Anisotropy Patterns. Anisotropy is shown as a function of the orientation of the NE. All patterns are Type I. Error bars are standard deviation.

Possible ψ and φ combinations were limited further by comparing the amplitudes between pairs of anisotropy patterns for the different constructs. For two constructs with type I patterns, the construct with the higher amplitude will have the lower value of α. For example, the amplitude for Nic96-GFP (-5/-4) was larger than for Nic96-GFP (-6/-4), Nic96-GFP (-5/-5), Nic96-GFP (-21/-4) and Nic96-GFP (-20/-5). Therefore, only combinations of ψ and φ for which Nic96-GFP (-5/-4) had smaller α values than these other four constructs were compatible with the data (Figure 25B).

By combining all these conditions, ψ can be restricted to values between 77º and 90º and φ to values between 20º and 45º. Notably, the high value of ψ means that the long axis of Nic96 must be close to perpendicular to the nucleocytoplasmic axis of the NPC. This arrangement of Nic96 is compatible with the model which has previously been suggested in the literature (Figure 26).

Orientation of Nup133

A question of major biological interest is the orientation of the Y-shaped complex within the NPC. This polarization microscopy technique can be used to determine the orientation of components of this complex. Since crystal structures of some of these components have been determined and modeled into a high resolution EM structure of the entire subcomplex, determining the orientation of these components should allow discrimination between different models for the arrangement of the Y-shaped complex in the NPC.

Figure 25: Analysis of Nic96 Anisotropy Patterns. A) Axes are defined in Nic96: ***u*** is parallel to the long axis of the molecule; ***v*** is perpendicular to ***u***. B) Top row: For each construct the values of θ and ω are calculated from the molecular model. α is calculated for every combination of Φ and ψ. Second row: Values of α which are compatible with the Type I curves observed are < 42°. Combinations of Φ and ψ which would yield such values are shown in white; incompatile combinations of Φ and ψ are shown in black. Third row: Amplitude of curves decreases as α increases between 0° and 42°. Comparisons of pairs of curves are shown, regions where the combination of Φ and ψ values gives a higher α for a lower amplitude curve are shown in white. Bottom row: Combination of all restrictions leaves a limited space of possible Φ and ψ values compatible with all observed experimental data.

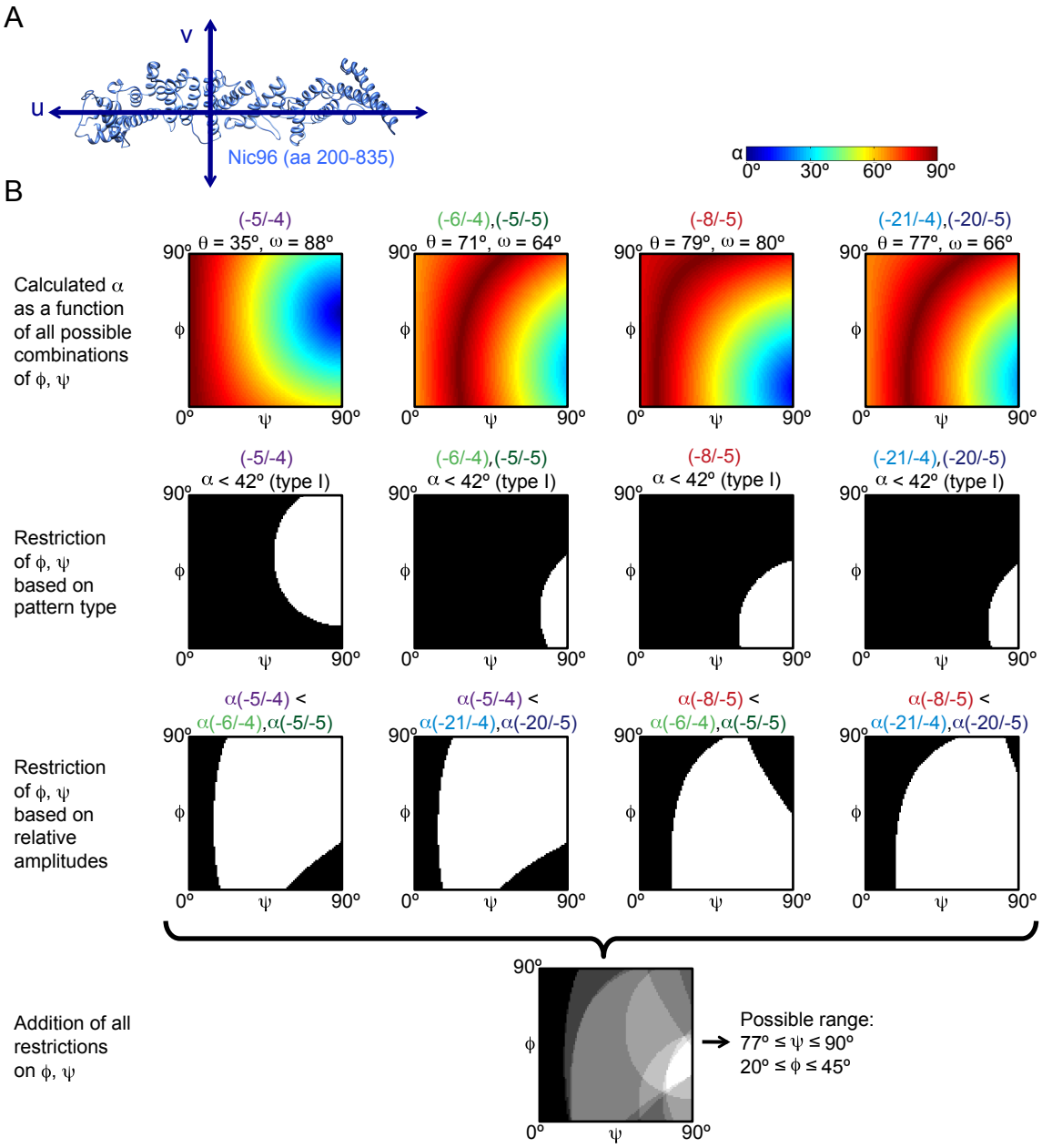
A
v
u
Nic96 (aa 200-835)
α
0°
30°
60°
90°
B
Calculated α as a function of all possible combinations of ϕ, ψ
(-5/-4)
θ = 35°, ω = 88°
(-6/-4),(-5/-5)
θ = 71°, ω = 64°
(-8/-5)
θ = 79°, ω = 80°
(-21/-4),(-20/-5)
θ = 77°, ω = 66°
Restriction of ϕ, ψ based on pattern type
α < 42° (type I)
Restriction of ϕ, ψ based on relative amplitudes
α(-5/-4) < α(-6/-4),α(-5/-5)
α(-5/-4) < α(-21/-4),α(-20/-5)
α(-8/-5) < α(-6/-4),α(-5/-5)
α(-8/-5) < α(-21/-4),α(-20/-5)
Addition of all restrictions on ϕ, ψ
Possible range:
77° ≤ ψ ≤ 90°
20° ≤ ϕ ≤ 45°

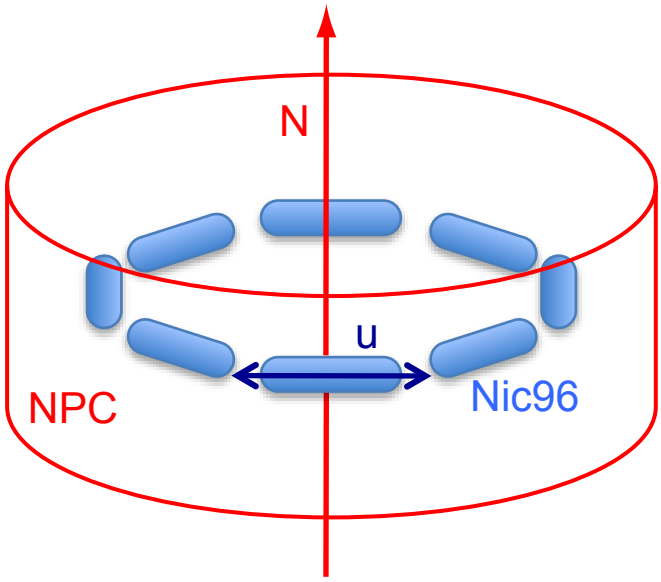

Figure 26: Model for Nic96 Arrangement in the NPC. Nic96 is arranged head-to-tail around the perimeter of the NPC. The long axis of Nic96 is perpendicular to N.

To test the feasibility of determining the orientation of the Y-shaped complex, yeast Nup84 was tagged with GFP, creating a series of helix fusions to the C terminus. These all showed modulated anisotropy curves of Type I or Type III, demonstrating that applying this technique to the Y-shaped complex would be possible (Figure 27). However, in order to determine the orientation of proteins within the NPC from anisotropy patterns, a crystal structure of the C terminal domain of the protein of interest is required, since this is necessary to determine the orientation of the GFP dipole relative to the protein. Unfortunately, no crystal structures are currently available for C terminal domains of Nup84, or any other members of the yeast Nup84 complex that contain a C terminal α helix.

However, the yeast Nup84 complex has a homolog in mammalian cells, the Nup107/160 complex. Structures of the C terminal domains of two members of the human Nup107/160 complex, Nup107 and Nup133, have been published. Nup107 is the homolog of Nup 84. When constructs with a continuous linker helix fusing GFP to Nup107 were tested they did not localize to the NE in HeLa cells. However, four Nup133-GFP constructs were fluorescent at the NE.

The Nup 133 constructs (–2/–5), (–3/–4), (–3/–5), and (–4/–4) displayed fluorescence at the NE, and no steric clashes were present between the GFP and Nup133 in the models of these constructs (Figure 28). Constructs (–2/–5) and (–3/–4) have a linker helix of the same length, as do constructs (–3/–5) and (–4/–4). The anisotropy of these constructs at the NE was determined (Figure 29). Constructs (–2/–5) and (–3/–4) showed a type I anisotropy pattern (blue curves). The anisotropy curves for constructs

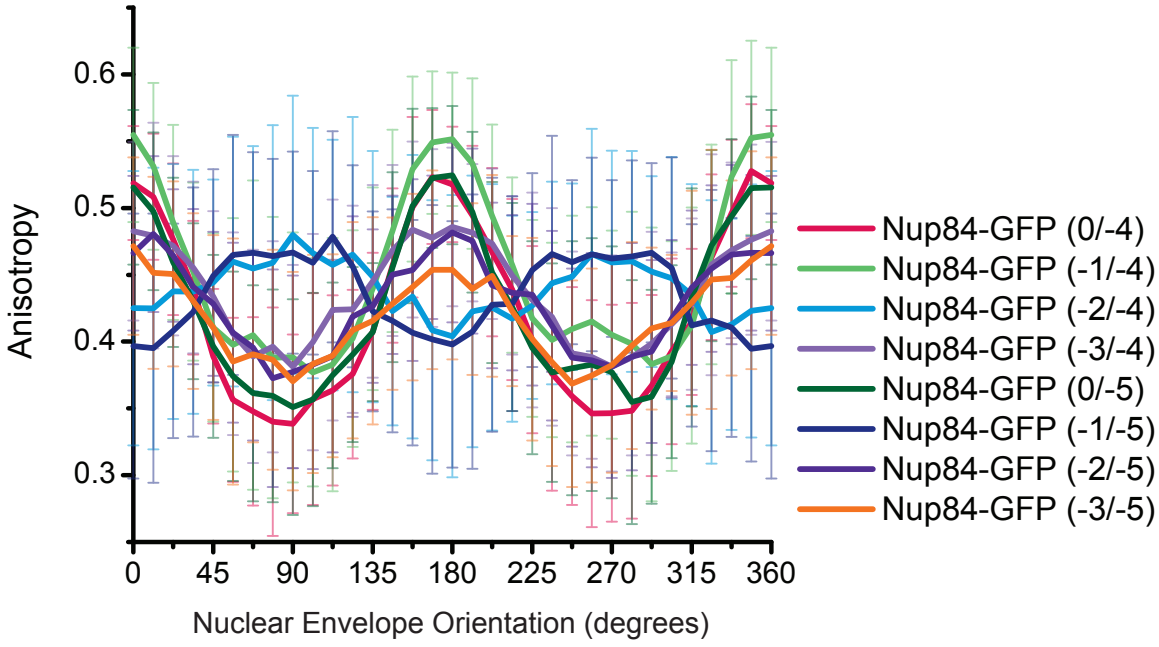

Figure 27: Anisotropy of Nup84-GFP Constructs. Anisotropy is plotted as a function of the position around the nuclear envelope. Constructs with the same length of linker helix are shown in different shades of the same color. Error bars are standard deviation.

(–3/–5) and (–4/–4) are of low amplitude and relatively noisy, but the presence of a clear maximum at $\gamma = 90^{\circ}$ is the hallmark of a type III anisotropy pattern (red curves).

Based on the structure of a complex between the C terminal domains of Nup107 and Nup133 (Berke et al., 2004; Boehmer et al., 2008; Whittle and Schwartz, 2009), the axis ***u*** was defined between the N terminal residues of the Nup107 and Nup133, thus pointing towards the remaining residues of the two nucleoporins (Figure 30A). ***v*** was defined perpendicular to ***u*** and passes through the C terminus of Nup133. On the basis of the structure of the homologous yeast Nup84 complex, it is assumed that Nup107 and Nup133 are arranged linearly along the stem of the Y-shaped subcomplex. Hence, ***u*** is likely to reflect the orientation of the stem of the Nup107 complex.

Maps of α as a function of φ and ψ were created for each of the Nup133-GFP constructs as described for the yeast Nic96 constructs (Figure 30B). Based on the observed anisotropy patterns, our conservative assumptions were $\alpha < 42^{\circ}$ for constructs (–2/–5) and (–3/–4) (type I pattern) and $\alpha > 60^{\circ}$ for constructs (–3/–5) and (–4/–4) (type III pattern). These conditions restricted the values of ψ to values between 76º and 90º and φ to values between 36º and 90º. This indicates that the long axis of the Nup107-Nup133 dimer, which is likely to represent the stem axis of the entire subcomplex, lies approximately perpendicular to the nucleocytoplasmic axis of the NPC (Figure 31). Such an arrangement is compatible with the "head-to-tail ring" model that was proposed for the homologous Nup84 complex, but not with the "lattice" model, which places the stem of the Y-shaped subcomplex parallel to the nucleocytoplasmic axis.

A complementary approach is to ask which anisotropy pattern types we would expect to observe on the basis of the alternative models for the arrangement of the Y-

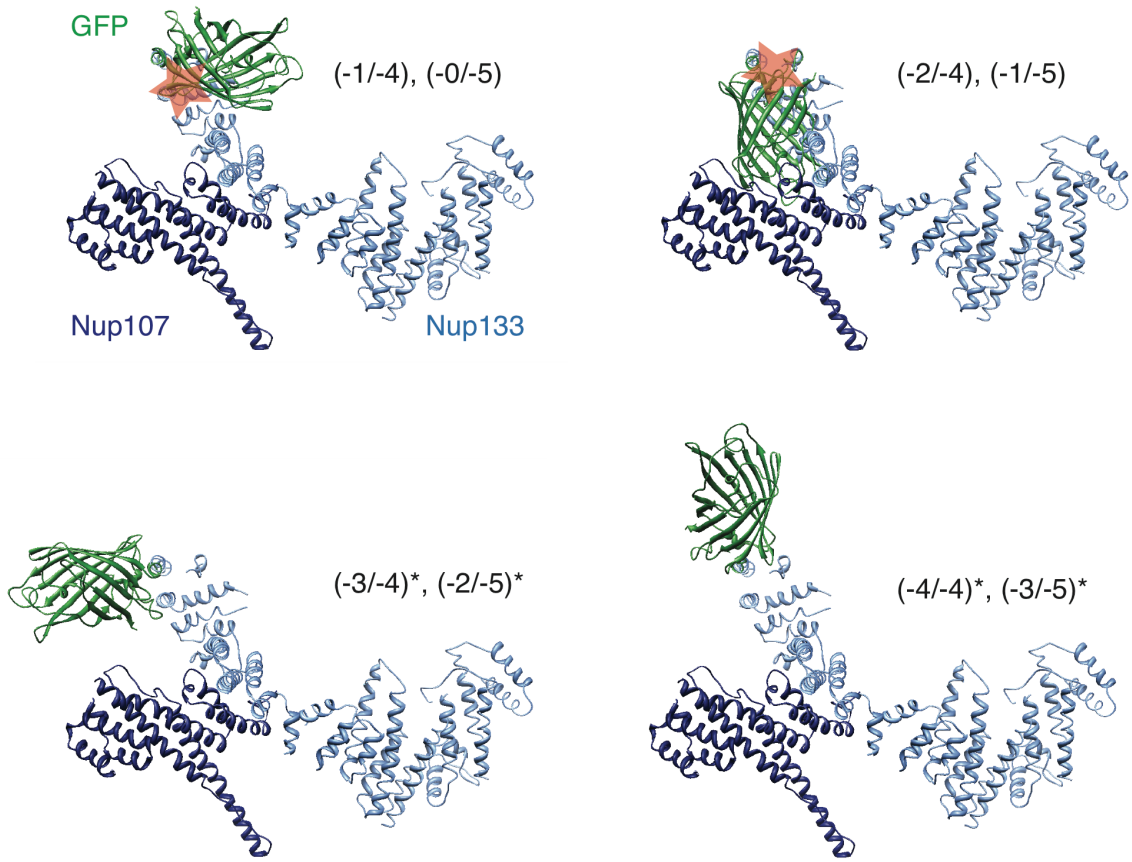

Figure 28: Molecular Models of Nup133-GFP Constructs. Nup133 is shown in light blue, Nup107 is shown in dark blue, GFP is shown in green. GFP is modeled joined to the C terminus of Nup133 with a helix of appropriate length. Internal steric clashes are indicated with a red star.

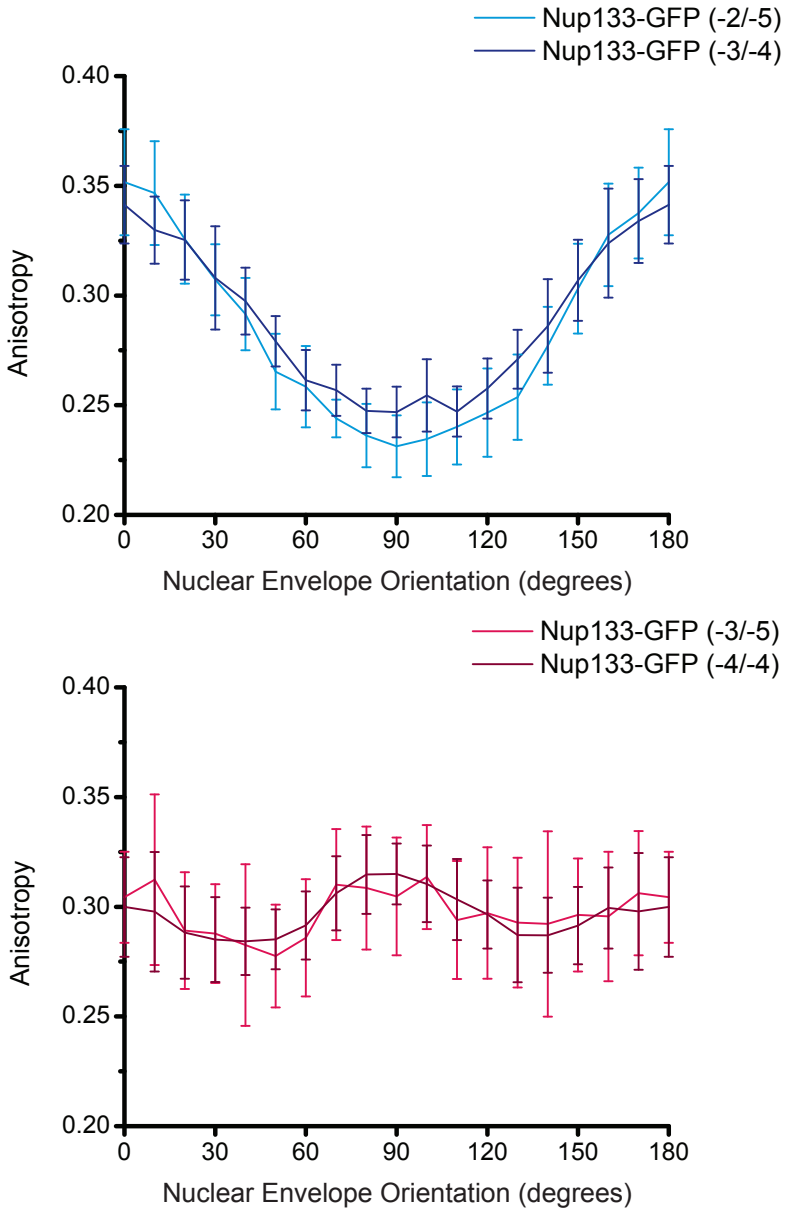

Figure 29: Nup133 Anisotropy Patterns. Anisotropy is shown as a function of the orientation of the NE. Constructs (-2/-5) and (-3/-4) show a Type I pattern; constructs (-3/-5) and (-4/-4) show a type III pattern. Error bars are standard deviation.

Figure 30: Analysis of Nup133 Aniosotropy Patterns. A) Axes were defined in Nup133: ***u*** connects the N termini of the crystallized Nup107 and Nup133 domains and therefore presumably runs parallel to the long arm of the Y; ***v*** is perpendicular and runs through the Nup133 C terminus. B) Top row: For each construct the values of θ and ω are calculated from the molecular model. α is calculated for every combination of Φ and ψ. Middle row: For constructs (-3/-4) and (-2/-5) a type I pattern was observed, indicating $\alpha < 42°$. For constructs (-4/-4) and (-3/-5) a type III pattern was observed, indicating $\alpha > 60°$. Combinations of θ and ω which meet these restraints are shown in white; incompatible combinations of θ and ω are shown in black. Bottom row: Combination of the restraints from all constructs shows the range of α values compatible with all experimental data.

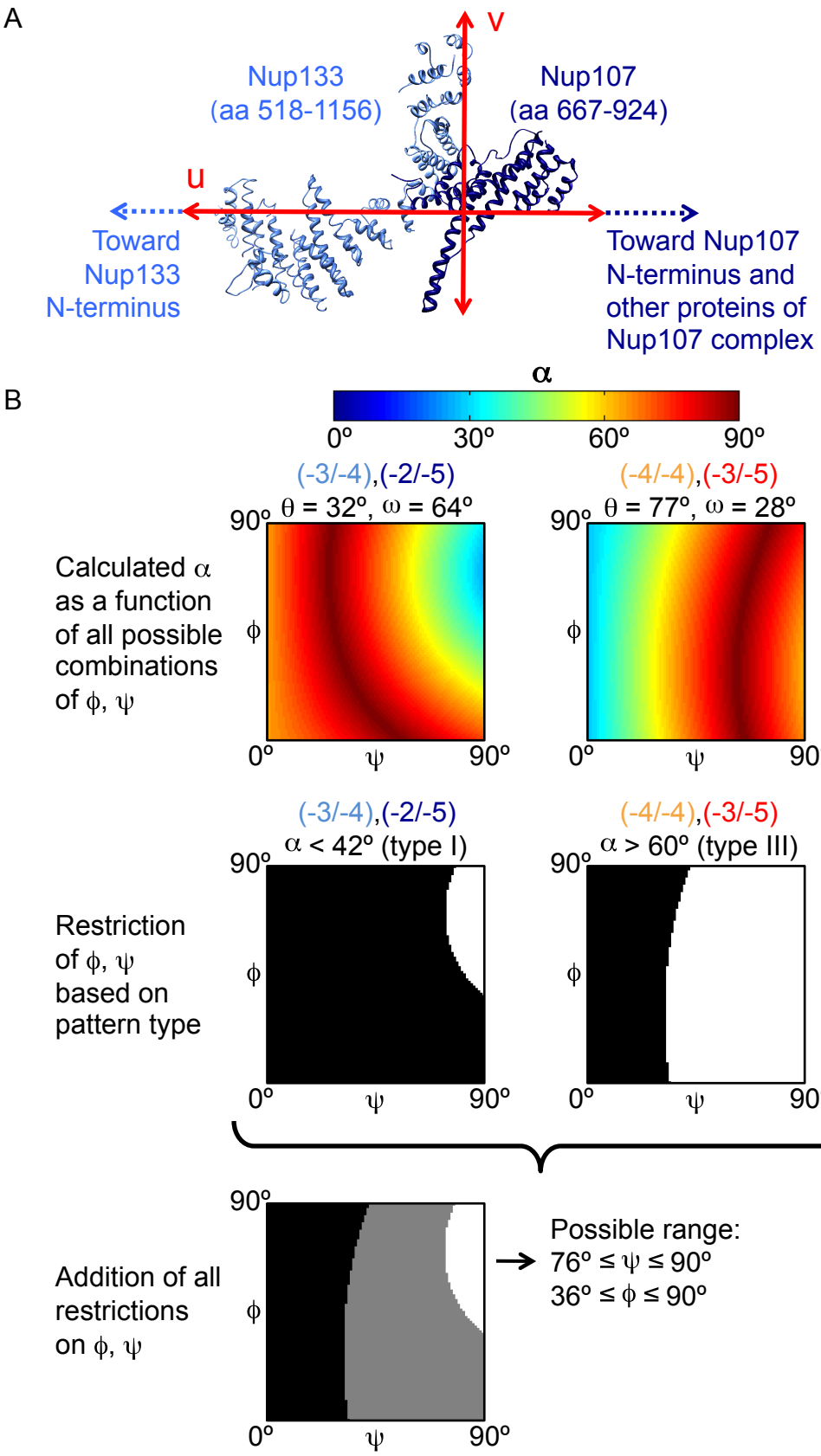
A
v
u
Nup133
(aa 518-1156)
Nup107
(aa 667-924)
Toward
Nup133
N-terminus
Toward Nup107
N-terminus and
other proteins of
Nup107 complex
B
α
0°
30°
60°
90°
Calculated α
as a function
of all possible
combinations
of ϕ, ψ
(-3/-4),(-2/-5)
θ = 32°, ω = 64°
(-4/-4),(-3/-5)
θ = 77°, ω = 28°
90°
ϕ
0°
ψ
90°
Restriction
of ϕ, ψ
based on
pattern type
(-3/-4),(-2/-5)
α < 42° (type I)
(-4/-4),(-3/-5)
α > 60° (type III)
Addition of all
restrictions
on ϕ, ψ
Possible range:
76° ≤ ψ ≤ 90°
36° ≤ ϕ ≤ 90°

shaped complex in the NPC. According to the "lattice" model, the long axis of the Y-shaped complex is approximately parallel to the nucleocytoplasmic axis; we will therefore assume $0^o \leq \psi \leq 30^o$ for this model. According to the "head-to-tail ring" model, the long axis of the Y-shaped complex is approximately perpendicular to the nucleocytoplasmic axis; we will therefore assume $60^o \leq \psi \leq 90^o$ for this model.

For constructs Nup133-GFP(-3/-4) and (-2/-5), α was calculated as a function of ψ and φ. For $0^o \leq \psi \leq 30^o$ ("lattice" model), the range of possible values for α is 64^o-90^o, which corresponds to a type II or type III anisotropy pattern. For $60^o \leq \psi \leq 90^o$ ("head-to-tail ring" model), the range of possible values for α is 27^o-88^o, which could result in a type I, II, or III anisotropy pattern. The pattern observed for Nup133-GFP(-3/-4) and (-2/-5) is type I, and thus compatible with the "head-to-tail ring" model, but not with the "lattice" model.

For constructs Nup133-GFP(-4/-4) and (-3/-5) α was calculated as a function of ψ and φ. For $0^o \leq \psi \leq 30^o$ ("lattice" model), the range of possible values for α is 28^o-58^o, which corresponds to a type I or type II anisotropy pattern. For $60^o \leq \psi \leq 90^o$ ("head-to-tail ring" model), the range of possible values for α is 63^o-90^o, corresponding to a type II or III anisotropy pattern. The pattern observed for Nup133-GFP(-3/-4) and (-2/-5) is type III, and thus again compatible with the "head-to-tail ring" model, but not with the "lattice" model (Figure 32).

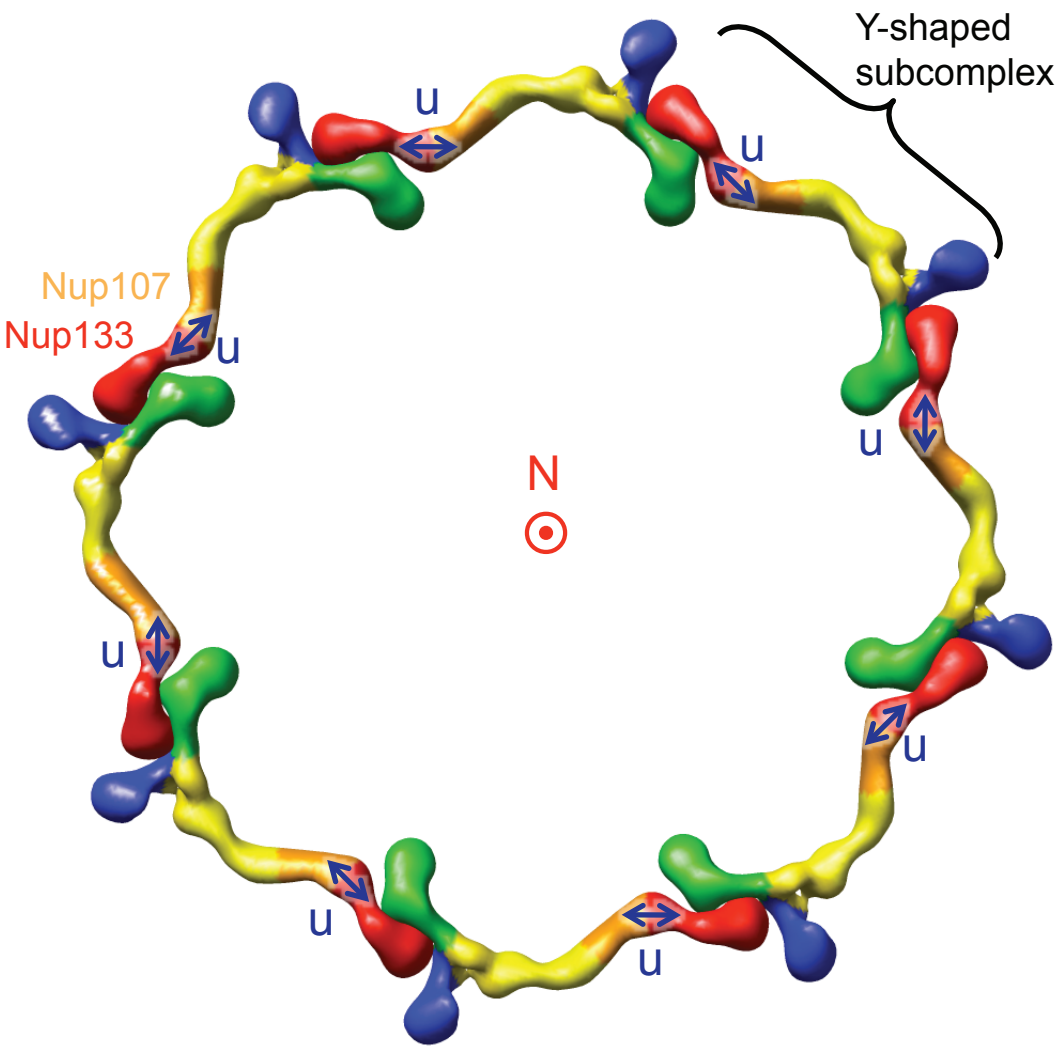

Figure 31: Model of Nup133 in the NPC. An arrangement of Nup133 which is compatible with the range of θ and ω determined is shown. The orientation of the ***u*** axis is indicated.

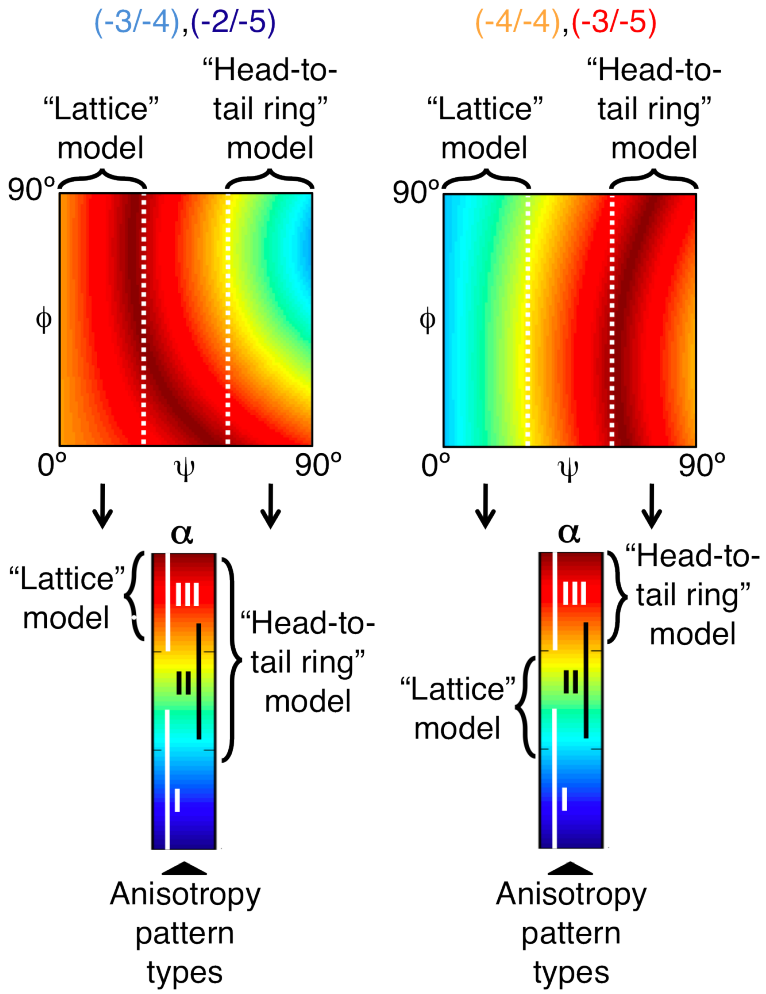

Figure 32: Relationships between Models for Y-Shaped Complex Orientation and Predicted Patterns. According to the lattice model, the long axis of the Y-shaped complex would lie approximately parallel to the nucleocytoplasmic axis of the NPC, for which ψ would have to fall between approximately 0° and 30°. For the head-to-tail ring model, the long axis of the Y-shaped complex would be perpendicular to the nucleocytoplasmic acis, and ψ would bebetween 60° and 90°. Top row: calculated α values for all combinations of ψ and φ for Nup133 constructs with different linker helix length. Ranges of ψ which are compatible with each model are indicates. Bottom row: Relationship of pattern types to α values. Ranges of α compatible with each of the models are indicated.Only the predictions made by the head-to-tail model are compatible with the observed experimental data.

Orientation of Tfp1

To further validate the method, it was applied to a different biological system, the vacuolar ATPase. This protein complex is embedded in the membrane of the yeast vacuole, a large, spherical organelle. The vacuolar ATPase/vacuole system and the NPC–nuclear envelope system thus have similar geometries. The vacuolar ATPase subunit Tfp1 was tagged with GFP. Previous studies have mapped the location and orientation of Tfp1 within the ATPase, therefore its orientation with respect to the vacuolar membrane is known (Maegawa et al., 2006). Models were created of GFP fused to Tfp1 with different linker helix lengths. For Tfp1-GFP(-7/-5), no clashes between the GFP moiety and the vacuolar ATPase occurred (Figure 33A). The angle between the GFP fluorescence dipole and the vector ***N*** normal to the vacuolar membrane was 22° for this construct. The anisotropy pattern around the vacuolar cross-section was determined as for the NPC, and for Tfp1-GFP(-7/-5) shows a Type I pattern, which is expected for $\alpha = 22°$ (Figure 33C). Tagging a protein of known orientation resulted in the anisotropy pattern predicted by the theoretical analysis, thus confirming the general applicability of the approach.

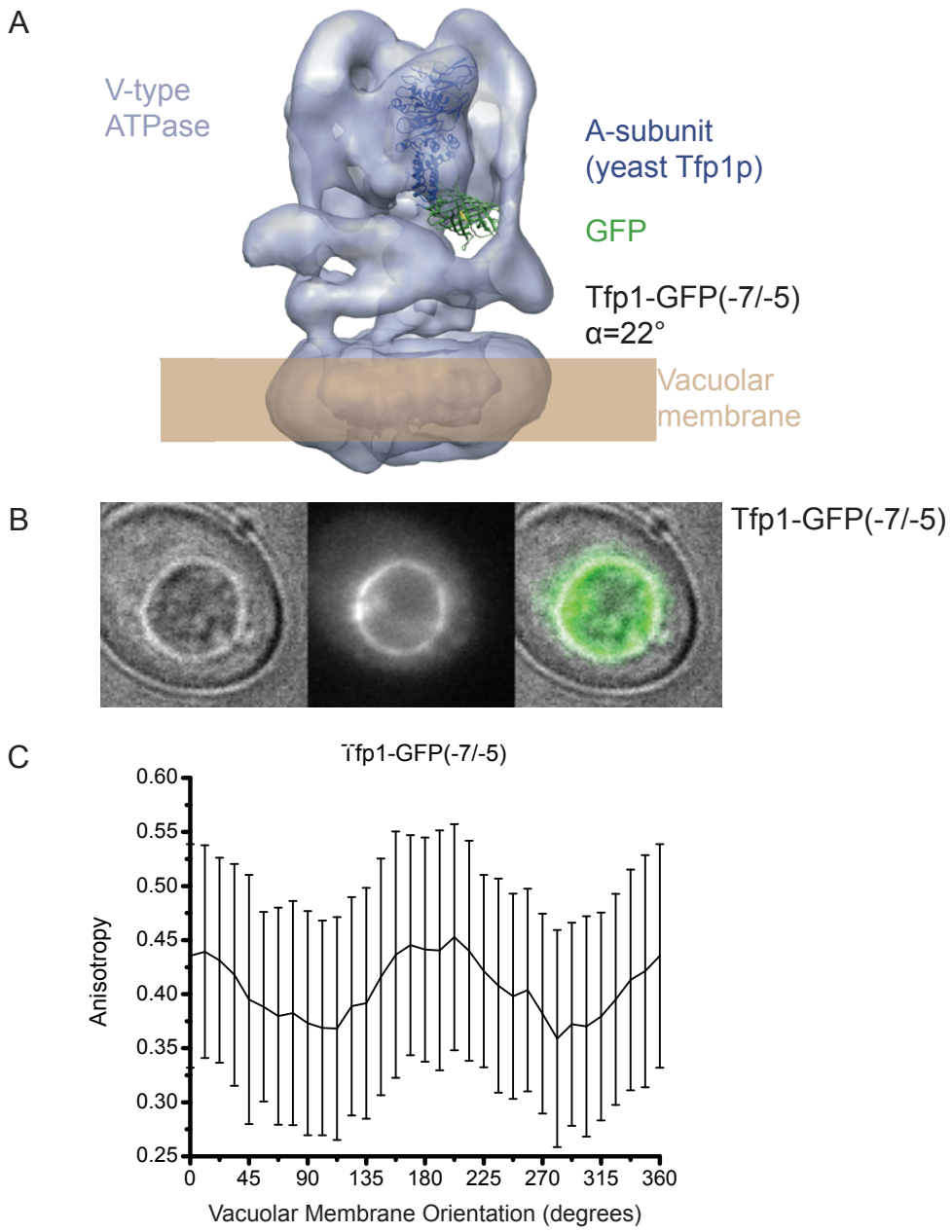

Figure 33: Orientation of a Known Subunit in the Vacuolar ATPase. A) The orientation of the Tfp1 subunit in the yeast vacuolar ATPase has previously been mapped. This subunit was tagged with GFP using a linker helix of varying length. For the construct Tfp1-GFP(-7/-5) there was no steric clash. The angle α, between the GFP dipole and the vector N nomal to the vacuolar membrane, was 22°. B) GFP-tagged Tfp1-GFP localized to the vacuole, which has a similar geometry to the nuclear envelope. C) The anisotropy was plotted as a function of membrane orientation. The pattern is type I, which is predicted for α=22°.

Chapter 4: Polarization Microscopy of FG Proteins

As described in Chapter 3, anisotropy measurements can be used to determine the orientation of structural proteins within the NPC. In this section, the application of polarization microscopy to the FG nups to determine the ordering and organization of the unstructured domains of these proteins in live cells will be discussed. This technique allowed determination of the biophysical behavior of the FG domains *in vivo* and provides information that can be used to discriminate between some of the models for transport.

Different Domains of the FG Proteins Show Different Behaviors

The FG nups consist of two distinct domains, one structured and one disordered. The structured, or folded, domains associate with structural nups and form part of the inner channel of the NPC. The disordered domains contain the FG repeats and fill the central channel of the NPC. Anisotropy has utility in determining the behavior of the FG domains within the NPC in order to place limits on different models for transport.

In these experiments, FG nups were tagged with GFP (Figure 34). These fusion proteins included no extra amino acids between the GFP and the nup; the anisotropy of the GFP should reflect the order/disorder of the tagged domain. However, unlike in the structural nup experiments, the GFP is not joined by a rigid helical linker, and the orientation of the GFP dipole relative to the protein is not known. If GFP is randomly oriented within the NPC, the anisotropy of the NE will be constant. If GFP is ordered

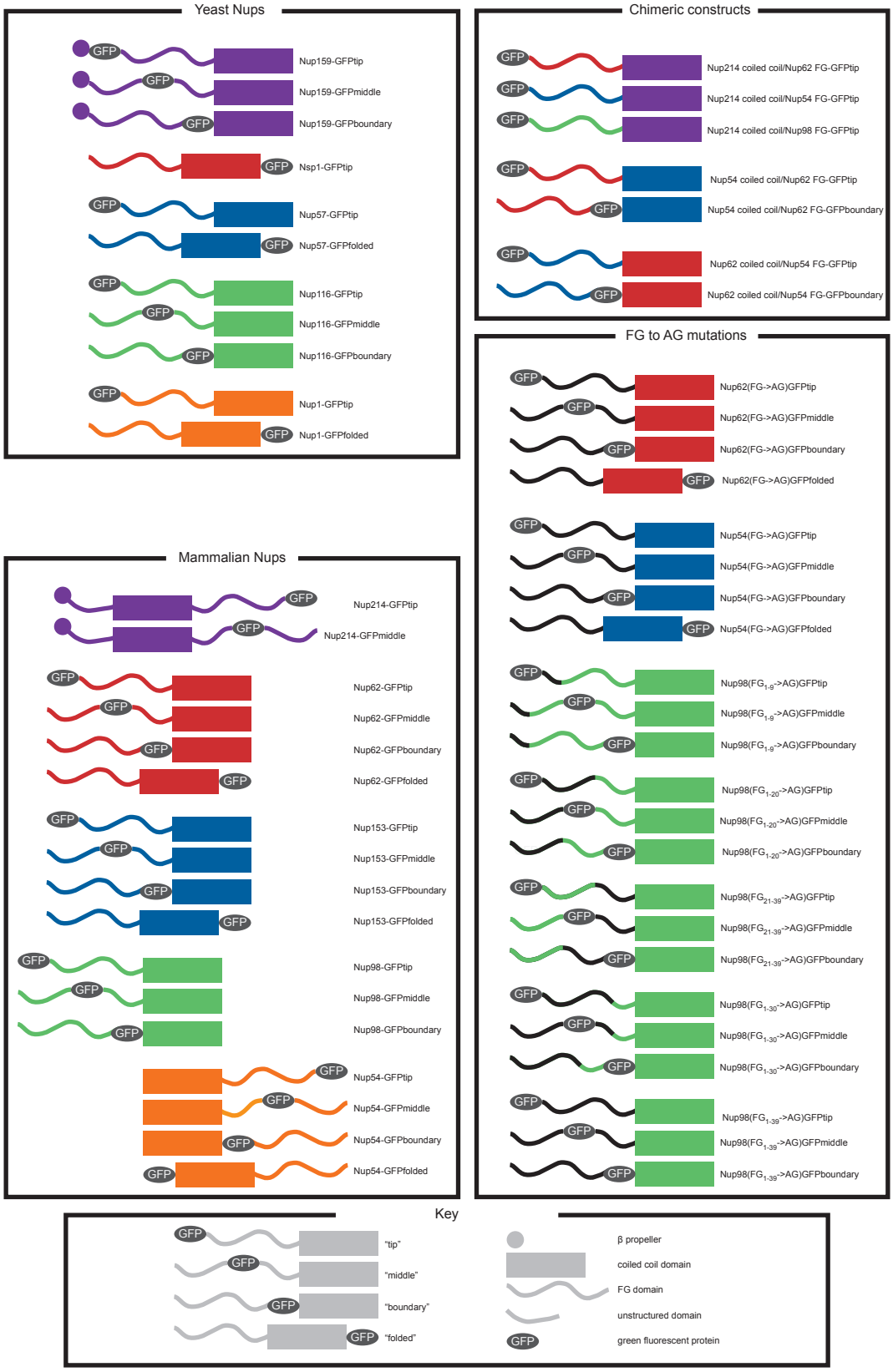

Figure 34: GFP Tagged FG Nup Constructs.

within the NPC, the observed anisotropy will vary according to the orientation of the NE, but the anisotropy pattern cannot be used to draw conclusions about the orientation of the protein.

As described in Chapter 2, experimental factors such as inaccurate background subtractions and non-ideal corrections for the high NA objective mean that it is difficult to determine how mobile the FG domains are based on absolute anisotropy measurements. One method which could potentially be used to investigate mobility is to use glycerol solutions of increasing concentration to increase the viscosity, thus changing the rotational properties of the fluorophore. For a mobile fluorophore, increasing viscosity should decrease rotation and increase anisotropy. In contrast, a fixed fluorophore should not be rotating, and will have an anisotropy independent of viscosity which will therefore not change. For solutions of fluorescein, increasing the glycerol concentration of the solution increased the anisotropy.

Yeast cells can grow on glycerol, and regulate their intracellular glycerol concentrations in response to osmotic stress. The anisotropy of cytosolic citrine expressed in yeast cells increased with viscosity (Figure 35A). To test if this method could be used to determine the mobility of FG nups, yeast cells expressing Nup57-GFPtip were imaged in increasing concentrations of glycerol. Unfortunately, the mismatch between the refractive index of the glycerol solution and the coverslip and immersion oil, and the morphological changes in the yeast at high glycerol concentrations made it difficult to focus on the midplane of the nucleus and therefore informative anisotropy measurements could not be obtained (Figure 35B).

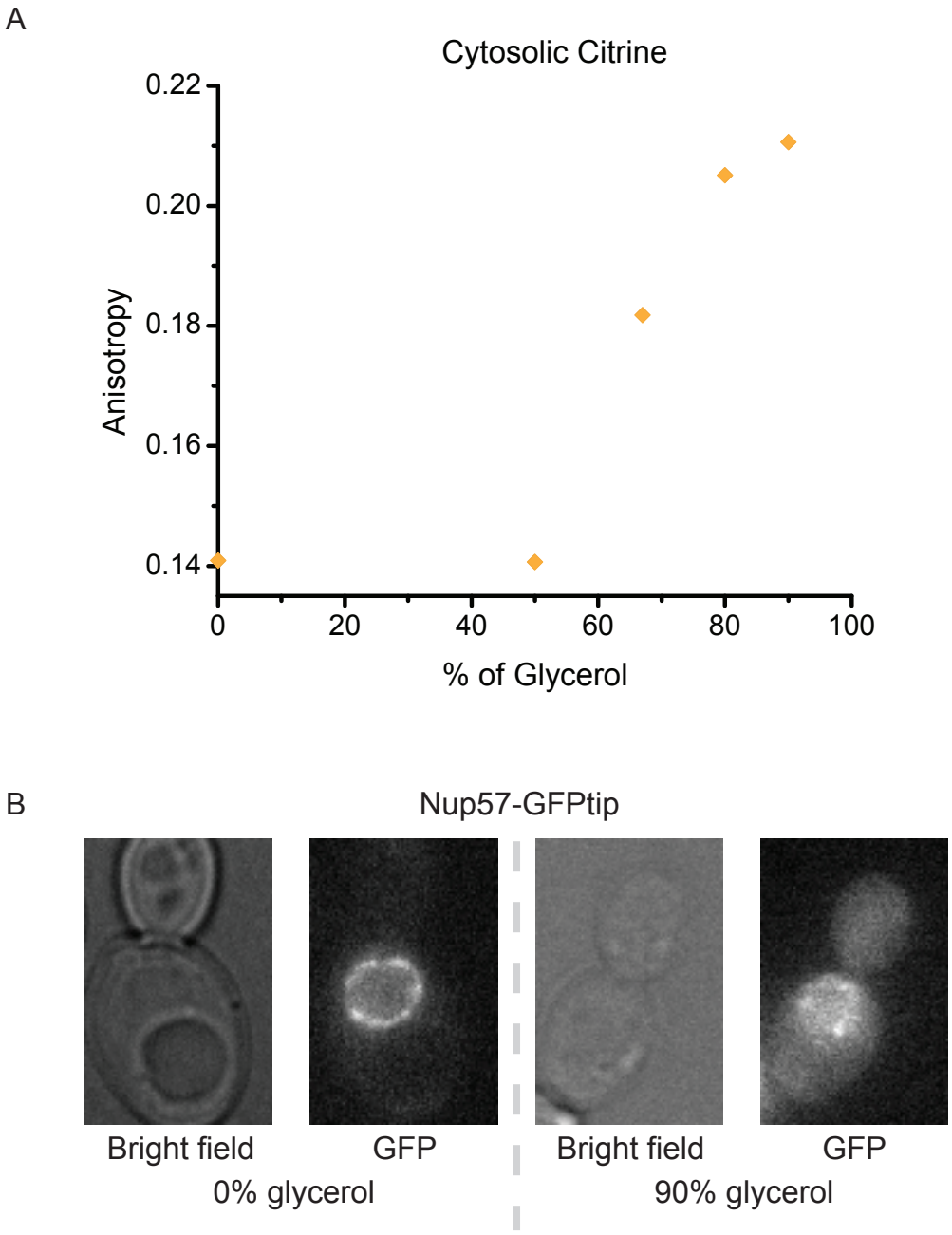

Figure 35: Effect of Viscosity on Anisotropy. A) Changes in anisotropy of Citrine in solutions of different viscosity. Citrine was expressed in the cytosol of yeast cells and viscosity was varied using increasing glycerol concentrations. B) Representative examples of Nup57-GFPtip yeast cells in 0% and 90% glycerol solutions.

However, this method can still be used to distinguish between ordered and disordered fluorophores in the NPC. As an initial test, anisotropy measurements were used to determine if it was possible to differentiate between the folded domain and the tip of the FG domain. For this test, Nup57 in yeast cells was used. Two strains expressing GFP-tagged Nup57 constructs were investigated: with GFP either at the C-terminus (Nup57-GFPfolded), or at the N-terminus (Nup57-GFPtip). In these experiments the protein was endogenously tagged, and could fully complement the function of the wild type protein.

The anisotropy of Nup57-GFPfolded varies with position around the NE, exhibiting a pattern characteristic of a highly ordered protein with maximal observed anisotropy values when the excitation polarization is parallel to the nucleocytoplasmic axis (0°) and minimal anisotropy values when it is at 90°. This regular modulation means that the GFP has a specific orientation with respect to the NPC, and the orientation of the dipoles depends on the position of the NPC around the NE (Figure 36A).

In contrast, the anisotropy of Nup57-GFP tip is only slightly modulated with respect to the NE. This is reflected in the amplitude of the anisotropy curve, which is lower than that of Nup57-GFPfolded, although the period remains the same. This indicates that the tip of the FG domain of Nup57 is much less ordered than the folded domain (Figure 36B). However, the small degree of order that was present for the tip was surprising for a tag on an unstructured domain. Altogether, this result demonstrates that anisotropy measurements can be used to distinguish between the behaviors of different domains of FG proteins in live cells.

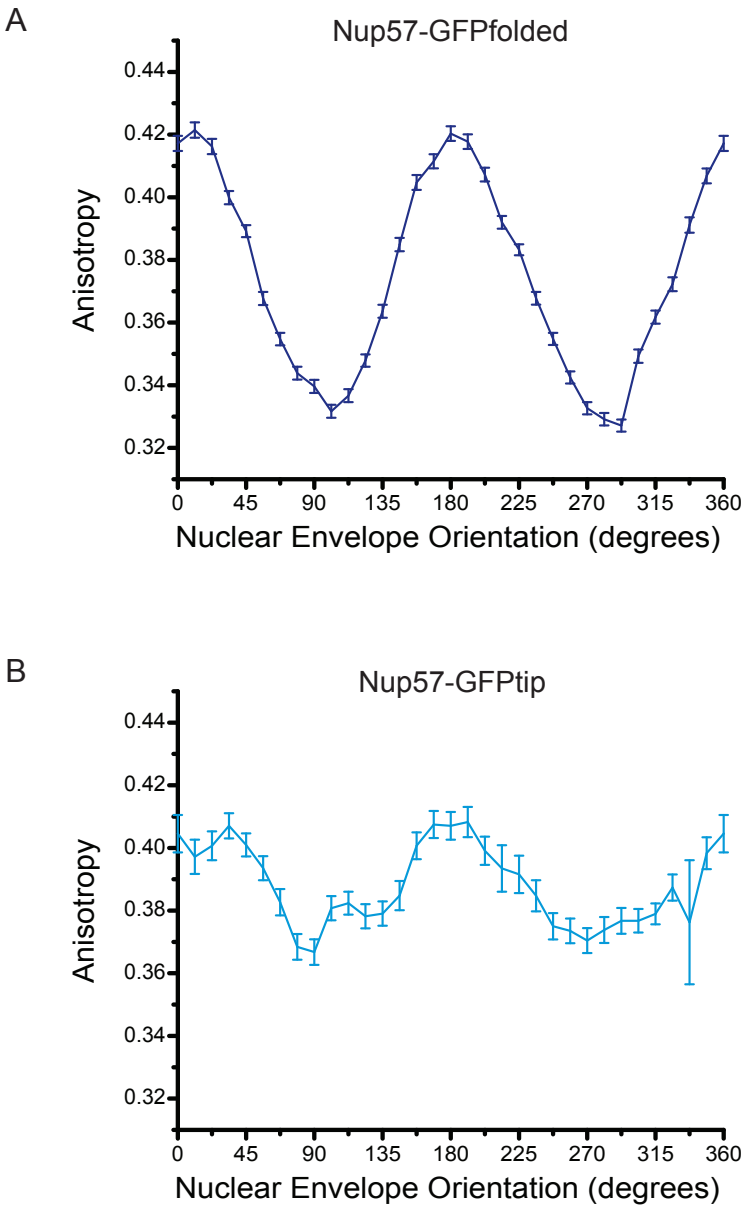

Figure 36: Anisotropy of FG and Folded Domains of Nup57. A) Anisotropy as a function of NE orientation for Nup57 tagged on the folded domain with GFP. A high amplitude pattern is measured, indicating the protein is ordered. B) Anisotropy as a function of NE orientation for Nup57 tagged at the tip of the FG domain. The patten has a lower amplitude, indicating less order. Error bars are SEM.

Anisotropy of the FG Domain Tips

To determine if the observations for Nup57-GFPtip generalized to the other FG proteins, yeast strains were generated expressing the FG nups Nup116, Nup1 and Nup159 tagged with GFP at the tip of the FG domain. Similarly to Nup57, GFP at the tip of the Nup116 FG domain displayed a small degree of order (Figure 37H). The Nup116-GFPtip anisotropy curve had the same phase as that of Nup57, with maxima at 0° and 180° and a minimum at 90°. In contrast, the anisotropy of both Nup159-GFPtip and Nup1-GFPtip was independent of the NE orientation, which means that these proteins are disordered with respect to the NPC (Figure 37F, I).

To investigate if these results were consistent across species, similar experiments were conducted in mammalian cells. The anisotropy of five FG nup-GFP fusions in HeLa cells was examined. These were: Nup214-GFPtip, Nup54-GFPtip, Nup98-GFPtip Nup153-GFPtip, and Nup62-GFPtip. These proteins display a range of behaviors. Nup54-GFPtip and Nup98-GFPtip are clearly somewhat ordered, and have anisotropy curves characterized by maxima at 0° and 180° and a minimum at 90° (Figure 37 B, C). Nup62-GFPtip and Nup153-GFPtip are less ordered, and Nup214-GFP is disordered (Figure 37 A, D, E).

The amplitudes of the anisotropy curves of mammalian nups are consistently higher than those of the yeast nups. This can be explained by physical differences. The mammalian nucleus is larger, so has less curvature of the NE in the focal plane; therefore the NPCs in the focal plane have a more similar orientation in ***z***. Greater curvature in the focal plane blurs the anisotropy pattern and decreases the measured amplitude.

Figure 37: Anisotropy of GFP at the Tip of the FG Domains. Anisotropy is plotted as a function of NE orientation. Error bars are SEM. A-E) Mammalian Nups.
A) Nup214-GFPtip. B) Nup54-GFPtip. C) Nup98-GFPtip. D) Nup153-GFPtip.
E) Nup62-GFPtip. F-I) Yeast Nups. F) Nup159-GFPtip. G) Nup57-GFPtip.
H) Nup116-GFPtip. I) Nup1-GFPtip. Yeast and mammalian homolgues of the same protein are shown in the same color. J) Amplitudes of curves A-I. Mammalian nups are shown in dark grey, yeast nups are shown in light grey.

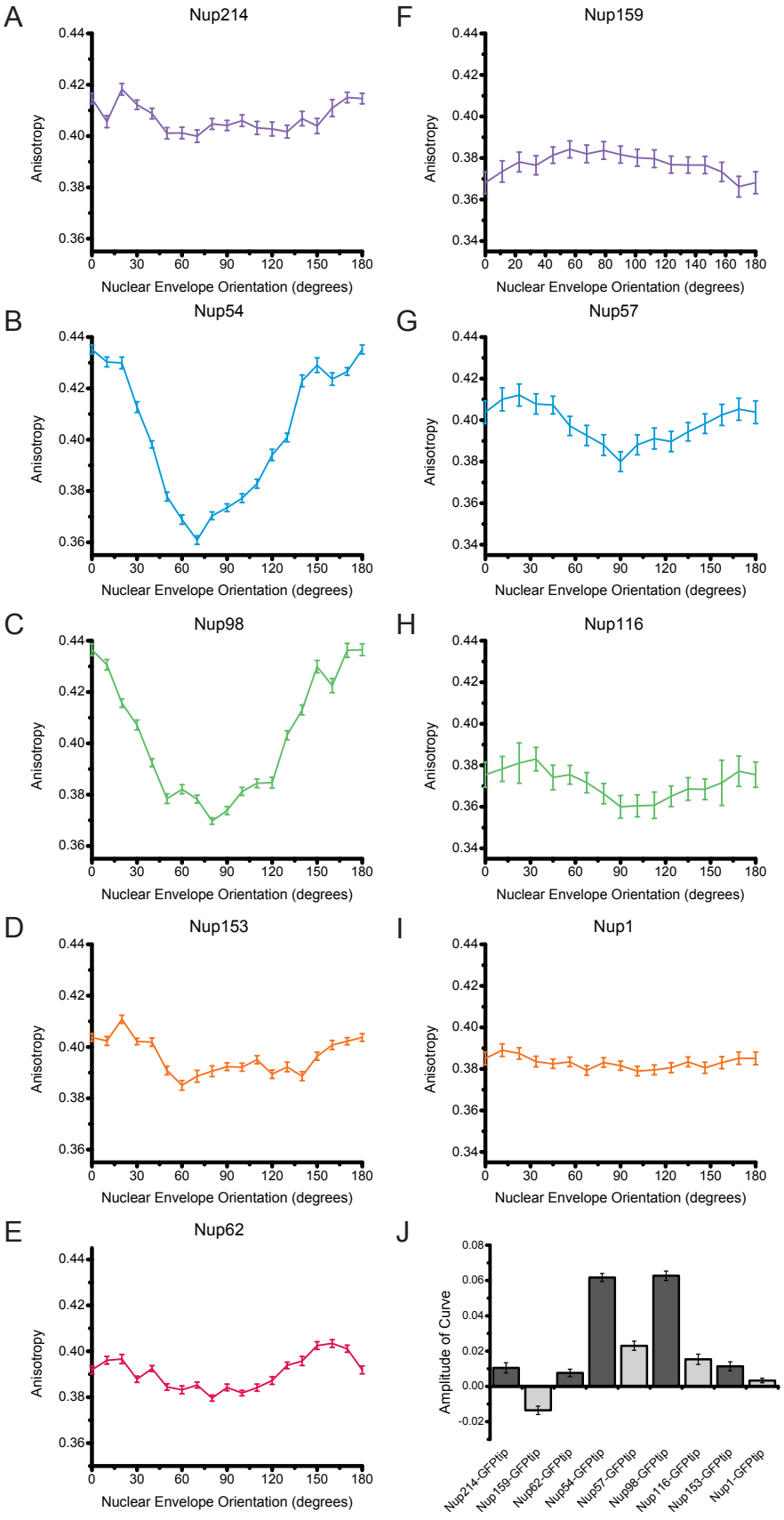
A
Nup214
F
Nup159
B
Nup54
G
Nup57
C
Nup98
H
Nup116
D
Nup153
I
Nup1
E
Nup62
J
Anisotropy
Nuclear Envelope Orientation (degrees)
Amplitude of Curve
Nup214-GFPtip
Nup159-GFPtip
Nup62-GFPtip
Nup54-GFPtip
Nup57-GFPtip
Nup98-GFPtip
Nup116-GFPtip
Nup153-GFPtip
Nup1-GFPtip

Additionally, the orientation of the NE can be assigned with more precision for a larger nuclear envelope.

The shape of the anisotropy curves was characterized by subtracting the value at 90° from the value at 0° to measure the amplitude. For a more ordered protein, the amplitude will be higher. In yeast, Nup57-GFPtip has the greatest amplitude of the nups tested, followed by Nup116-GFPtip, then Nup159-GFPtip, and last Nup1-GFPtip. In mammalian cells, Nup54-GFPtip has the greatest amplitude, then Nup98-GFPtip, followed by Nup62-GFPtip and Nup153-GFPtip, with Nup214-GFPtip displaying the lowest amplitude (Figure 37J). The tips of the FG proteins are therefore not behaving the same as each other in the NPC.

Even though the absolute amplitudes of the curves differ between mammalian and yeast cells, the relative behavior of homologous proteins is similar. Of the proteins assayed in both model systems, the homologues Nup57 and Nup54 display the greatest order. The homologues Nup98 and Nup116 both have periodic NE amplitudes, whereas the homologues Nup159 and Nup214, and Nup153 and Nup1 are all more disordered.

The order of an FG nup does not correlate with the total length of the FG domain. For example, Nup98-GFPtip has less order than Nup54-GFPtip and more order than Nup62-GFPtip, but has a larger FG domain than these proteins (504 amino acids for Nup98, 114 and 285 amino acids for Nup54 and Nup62 respectively). The degree of order also does not correlate to the type of FG repeat present. For example, Nup214 and Nup54 both contain only FG repeats and no SxFG or FxFG repeats, but Nup54 is the most ordered of the mammalian nups studied while Nup214 is the least ordered.

Anisotropy Changes along FG Domains

Each of the tips of the FG domains tips has a unique NE anisotropy pattern, indicating they are ordered differently. As described above for Nup57, the anisotropy is different depending on where the protein is tagged, and can be used to distinguish between folded and unfolded domains. When GFP is placed at the tip of the FG domain, it is anchored only on one side and may have more rotational freedom than a GFP anchored at both sides; experiments with the MHC complex had previously shown that a tag placed at the terminus of a domain behaves differently to one embedded in the sequence (Rocheleau et al., 2003). It is possible that the tag at the tip of the FG domain does not reflect the behavior of the rest of the domain. Therefore, FG nups were tagged in different positions to characterize the behavior along the length of the FG domain as well as between the FG and the folded domain of the FG proteins.

Constructs were created with the GFP tag in one of four positions: at the tip of the FG domain "-GFPtip", in the middle of the FG repeats of the FG domain "-GFPmiddle", at the boundary between the FG domain and the coiled coil domain "-GFPboundary", and at the opposite side of the coiled coil domain to the FG domain "-GFP folded". The following yeast proteins were endogenously tagged: Nup159, Nsp1, Nup57, Nup116, and Nup1. The following tagged mammalian proteins which were expressed in HeLa cells: Nup214, Nup62, Nup54, Nup98, and Nup153. The anisotropy of each of these proteins was determined as a function of NE orientation.

For Nup116, Nup98, Nup57, Nup54, Nsp1 and Nup62 the NE anisotropy was periodic and increased in amplitude as GFP was placed further away from the tip of the

Figure 38: GFP Tagged FG Nups. GFP tags were placed in different positions along the FG domain. A) Amplitude of all yeast anisotropy curves. B) Amplitude of all mammalian anisotropy curves. Yeast and mammalian homologues are shown in the same color. C-E) Example of curves from the yeast protein Nup116. C) Nup116-GFPtip. D) Nup116-GFPmiddle. E) Nup116-GFPboundary. F-I) Example of curves from the mammalian protein Nup54. F) Nup54-GFPtip. G) Nup54-GFPmiddle. H) Nup54-GFPboundary. I) Nup54-GFPfolded. All error bars are SEM.

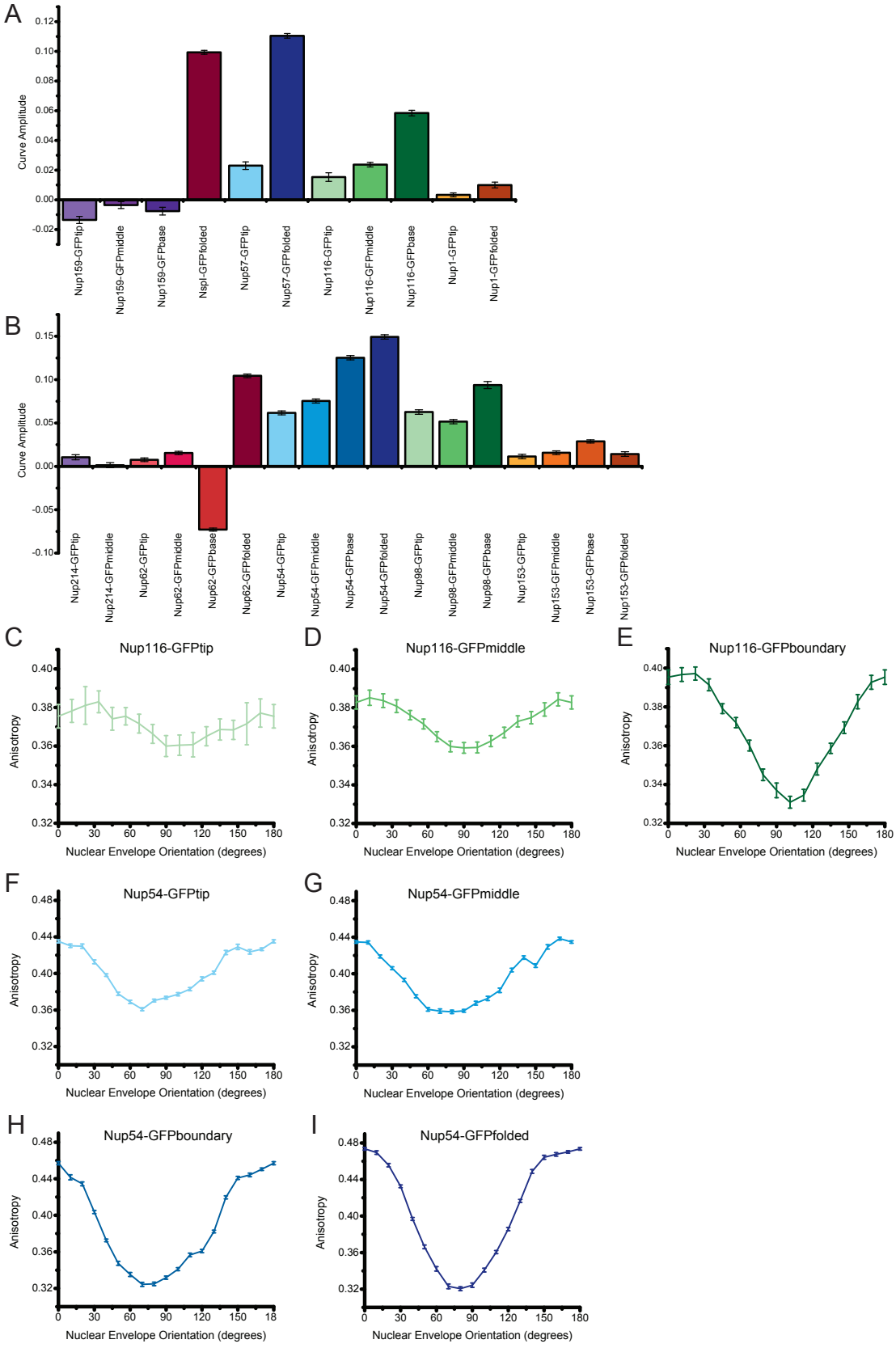
A
Curve Amplitude
Nup159-GFPtip
Nup159-GFPmiddle
Nup159-GFPbase
Nspl-GFPfolded
Nup57-GFPtip
Nup57-GFPfolded
Nup116-GFPtip
Nup116-GFPmiddle
Nup116-GFPbase
Nup1-GFPtip
Nup1-GFPfolded
B
Curve Amplitude
Nup214-GFPtip
Nup214-GFPmiddle
Nup62-GFPtip
Nup62-GFPmiddle
Nup62-GFPbase
Nup62-GFPfolded
Nup54-GFPtip
Nup54-GFPmiddle
Nup54-GFPbase
Nup54-GFPfolded
Nup98-GFPtip
Nup98-GFPmiddle
Nup98-GFPbase
Nup153-GFPtip
Nup153-GFPmiddle
Nup153-GFPbase
Nup153-GFPfolded
C
Nup116-GFPtip
D
Nup116-GFPmiddle
E
Nup116-GFPboundary
F
Nup54-GFPtip
G
Nup54-GFPmiddle
H
Nup54-GFPboundary
I
Nup54-GFPfolded
Anisotropy
Nuclear Envelope Orientation (degrees)

FG domain (i.e. tip < middle < boundary < folded) (Figure 38A, B). This increase in amplitude is illustrated by examples of the yeast protein Nup116 in Figure 38C-E, and the mammalian protein Nup57 in Figure 38F-I. These results show that for these proteins there is an increase in order along the length of the FG domain, from tip to base.

The anisotropy curves of all these constructs apart from Nup62-GFPboundary have maxima at 0° and 180° and a minimum at 90°; the GFP dipoles must therefore be oriented more parallel than perpendicular to the nucleocytoplasmic axis. For Nup62-GFPboundary, the NE anisotropy curve has the opposite phase with minima at 0° and 180° and a maximum at 90°, orienting the GFP dipole more perpendicular to the nucleocytoplasmic axis. This is shown in Figure 38B, where Nup62-GFPboundary is the only construct with a negative amplitude, although the absolute value of this amplitude is still relatively high. As the anisotropy curve of Nup62-GFPtip shows the opposite phase, the GFPs at the tip and base of the Nup62 FG domain have opposite orientations. This demonstrates that the orientation of the tip of the FG domain is not necessarily determined by the orientation of the base.

The absolute amplitudes of the curves vary between these six proteins. For the mammalian constructs, Nup54 displays the highest amplitude pattern at each position (tip =0.062, middle =0.075, boundary =0.125, folded =0.149), followed by Nup98 (tip =0.062, middle =0.052, boundary = 0.094), and then Nup62 (tip = 0.007, middle =0.015, boundary =0.073, folded =0.104). Similarly, among the yeast proteins the amplitude of the Nup57 curves (tip =0.024, folded =0.110) is higher than that of the Nup116 (tip =0.015) and Nsp1 (folded =0.099) curves when comparing GFP placed at the same position (Figure 38A, B).

The tip and middle of the FG domains are less ordered than the boundary and folded domains for Nup98, Nup54, Nup62, Nup116 and Nup57, but this trait does not hold true for all the proteins. Nup159, Nup214, Nup1 and Nup153 do not show any changes in amplitude along the length of the FG domain. Nup159 shows very little order for any position of the GFP within the FG domain, and both Nup214-GFPtip and Nup214-GFPmiddle show no periodicity, which is consistent with the GFP being disordered for these two proteins. Strikingly, these FG nups which are less ordered are the peripheral FG domains, whereas the more ordered FG domains are in the central channel.

Nup1 and Nup153 are the only constructs in which GFP adjacent to the coiled coil domain (in the "folded" position) does not display more order than GFP at the tip of the FG domain. This may be because the GFP is fixed in one of the specific orientations for which a curve of a very low amplitude will be measured, or it may indicate that the N terminus of this protein is somewhat mobile or randomly oriented. It is notable that Nup153 was measured to have the lowest residency time at the NPC. While its residence time is still longer than the exposure time for the images, it is possible that the mobility of Nup153 contributes to its low amplitude anisotropy pattern.

Each FG nup has a unique behavior and variation in order along its length, i.e. the FG domains do not behave homogenously. Importantly, the pattern of behavior for a particular nup is conserved between yeast and mammalian homologues. The nups which have an increasing degree of order from the base of the FG domain to the tip are the homologous pairs (mammalian/yeast) of: Nup98 / Nup116; Nup54 / Nup57; Nup62/ Nsp1. In both organisms Nup54/Nup57 is more ordered than Nup98/Nup116, and the

folded domain of Nup54/Nup57 has a higher amplitude than that of Nup62/Nsp1. The proteins which have lower amplitudes are also homologues of each other: Nup214 / Nup159; Nup153/Nup1. This similarity of FG behaviors supports the idea that the observed patterns reflect evolutionarily conserved and therefore functionally relevant aspects of the NPC, despite the low degree of sequence conservation between yeast and mammalian FG domains.

Anisotropy Patterns in Single Cells

Each of the FG nups examined shows a characteristic anisotropy pattern; these patterns represent an average over many cells. A pattern could arise from the average of multiple cells showing many different individual patterns; however if the pattern for a particular nup is due to a fixed orientation of the GFP in the NPC, the same pattern should be present in every cell and it should be maintained over time. The similarity of anisotropy patterns were between individual cells was used to determine if GFP is present in a range of orientations or if it has a single, fixed position relative to the NPC.

Data from individual cells are noisy, and it can be difficult to determine a pattern by eye. To quantify the degree to which the anisotropy pattern of an individual cells was ordered or disordered a Fourier transform of the anisotropy values was used. For a modulated pattern with 180° periodicity, there will be a characteristic spike in the Fourier transform. The value of the transform at this position was measured, and then divided by the standard deviation of the values at all the other positions. This gave an "orderedness score" which indicated how periodic the anisotropy pattern is.

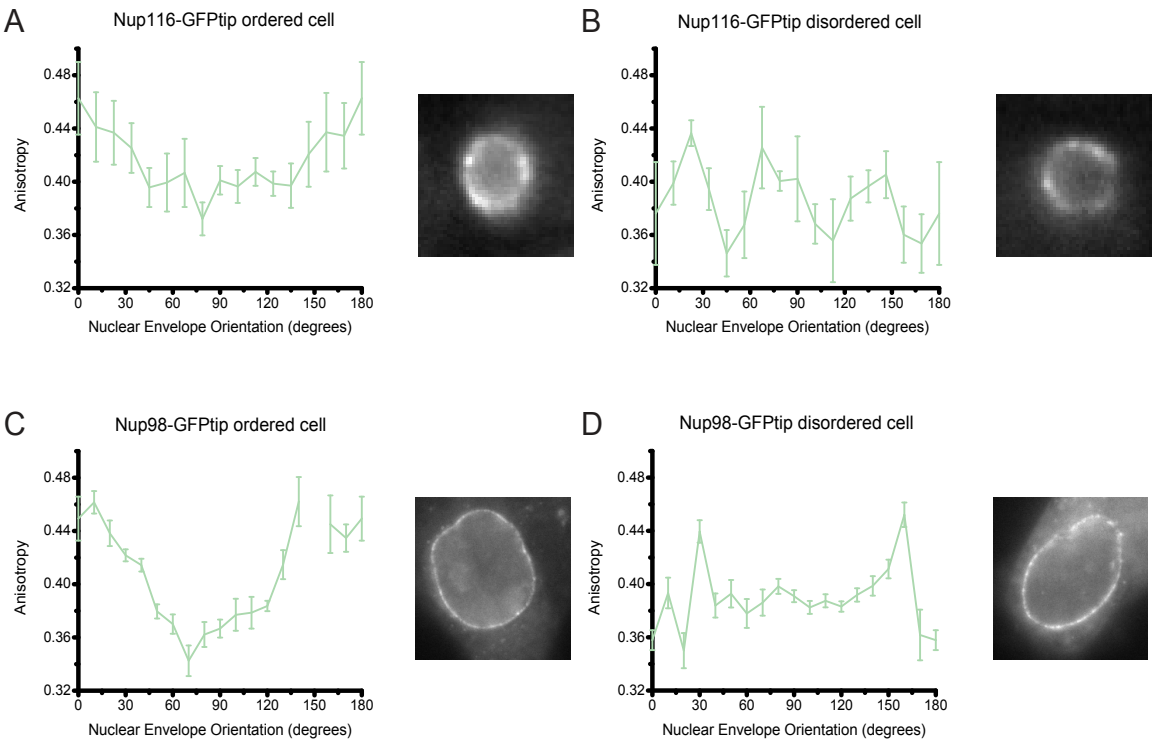

Figure 39: Examples of Anisotropy Patterns of Single Cells. A) Nup116-GFPtip, example of a yeast cell with an ordered pattern. B) Nup116-GFPtip, example of a yeast cell with a disordered patten. C) Nup98-GFPtip, example of a mammalian cell with an ordered pattern. D) Nup98-GFPtip, example of a mammalian cell with a disordered pattern.

For both yeast and mammalian cells there was a range of behaviors between individual cells, with some cells displaying a strongly periodic anisotropy pattern and some cells displaying disordered behavior, even when they were from a clonal population Examples of individual cells are shown in Figure 39.

However, there were differences in the overall distributions of scores depending on where GFP was placed in the sequence. When GFP was placed at the tips of the FG domains there tended to be fewer cells displaying an ordered pattern than for GFP at the middle of the FG domain, which had fewer ordered cells than GFP placed at the boundary, which in turn had fewer ordered cells than the folded domain. This is apparent in the histograms of orderedness scores for Nup57, Nup54, Nup62 and Nup116, which have more cells with higher values for the folded and boundary tag positions (Figure 40A, C, F and G).

Strains and constructs for which the population average anisotropy curves had lower amplitudes had more cells in a disordered state, and the range of orderedness score values was skewed towards lower values. For example, all Nup214 and Nup159 cells showed low scores, which were similar for all constructs (Figure 40D, E, I and J). For more constructs with higher amplitude curves, such as Nup62-GFPfolded and Nup57-GFPfolded, more cells tended show an ordered pattern (Figure 40, darker shades), and the orderedness factor was on average higher for these cells.

To determine if the order within an individual cell is fixed or variable over time, images of a field of cells over time were taken. This also means that for an individual cell the shape and intensity are constant, and therefore changes in the anisotropy pattern are independent of these two factors. The data from constructs tagged at the tip, middle, and

Figure 40: Histograms of Orderedness Scores for Single Cells. Homologous proteins are shown in the same colour. The higher the score, the more regular the anisotropy pattern. A-E) Yeast Nups. A) Nup54. B) Nsp1. C) Nup116. D) Nup159. E) Nup1. F-J) Mammalian Nups. F) Nup57. G) Nup62. H) Nup98. I) Nup214. J) Nup153.

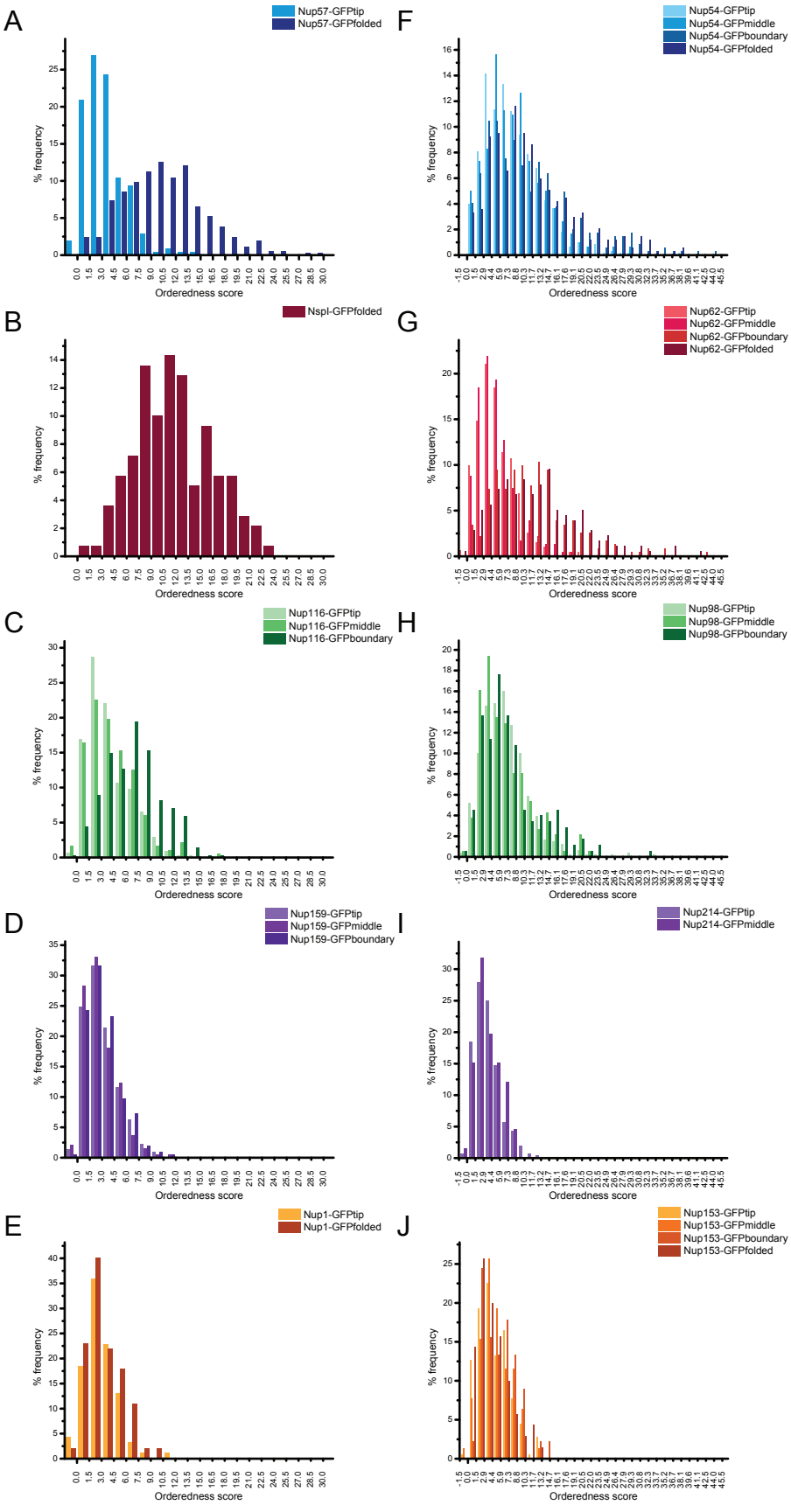
A
Nup57-GFPtip
Nup57-GFPfolded
% frequency
Orderedness score
B
NspI-GFPfolded
% frequency
Orderedness score
C
Nup116-GFPtip
Nup116-GFPmiddle
Nup116-GFPboundary
% frequency
Orderedness score
D
Nup159-GFPtip
Nup159-GFPmiddle
Nup159-GFPboundary
% frequency
Orderedness score
E
Nup1-GFPtip
Nup1-GFPfolded
% frequency
Orderedness score
F
Nup54-GFPtip
Nup54-GFPmiddle
Nup54-GFPboundary
Nup54-GFPfolded
% frequency
Orderedness score
G
Nup62-GFPtip
Nup62-GFPmiddle
Nup62-GFPboundary
Nup62-GFPfolded
% frequency
Orderedness score
H
Nup98-GFPtip
Nup98-GFPmiddle
Nup98-GFPboundary
% frequency
Orderedness score
I
Nup214-GFPtip
Nup214-GFPmiddle
% frequency
Orderedness score
J
Nup153-GFPtip
Nup153-GFPmiddle
Nup153-GFPboundary
Nup153-GFPfolded
% frequency
Orderedness score

base of the FG domain showed that the anisotropy pattern of a single cell is able to change over time, although the patterns for GFP at the tip of the FG domains were disordered much of the time. For GFP at the folded domain of proteins the pattern rarely changed. This suggests that the tips are more dynamic than the folded domains and may be changing in orientation over time.

For an individual cell the data are extremely noisy due to the limited number of pixels analyzed, and there are several experimental factors that may introduce artifacts which could affect the anisotropy pattern, including the intensity of fluorescence, the number of pixels analyzed, and how well the nuclear envelope orientation could be assigned.

The total intensity can be calculated from $I_{\parallel}+2I_{\perp}$; the average intensity for each cell was calculated from pixels corresponding to the NE in the total intensity image. The amount of order a cell displayed was not correlated to its brightness, which is expected as anisotropy should be independent of intensity (Figure 41 B, C). Therefore, the intensities recorded were high enough over background to accurately pick the NE and determine the anisotropy.

Computational image analysis routines were created to determine the number of pixels analyzed per segment or NE orientation per cell. For cells where there were very few or no pixels for most orientations, the noise was too high to be able to determine an accurate anisotropy pattern. These cells then tended to be assigned a low "orderedness score", which was interpreted as disorder. Therefore, some number of the low orderedness scores resulted from noisy data. However, even when cells with high numbers of pixels representing all NE orientations were analyzed, a range of orderedness

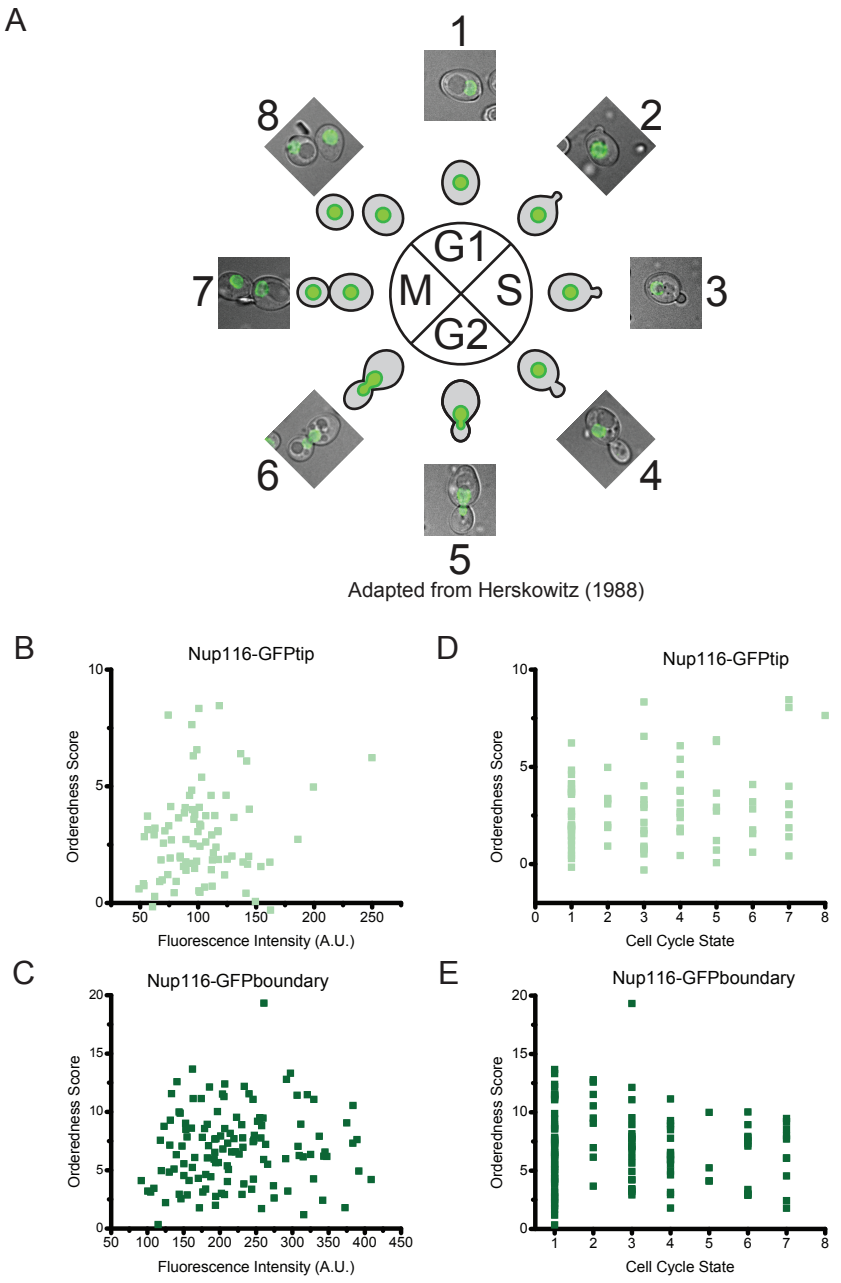

Figure 41: Analysis of Single Cells. A) Single yeast cells were assigned one of eight cell cycle categories based on their morphology in bright field. B-E) Examples of single cell analysis. B) Relationship between order and total fluorescence intensity for Nup116-GFPtip cells. C) Relationship between order and total fluorescence intensity for Nup116-GFPboundary cells. D) Relationship between order and cell cycle state for Nup116-GFPtip cells. E) Relationship between order and cell cycle state for Nup116-GFPboundary cells.

scores were present, showing that there are cells which are genuinely disordered. The value recorded for a single pixel had no correlation to the number of pixels with the same orientation angle.

An artifact could also be present if the sections of NE were being assigned the wrong orientation. For yeast cells, the accuracy of NE orientation assignment depends on the symmetry of the cell, as the segmental analysis assumes the NE to be circular. To determine how symmetrical the cells were, routines were created which determined the difference between number of pixels, and their average locations, in segments which were opposite one another. For symmetrical cells, these values should be 0, and there should be very little variation between all pairs of segments. This analysis showed that the order or disorder of an individual cell did not depend on its symmetry or circularity. Together, these data suggest that the differences between cells are not an artifact of the analysis.

There is also the possibility that differences between cells could have a biological basis. In yeast, cells were classified according to their position in cell cycle to determine if overall cell state changes through the cell cycle could be affecting behavior (Figure 41A). The orderedness score of a cell was not correlated to its position in the cell cycle (Figure 41 D, E). However, other biological factors could be affecting behavior of the NPC.

These results indicate that the FG domains are more mobile than the folded domains, which would be expected. They also suggest that the organization of the FG domains represents an average of a range of conformations; the FG domains may be dynamic and able to sample multiple orientations. However, the presence of order in

many cells suggests that certain orientations may be preferred, and that the FG domain may spend more time in these orientations. More analysis is needed to determine the origin of the differences between cells.

Dependence of FG Domain Behavior on Context within the NPC

The FG nups with the most ordered FG domains are centrally located within the NPC; the FG nups which are more disordered are peripherally located. It is possible that behavior of the FG domains is dependent on their position and context within the NPC. To test this, a series of domain swap experiments was carried out, in which the FG domains of central nups were swapped onto the folded domain of a peripheral nup. It has been shown in yeast that when FG domains from cytoplasmic nups are swapped onto the folded domain of nucleoplasmic nups and vice versa, it is the folded domain that determines the localization of the chimera (Zeitler and Weis, 2004).

Fusions of the FG domain of Nup98, Nup62 or Nup54 to the amino terminal side of the Nup214 folded domain were created (Figure 42 A-D). The chimeric constructs were tagged with a GFP at the tip of the FG domain. The Nup214/54-GFPtip and Nup214/62-GFPtip constructs displayed fluorescence primarily at the NE. The Nup214/98-GFPtip construct displayed fluorescence at the NE but had a high cytoplasmic background.

The anisotropy of Nup214-GFPtip has no dependence on NE orientation (Figure 42A). When the FG domains of Nup54 and Nup98 were fused to the coiled coil of Nup214, the GFP at the tip of the FG domain was disordered (Figure 42B, D). The

Figure 42: Anisotropy of Chimeric Constructs. Cartoons of the constructs are shown above each graph. A-D) Swapping the FG domains of central nups onto the Nup214 folded domain. A) Nup214-GFPtip. B) Nup54-GFPtip and Nup214 folded/Nup54 FG-GFPtip. C) Nup62-GFPtip and Nup214 folded/Nup62 FG-GFPtip. D) Nup98-GFPtip and Nup214 folded/Nup98 FG-GFPtip. E-H) Domain swaps between the folded and FG domains of Nup54 and Nup 62. E) Nup54-GFP tip and Nup62-GFP tip. F) Nup54 folded/Nup62 FG-GFPtip and Nup62 folded/Nup54 FG-GFPtip. G) Nup54-GFPboundary and Nup62-GFP boundary. H) Nup54 folded/Nup62 FG-GFP boundary and Nup62 folded/Nup54 FG GFP-boundary. All error bars are SEM.

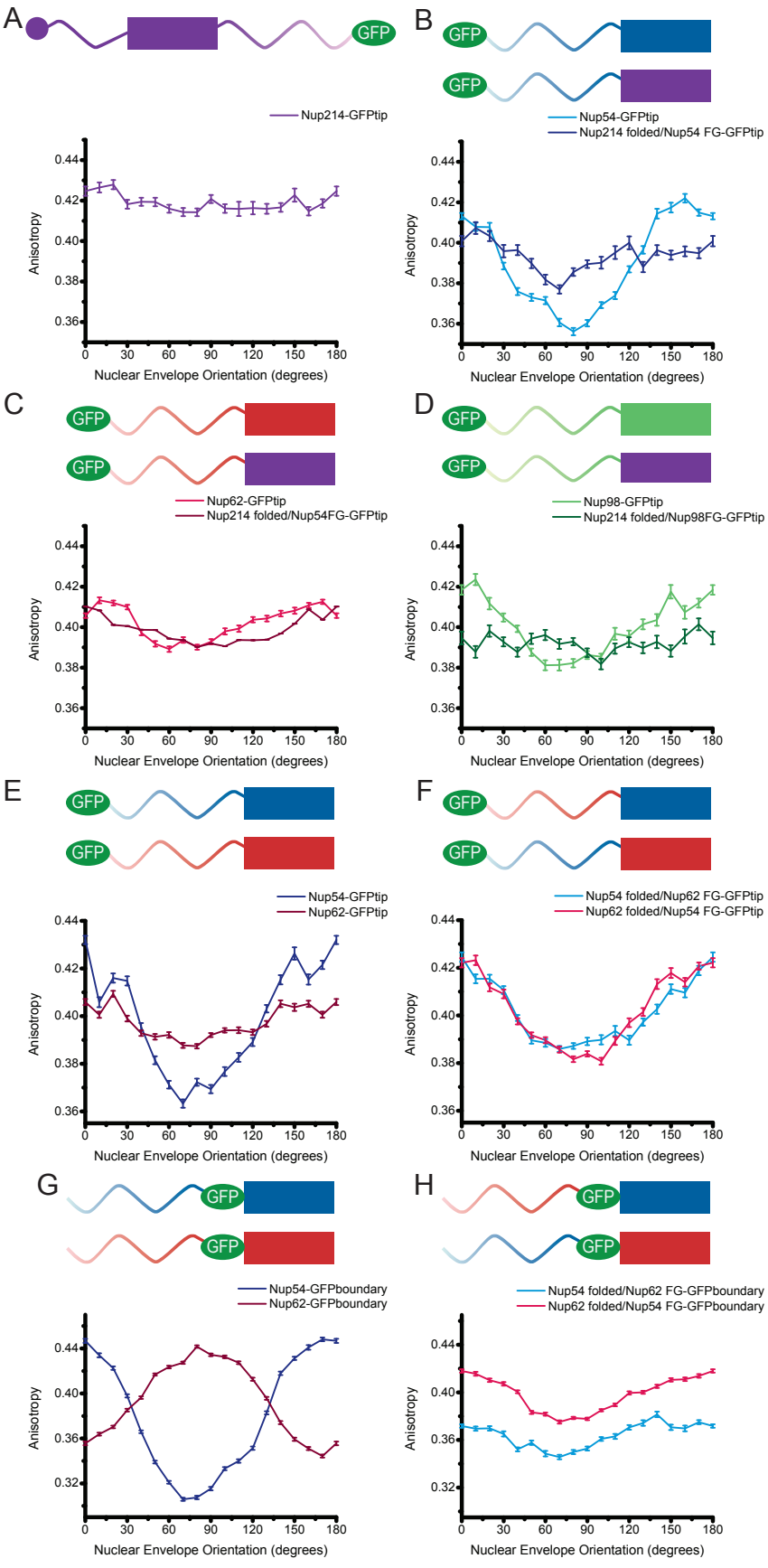
A
GFP
Nup214-GFPtip
Anisotropy
Nuclear Envelope Orientation (degrees)
B
GFP
GFP
Nup54-GFPtip
Nup214 folded/Nup54 FG-GFPtip
C
Nup62-GFPtip
Nup214 folded/Nup54FG-GFPtip
D
Nup98-GFPtip
Nup214 folded/Nup98FG-GFPtip
E
Nup54-GFPtip
Nup62-GFPtip
F
Nup54 folded/Nup62 FG-GFPtip
Nup62 folded/Nup54 FG-GFPtip
G
Nup54-GFPboundary
Nup62-GFPboundary
H
Nup54 folded/Nup62 FG-GFPboundary
Nup62 folded/Nup54 FG-GFPboundary

amplitude of Nup54-GFPtip decreased from 0.053 ± 0.003 to 0.011 ± 0.003 (blue curve compared to dark blue curve); the amplitude of Nup98-GFP tip decreased from 0.032 ± 0.003 to 0.001 ± 0.005 (green curve compared to dark green curve). A change in amplitude of Nup214/62- relative to that of Nup62-GFPtip was not possible to detect because of the initial low amplitude of the Nup62-GFPtip anisotropy (red curves) (Figure 42C).

These results indicate that the behavior of an FG domain can be influenced by its position within the NPC. These experiments used a relatively large change in the location of the domains, but it is possible that more local factors could also be affecting FG domain behavior. The folded domain, the surrounding nups, or the intrinsic properties of the FG domain could all be influencing the different patterns observed.

This was examined further by switching two FG domains that are part of the same structural subcomplex: Nup54 and Nup62. Although they are both in a central position in the NPC, they have different anisotropy patterns; Nup54-GFPtip exhibits the greatest amount of order for the constructs in which GFP is placed at the tip of the FG domain, whereas Nup62-GFPtip exhibits a lower degree of order (Figure 42E). The GFP tags at the base of the FG domain of these proteins are both highly ordered but the GFP is in different orientations relative to the nucleocytoplasmic axis (Figure 42G).

To investigate the relative influence of the FG domain and folded domain, these were swapped between Nup54 and Nup62. Four fusion proteins were created: Nup54/Nup62-GFPtip, in which the FG domain of Nup62 is fused to the folded domain of Nup54 with GFP at the tip of the FG domain; Nup62/Nup54-GFPtip, which has GFP at the tip of the Nup54 FG domain attached to the folded domain of Nup62;

Nup54/Nup62-GFPboundary, which contains the FG domain of Nup62 and the folded domain of Nup54 with GFP at the interface between the two; Nup62/Nup54-GFPboundary, which has the folded domain of Nup62 joined to the FG domain of Nup54, with the GFP between the two. These constructs are schematized in Figure 41F and H.

In all of the chimeric constructs, the anisotropy pattern was intermediate between that of Nup54 and Nup62 (Figure 42F, H). Nup54/62-FGtip and Nup62/54-FGtip had patterns of lower amplitude than Nup54 and higher amplitude than Nup62 (Figure 42E and F). This indicates that it is not just the overall position within the middle of the NPC that is determining behavior; specific interactions of the FG domain with its surroundings are probably also important for ordering the FG domain.

Nup54/62-GFPboundary and Nup62/54-GFPboundary displayed similar patterns to each other. These patterns had a lower amplitude than either that of Nup54-GFPboundary or Nup62-GFPboundary and had maxima at 0° and 180° and a minimum at 90°, which is the same phase as Nup54-GFPboundary curve. This pattern is similar to what would result if the patterns of Nup54-GFPboundary and Nup62-GFPboundary were averaged (Figure 42G and H). These results indicate that the pattern of the GFP at the boundary between the FG and folded domains is not simply a result of interactions between the GFP and the folded domain itself, but can influenced by the upstream behavior of the FG domain.

To test how much the upstream domain contributes to order at the boundary, the FG domains were removed from Nup54 and Nup62, and the folded domains were tagged on the N terminal side (i.e. in the ”boundary” position). For Nup54-GFPboundaryΔFG,

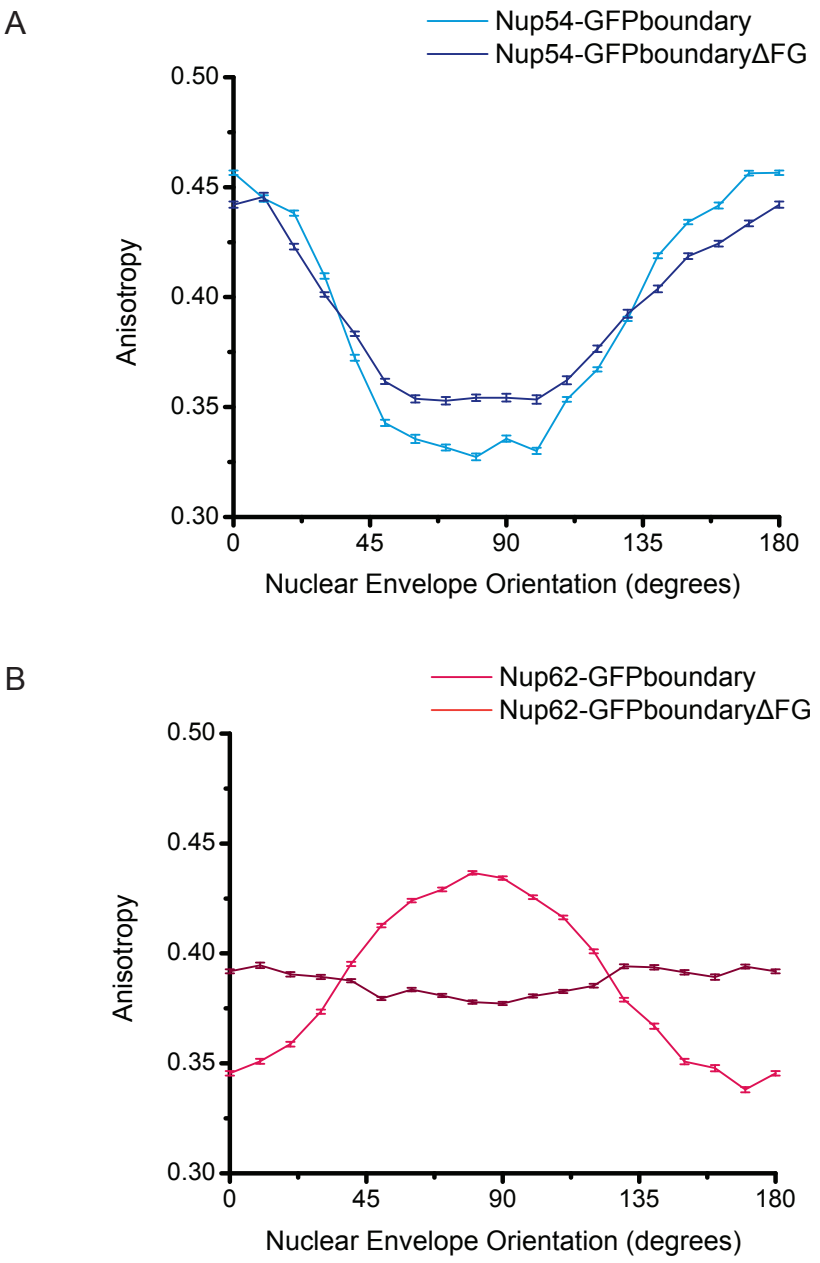

Figure 43: Anisotropy of Nup54 and Nup62 without the FG Domains. The FG domains were removed from Nup54 and Nup62 and the folded domains were tagged with GFP on the N terminal side. A) Nup54. B) Nup62.

there was a slight decrease in amplitude, indicating a loss in order or change in orientation. The amplitude was less than that of Nup54-GFPboundary but greater than that of Nup54/62-FGboundary, indicating that the Nup54 FG domain increases the order of GFP attached to Nup54 at this position, but that the Nup62 FG domain decreases it (Figure 43A).

For Nup62-GFPboundaryΔFG, the anisotropy curve has a much lower amplitude and the phase has been shifted through 90°. This curve is similar in shape to that of Nup62/54-GFPboundary (Figure 43B). Together, these results suggest that the behavior of the FG domain modifies the orientation and order of a GFP in the "boundary" position at the FG facing side of the folded domain; the behavior of the base of the FG domain may be determined by what is happening at the tip.

Additionally, the FG domains of the peripheral nups Nup153 and Nup214 were moved into the centre of the NPC by fusing them to the folded domain of Nup54. In these experiments, the FG domains were joined to the N terminus of the Nup54 folded domain, replacing its own FG domain. However, the FG domains of Nup153 and Nup214 are C terminal to the folded domain in their native context and are therefore in the reversed orientation in the chimeras, with the opposite end (the tip) of the FG domain attached to the folded domain. The anisotropy of Nup153-GFPtip and Nup214-GFPtip shows little dependence on NE orientation, and there was no change in this for Nup54 folded/Nup153 FG-GFPtip or Nup54 folded/Nup214 FG-GFPtip. Therefore, these FG domains are still disordered in the centre of the NPC lumen, but because they are not oriented correctly with respect to the folded domain this behavior may not be relevant.

In summary, these data indicate that the degree to which the FG domain is ordered, and its organization within the pore, depends on the specific context around it.

Behavior of the FG Domains Outside of the NPC

Many of the previous studies of FG domains have used exogenously expressed FG domains outside of the geometry and context of the NPC. Our results suggest that the behavior of an FG nup is dependent on its context within the NPC. However, the different behaviors of individual nups may reflect intrinsic properties of the proteins, as well being influenced by interactions within the pore lumen. To test this, constructs were created that are made up of FG domains tagged with GFP at the tip, fused to a C terminal palmitoylation sequence (El-Husseini et al., 2001). This localized the FG domain to the plasma membrane, removing it from the NPC but keeping it in a cellular context in the correct C terminally anchored conformation. Localizing proteins to the plasma membrane rather than the nuclear envelope still allows for anisotropy to be quantified as a function of membrane orientation.

To test whether structured proteins can be ordered with respect to the plasma membrane, GFP fused to the C terminal palmitoylation tag was tested. Cells expressing this construct showed plasma membrane fluorescence (Figure 44A). The anisotropy as a function of plasma membrane orientation was determined. The anisotropy curve for GFP-palm was modulated, with maxima at 0° and 180° and a minimum at 90°. This indicates that GFP is being held in a defined orientation to the plasma membrane, showing that for

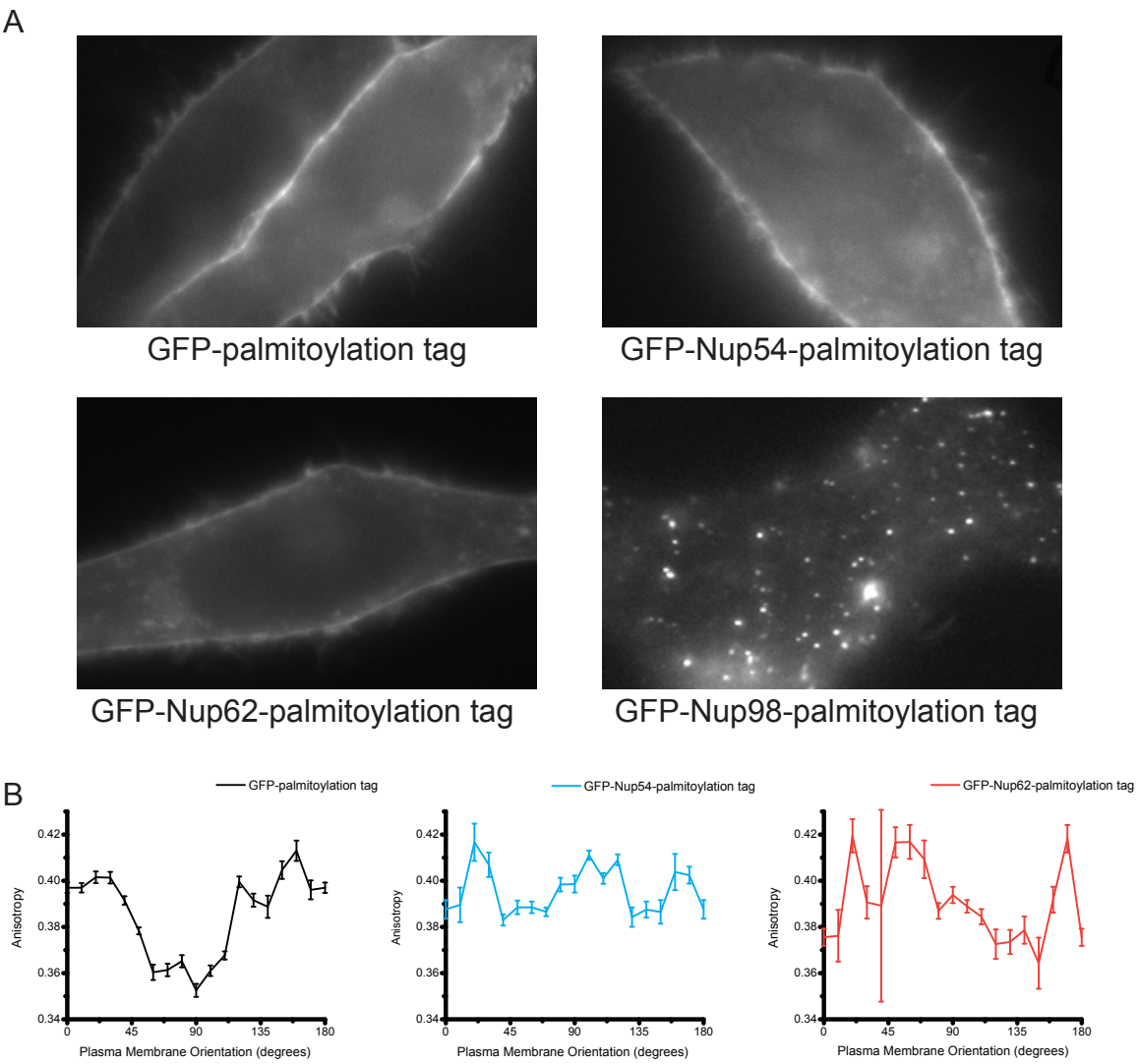

Figure 44: Anisotropy of FG Domains at the Plasma Membrane. GFP and FG domains tagged at the N terminus with GFP were localized to the plasma membrane by a C terminal palmitoylation signal. A) Representative images of cells expressing the four constructs. B) Anisotropy as a function of plasma membrane orientation for GFP-palmitoylation tag (black), GFP-Nup54-palmitoylation tag (blue) and GFP-Nup62-palmitoylation tag (red). All error bars are SEM.

a folded protein the C terminal palmitoylation signal is sufficient to hold it rigidly (Figure 44B).

The FG domains tested were Nup54, Nup62 and Nup98, since they show ordering within the NPC. The GFP-Nup98FG-palmitoyl construct aggregated in the cytoplasm of the cell and could not be detected at the plasma membrane. GFP-Nup54FG-palmitoyl and GFP-Nup62FG-palmitoyl both localized to the plasma membrane (Figure 44A). The anisotropy of both of these constructs was independent of plasma membrane orientation, suggesting that they are disordered, in keeping with the unfolded nature of these domains (Figure 44B). This result suggests that the order we see for these domains in the NPC is dependent on geometric constraints and interactions within the pore lumen itself rather than an intrinsic structure to the proteins.

Effect of FG Repeats on FG Domain Behavior

Mutation of the phenylalanine within the FG repeats to alanine disrupts both cargo binding and the interaction between FG domains *in vitro* (Patel et al., 2007). To investigate if FG repeats contribute to the organization of FG domains *in vivo*, the FG repeats of Nup54, Nup62 and Nup98 were mutated to AG. The anisotropy of the GFP in all positions along the FG domain was measured for each of these mutants. Mutating FG to AG had no effect on the anisotropy of any of the Nup62 constructs. The organization of Nup62 within the NPC is therefore not dependent on the FG repeats (Figure 45B, red curves compared to maroon curves).

Figure 45: Effect of FG to AG Mutations on Anisotropy. All the FG repeats in Nup54 and Nup62 were mutated to AG. 25% and 50% of the FG repeats in Nup98 were mutated to AG. Comparisons of the anisotropy for the wild type proteins and the mutants are shown. All error bars are SEM. A) Nup54 constructs. B) Nup62 constucts.
C) Nup98 constructs.

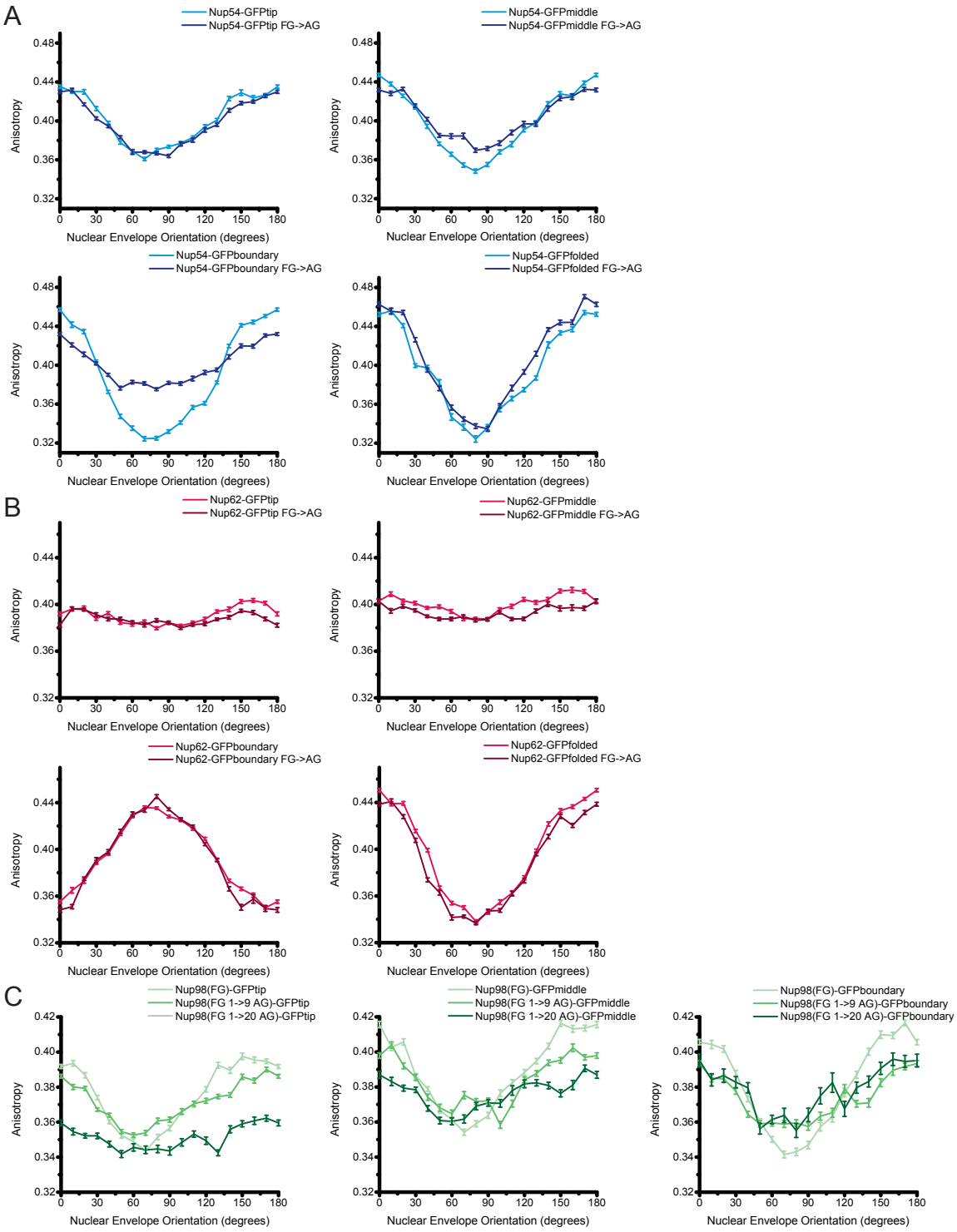
A
Nup54-GFPtip
Nup54-GFPtip FG->AG
Nup54-GFPmiddle
Nup54-GFPmiddle FG->AG
Nup54-GFPboundary
Nup54-GFPboundary FG->AG
Nup54-GFPfolded
Nup54-GFPfolded FG->AG
B
Nup62-GFPtip
Nup62-GFPtip FG->AG
Nup62-GFPmiddle
Nup62-GFPmiddle FG->AG
Nup62-GFPboundary
Nup62-GFPboundary FG->AG
Nup62-GFPfolded
Nup62-GFPfolded FG->AG
C
Nup98(FG)-GFPtip
Nup98(FG 1->9 AG)-GFPtip
Nup98(FG 1->20 AG)-GFPtip
Nup98(FG)-GFPmiddle
Nup98(FG 1->9 AG)-GFPmiddle
Nup98(FG 1->20 AG)-GFPmiddle
Nup98(FG)-GFPboundary
Nup98(FG 1->9 AG)-GFPboundary
Nup98(FG 1->20 AG)-GFPboundary
Anisotropy
Nuclear Envelope Orientation (degrees)

There was no effect of mutating the FG repeats to AG on the anisotropy pattern of Nup54-GFPtip or Nup54-GFPfolded, but the anisotropy patterns of Nup54-GFPmiddle and Nup54-GFPboundary decreased in amplitude. The patterns of the FG to AG Nup54-GFPmiddle and Nup54-GFPboundary mutants were still periodic, with anisotropy maxima at 0° and 180°excitation, but both had similar amplitudes to that of Nup54-GFPtip (Figure 45A, blue curves compared to dark blue curves). Therefore, the order of the domain these positions is partially affected but not completely lost, showing that some of the organization of Nup54 depends on the FG repeats. Since Nup54-GFPtip was unaffected by the FG to AG mutations, not all of the Nup54 FG domain is affected the same way. This result also suggests that the effect on order occurs only C terminally to the mutated FG repeats.

When all of the FG repeats of Nup98 were altered to AG, the protein was no longer present at the NE and the fluorescence was localized to the cytoplasm. Figure 46A shows representative examples of these constructs. It has been shown that the FG domain of Nup98 is required for its localization (Griffis et al., 2002); these data suggest that it is the FG motifs themselves which are required for Nup98 localization to the NE.

To determine if the localization of the Nup98 coiled coil domain was dependant on the Nup98 FG repeats specifically, the Nup98 FG domain was replaced with FG domains from Nup54, Nup62, and Nup214. These chimeras did not rescue the NE localization, indicating that the Nup98 FG motifs in the context of the rest of the Nup98 FG domain are important for localization. Nup98 is the only mammalian nucleoporin with GLFG repeats; this type of repeat may be required for localization.

Figure 46: FG to AG Mutations Prevent Nup98 from Localizing to the Nuclear Envelope. A) Representative images of the localization of Nup98 with varying percentages of FG repeats mutated to AG. First column: Nup98 tagged at the tip. Second column: Nup98 tagged in the middle of the FG domain. Third column: Nup98 tagged at the base of the FG domain. First row: wild type Nup98. Second row: 25% AG repeats. Third row: 50% AG repeats. Fourth row: 75% AG repeats. Last row: 100% AG repeats. B) Quantification of the relative amount of fluorescence in the cytosol and at the NE. Error bars are standard deviation.

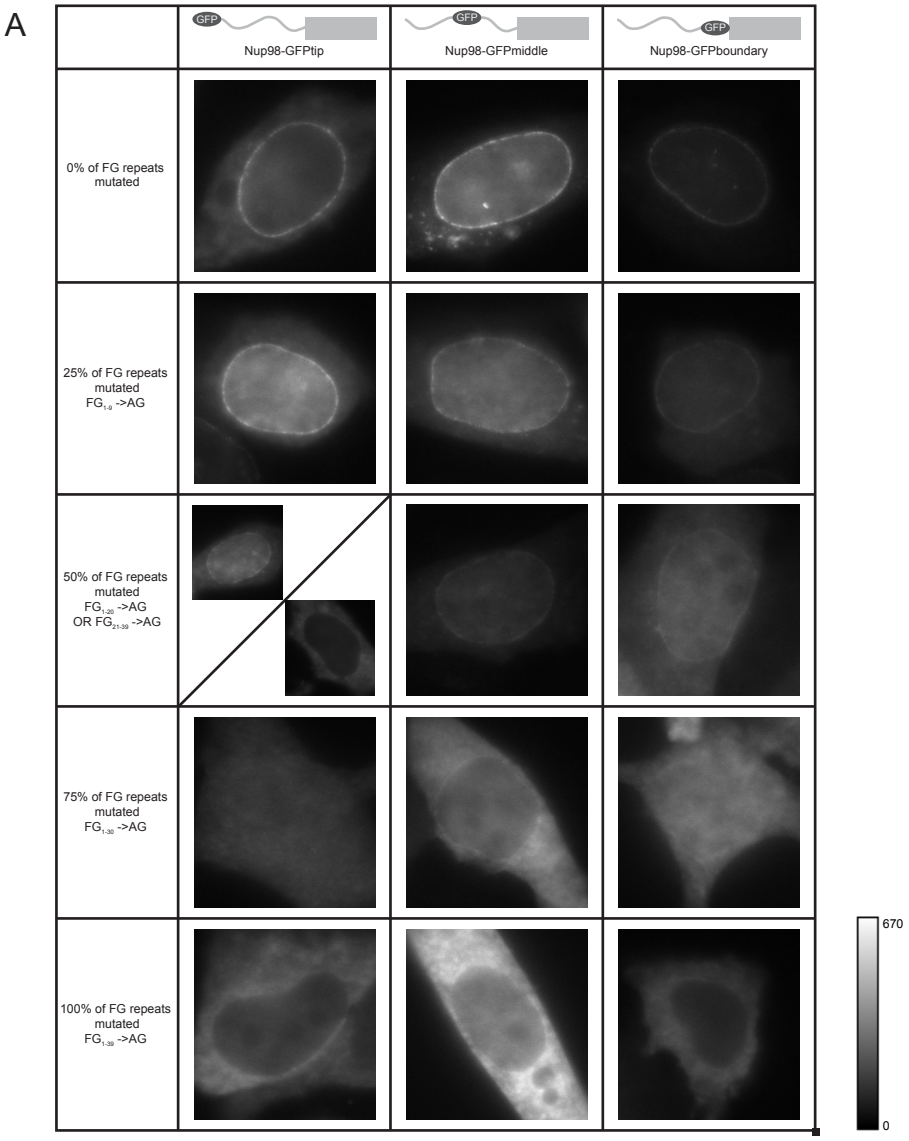
A
GFP
Nup98-GFPtip
GFP
Nup98-GFPmiddle
GFP
Nup98-GFPboundary
0% of FG repeats mutated
25% of FG repeats mutated FG1-9 ->AG
50% of FG repeats mutated FG1-20 ->AG OR FG21-39 ->AG
75% of FG repeats mutated FG1-30 ->AG
100% of FG repeats mutated FG1-39 ->AG
670
0

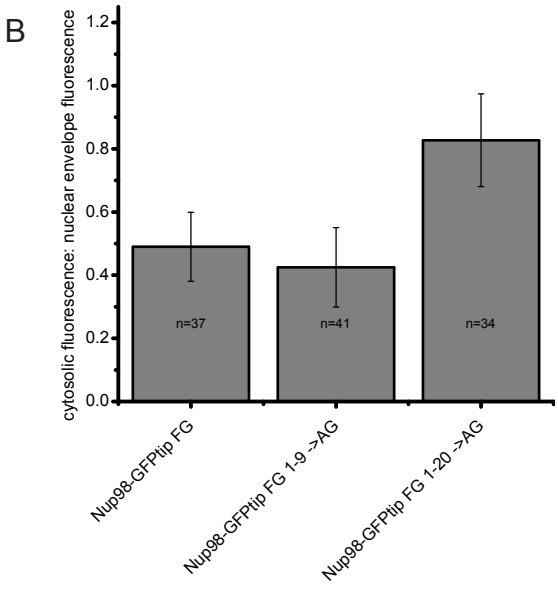
B
cytosolic fluorescence: nuclear envelope fluorescence
1.2
1.0
0.8
0.6
0.4
0.2
0.0
n=37
n=41
n=34
Nup98-GFPtip FG
Nup98-GFPtip FG 1-9 ->AG
Nup98-GFPtip FG 1-20 ->AG

To investigate the role of the FG motifs in Nup98, Nup98 constructs were generated with 25%, 50% or 75% of the FG repeats mutated to AG. When 25% of the FG repeats were mutated the Nup98 construct localized to the nuclear envelope similarly to the wild type protein. When the N terminal 50% of the FG repeats were mutated, the protein localized to the NE but a higher cytoplasmic background was also present (Figure 46B). When the C terminal 50% of FG repeats were mutated, the protein localized less well to the NE. This is consistent with GLFG repeats being important for localization as there is a higher proportion of GLFG repeats in the C terminal half of the domain. When 75% of the FG repeats were mutated, the protein was no longer detectable at the NE. This suggests that the ability of Nup98 to localize to the NPC is directly related to how many of the the Nup98 FG repeats are present.

The anisotropy was characterized for constructs with 50% or 25% of the FG repeats mutated to AG and GFP at the tip, middle or base of the FG domain. These experiments were carried out in permeabilized cells to reduce the contribution from the fluorescence in the cytosol. There was a decrease in the amplitude of the anisotropy pattern for the constructs with 25% of the FG repeats mutated to AG, indicating that these proteins are less well ordered than the wild type (Figure 45C, light green curves compared to green curves). The constructs with 50% of the FG repeats mutated to AG have a further decrease in the amplitude of the anisotropy pattern (light green curves compared to dark green curves). These data show that the FG repeats are contributing to the organization of Nup98 within the NPC. However, the decrease of order may be due to the mislocalization of the protein itself, rather than a change in the orientation of the FG domain due to loss of FG-FG interactions.

Altogether, the results from Nup54, Nup62 and Nup98 show that the FG repeats make different contributions to ordering the FG domains depending on the protein. This shows that factors influencing the order of the different domains are not the same for all FG nups, and further highlights that the domains are not behaving homogenously *in vivo*.

Different Regions of the Same FG Domain can Behave Independently

The FG domains of Nup62, Nup98, Nup214 and Nup153 and Nup54 are modified by O-linked glycosyl groups that can bind the lectin wheat germ agglutinin (WGA) (Finlay et al., 1987; Newmeyer, 1988). The addition of WGA to permeabilized cells allows cargo binding but prevents transport. It is hypothesized that this is due to cross-linking of the FG nups, which would be expected to immobilize them.

To test if WGA binding affects the order of the FG domains, it was added to permeabilized cells. After addition of WGA there were no changes in the anisotropy of Nup54 and Nup62 constructs with GFP at the tip, middle, or folded domain (Figure 47B-C). However, the anisotropy patterns of Nup54-GFPboundary and Nup62-GFPboundary decreased in amplitude, indicating an increase in disorder; this change is apparent in the difference between the dark and light curves of the third panel of Figure 47B and C. This shows that protein binding (and possibly cross-linking) can affect FG domain order.

Interestingly, the glycosylation sites in Nup62 are predicted to lie in between the FG repeats and the coiled coil domain (Figure 47A); WGA binding may only have an effect on the tags which are close to the glycosylation sites. Since the NE anisotropy remains the same for the tip and middle of the FG domains, but is altered for the base,

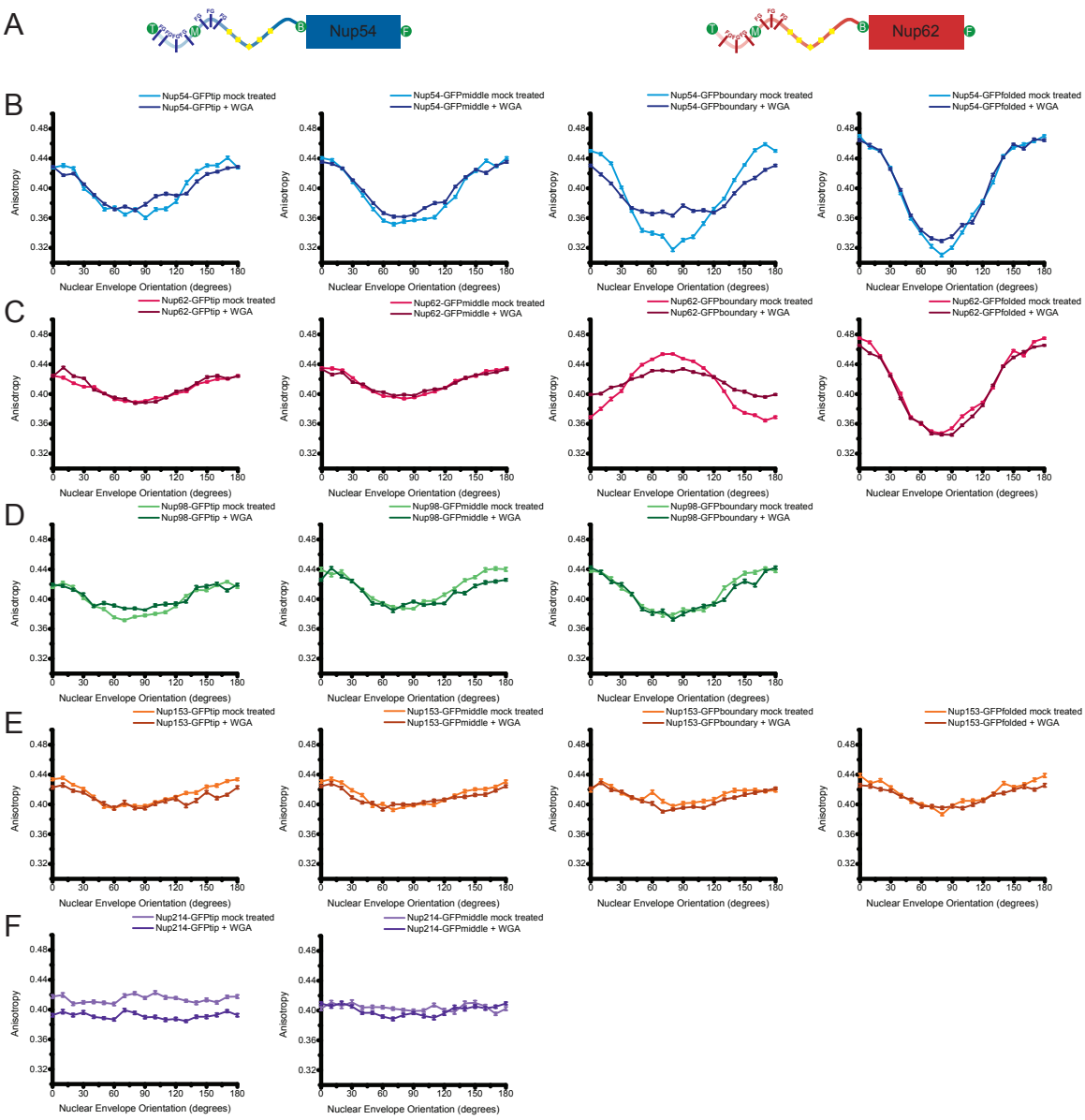

Figure 47: Effect of WGA Binding on Anisotropy. Comparisons of anisotropy curves for cells either mock treated or treated with WGA. All error bars are SEM. A) Schematic of approximate sites of glycosylation relative to GFP tags and FG repeats for Nup54 and Nup62. GFP tag sites are shown as green circles; FG repeats are shown as blue and red lines; glycosylated regions are indicated by yellow diamonds. B) Nup54 constructs. C) Nup62 constructs. D) Nup98 constructs. E) Nup153 constructs. F) Nup214 constructs.

this result suggests that the upstream regions of the FG domain are able to act independently of changes at the base.

These results are in contrast to the FG to AG mutations in Nup54 and the chimeric constructs Nup54/Nup62-GFPboundary and Nup62/Nup54-GFP boundary, in which changes made to the tip of the FG domain altered the behavior of the base of the FG domain. Here, the behavior of the GFP at the boundary position is being altered for Nup54 and Nup62, but there is no change to the remainder of the FG domain. This suggests that orientational and organizational changes that occur at the tip of the FG domain can be transmitted to the base, but not vice versa.

The addition of WGA had no effect on the anisotropy patterns of the Nup98, Nup214 and Nup153 constructs (Figure 47D-F). If the glycosyl groups within these domains are not located close to the positions of the tags it is possible that any perturbations caused by WGA are not being transmitted to the rest of the domain and are therefore not detectable as a change in anisotropy.

Active Transport and FG Domain Behavior

It is possible that the behavior of the FG domains is modified by cargo. The individual FG domain types bind distinct repertoires of cargo; this may account for the behavioral differences between the domains. If this were the case, when no cargo is present in the NPC, they would be expected to behave the same as one another. Additionally, some models for transport specifically predict conformational changes of the FG domain upon cargo binding, which should be detectable as a change in anisotropy.

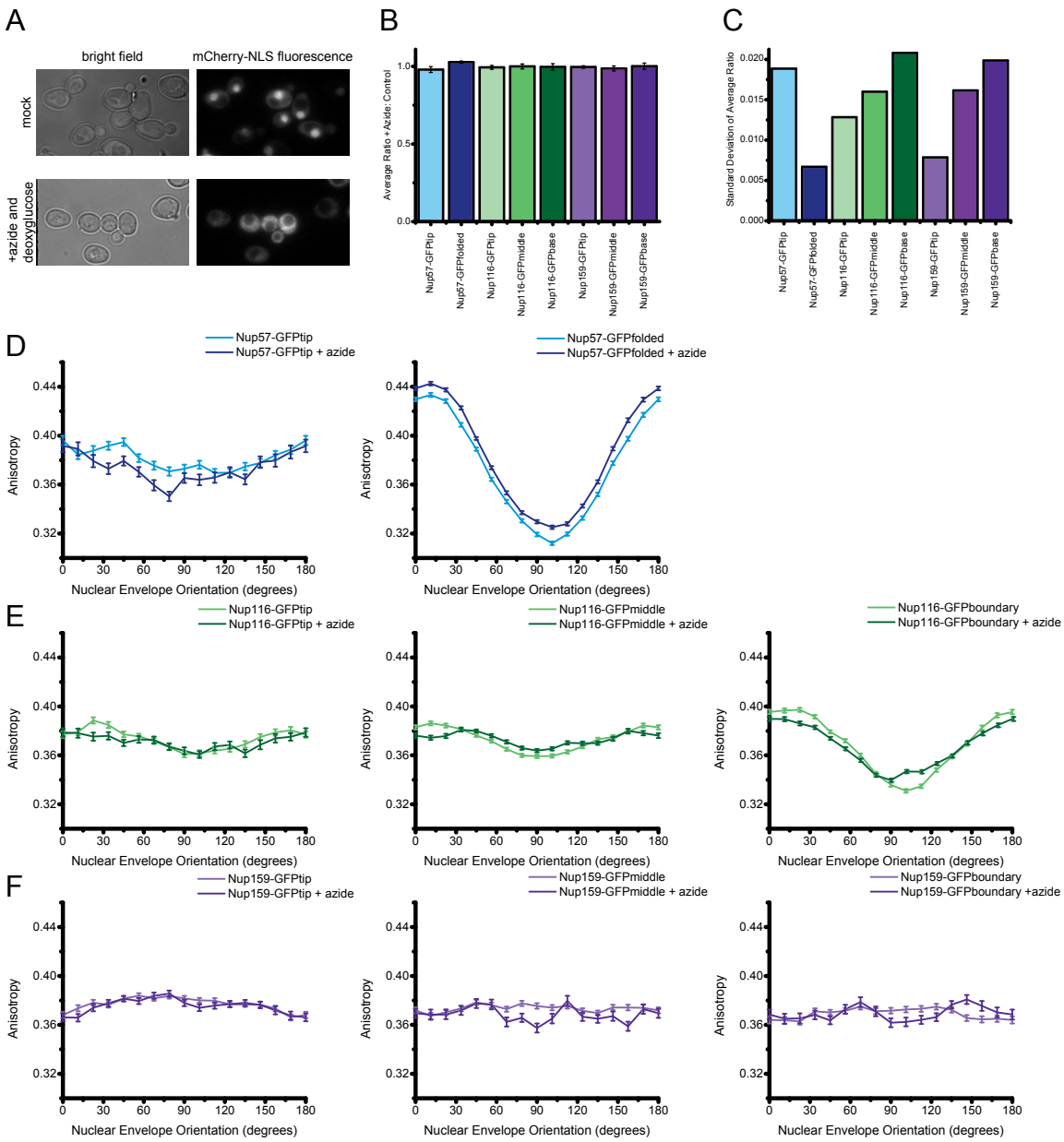

Figure 48: Azide Treatment of Yeast Cells to Stop Transport. A) Azide and deoxyglucose treatment shuts down active transport and mCherry-NLS equilibrates between the nucleus and the cytoplasm. B) Ratio of the anisotropy values of the treated and untreated cells averaged over all membrane orientations. Error bars are standard deviation. C) Standard deviations of the average anisotropy ratio. D-F) Anisotropy curves for azide treated and untreated cells. For all anisotropy curves, error is SEM.
D) Nup57 constructs. E) Nup116 constructs. F) Nup159 constructs.

To determine if active transport through the NPC affects the ordering and behavior of the FG nups, active transport in yeast was shut down using sodium azide and deoxyglucose to disrupt the RanGTP gradient (Schwoebel et al., 2002). Transport was assayed with mCherry-NLS, which accumulates in the nucleus during active transport and passively diffuses through the NPC to equilibrate between the nucleus and cytoplasm when transport is blocked (Figure 48A) (Shulga et al., 1996). This assay showed that the azide treatment was effectively blocking transport in all cells.

The anisotropies of the nup-GFP fusion strains Nup57-GFPtip, Nup57-GFPfolded, Nup116-GFPtip, Nup116-GFPmiddle, Nup116-GFPboundary, Nup159-GFPtip, Nup159-GFPmiddle, and Nup159-GFPboundary were not affected by azide and deoxyglucose treatment (Figure 48D-F). The slight differences in the absolute values of the Nup57-GFPfolded constructs (Figure 48D, second panel) are probably due to changes in the background subtraction, as the azide treatment results in an increase of cytoplasmic autofluorescence. However, these curves have the same amplitude, suggesting no change in the order between treated and control cells. To compare the shapes of the curves, the ratio of the values in the treated and untreated cells at each NE orientation was taken, and these values were averaged. If the curves are the same, this ratio should be 1, and the standard deviation should be low, indicating that the two values are the similar at every point on the curve. This was the case for azide treatment; the averages and standard deviations are shown in Figure 48 B and C.

To shut down active transport in mammalian cells, the plasma membrane was permeabilized with digitonin and the cytoplasmic content of the cell was washed out. It has been shown previously that transport cannot be supported under these conditions. The

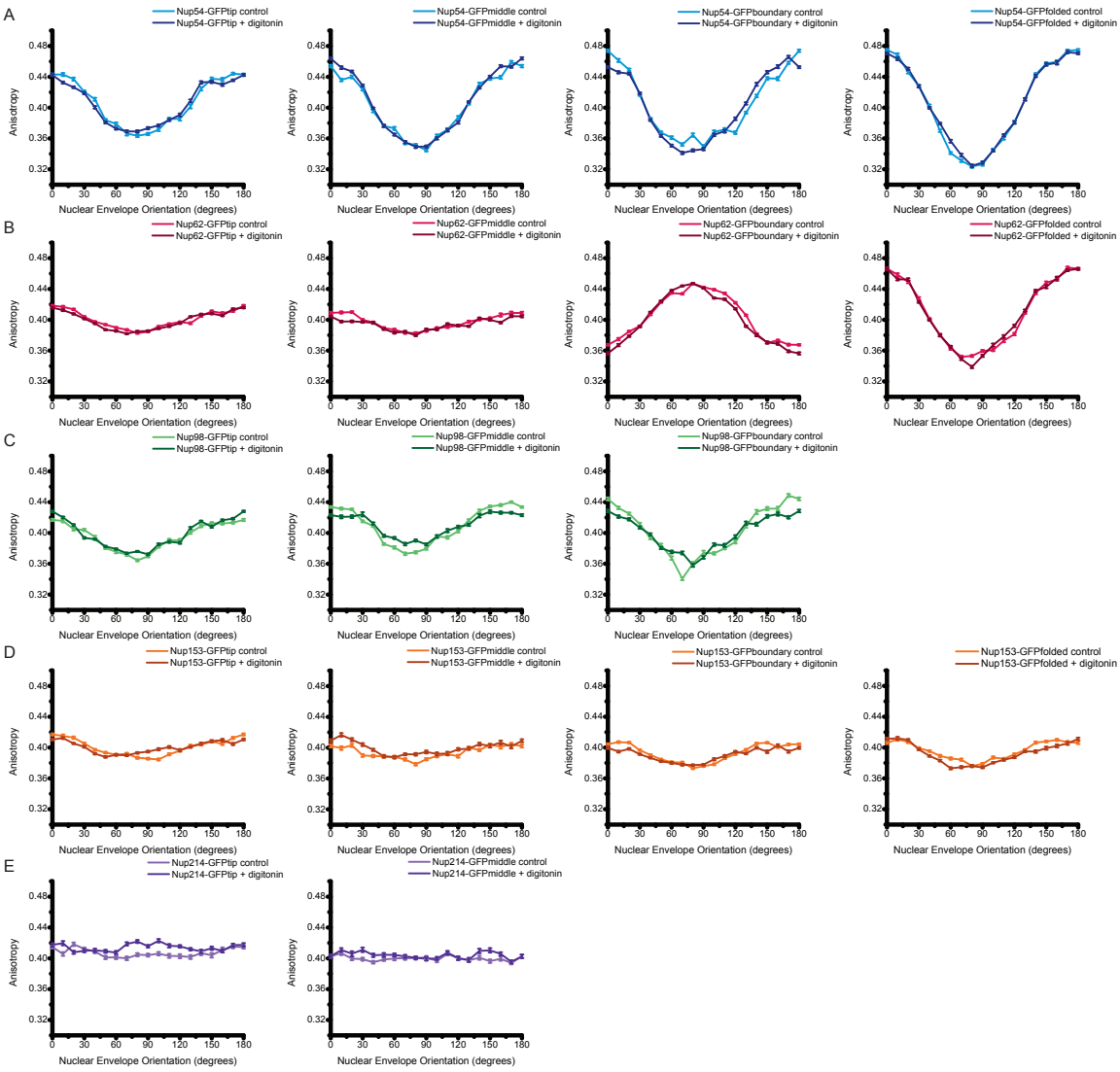

Figure 49: Permeabilization of Mammalian Cells to Stop Active Transport.

Comparison of anisotropy curves for cells treated with digitonin to permeabilize their plasma membranes, and untreated cells. All error bars are SEM. A) Nup54 constructs. B) Nup62 constructs. C) Nup98 constructs. D) Nup153 constructs. E) Nup214 constructs.

anisotropy of each of the mammalian constructs was measured in permeabilized cells. Permeabilization had no effect on the anisotropy patterns of any construct compared to mock treated cells (Figure 49). Thus, in both yeast and mammalian cells the behavior and ordering of the FG nups was not dependent on the presence of active transport.

Effect of Cargo Binding on FG Nup Behavior

There was no change in FG nup behavior when the Ran gradient was disrupted either in azide treated yeast cells or in permeabilized mammalian cells. In both of these cases, although active transport has been stopped, there may still be cargo which remains bound within the NPC and could still be affecting the behavior of the FG domains. Three markers for cargo were tagged with GFP and examined in mammalian cells prior to and after permeabilization to determine if they remained bound at the NE. The cargo molecules used were the import karyopherin-β1 (kapβ1-GFP), the export karyopherin Crm1 (Crm1-GFP), and TAP (TAP-GFP) as a marker for mRNA export. Nup62-mCherry was used as a marker of the NPC.

In unpermeabilized cells, kapβ1-GFP was present at high levels in the cytoplasm and enriched at the NE. When cells expressing kapβ1-GFP and Nup62-mCherry were permeabilized, the kapβ1-GFP signal in the cytoplasm was lost, but fluorescence was retained at the NE for longer than 30 minutes, showing that import cargo remains bound (Figure 50A). TAP-GFP behaved similarly, with a high cytoplasmic signal prior to permeabilization. In the TAP-GFP cells the fluorescence in the cytoplasm and inside the nucleus was higher than in the kapβ1-GFP cells, and obscured the NE itself. Following

Figure 50: Cargo Unbinding from the NPC. A) Example of cells expressing Nup62-mCherry and karyopherinβ1-GFP. Top 3 panels are mock treated at time 0, bottom 3 panels have RanGTP added at time 0. B) Quantification of loss of total NE fluorescence for Nup62-mCherry and karyopherinβ1-GFP in mock treated and RanGTP treated cells. Error bars are standard deviation. C) Quantification of NE fluoresence remaining 10 minutes after addition of RanGTP or mock treatment. Error bars are standard deviation. D) Examples of cells expressing Nup62-mCherry and Crm1-GFP. Top 3 panels are mock treated at time 0, bottom 3 panels are treated with digitonin at time 0. E) Quantification of loss of total NE fluorescence for Nup62-mCherry and Crm1-GFP in mock treated and digitonin treated cells, aligned to addition of digitonin. Error bars are standard deviation. F) Quantification of loss of total NE fluorescence for Nup62-mCherry and Crm1-GFP in digitonin treated cells, aligned to time of permeabilization of individual cells. Error bars are standard deviation. G) Example of cells expressing Nup62-mCherry and TAP-GFP. Top 3 panels are mock treated at time 0, bottom 3 panels have RanGDP added at time 0. H) Quantification of loss of total NE fluorescence for Nup62-mCherry and TAP-GFP in mock treated andRanGTP treated cells. Error bars are standard deviation. I) Quantification of loss of total NE fluorescence for Nup62-mCherry and TAP-GFP in mock treated andRanGDP treated cells. Error bars are standard deviation.

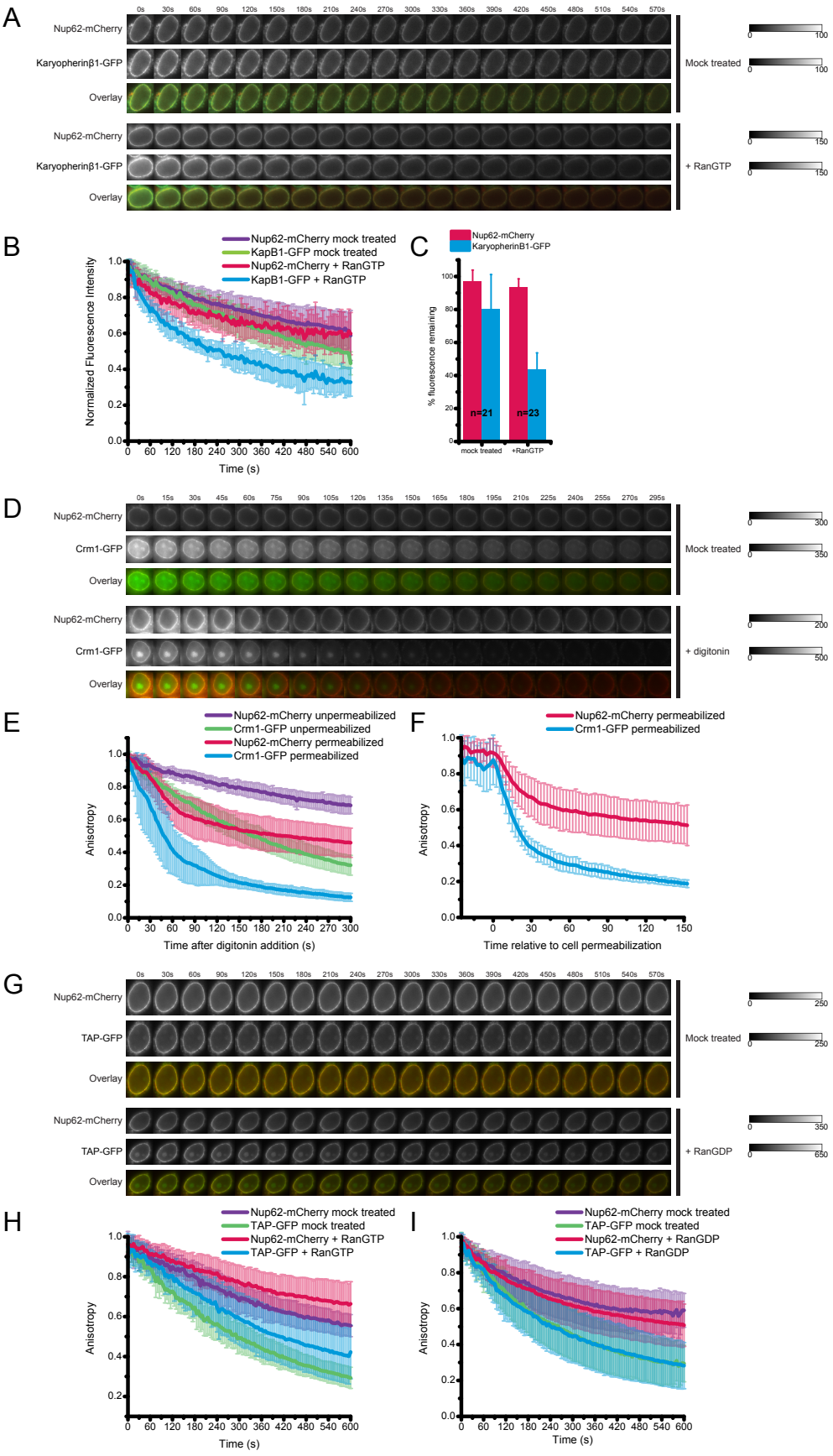
A
Nup62-mCherry
Karyopherinβ1-GFP
Overlay
Mock treated
+ RanGTP
B
Nup62-mCherry mock treated
KapB1-GFP mock treated
Nup62-mCherry + RanGTP
KapB1-GFP + RanGTP
Normalized Fluorescence Intensity
Time (s)
C
Nup62-mCherry
KaryopherinB1-GFP
% fluorescence remaining
n=21
n=23
mock treated
+RanGTP
D
Crm1-GFP
+ digitonin
E
Nup62-mCherry unpermeabilized
Crm1-GFP unpermeabilized
Nup62-mCherry permeabilized
Crm1-GFP permeabilized
Anisotropy
Time after digitonin addition (s)
F
Time relative to cell permeabilization
G
TAP-GFP
+ RanGDP
H
TAP-GFP mock treated
TAP-GFP + RanGTP
I
TAP-GFP + RanGDP

permeabilization, the TAP signal was visible at the NE and the nucleolus. Signal was present at the NE for longer than 30 minutes after permeabilization, showing that TAP remains bound at the NPC (Figure 50G).

Crm1-GFP was present in the cytoplasm of cells, but was enriched at the NE and the nucleolus (Figure 50D). In contrast to TAP-GFP and kapβ1-GFP, the Crm1-GFP signal at the NE was lost within a few seconds of permeabilization, indicating that Crm1-GFP rapidly unbinds from the NPC (Figure 50E, F). Over 5 minutes the nucleolar signal also disappeared, albeit at a slower rate than the NE signal. Therefore, even in permeabilized cells the majority of the export cargo has been lost from the NPC with no effect on FG domain behavior as assayed by anisotropy.

To test if dissociation of import cargo has an effect on FG domain behavior, RanGTP was added to unbind it. 10 minutes after addition of RanGTP (0.3mg/ml) the kapβ1-GFP signal at the NE decreased to 43% of the initial signal, while in control cells 80% of the signal remained (Figure 50C). The majority of the kapβ1-GFP unbinding occurred in the first 5 minutes after addition of RanGTP (Figure 50B). In contrast, addition of RanGTP or RanGDP had no effect on the rate if TAP-GFP dissociation, which is expected as TAP dependent export is a Ran independent process (Figure 50H, I).

The anisotropy was then assayed in cells after 10 minutes of treatment with RanGTP in the absence of the cargo marker. There was no effect of dissociating kapβ1-GFP from the NPC on the anisotropy patterns of any of the Nup54, Nup62, Nup98 Nup214 or Nup153 constructs (Figure 51A-E). This is reflected in the average ratio between the RanGTP treated and mock treated anisotropy values; for all constructs this was close to 1 with a low standard deviation (Figure 51F, G). This indicates for the FG

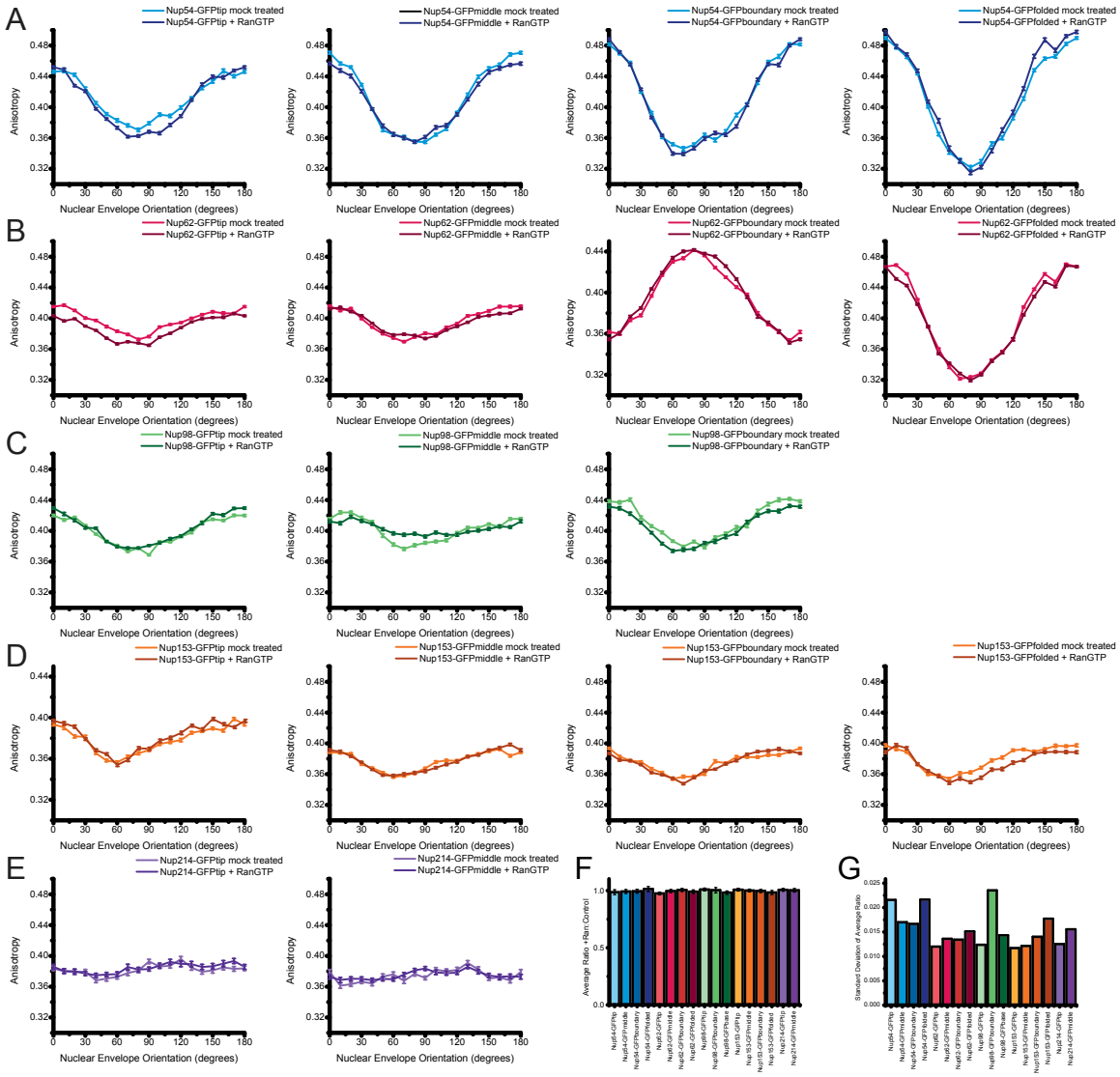

Figure 51: Anisotropy of FG Nups with Cargo Unbound. Comparison of anisotropy of FG nups in cells treated with RanGTP or mock treatred. All error bars are SEM.

A) Nup54 constructs. B) Nup62 constructs. C) Nup98 constructs. D) Nup153 constructs. E) Nup214 constructs. F) Ratio of RanGTP treated to untreated anisotropy values averaged over all membrane orientations for all constructs. G) Standard deviations of average treated: untreated ratio.

nucleoporins studied, the amount of cargo bound has little effect on their organization and behavior.

Behavior of Cargo within the NPC

To try and determine the dynamics of cargo interacting with the FG domains, the anisotropy of kapβ1-GFP as a function of NE orientation was determined. A construct of kapβ1 fused to GFP with no linker between the two proteins was imaged. A randomly tumbling or freely diffusing molecule would be expected to have anisotropy independent of NE orientation. In the cytoplasm, kapβ1-GFP has an anisotropy of 0.329 ± 0.01, which is only slightly higher than that of free GFP (r = 0.326±0.008), suggesting that it is freely rotating when not at the NE. The anisotropy at the NE showed an ordered curve with the opposite phase to the majority of the FG nups, with a maximum at 90° and a minimum at 0° (Figure 52A). These results show that kapβ1-GFP is ordered at the NE, suggesting that it remains bound to FG domains long enough to adopt ordering within the NPC.

TAP-GFP and Crm1-GFP showed different unbinding properties to kapβ1-GFP in permeabilized cells. To examine their behavior at the NPC using anisotropy, constructs of these two proteins fused to GFP with no linker were created. TAP-GFP showed an ordered pattern, which was of the opposite phase to that of kapβ1-GFP and had a lower amplitude (-0.043 ±0.003 for kapβ1-GFP; 0.013 ±0.002 for TAP-GFP) (Figure 52B). The Crm1-GFP anisotropy curve also had a low amplitude (-0.010 ±0.002) with a maximum at 90° and minima at 0° and 180° (Figure 52C). Thus, all three markers for cargo showed

Figure 52: Anisotropy of Cargo Molecules. A) Anisotropy as a function of NE orientation for kapβ1-GFP. B) Anisotropy as a function of NE orientation for TAP-GFP. C) Anisotropy as a function of NE orientation for Crm1-GFP. All error bars are SEM.

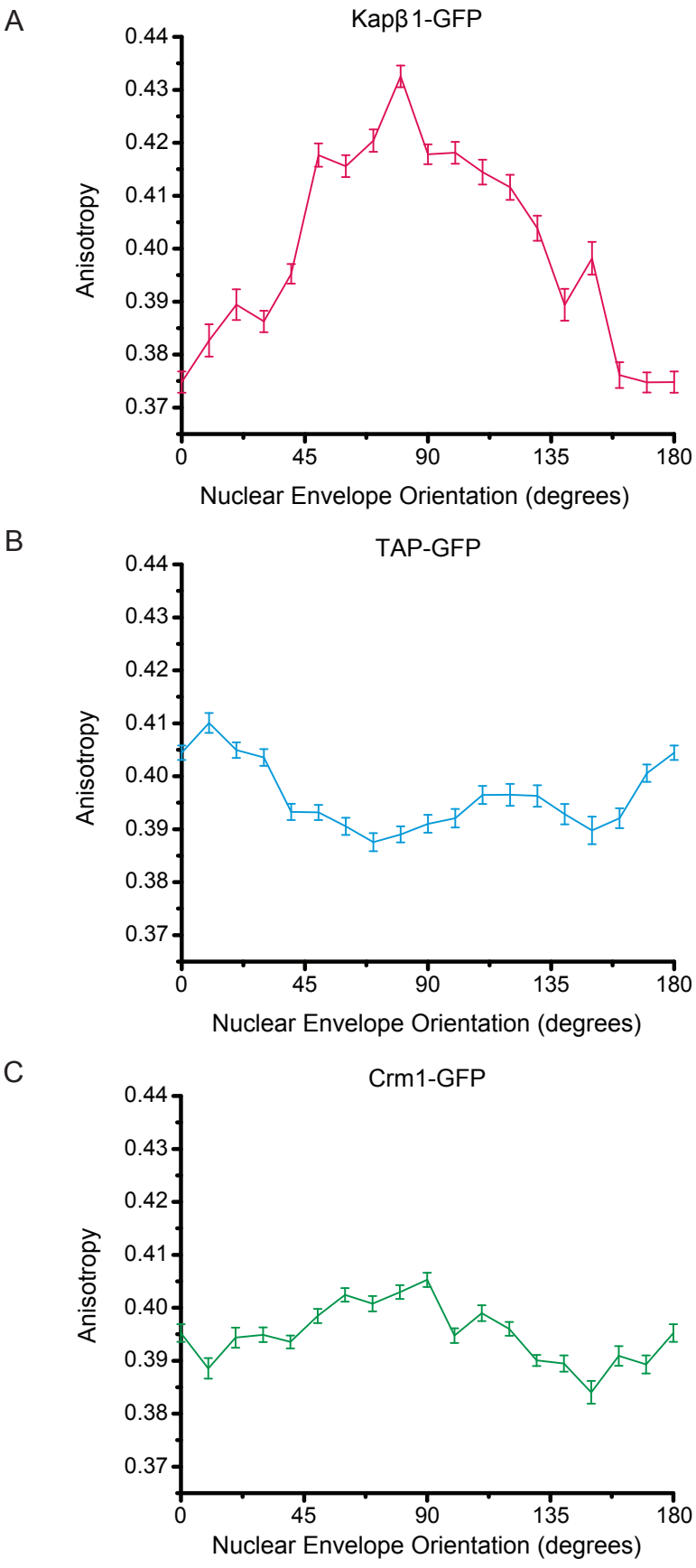
A
Kapβ1-GFP
Anisotropy
0.44
0.43
0.42
0.41
0.40
0.39
0.38
0.37
0
45
90
135
180
Nuclear Envelope Orientation (degrees)
B
TAP-GFP
Anisotropy
0.44
0.43
0.42
0.41
0.40
0.39
0.38
0.37
0
45
90
135
180
Nuclear Envelope Orientation (degrees)
C
Crm1-GFP
Anisotropy
0.44
0.43
0.42
0.41
0.40
0.39
0.38
0.37
0
45
90
135
180
Nuclear Envelope Orientation (degrees)

ordered behavior at the NPC, although kapβ1-GFP has more order than TAP-GFP or Crm1-GFP.

Discussion and Future Directions

This thesis describes two applications of polarization microscopy to study the NPC. In both of these cases, polarization microscopy allowed the investigation of problems which are not amenable to traditional structural biology methods. This technique also permitted the study of NPC proteins in their native context to determine novel structural and organizational aspects of the complex.

Determining the Orientation of Structural Proteins in the NPC

Anisotropy can be used as a method to determine orientation of nucleoporins within the NPC of live yeast and mammalian cells. The results indicate that both yeast Nic96 and human Nup133-Nup107 are oriented with their long axes approximately perpendicular to the nucleocytoplasmic axis of the NPC. These findings confirm a previous model for the arrangement of Nic96 (Schrader et al., 2008b) and support the "head-to-tail ring" model that was proposed for the yeast homologue of the Nup107 complex (Debler et al., 2008; Nagy et al., 2009).

This is the first time the orientation of these proteins has been measured experimentally *in vivo*. The technique provides a method for placing individual proteins in macromolecular complexes, and is a valuable tool for bridging the "resolution-gap" problem. This technique is applied in live cells, and therefore permits measurements of such large complexes to be made in a physiologically relevant system.

The biological results of these experiments rely on the interpretation of experimentally measured anisotropy patterns to determine the orientation of fluorophores within the NPC. There are several issues to be aware of in the interpretation of anisotropy patterns. A primary concern is the experimental error in the anisotropy, which could be affected by the factors outlined in Chapter 2. This issue was overcome by categorizing anisotropy curves into three pattern types on the basis of phase, rather than relying on absolute anisotropy values. The conclusions made based on anisotropy patterns were extremely conservative, yet they efficaciously restricted the space of possible nucleoporin orientations. The results from all of the nucleoporin-GFP constructs investigated were consistent with each other (i.e. no two anisotropy patterns gave mutually exclusive predictions of φ and ψ); this supports the validity of the experimental approach and shows that anisotropy phase patterns can be used to determine protein orientation in a macromolecular complex.

A second potential concern is that, as in all GFP-tagging experiments, the structure and localization of the protein may be disrupted by the GFP tag. In the yeast experiments the endogenous gene was tagged, and since Nic96 is an essential protein, viability of strains expressing the tagged protein was tested directly. If this technique were applied to non-essential nucleoporins, function could be assayed in a genetic background lacking a second gene that is synthetic lethal with the nucleoporin of interest.

As well as viability, two other criteria were used in both yeast and mammalian cells to select nucleoporin-GFP constructs for further analysis: the molecular model of the nucleoporin-GFP construct had to be free of steric clashes, and the construct needed to show a robust nuclear envelope localization *in vivo*. The three criteria were correlated

for most Nic96-GFP constructs- those that had a steric clash tended to fail to complement a deletion of wild type Nic96 and did not show fluorescence at the NE. The constructs which were analyzed met all three criteria. This makes it unlikely that the tagged proteins were localizing incorrectly or were structurally perturbed, and suggests that the analyzed constructs were behaving as wild type.

The third potential caveat is that the *in vivo* conformation of a nucleoporin-GFP fusion construct may differ from the conformation predicted by the molecular model. This possibility is difficult to exclude experimentally, since even a crystal structure of the nucleoporin-GFP construct may not reflect the geometry adopted in the context of the NPC. As an internal control, different constructs with the same linker helix length were created. These had the same predicted geometry. Constructs with identical linker helix lengths produced indistinguishable anisotropy patterns; a small divergence was only observed in the case of Nic96-GFP (-5/-5) and (-6/-4). These results support the conclusion that the molecular model was generally an adequate description of the nucleoporin-GFP geometry. Additionally, the conclusions from all the individual constructs were consistent with each other, and this would not be the case if the geometry of some constructs grossly deviated from the model. As described above, models that did not show steric clashes both localized properly at the nucleus and could complement loss of the endogenous gene whereas this was not true of those constructs that were predicted to contain a steric clash, suggesting that the predictions were valid.

The fourth potential caveat is that the analysis of the anisotropy patterns assumes a single orientation for the nucleoporin, but it is also possible that a nucleoporin present in 32 or more copies per NPC may have more than one orientation (nucleoporins present

in eight or sixteen copies per NPC must have the same orientation with respect to the nucleocytoplasmic axis, as dictated by the eightfold and dyad symmetry axes of the NPC). If the protein exists in more than one conformation, there would be multiple orientations for the dipole even if it is not mobile. These scenarios would result in an anisotropy curve which would reflect the vector sum of all orientations as the measured anisotropy would be an average of these. This would reduce the amplitude, and possibly change the shape of the curve. However, in these experiments high amplitude curves were measured, and these curves were extremely reproducible. The robust results and the narrow definition of the possible orientations of Nic96 and Nup133 obtained here indicate that if these nucleoporins occur in more than sixteen copies per NPC, the orientations of the different copies with respect to the nucleocytoplasmic axis should be similar or identical.

A final concern is whether there is some limited mobility of the protein resulting in a range of α values distributed around a common value. This would serve to depress the amplitude of the curve, but would not change the interpretation of results as long as all the constructs in a series have a similar mobility, as the relative amplitudes would remain the same. However, if one construct in a series were more mobile than the others, it would lead to a misinterpretation of the meaning of the relative curve amplitudes. Since introducing the comparison of curve amplitudes only served to further restrict the possible orientations of the protein, and did not result in any mutually exclusive predictions, it is unlikely that this is the case.

Altogether, the robustness of these data suggests that a single nup orientation is being measured. Additionally, the models derived from this analysis are consistent with

NPC dimensions. In particular, the conclusion that the long axis of the Nup107 (Nup84) complex is close to perpendicular to the nucleocytoplasmic axis is compatible with the size of the central NPC, whereas an arrangement of the subcomplex with its long axis (~45 nm long) parallel to the nucleocytoplasmic axis would exceed the height of one half of the central NPC (~15–20 nm). Furthermore, a recent paper analyzing the configuration of the Nup84 complex using a combination of negative stain EM, protein domain mapping, and phenotypic data a also supports the head-to-tail arrangement for the Nup84 complex within the NPC (Fernandez-Martinez et al., 2012).

Future Applications of Orientation Technique

The method described here can be applied to all nucleoporins that feature an α-helical C terminal domain. According to secondary structure predictions, ~60% of nucleoporins meet this requirement. While it should be possible to collect anisotropy data from all of these nucleoporins, a crystal structure of the C terminal domain is required to create models and derive orientational information from the anisotropy patterns. This is why the data from Nup84 in yeast could not be interpreted. If a crystal structure is available for a complex of two or more nucleoporins, anisotropy measurements for one member of the complex can be used to make conclusions about the orientation of the entire complex, as demonstrated here for the Nup107–Nup133 dimer. If the elucidation of nucleoporin crystal structures progresses at the current pace, this method should help to map the orientation of most NPC components over the next few years. This experimental determination of nucleoporin orientations will complement crystallographic and EM data

in the construction of a high-resolution map of the entire complex, which will be the basis of a detailed mechanistic understanding of the NPC.

Since the orientation technique is applied to live cells, unlike techniques such as EM, it can be used to monitor changes in nucleoporin orientation that correlate with NPC transport. Structural studies suggest that the architectural components of the NPC are dynamic, and that the scaffold may be able to change in shape. It has been proposed that changes in diameter may allow the NPC to transport cargo of different sizes while maintaining selectivity. However, the biological significance of this flexibility is unclear, since it has not been demonstrated in intact cells. Using small-molecule inhibitors of nucleocytoplasmic transport or temperature-sensitive transport mutants, NPCs can be arrested in an inactive state, and nucleoporin orientations in the inactive state can be compared to the active state to reveal conformational changes to the scaffold that occur specifically during active transport. This could be complemented by measurements of changes in the distance between structural nups using FRET. There may also be structural changes during the formation of NPCs. Time-resolved studies of NPC assembly can yield insights into nucleoporin rearrangements during this assembly process.

Finally, this method can be adapted to study systems other than the NPC, as demonstrated for the vacuolar ATPase Tfp1. However, there are certain requirements for the application of this technique. The target protein being studied must be oriented with respect to a larger cellular structure, such as the plasma membrane or ordered cytoskeletal structures. It is also required that there is a known crystal structure containing a C terminal α-helix for at least one component of the system, and the local concentration of the macromolecular complex needs to be high enough to collect data with a sufficient

signal-to-noise ratio. Note that while the NPC is a highly symmetrical structure, this is not a requirement for the application of the technique.

One example for a different suitable system is co-translational protein translocation into the endoplasmic reticulum (ER). The rough ER is continuous with the outer nuclear envelope, which is densely covered with ribosomes engaged in co-translational translocation: in yeast, the ribosome-to-NPC ratio is ~25. Since the cytoplasmic-luminal axis of the protein-conducting channel/ribosome system is always perpendicular to the surface of the ER segment it is attached to, the average steady-state orientation of different GFP-tagged components of the system can be determined exactly as for the NPC. Using inhibitors or temperature-sensitive mutants, it should be possible to dissect rearrangements at different stages of co-translational translocation in live cells.

Distinguishing Between Ordered and Disordered Domains

As well as determining the orientation of structural components of the nuclear pore complex, fluorescence anisotropy microscopy is a valuable tool for studying the *in vivo* organization of nups, and in particular the FG domains, which are inaccessible to traditional structural methods due to their intrinsic disorder. In contrast to intensity measurements, which reveal localization but not organization, fluorescence anisotropy allows exploration of sub-resolution order and disorder of the different domains of FG nups.

Similar caveats to those raised for the orientational data are also applicable here. The technique still introduces a GFP molecule attached to a nucleoporin, and it is

possible that this could be altering its structure or behavior. One observation suggesting that the GFP is not affecting the structure or behavior is the observation that haploid yeast in which all the copies of the FG nup of interest were tagged were viable, although the redundancy of many FG domains makes it difficult to test if the endogenous copy is being fully complemented for by the tagged protein. However, essential proteins such as Nsp1 and proteins which result in temperature sensitivity when lost like Nup98 could be tagged with no detriment to the cell. A further assay which could be applied is to measure transport rate and cargo unbinding, and test if it is the rates are the same whether the nup is labeled with GFP or not.

One way in which to test whether GFP is perturbing the behavior of the FG domains is to compare the results obtained with GFP to those collected with a different fluorescent marker. Many fluorescent probes are inapplicable for these experiments since their linkage to the protein allows them to rotate rapidly and they therefore do not maintain polarization. A possibility that was explored in limited tests was the small molecule FlAsH, which is linked to the protein of interest via four cysteine bonds, so that it cannot rotate (Adams et al., 2002). In yeast, the nucleoporins Nup49 and Nup1 were tagged at their C termini with the FlAsH binding motif. In the Nup1 strains, the FlAsH label accumulated at the cell membrane and the anisotropy at the NE could not be determined. However, the Nup49 strains gave results compatible with those obtained from GFP, suggesting that the GFP anisotropy is reflecting the behavior of the native protein. In mammalian cells, a Nup98 construct was generated with the FlAsH binding motif at the tip of the FG domain. Unfortunately, in mammalian cells the FlAsH ligand accumulated in the mitochondria, making the cells unsuitable for imaging. This effect has

been described in the literature (Langhorst et al., 2006). FlAsH may therefore be a useful tool for studying anisotropy in only a subset of the yeast nups.

One consideration when interpreting the order measured for FG nups in the NPC is the difference between the bulk behavior of the proteins, and the behavior of a single FG nup during a transport. In these experiments the anisotropy patterns observed represent an average of many GFP molecules in separate NPCs and an average in time over many transport events. Changes in orientation or dynamics of a single protein during a single transport event will not be detected. Due to the low number of GFP molecules within each NPC, data from a single cell is noisy, and averaging over many cells is therefore important to get reliable patterns for a particular construct.

For disordered nucleoporins, the pattern alone is not enough to distinguish between static and dynamic disorder. The experimental uncertainty caused by factors such as background subtraction (described in Chapter 2) also means that the absolute values of the anisotropy cannot be used to accurately determine mobility. Fluorophores could be held immobile in a disordered orientation, or they could have different orientations because they are mobile.

For weakly ordered nucleoporins, because the data are averaged in space and time, the possibility remains that individual FG domains are mobile. A likely explanation for low amplitude patterns is that they result from GFP molecules in a range of orientations; if one orientation is favored a pattern will appear in the average. Therefore, even though there is an ordered pattern present, the FG nups may be dynamic with a particular orientation or conformation preferred. This is supported by the observed

differences in FG nup behaviors between single cells. However, since the origin of these differences could not be determined, further study of this phenomenon is warranted.

When interpreting differences between anisotropy patterns, it is important to note that the phase and amplitude of the anisotropy curve are determined by two factors: the mobility of the protein, and the orientation of the protein. In these data there is a disordered or a low amplitude anisotropy pattern for GFP placed at the tip or middle of the FG domains. An ordered anisotropy pattern could arise if every GFP molecule within the NPC is held statically in a particular orientation; this would be of a low amplitude for certain specific orientations. However, the observation that GFP tags on the folded domains of FG nups have anisotropy curves with higher amplitudes than GFP tags at the tips of FG domains suggests that the observed differences are largely due to mobility. The relative amplitudes of the patterns for GFP at these positions correlates with expected differences in mobility for a GFP attached to a folded domain versus a flexible, unfolded region. The probability that the specific orientations required to give these patterns for a fixed GFP would be occurring for all FG nups is extremely low, and therefore it is unlikely that the loss of order from tip to folded domains is as a result of orientational changes.

Thus, when we measure a loss of amplitude due to an experimental treatment such as WGA or mutation of the FG domains, it is more likely that it is due to an increase in disorder than in a precise change in orientation. The observation that different proteins, such as Nup62 and Nup54, have a similar decrease in amplitude on WGA treatment, further supports this idea.

Ordering of the FG Domains within the NPC

Within the NPC, FG nups are surrounded by a high density of other proteins in a limited cylindrical geometry. Fluorescence anisotropy reveals for the first time that different types of FG domains behave heterologously *in vivo*, and in some cases adopt orientational order, suggesting that these geometrical constraints affect their behavior and organization. This order was not predicted from *in vitro* experiments, and thus highlights the utility of *in vivo* techniques.

The FG domains of different FG nups may play redundant roles, and many FG nucleoporins are dispensable for transport. Therefore the organization of an individual FG domain may not be as crucial as the overall organization of the lumen of the pore. However, these data show that different FG domains are not behaving the same; they show varying degrees of order in the steady state and do not respond identically to perturbations of the proteins, such as WGA binding or mutation of the FG repeats. Additionally, the relative amount of order displayed by the FG nucleoporins is conserved between yeast and mammalian cells when comparing homologues of the same protein. This suggests that the behavior of individual nucleoporins within the context of the pore may have relevance for function.

The order of the FG domains is surprising because *in vitro* studies using circular dichroism and gel filtration show these domains to be in an unfolded conformation (Denning et al., 2003). The linker regions between the FG repeats are poorly conserved, suggesting that their sequence is not important for formation of secondary structural elements (Denning and Rexach, 2007). However, the order we see does not mean that a

specific tertiary structure is present. These experiments show that different portions of the FG domain are behaving independently of one another, which is consistent with the idea that these proteins are unfolded: WGA perturbs the base of the Nup54 and Nup62 FG domains without affecting the middle or tip, and mutation of the FG repeats of Nup54 affects the middle and base of the domain but not the tip; exogenously expressed FG domains are disordered at the plasma membrane. It might be expected that unstructured domains would be random within the pore but these data show that unstructured domains can be organized within the NPC in an oriented manner. This order is not specifically predicted by any of the current models of nucleocytoplasmic transport.

A factor to take into account when considering the organization of the FG domains within the NPC is how they fit into the pore lumen. Packing a high density of unfolded protein domains within the physical space of the NPC may cause them to align in a preferred orientation. The anisotropy patterns for the tips and middles of the ordered FG domains all indicate that the GFP dipole is oriented more parallel than perpendicular to the nucleocytoplasmic axis i.e. all the GFPs are broadly oriented in the same direction. We do not know the orientation of GFP relative to the FG domain; however if all the GFP molecules are oriented in the same way to the filaments, this result suggests that the FG domains are all oriented in the same direction. One possibility is that that the FG domains may be in an extended conformation and aligned along the nucleocytoplasmic axis. Such an arrangement for Nup54 and Nup62 was recently proposed (Solmaz et al., 2011). This is also supported by immuno-EM data that shows the FG domains can extend through the lumen of the pore, appearing on both sides of the NE (Paulillo et al., 2005; Chatel et al., 2012).

Context has an impact on FG domain order, since their behavior was altered by changing the placement of the FG domain within the pore. The peripheral FG domains were less ordered than those in the centre of the NPC; this may be because at the periphery their orientation is less constrained by their surroundings. The change in order seen on swapping the FG domains into different locations suggests that the organization of these domains is not intrinsic but depends on the specific local milieu which they experience within the NPC. This local context may consist of interactions with the surrounding nucleoporins, the spatial location within the pore, or interactions with the coiled coil domain to which the FG domain is attached.

Interactions of the FG domain with the surroundings could occur through linker regions, through FG-FG interactions, or through cargo cross-linking of FG repeats. Cargo did not have a dominant effect on the organization of the nups, so for Nup54 where there is a decrease in the amplitude of anisotropy pattern upon loss of the FG repeats, the change is likely to be due to loss of FG-FG interactions rather than loss of cross-linking via cargo. Not all of these proteins are organized by their FG repeats in the same manner, indicating that more than one type of interaction may be important in organization. Consistent with the idea that factors other than FG-FG interactions may be involved, it has been suggested that the characteristics of the linker regions of the FG domains are important for their shape and hydrodynamic properties (Yamada et al., 2010).

For Nup54, the FG repeats had a limited role in the ordering of the protein, as order was not fully eliminated when they were mutated to AG. It is interesting to speculate that the initial ordering of Nup54 may occur due to the overall organization of FG domains within the pore lumen, but that this ordering may be reinforced by FG-FG

interactions which cause the Nup54 domains to align. It is possible that Nup54 is interacting heterologously via FG-FG interactions with other types of FG domain, or it could be interacting only with other Nup54 domains. If it were interacting with other FG domains, it might be expected that these interactions would cause them to have a similar response to the loss of FG domains as Nup54, which was not the case for Nup62.

In Nup98 the FG repeats play a role in localizing the protein to the NPC, and the loss of order that occurs when 25% or 50% of the FG repeats are mutated to AG may represent loss of local organization of the FG domain or occur as a result of mislocalization of the entire protein. The FG repeats could be directly interacting with other FG repeats or cargo molecules to traffic Nup98 into the pore, or may be creating a conformation of Nup98 that is required for it to localize. The trafficking and localization of Nup54 and Nup62 was unaffected by mutation of the FG repeats, suggesting that they may be localized to the NPC by a different mechanism to Nup98.

Interpretation of Models for Nucleocytoplasmic Transport

Together, these observations are compatible with some features of the proposed models, but not others. The order seen for some FG domains shows that there is an overall organization of the FG nups. Since these are average measurements, it is still compatible with the idea that a single FG domain could be mobile. However, it suggests that there is some limit to the space the FG domains are exploring, in contrast to a model in which FG domains are completely free to move randomly according to entropy (Figure 6B) (Rout et al., 2003).

The FG repeats are not involved in the order of Nup62, and have a limited role in ordering Nup54. This result does not rule out FG-FG interactions between FG nups, but suggests that it is not the primary force in organizing the FG nups, in contrast to the hydrophobic gel model, which states that there is a saturated network of FG repeats (Figure 6A) (Frey and Görlich, 2007).

Many models for transport treat the FG domains as interchangeable protein domains within a homogenous network. The observation that different FG nups show different behaviors is incompatible with this. This does support some aspects of the "forest" model, which proposes that there are heterogeneous behaviors for the FG nups (Figure 6D). In the study on which this model is based, determination of the Stokes radii of purified FG domains showed that some domains are molten, collapsed coils, while others form relaxed or extended coils. This study also suggests that the FG domains interact with each other differently depending on the content of their non-FG amino acids; this is in keeping with our observation that FG repeats are not the primary determinant of FG domain order.

Interestingly, Nup57, which has the most ordered tip of the yeast nups, is predicted to adopt a collapsed coil proximal to the pore wall, whereas Nup159, for which we measure less order at the tip, is predicted to adopt an extended conformation (Yamada et al., 2010). However, this relationship does not appear to hold up in all cases, since in solution Nup1 is predicted to have a cohesive, collapsed coil at the N terminus, but does not show an ordered pattern *in vivo*. This shows the importance of *in vivo* context for FG domain behavior.

Cargo binding and unbinding to the FG nups is specifically invoked in several models of the nucleocytoplasmic transport. Decreasing the cargo load does not affect the behavior of the FG nups. A caveat to this assay is that not all cargo may unbind from the NPC, and if any remaining cargo were affecting FG nup behavior in an all-or-none fashion a difference would not be detected. It is difficult to imagine what the mechanism for such an effect would be. However, it is clear that cargo load is not affecting the behavior of the FG nups in a linear manner. The observation that WGA binding can alter the anisotropy of Nup54-GFPboundary and Nup62-GFPboundary shows that changes in behavior caused by protein binding events can be detected. This suggests that when no such changes are observed on cargo unbinding it reflects a biologically relevant behavior for the FG domains.

The data are not compatible with models where cargo would alter the gross behavior of the FG nups. A model has been proposed in which cargo causes collapse of the FG domains, which should be detectable as a change in orientation visible in the anisotropy (Figure 6C) (Lim et al., 2006). This was never observed. However, it is possible that depending on how many FG domains are binding cargo and collapsing at one time, such changes would not be detectable in the average. For collapse to go undetected, a minority of FG domains would have to be undergoing conformation change at any one time; these data are certainly incompatible with all FG domains in the NPC undergoing conformational change simultaneously.

The collapse model also proposes that the FG domains form a polymer brush. This seems unlikely to be occurring in vivo, since it does not explain why FG domains would behave differently to one another, and why behavior would change depending on

location within the NPC. However, “reeling in” of cargo based on multiple FG repeats from a single domain binding one karyopherin was raised as a possibility based on modeling of the FG domains, and may account for the stability of kapβ1 binding in the absence of RanGTP (Mincer and Simon, 2011). This mechanism could be viewed as a modification of the collapse model, but requires less dramatic conformational change, and would therefore be more compatible with the anisotropy data.

Import cargo remains at the NE for tens of minutes following permeabilization, putting limits on the rate of cargo unbinding from FG domains in the absence of Ran. It is possible that there is another soluble protein factor which stimulates dissociation of the karyopherinβ1-cargo complex from the FG repeats that is also being washed out, but no such factor has been isolated. For import cargo to remain bound at the NPC following permeabilization, it must either remain stably bound to the FG domains or the on rate of binding must be such that unbound cargo rebinds a FG repeat before it has had a chance to exit the pore lumen. The anisotropy of the cargo itself suggests that cargo is remaining bound to FG domains long enough to adopt order.

These data therefore support the idea that import cargo must interact with Ran to unbind from an FG repeat. It is unclear how this would be compatible with models which suggest that rapid binding and unbinding of cargo from FG repeats is required for transport across the pore. In order for import cargo to be rapidly unbinding, RanGTP would have to be distributed throughout the lumen of the NPC, and it is not apparent how directional transport could operate if this were the case. The penetration of RanGTP into the pore remains unknown *in vivo* making it difficult to tell to what extent RanGTP is able to unbind cargo inside the NPC lumen. A study which investigated the behavior of

Ran at the NPC based on its diffusion estimated that there is on the order of 200 molecules of Ran present at the NPC, of which between 1 and 50 are within the pore lumen, suggesting that the majority of Ran associated with the NPC is concentrated at the nuclear and/or cytoplasmic faces (Abu-Arish et al., 2009). Single molecule studies have suggested that Ran does not change cargo behavior within the pore itself, but acts exclusively to unbind cargo at the nuclear face (Lowe et al., 2010). Additionally, if RanGTP were unbinding cargo within the pore lumen, it would presumably also be dissociating the karyopherin from the cargo, and the complex would have to reform before transport could resume.

In contrast, the exit cargo rapidly leaves the NPC following permeabilization. This may be because GTP hydrolysis is still occurring in the permeabilized cells, allowing the cargo to unbind. An alternative explanation is the GTP hydrolysis is not required for the export cargo to unbind from the FG repeats, but only to dissociate the karyopherin-cargo complex, preventing re-entry into the NPC. It is also possible that different karyopherins could transit the pore differently, depending on which nucleoporins they interact with and their specific on and off rates. As well as heterogeneity in the behavior of the FG domains, there may be heterogeneity in the way karyopherins are transported.

Together, these data are compatible with some aspects of the forest, entropic exclusion, and Brownian ratchet models, but are incompatible with the hydrophobic gel model.

Nematic Ordering of the FG Domains

A possible scheme for how order could arise from unstructured domains within the NPC is summarized in Figure 53. In this scheme, the behavior of each type of FG domain is uniquely determined both by its biophysical properties and its interaction with its surroundings. There is a decrease in order from base to tip for the central domain nups, as the base is more constrained than the tip of the FG domain by the wall of the NPC. The geometric constraints of the narrow lumen of the pore require the majority of central FG domains to align, orienting them with respect to the NPC. For some proteins, such as Nup54, this overall organization is reinforced by interactions with their neighbors via the FG repeats. Therefore, while an individual domain may be mobile and changing conformation, overall on average the FG domains of the central nups are ordered. This order is nematic, characterized by orientational order along the nucleocytoplasmic axis without implications for positional order (Coppin and Leavis, 1992; Oskolkov et al., 2011). In contrast, at the periphery of the NPC, the FG domains are less constrained in the geometry of the space they can explore, so are disordered.

If the dense packing in a cylindrical geometry of the FG domains is the cause of the order observed, it suggests a mechanism for cargo selectivity. In this model, the pore lumen would be filled with FG proteins, sterically preventing the entry of non specific cargo. However, cargo which can bind the FG repeats is able to enter the pore space, and move through the NPC. If the individual FG domains are flexible and mobile within the context of the overall order, import cargo could be binding to a FG domain on one side of

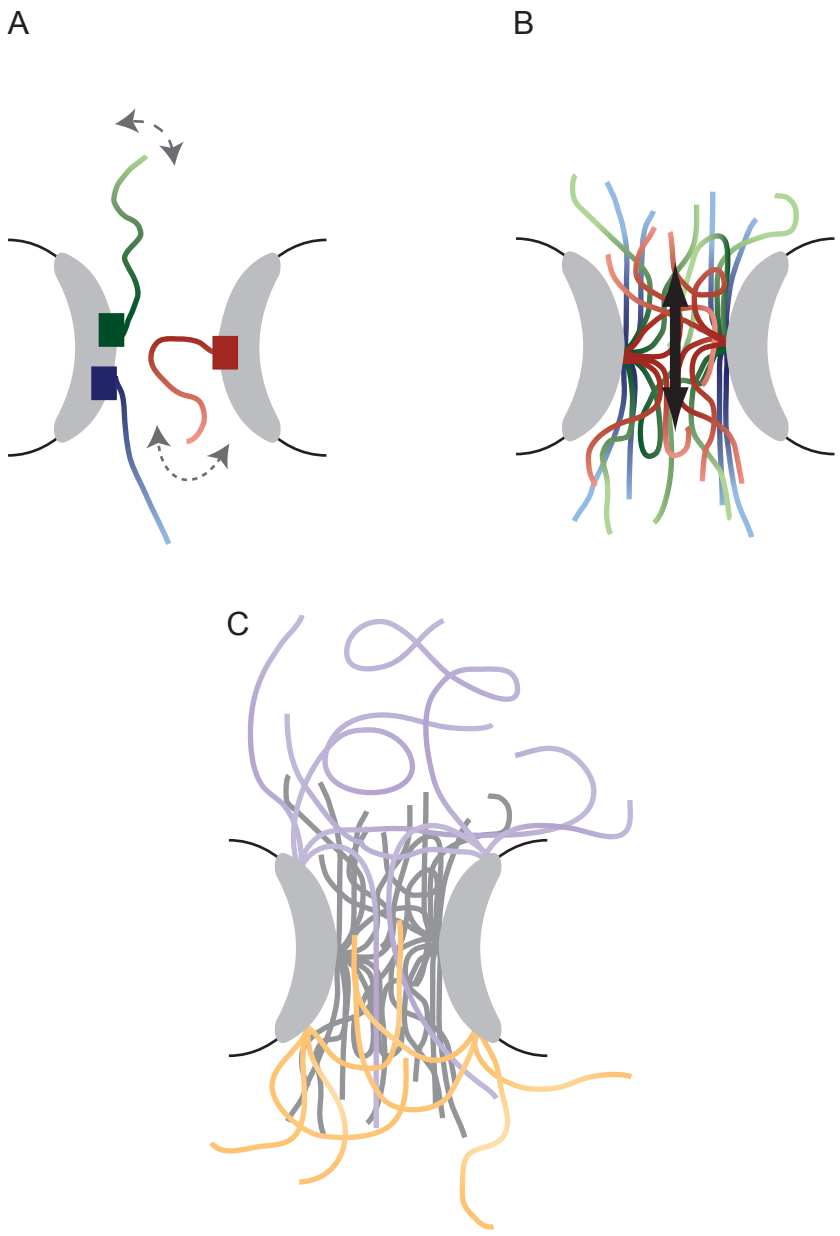

Figure 53: Nematic Ordering of FG Domains. A) Each type of FG domain behaves differently depending on its local environment and interactions. B) The limited cylindrical geometry of the NPC lumen causes overall alignment of the central FG domains, although individual FG domains are flexible. C) The peripheral domains have a greater space to explore and are therefore more disordered.

the pore, which would eventually move through the lumen of the NPC until the cargo encounters RanGTP and is released in the nucleus.

These experiments explore the properties of FG nups *in vivo*, using a method which allows characterization of their structure in intact live cells. This shows order in the FG domains which is conserved from yeast to humans, and had not been predicted by any of the previous models. FG-FG interactions are not dominant in imparting this order to the FG nups, and cargo has no effect. The orientational order of the FG domains is therefore best understood in the constraints of the local geometry of the central channel of the NPC in which they are situated.

Future Studies of the FG Domains in Live Cells

Further study of the organization of the organization and dynamics of the FG nups in live cells is needed to determine the mechanism of transport. We propose a model whereby the packing of FG domains into the cylindrical geometry of the NPC causes them to become ordered. This model requires further testing to be validated. One way to do so would be to alter the density of FG domains in the lumen of the pore. Strains of yeast with up to 50% of the mass of FG domains deleted have been created. Comparison of the behavior of the remaining nups with the wild type strains would be one way to test this model.

It would also be interesting to determine exactly which interactions an FG nup makes with other proteins within the NPC, and how these affect its ordering. While the position of a nucleoporin within the NPC affects its behavior, it is not clear whether this

is through specific interactions with the surrounding proteins, or because of the overall environment the protein is experiencing. If these proteins are making specific interactions, these results suggest that these interactions are not mediated by the FG repeats. Determination of the molecular mechanism of how these proteins interact with their surroundings is necessary. Mutational analysis of FG nups showed that the linker regions of the domains play a role in FG behavior *in vitro* (Yamada et al., 2010); similar mutations could be introduced to cells and tested *in vivo*.

A limitation of the existing data is that it represents an average, both over many NPCs and in time. However, the differences in anisotropy patterns between single cells may suggest that not all copies of a single FG protein are behaving the same way at any one time. It would be informative to study the orientation and dynamics of single FG proteins during transport. This would involve selectively labeling proteins at a low density. One avenue to do so would be through the use of photoactivatable XFPs. However, detection of signal above noise would be a problem.

There is a question as to whether all NPCs are behaving alike; differences in individual NPCs could be causing the differences in anisotropy that were seen in single cells. It has been proposed that different NPCs are involved in import and export processes. One way in which we attempted to study the behavior of single NPCs is by using through the objective total internal reflection fluorescence microscopy (TIR-FM). In TIRFM, an evanescent wave is used to selectively illuminate fluorophores in a restricted region (penetration depth ~100nm) at the water-glass interface. This provides a high signal: noise for fluorophores within this region, as there is no background from the rest of the sample. In yeast, the cell wall has been estimated to be ~115nm thick (Dupres

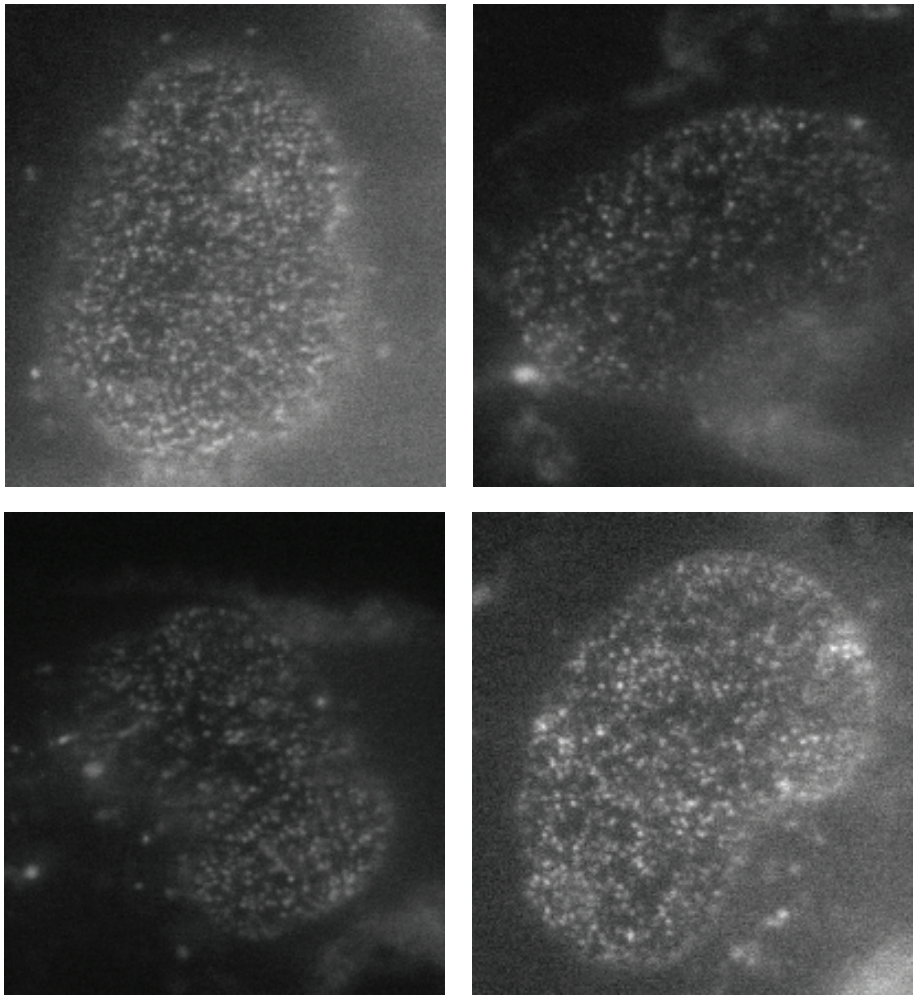

Figure 54: Images of Mammalian Nuclei Using TIR-FM. Representative images of mammalian nuclei expressing GFP tagged FG nups. Clockwise from to left: Nup54-GFPtip, Nup54-GFPmiddle, Nup54-GFPfolded, Nup54-GFPboundary.

et al., 2010), which means the nucleus is not visible in the TIR field. In mammalian cells, if the nucleus sits low enough in the cell its bottom surface can be visualized with TIR-FM. This surface is covered with diffraction limited puncta which presumably correspond to single NPCs (Figure 54). Unfortunately, scattering of the light by the cytoplasm of cells meant that accurate anisotropy measurements could not be determined. Using prism-based TIR-FM in the s-pol orientation may help to ameliorate this problem. Additionally, when observing polarization in TIR-FM, effects of proximity to the interface on the transmission of emitted light must be considered (Hellen and Axelrod, 1987). However, this system would still be amenable to other live cell imaging modalities. For example, two-color imaging could be used to simultaneously examine cargo and FG nups, or import and export cargoes, to determine if different cargo types are interacting with all the NPCs in the same way.

These data show that kapβ1-GFP and Crm1-GFP unbind at different rates from the NPC in permeabilized cells. These molecules were chosen to be markers of Ran dependent import and export, respectively. Because only one cargo was used to assay each process, it is not clear whether their different behaviors are specific to all import and/or export processes, or if they are specific only to the molecules chosen. This could be investigated by expanding these studies to other import and export karyopherins. This would also allow the anisotropy of these molecules at the NE to be determined, to see if all cargo becomes ordered at the NPC. Overall, fluorescence polarization microscopy of the NPC provides a powerful tool for studying many aspects of nucleocytoplasmic transport in live cells.

Materials and Methods

Yeast Strains

A Saccharomyces cerevisiae parent strain, named MKY363, was constructed as follows: W303a and W303α cells (American tissue culture collection) were transformed with the BglII fragment of pRS422 containing the ADE2 gene and adenine-prototroph transformants were selected. Transformants from the a and α mating types were crossed to obtain the diploid MKY363. Nucleoporins were genomically tagged with EGFP in MKY363 using standard methods (Reid et al., 2002). DNA cassettes for the different constructs were obtained by PCR and the template plasmids pKT127 and pKT128 (Sheff and Thorn, 2004). The identity of the different Nic96-GFP strains was confirmed by cloning and sequencing of the genomic DNA junction region between Nic96 and GFP. Sporulation and tetrad dissection of diploid cells followed standard procedures.

EGFP was introduced in four different regions with respect to the FG domains: at the terminus of the folded domain: nup-GFPfolded; at the junction between the folded and the FG domain: nup-GFPboundary; in the middle of the FG domain: nup-GFPmiddle; at the end of the FG domain: nup-GFPtip.

For the azide experiments, cells were transiently transfected with the plasmid pMK511, which contains mCherry-NLS. This plasmid was constructed by replacing GFP with mCherry in plasmid CP429 (a gift from Susan Wente, Vanderbilt University). For the citrine expressing strains in the homo-FRET experiment the plasmids pMK137 and pMK352 were used.

Details of strains and plasmids are outlined in Tables 1 and 2.

Table 1: Yeast strains used in this study. All strains were constructed by Martin Kampmann.

Strain Number	Description	Name	Mating Type
MKY363	ADE2 ADE3		a/α
MK1182	180xpMK128	Citrine monomer	α
MK1187	180::pMK352	Citrine dimer	α
MKY1210	Nsp1-GFP (KanR)	Nsp1-GFPfolded	a/α
MKY1221	Nup1-GFP (His)	Nup1-GFPtip	a/α
MKY1212	Nup57-GFP (KanR)	Nup57-GFPfolded	a/α
MKY1301	Nup84_0_GFP_5		a/α
MKY1302	Nup84_-1_GFP_5		a/α
MKY1303	Nup84_-2_GFP_5		a/α
MKY1304	Nup84_-3_GFP_5		a/α
MKY1305	Nup84_0_GFP_6		a/α
MKY1306	Nup84_-1_GFP_6		a/α
MKY1307	Nup84_-2_GFP_6		a/α
MKY1308	Nup84_-3_GFP_6		a/α
MKY1331	Nic96-GFP (-5/-4)		a/α
MKY1332	Nic96-GFP (-6/-4)		a/α
MKY1333	Nic96-GFP (-7/-4)		a/α
MKY1334	Nic96-GFP (-8/-4)		a/α
MKY1335	Nic96-GFP (-5/-5)		a/α
MKY1336	Nic96-GFP (-6/-5)		a/α
MKY1337	Nic96-GFP (-7/-5)		a/α
MKY1338	Nic96-GFP (-8/-5)		a/α
MKY1339	Nic96-GFP (-20/-4)		a/α
MKY1340	Nic96-GFP (-21/-4)		a/α
MKY1341	Nic96-GFP (-22/-4)		a/α
MKY1342	Nic96-GFP (-23/-4)		a/α
MKY1343	Nic96-GFP (-20/-5)		a/α
MKY1344	Nic96-GFP (-21/-5)		a/α
MKY1345	Nic96-GFP (-22/-5)		a/α
MKY1346	Nic96-GFP (-23/-5)		a/α
MKY216	GFP-Nup57	Nup57-GFPtip	a/α

Table 1 (continued)

MKY219	GFP-Nup116	Nup116-GFPtip	a/α
MKY221	GFP-Nup159	Nup159-GFPtip	a/α
MKY224	Nup159: middle of FG	Nup159-GFPmiddle	a/α
MKY225	Nup159: FG-rigid boundary	Nup159-GFPboundary	a/α
MKY226	Nup116: middle of FG	Nup116-GFPmiddle	a/α
MKY227	Nup116: FG-rigid boundary	Nup116-GFPboundary	a/α
MKY241	GFP-Nup1	Nup1-GFPfolded	a/α
MKY455	GFP-Nup57	Nup57-GFPtip	a
MKY453	Nup57-GFP (KanR)	Nup57-GFPfolded	α

Table 2: Yeast plasmids used in this study.

Plasmid Number	Description	Parent	Source
pMK137	Citrine monomer	pMK128	Martin Kampmann
pMK352	Cit-Cit dimer	pMK128	Martin Kampmann
pMK511	mCherry-NLS	CP429	Martin Kampmann
pMK490	URA3-GFP-spc	pMK489	Martin Kampmann
pMK485	spcGFP(URA)	pKT174	Martin Kampmann

Construction of Mammalian Nucleoporin-GFP Plasmids

Sources of purchased and gifted plasmids used in this study are outlined in Table 3.

Table 3: Mammalian plasmids used in this study which were gifted from other people or purchased.

Plasmid Name	Description	Backbone	Source
mGFP-N1		Clontech GFP-N1	Marina Fix
mGFP-C1		Clontech GFP-C1	Marina Fix
mCherry-N1			Clontech
mCitrine-N1			Clontech
GFP-Nup98		Clontech GFP-C1	Elias Coutavas
Nup133		pBluescript	Open Biosystems
Nup54			Ivo Melčák
GFP-Nup62		Clontech GFP-C1	Florence Koeppel
Nup214		pBluescript II SK	KAZUSA DNA
Nup153		pCMV-Sport6	Open Biosystems
Ran-thrombin-His		pET28	Elias Coutavas
Karyopherin β1		pGEX	Sozanne Solmaz
Crm1		pBluescriptR	Open Biosystems
TAP		pCMV-Sport6	Open Biosystems
pMK536	Nup133-hx-GFP EYYVQGelf (-2/-5)		Martin Kampmann
pMK537	Nup133-hx-GFP EYYVQeelf (-3/-4)		Martin Kampmann
pMK538	Nup133-hx-GFP EYYVQelf (-3/-5)		Martin Kampmann
pMK559	Nup133-hx-GFP EYYVeelf (-4/-4)		Martin Kampmann

Construction of rigid helix fusions

Plasmid containing the full-length human Nup133 cDNA under the control of the CMV promoter was purchased (Open Biosystems, MHS1010-58232). In a first PCR, the EGFP coding sequence was amplified from plasmid pEGFP-C1 (Clontech) using primers GFP-f and GFP-NotI-r, introducing a NotI site downstream of the stop codon. In a second PCR, a fragment of the Nup133 coding sequence was amplified from plasmid MHS1010-58232 and the junction with the EGFP sequence was introduced using the forward primer Nup133-f and different reverse primers for the different Nup133-GFP constructs. In a third PCR, products from the first two PCRs were used as templates with primers Nup133-f and GFP-NotI-r to fuse the Nup133 fragment to the full-length GFP sequence. The product of this PCR and plasmid MHS1010-58232 were digested with PflFI and NotI, and the PCR product was ligated into the larger background fragment from the MHS1010-58232 digest to obtain Nup133-GFP expression plasmids. The sequence of the insert was verified by sequencing.

GFP tagged FG Nups

Plasmids containing Nup54, Nup62, Nup98, Nup214 and karyopherin-β1 were a gift from Dr Günter Blobel, The Rockefeller University, New York. The plasmid containing Nup153 was purchased from Open Biosystems. The plasmid EGFP-N1 was purchased from Clontech. The EGFP sequence was removed from this plasmid by digestion with AgeI and BsrGI followed by digestion with mung bean nuclease (NEB). PCR was used to amplify all nucleoporins and introduce them to this backbone. Standard

molecular biology techniques were used to tag the nucleoporins in the clontech backbone in four different regions relative to the FG domains: at the terminus of the folded domain: nup-GFPfolded; at the junction between the folded and the FG domain: nup-GFPboundary; in the middle of the FG domain: nup-GFPmiddle; at the end of the FG domain: nup-GFPtip. In these constructs, the GFP was fused directly to the protein of interest with no linker amino acids. Nup62-mCherry was created by PCR amplification of Nup62 and ligation into the mCherry-N1 backbone (Clontech). TAP-GFP was created by PCR amplification of TAP and ligation into the EGFP-C1 backbone. Karyopherin-β1 and Crm1 were amplified using PCR and introduced to EGFP-N1 using the In-Fusion PCR Cloning System (Clontech). The chimeric proteins were created using standard molecular biology techniques from the nucleoporin-GFP constructs. FG repeats were mutated to AG using the QuikChange Lightning Site-Directed Mutagenesis kit (Agilent). Details of plasmids and techniques are outlined in Table 4.

Table 4: Mammalian plasmids constructed for this study.

Plasmid Number	Description	Parent Plasmid	Construction Method
pCA007	Nup54-C1	GFP-N1, Nup54	AgeI, BsrGI
pCA009	Nup54-GFPtip	pCA7	SgrAI, BamHI
pCA010	Nup54-GFPboundary	pCA7	NotI, BamHI
pCA011	Nup54-GFPmiddle	pCA7	SpeI, BamHI
pCA012	Nup98-N1	GFP-Nup98	AgeI, BsrGI, Mung Bean Nuclease
pCA013	Clontech C1 vector with XFP removed	mCitrine-C1	AgeI, BsrGI, Mung Bean Nuclease
pCA014	Nup98-GFPtip	pCA12	NheI, SexAI
pCA015	Nup98-GFPmiddle	pCA12	NheI, SexAI
pCA016	Nup98-GFPboundary	pCA12	BamHI, SexAI
pCA017	Nup54-GFPfolded	pCA7	SpeI, NotI
pCA024	Nup54-GFPtip FG->AG	PCA9	QuikChange mutagenesis
pCA030	Nup62-C1	pCA13, GFP-Nup62	Xho, HindIII
pCA034	Nup62-GFPtip	pCA30	NheI, BstXI
pCA037	Nup62-GFPmiddle	pCA30	NheI, BstXI
pCA038	Nup214-C1	pCA13, Nup214	EcoRI InFusion reaction
pCA039	Nup62-GFPboundary	pCA30	HindIII, BstXI
pCA040	Nup62-GFPfolded	pCA30	HindIII, BstXI
pCA046	Nup214-GFPtip	pCA38	SalI, MfeI , QuikChange mutagenesis
pCA048	Nup98-GFPtip FG(1-9) -> AG	pCA14	QuikChange mutagenesis
pCA054	Nup214 folded/Nup98 FG-GFPtip	pCA14, pCA38	MfeI, XcmI
pCA070	Nup214-GFPmiddle	pCA38	BbvCI InFusion reaction , QuikChange mutagenesis
pCA072	Nup214 folded/Nup54 FG-GFPtip	pCA9, pCA38	MfeI, EcoRI
pCA078	Nup62-GFPtip FG ->AG	pCA34	MfeI, BstXI
pCA082	Nup98-GFPtip FG(1-20)->AG	pCA14	QuikChange

Table 4 (continued)

			mutagenesis
pCA083	Nup54middle FG ->AG	pCA11	QuikChange mutagenesis
pCA084	Nup54boundary FG ->AG	pCA10	QuikChange mutagenesis
pCA090	Nup214 folded/ Nup62 FG-GFPtip	pCA34, pCA46	MfeI, BstXI
pCA100	Nup62-GFPfolded FG ->AG	pCA40	NheI, BstXI
pCA101	Nup98-GFPtip FG(1-30) ->AG	pCA14	QuikChange mutagenesis
pCA102	Nup54-GFPfolded FG ->AG	pCA17	QuikChange mutagenesis
pCA104	Nup62-GFPboundary FG ->AG	pCA39	XhoI, BstXI
pCA106	Nup62-GFPmiddle FG ->AG	pCA37	XhoI, BstXI
pCA107	Nup153-C1	pCA13, Nup153	HindIII InFusion
pCA112	Nup153-GFPfolded	pCA107	NheI, AclI
pCA115	Nup153-GFPtip	pCA107	XmaI, XcmI
pCA116	Nup153-GFPmiddle	pCA107	XmaI, XcmI
pCA121	Nup98 FG ->AG	pCA14	QuikChange mutagenesis
pCA128	Nup153-GFPboundary	pCA107	PacI InFusion reaction, QuikChange mutagenesis
pCA150	Nup54 folded/Nup62 FG-GFP	pCA34, pCA09	AgeI , PacI , QuikChange mutagenesis
pCA156	Nup62 folded/Nup54 FG-GFP	pCA34, pCA09	MfeI , PacI , QuikChange mutagenesis
pCA169	Karyopherinβ1-mCherry	mCherry-N1, Kapβ1	AgeI InFusion reaction
pCA171	Nup98-GFPmiddle FG(1-9) ->AG	pCA48	AfeI, BsrGI, Mung Bean Nuclease, QuikChange mutagenesis, EcoRI InFusion reaction
pCA172	Nup98-GFPmiddle FG(1-20) -> AG	pCA82	AfeI, BsrGI, Mung Bean Nuclease,

Table 4 (continued)

			QuikChange mutagenesis, EcoRI InFusion reaction
pCA173	Nup98-GFPmiddle FG(1-30) -> AG	pCA101	AfeI, BsrGI, Mung Bean Nuclease, QuikChange mutagenesis, EcoRI InFusion reaction
pCA175	Nup98-GFP middle FG(1-39) -> AG	pCA121	AfeI, BsrGI, Mung Bean Nuclease, QuikChange mutagenesis, EcoRI InFusion reaction
pCA179	Nup98-GFPtip FG(21->39) AG	pCA14, PCA121	AclI, BsrGI, QuikChange mutagenesis
pCA184	Nup62 folded/Nup54 FG-GFPboundary	pCA39, pCA10	BsrGI, NheI
pCA187	Nup98-GFPboundary FG(1-9) -> AG	pCA48	AfeI, BsrGI, Mung Bean Nuclease, QuikChange mutagenesis, EcoRI InFusion reaction
pCA188	Nup98-GFP boundary FG(1-20) -> AG	pCA82	AfeI, BsrGI, Mung Bean Nuclease, QuikChange mutagenesis, EcoRI InFusion reaction
pCA189	Nup98-GFP boundary FG(1-30) -> AG	pCA101	AfeI, BsrGI, Mung Bean

Table 4 (continued)

			Nuclease, QuikChange mutagenesis, EcoRI InFusion reaction
pCA190	Nup98-GFPboundary FG(1-39) -> AG	pCA121	AfeI, BsrGI, Mung Bean Nuclease, QuikChange mutagenesis, EcoRI InFusion reaction
pCA191	Nup98 folded /Nup54-GFPtip	pCA14, pCA09	EcoRI, PacI, QuikChange mutagenesis
pCA192	Nup98 folded/Nup62 FG-GFPtip	pCA14, pCA34	BsrGI, PacI, QuikChange mutagenesis
pCA194	Nup54 folded/Nup62 FG-GFPboundary	pCA10, pCA39	BmtI, BcgI
pCA195	Kapβ1-GFP (4 amino acid linker)	GFP-N1, KapB1	AgeI Infusion reaction
pCA197	Nup98 folded/Nup214 FG-GFPtip	pCA14, pCA46	AgeI, PacI, QuikChange mutagenesis reaction
pCA201	Nup62-linker-mCherry	mCherry-N1, pCA30	HindIII, MfeI
pCA202	Kapβ1-GFP (no linker)	pCA195	QuikChange mutagenesis
pCA208	GFP-palmitoylation tag	GFP-C1, oligonucleotide insertion	XhoI, XmaI
pCA209	GFP-Nup54 FG domain-palmitoylation tag	pCA208	BsrGI, XhoI
pCA210	GFP-Nup62 FG domain-palmitoylation tag	pCA209	BsrGI, XhoI
pCA211	GFP-Nup98 FG domain-palmitoylation tag	pCA210	BsrGI, XhoI
pCA220	Nup62-GFPboundaryΔFG	pCA39	XcmI, AfeI, Mung Bean Nuclease
pCA224	TAP-GFP (5 amino acid linker)	TAP, GFP C1	NheI, AgeI
pCA237	Nup54-GFPboundaryΔFG	pCA10	HindIII Infusion reaction

Table 4 (continued)

pCA239	Crm1-GFP (7 amino acid linker)	Crm1, GFP-C1	BamHI InFusion reaction
pCA240	TAP-GFP (no linker)	pCA224	QuikChange mutagenesis
pCA241	Crm1-GFP (no linker)	pCA239	QuikChange mutagenesis

Sample preparation

Imaging of Yeast

Yeast were grown in log phase for >24 hours by sequential dilution at 30ºC in low-fluorescence medium (Sheff and Thorn, 2004). Cells were harvested from 1-3 ml of suspension culture by centrifugation, and resuspended in low-fluorescence medium (Sheff and Thorn, 2004). 1 µl of this suspension was dispensed onto a glass slide, and a coverslip (Number 1.5, VWR, West Chester, PA) was applied with slight pressure. Images were collected at room temperature with 2000ms exposure time for the anisotropy experiments. For the azide experiments, 100ms exposure time was used to image mCherry-NLS. 50-150 cells were imaged per experiment.

Imaging of Mammalian Cells

HeLa cells were grown in DMEM (GIBCO) containing penicillin / streptomycin and fetal bovine serum (GIBCO) in 35mm glass bottom dishes (No. 1.5, MatTek, Ashland MA). Cells were transfected with expression plasmids using lipofectamine (Invitrogen), following the manufacturer's protocol. Cells were imaged 18-48 hours after transfection in CIM [Hanks BBS (Sigma) containing 5% fetal bovine serum and 10mM HEPES pH 7.4] at 37ºC with 2000 ms exposure time for the anisotropy experiments and 1000 ms exposure time for the dual color experiments. 30-60 cells were imaged per experiment.

Microscope Set-up

Widefield polarized fluorescence images were acquired using an Olympus IX70 microscope and a 60x 1.45 NA objective (Olympus, Center Valley, PA). The sample was excited with a 488 nm argon laser (SpectraPhysics, now Newport Irvine, CA). The excitation light passed though a clean-up polarizer and a half wave plate (Thorlabs, Newton, NJ). Rotation of the half wave plate controlled the direction of polarization of the excitation light allowing for fine alignment. The light was centered and focused at the back focal plane, and thus emerges collimated from the objective. The microscope was equipped with a 500lp dichroic mirror and an ET535/30 or an ET 525/50 emission filter. Fluorescence emission was split into two channels based on polarization with a Cairn Optosplit III (Cairn Research Limited, Faversham, England). One emission channel collected light parallel to the excitation polarization ($I_{//}$), the other perpendicular ($I_{\perp}$), each with a clean-up polarizer, and imaged simultaneously side by side on an OrcaER CCD camera (Hamamatsu, Hamamatsu City, Japan). The dual color experiments were carried out using the same setup but the laser excitation was 488nm and 568nm (Melles Griot), the dichroic used was a 488/568 polychroic (Chroma) and the emission was split using a Cairn Optosplit III emission splitter (Cairn Research Limited, Kent, UK) with a ET525/50 bandpass filter to collect GFP emission, a ET632/60 bandpass filter for mCherry emission, and a 580lp dichroic mirror to split the emission. Image acquisition was controlled by Imaging software (Metamorph). Exposure time was 2000ms. All filters, dichroics, and polarizers were from Chroma (Bellows Falls, VT).

Microscope G-factor.

A system dependent factor, G, accounting for differences in sensitivity in the detection channels $I_{//}$ and $I_{\perp}$, was determined. A deep-well solution of dilute fluorescein, for which we assumed an anisotropy of 0, was imaged with both excitation polarizations, averaged, and used as a correction image.

Corrections for large NA.

The excitation light was ***y***-polarized, and in an ideal system $I_{//} = I_y$ and $I_{\perp} = I_x$. In our experimental system the sample was observed with a high (1.45) NA objective lens which causes a mixing of polarization since at high angles of collection there is a "***z***" polarization component mixed in to both $I_{//}$ and $I_{\perp}$. With the ***z***-axis corresponding to the optical axis and imaging the xy plane, the observed intensities are given by:

$$I_{\parallel} = K_a I_z + K_b I_y + K_c I_x \; ; \; I_{\perp} = K_a I_z + K_c I_y + K_b I_x$$

Where I_x, I_y, and I_z are the intensities observed with a polarizer oriented along the ***x***, ***y***, or ***z*** axis as detected by a small aperture. I_x and I_y, the corrected $I_{//}$ and $I_{\perp}$, can be calculated using weighing factors derived for our system: $K_a = 0.385$, $K_b = 1.006$, $K_c = 0.030$, and the simplifying assumption $I_x = I_z$ as in a randomly oriented system.

Microscope Calibration.

The system was calibrated by measuring steady-state anisotropies for small inorganic dyes in dilute solution as well as monomeric GFP expressed in the cytoplasm of living cells. The anisotropy of these fluorophores was measured with both horizontal

and vertical excitation polarizations. The fluorescent dyes used, their lifetimes (τ) and measured anisotropy were: Rose Bengal (τ = 76ps; r = 0.28±0.01), Erythrosin B (τ = 75ps r = 0.27±0.004), and fluorescein (τ = 4ns r = 0.019±0.002) (Sigma-Aldrich, St. Louis, MO). For monomeric GFP expressed in the cytosol of HeLa cells r = 0.326±0.008 which agrees with previously published values. These values were not sensitive to the polarization of the exciting light.

Data Analysis

Anisotropy Image Analysis

Data analysis was semi-automated for individual data sets. Analysis routines were implemented in MATLAB (The MathWorks, Natick, MA) unless otherwise noted. Initial corrections were applied to the entire image. An image of only medium with the same acquisition parameters as the sample was subtracted to correct for background fluorescence. The image was corrected for transmission differences and spatial differences with the normalized fluorescein image.

Individual cells were identified for further analysis allowing exclusion of cells not in focus, sick cells, or cells with aberrantly shaped nuclei. A rough overlay of $I_{\parallel}$ and $I_{\perp}$ is achieved with standard x-y shift values. $I_{\parallel}$ and $I_{\perp}$ pairs of individual nuclei were exported either to SPIDER or to MATLAB for alignment. The image pairs were registered using a translational sub-pixel alignment based on image cross correlation.

Corrections for the high NA objective were applied on a pixel-by-pixel basis as described above.

For yeast cells:

The remaining processing steps were implemented in MATLAB. The level of background fluorescence varied between cells and was corrected on a cell-by-cell basis. A cytoplasmic region was selected manually and its average intensity was the cell background; calculated for $I_{/\!/}$ and $I_{\perp}$.

An anisotropy image was calculated from the aligned parallel and perpendicular images pixel-by-pixel according to the definition of anisotropy.

A mask was created for each aligned pair to allow analysis of the NE. The image $I_{/\!/}+2I_{\perp}$ was processed with the imopen function in MATLAB and subtracted from $I_{/\!/}+2I_{\perp}$. The resultant image was thresholded: the 200 brightest pixels were used to generate the mask. The mask was processed to remove any single pixels and blocks of pixels that touched the image boundary. This yielded I_{mask} and only pixels within this mask were analyzed. This routine robustly and reproducibly selected the NE. This mask was applied to the anisotropy image.

The image was divided in 32 sectors, each corresponding to an angle of 11.25º, and the average anisotropy was calculated for pixels falling within this sector. These sector anisotropy values were then averaged for all cells with a given nucleoporin-GFP construct, and the standard deviation was calculated.

For mammalian cells:

For the analysis of Nup133, 16x16 pixel images of nuclear envelope segments were cropped from micrographs. In SPIDER, the cross-correlation was calculated between these segments and 18 artificial images of a line with different orientations. Each

image was assigned to the most similar template. Only pixels with intensities of one standard deviation of the average pixel intensity were included in the further analysis. The average anisotropy was calculated for each image. For each class of images aligned to one template, the average and standard anisotropy were then calculated.

For the analysis of the FG nups, the brightest 2.5% of pixels in the summed image of the perpendicular and parallel channels were selected for further analysis. Pixels contiguous with the edge of the image were discarded. Pixels that had fewer than 4 direct neighbor pixels were cleared. The remaining pixels were used to create a mask for the nuclear envelope. For every pixel in the mask, a 33 by 33 square centered on the pixel was analyzed to determine the orientation of the nuclear envelope within this region by fitting a straight line. Pixels were binned according to the orientation of the nuclear envelope in 10° increments. The average anisotropy of the pixels in each bin was calculated and the standard deviation determined.

Single cell analyses.

Analysis of the degree to which individual cells were ordered was carried out in the same way for yeast and mammalian cells. For each cell, the anisotropy pattern was normalized to its minimum and maximum and repeated 4 times for yeast cells (for which the pattern is characterized over 360°) and 8 times for mammalian cells (for which the pattern is characterized over 180°). A Fourier transform was taken of these values and the value of the frequency component which corresponds to the 180° periodicity characteristic of an “ordered” pattern was determined. This was divided by the standard deviation of the values of all higher frequency components, to give a value which reflects

how much greater the value of the “ordered” frequency component is above the noise of all other frequency components. We refer to this value as the “orderedness score”.

Determination of cell cycle state.

Bright field images of each field of cells were taken prior to the fluorescence image. Cells were assigned to eight cell cycle stage categories based on their bud morphology in the bright field image (Herskowitz, 1988) and their nuclear morphology in the fluorescence image.

Dual color image analysis

Images were analyzed in ImageJ. The contribution from the camera background and the media background was subtracted from each image. Individual cells were cropped from the micrographs and aligned between the red and green channels using the Cairn Image Splitter Analyzer plugin. To create a mask for the nuclear envelope for each cell, the Nup62-mCherry image was used. The local background was subtracted using the rolling ball background subtract function with a radius of 10. The image was then thresholded to create a mask corresponding to the brightest pixels. This mask was then applied to the original Nup62-mCherry and kap-β1-GFP images and the average fluorescence at the nuclear envelope was determined. For the time-lapse images, the fluorescence intensity of individual cells was normalized to the maximum prior to averaging the signal from all the cells.

Simulation of background subtraction.

A MATLAB simulation explored the effects of background subtraction. A stack with 200 planes each containing a circle with 32 segments was created for $I_{//}$ and $I_{\perp}$. First, an intensity, which varied around 200 with a Gaussian of width 0.1, was assigned to each plane in $I_{\perp}$. Then, the anisotropy and modulation of anisotropy were defined and $I_{//}$ was created from $I_{\perp}$. A background ($I_{//}$=100 and $I_{\perp}$=45) was added to each image and $I_{\perp}$ was altered to simulate G. Poisson-distributed photon noise was added depending on intensity. The simulation data was then analyzed as described with the exception that the background subtracted was 0, 100, or 200 and 0, 45, or 90 for $I_{//}$ and $I_{\perp}$, respectively.

Azide Treatment of Cells

Prior to imaging, yeast cells were spun down and resuspended in 1ml low-fluorescence medium in the absence of glucose. They were spun down a second time and resuspended in 100ul low-fluorescence medium containing 20mM sodium azide, 20mM deoxyglucose, and no glucose. The cells were grown at 30°C for 20 minutes before being spun down for imaging.

Permeabilized Cells

Cells were incubated on ice for 5 minutes, washed in ice cold transport buffer (20mM HEPES, 100mM potassium acetate, 1mM EGTA, 2mM magnesium acetate,

2mM DTT), and then incubated on ice in transport buffer and 70ug/ml digitonin for 5 minutes. Cells were then washed twice in ice cold transport buffer and twice in transport buffer at 37°C before imaging.

WGA Binding

In the WGA binding experiments, modified transport buffer which did not contain EGTA was used. Cells were permeabilized using digitonin as above, and washed once in ice cold transport buffer. WGA was added at a concentration of 2mg/ml and cells were incubated on ice for 15 minutes. They were then washed twice in ice cold transport buffer and twice in transport buffer at 37°C before imaging.

Ran Purification and GTP Loading

Ran purification

His tagged Ran in the pET28 vector (a gift from Dr Günter Blobel) was transformed into BL21 (DE3) RIL competent cells (Strategene). Ran expression was induced with 0.5mM IPTG and cells were grown for 3 hours. Cells were spun down at 63000 rpm for 10 minutes and the pellet was frozen overnight before lysis in BugBuster solution and 10mM imidazole. The lysate was spun at 18000rpm for 60 minutes. The supernatant was added to Ni2+ beads (Qiagen) and mixed at 4°C for 1 hour before washing in 10mmM Tris pH8, 250mM NaCl, 1mM MgCl, 20mM imidazole and 1mM β-mercaptoethanol. The protein was eluted from the beads in 10mM Tris pH8, 250mM

NaCl, 1mM MgCl, 250mM imidazole and 1mM β-mercaptoethanol. The fractions containing the most protein were combined and purified on a PD-10 salt exchange column (GE), and eluted into transport buffer.

GTP loading

Ran was loaded in 50mM HEPES pH 7.3, 10mM EDTA, 1mM magnesium acetate, 2.5mM DTT, and 1mM GTP at room temperature for 30 minutes, before 2.5 fold dilution and addition of magnesium acetate to 5mM. Free nucleotides were removed by gel filtration on a PD-10 column.

Addition of Ran to Cells

Dual color experiments

Cells were permeabilized and washed in transport buffer as above. 0.5ml of transport buffer at 37°C was added to the cells and they were transferred to the microscope. Cells which were transfected with both Nup62-mCherry and kapβ1-GFP were identified before the addition of 0.5ml of RanGTP at a concentration of 0.3mg/ml Images were taken before the addition of Ran and 10 minutes after the addition of Ran. For the time-lapse image sequences, images were taken every 5 seconds following the addition of RanGTP for 10 minutes.

Anisotropy experiments

Cells were permeabilized and washed in transport buffer as above. 0.5ml RanGTP was added at a concentration of 0.3mg/ml and cells were incubated at 37°C for 5 minutes. A further 0.5ml of transport buffer at 37°C was added and the cells were imaged. For control cells, 0.5ml of transport buffer was added instead of RanGTP.

Molecular Models

Models of fusion proteins were built in UCSF Chimera from the following crystal structures: EGFP, PDB 1EMG (Elsliger et al., 1999); Nic96, PDB 2QX5 (Jeudy and Schwartz, 2007); Nup133-Nup107, PDB 3I4R (Whittle and Schwartz, 2009); Tfp1, PDB 1VDZ (Maegawa et al., 2006). GFP was positioned with respect to the nucleoporins such that the linker helix was continuous. Vectors were calculated from PDB coordinates as follows: μ, vector between fluorophore atoms CE1 and O2; Nic96-u, vector between atoms Trp334-CA and Ile723-CG1; Nic96-v, vector normal to Nic96-u passing through atom Leu200-N; Nup133-Nup107-u, vector between atoms Nup107-Glu667-CA and Nup133-Lys518-CA; Nup133-Nup107-v, vector normal to Nup133-Nup107-u passing through atom Nup133-Ile1156-CA. Angles θ and ω for each construct were calculated from these vector coordinates. From these, maps of α as a function of φ and ψ were calculated in MATLAB. The following EM structures were used: EMDB-5152 (Kampmann and Blobel, 2009); EMDB-1640 (Diepholz et al., 2008). Registration of the yeast Tfp1 sequence with PDB 1VDZ was determined using FUGUE (Shi et al., 2001).

Bibliography

Abu-Arish, A., Kalab, P., Ng-Kamstra, J., Weis, K., and Fradin, C. (2009). Spatial distribution and mobility of the Ran GTPase in live interphase cells. Biophys. J. *97*, 2164–2178.

Adam, S.A., and Gerace, L. (1991). Cytosolic proteins that specifically bind nuclear location signals are receptors for nuclear import. Cell *66*, 837–847.

Adams, S.R., Campbell, R.E., Gross, L.A., Martin, B.R., Walkup, G.K., Yao, Y., Llopis, J., and Tsien, R.Y. (2002). New biarsenical ligands and tetracysteine motifs for protein labeling in vitro and in vivo: synthesis and biological applications. J. Am. Chem. Soc. *124*, 6063–6076.

Akey, C.W. (1990). Visualization of transport-related configurations of the nuclear pore transporter. Biophys. J. *58*, 341–355.

Akey, C.W. (1995). Structural plasticity of the nuclear pore complex. J. Mol. Biol. *248*, 273–293.

Akey, C.W., and Goldfarb, D.S. (1989). Protein import through the nuclear pore complex is a multistep process. J. Cell Biol. *109*, 971–982.

Akey, C.W., and Radermacher, M. (1993). Architecture of the Xenopus nuclear pore complex revealed by three-dimensional cryo-electron microscopy. J. Cell Biol. *122*, 1–19.

Akhtar, N., Hagan, H., and Lopilato, J. (2001). Functional analysis of the yeast Ran exchange factor Prp20p: in vivo evidence for the RanGTP gradient model. Mol Genet Genomics. *265*, 851-864.

Alber, F., Dokudovskaya, S., Veenhoff, L.M., Zhang, W., Kipper, J., Devos, D., Suprapto, A., Karni-Schmidt, O., Williams, R., Chait, B.T., et al. (2007). Determining the architectures of macromolecular assemblies. Nature *450*, 683–694.

Allen, N.P., Huang, L., Burlingame, A., and Rexach, M. (2001). Proteomic analysis of nucleoporin interacting proteins. J. Biol. Chem. *276*, 29268–29274.

Anantharam, A., Onoa, B., Edwards R.H., Holz, R.W., and Axelrod, D. (2010) Localized topological changes of the plasma membrane upon exocytosis visualized by polarized TIRFM. J. Cell Biol. *118*, 415-28.

Antonin, W., Franz, C., Haselmann, U., Antony, C., and Mattaj, I.W. (2005). The integral membrane nucleoporin pom121 functionally links nuclear pore complex assembly and nuclear envelope formation. Mol. Cell *17*, 83–92.

Arts. G., Fornerod, M., and Mattaj, I.W. (1998). Identification of a nuclear export receptor for tRNA. Curr. Biol. *8*, 305-314.

Axelrod, D. (1979). Carbocyanine dye orientation in red cell membrane studied by microscopic fluorescence polarization. Biophys. J. *26*, 557–573.

Bayliss, R., Littlewood, T., and Stewart, M. (2000). Structural basis for the interaction between FxFG nucleoporin repeats and importin-beta in nuclear trafficking. Cell *102*, 99–108.

Bayliss, R., Ribbeck, K., Akin, D., Kent, H.M., Feldherr, C.M., Görlich, D., and Stewart, M. (1999). Interaction between NTF2 and xFxFG-containing nucleoporins is required to mediate nuclear import of RanGDP. J. Mol. Biol. *293*, 579–593.

Beck, M., Förster, F., Ecke, M., Plitzko, J.M., Melchior, F., Gerisch, G., Baumeister, W., and Medalia, O. (2004). Nuclear pore complex structure and dynamics revealed by cryoelectron tomography. Science *306*, 1387–1390.

Beck, M., Lucić, V., Förster, F., Baumeister, W., and Medalia, O. (2007). Snapshots of nuclear pore complexes in action captured by cryo-electron tomography. Nature *449*, 611–615.

Belgareh, N., Rabut, G., Baï, S.W., van Overbeek, M., Beaudouin, J., Daigle, N., Zatsepina, O.V., Pasteau, F., Labas, V., Fromont-Racine, M., et al. (2001). An evolutionarily conserved NPC subcomplex, which redistributes in part to kinetochores in mammalian cells. J. Cell Biol. *154*, 1147–1160.

Ben-Efraim, I., and Gerace, L. (2001). Gradient of increasing affinity of importin β for nucleoporins along the pathway of nuclear import. J. Cell. Biol. *152*, 411-417.

Berke, I.C., Boehmer, T., Blobel, G., and Schwartz, T.U. (2004). Structural and

functional analysis of Nup133 domains reveals modular building blocks of the nuclear pore complex. J. Cell Biol. *167*, 591–597.

Bischoff, F.R., and Ponstingl, H. (1991). Catalysis of guanine nucleotide exchange on Ran by the mitotic regulator RCC1. Nature *354*, 80–82.

Bischoff, F.R., Klebe, C., Kretschmer, J., Wittinghofer, A., and Ponstingl, H. (1994). RanGAP1 induces GTPase activity of nuclear Ras-related Ran. Proc. Natl. Acad. Sci. U.S.A. *91*, 2587–2591.

Blackman, S.M., Cobb, C.E., Beth, A.H., and Piston, D.W. (1996). The orientation of eosin-5-maleimide on human erythrocyte band 3 measured by fluorescence polarization microscopy. Biophys. J, *71*, 194-208.

Boehmer, T., Jeudy, S., Berke, I.C., and Schwartz, T.U. (2008). Structural and functional studies of Nup107/Nup133 interaction and its implications for the architecture of the nuclear pore complex. Mol. Cell *30*, 721–731.

Brohawn, S.G., and Schwartz, T.U. (2009a). A lattice model of the nuclear pore complex. Commun Integr Biol *2*, 205–207.

Brohawn, S.G., and Schwartz, T.U. (2009b). Molecular architecture of the Nup84-Nup145C-Sec13 edge element in the nuclear pore complex lattice. Nat. Struct. Mol. Biol. *16*, 1173–1177.

Brohawn, S.G., Leksa, N.C., Spear, E.D., Rajashankar, K.R., and Schwartz, T.U. (2008). Structural evidence for common ancestry of the nuclear pore complex and vesicle coats. Science *322*, 1369–1373.

Brohawn, S.G., Partridge, J.R., Whittle, J.R.R., and Schwartz, T.U. (2009). The nuclear pore complex has entered the atomic age. Structure *17*, 1156–1168.

Cantor, C.R., and Schimmel, P.R. (1980). Biophysical Chemistry, Part II: Techniques for the Study of Biological Structure and Function (San Francisco, W.H. Freeman).

Capelson, M., Liang, Y., Schulte, R., Mair, W., Wagner, U., and Hetzer, M.W. (2010). Chromatin-bound nuclear pore components regulate gene expression in higher eukaryotes. Cell *140*, 372–383.

Cardarelli, F., Gratton., E. (2010). In vivo imaging of single-molecule translocation through nuclear pore complexes by pair correlation functions. PLoS One *5*, e10475-e10490.

Cardarelli, F., Lanzano, L., and Gratton, E. (2011). Fluorescence correlation spectroscopy of intact nuclear pore complexes. Biophys. J. *101*, L27-L29.

Chadrin, A., Hess, B., San Roman, M., Gatti, X., Lombard, B., Loew, D., Barral, Y., Palancade, B., and Doye, V. (2010). Pom33, a novel transmembrane nucleoporin required for proper nuclear pore complex distribution. J. Cell Biol. *189,* 795–811.

Chatel, G., Desai, S.H., Mattheyses, A.L., Powers, M.A., and Fahrenkrog, B. (2012). Domain topology of nucleoporin Nup98 within the nuclear pore complex. J. Struct. Biol. *177*, 81–89.

Clayton, A.H.A., Hanley, Q.S., Arndt-Jovin, D.J., Subramaniam, V., and Jovin, T.M. (2002). Dynamic fluorescence anisotropy imaging microscopy in the frequency domain (rFLIM). Biophys. J. *83*, 1631–1649.

Clouse, K.N., Luo, M.J., Zhou, Z., and Reed, R. (2001). A Ran-independent pathway for export of spliced mRNA. Nat. Cell Biol. *3,* 97–99.

Conti, E., and Kuriyan, J. (2000). Crystallographic analysis of the specific yet versatile recognition of distinct nuclear localization signals by karyopherin alpha. Structure *8,* 329–338.

Coppin, C.M., and Leavis, P.C. (1992). Quantitation of liquid-crystalline ordering in F-actin solutions. Biophys. J. *63,* 794–807.

Corbett, A.H., and Silver, P.A. (1996). The NTF2 gene encodes an essential, highly conserved protein that functions in nuclear transport in vivo. J. Biol. Chem. *271*, 18477–18484.

Cordes, V.C., Reidenbach, S., Köhler, A., Stuurman, N., van Driel, R., and Franke, W.W. (1993). Intranuclear filaments containing a nuclear pore complex protein. J. Cell Biol. *123*, 1333–1344.

Cronshaw, J.M., Krutchinsky, A.N., Zhang, W., Chait, B.T., and Matunis, M.J. (2002). Proteomic analysis of the mammalian nuclear pore complex. J. Cell Biol. *158*, 915–927.

D'Angelo, M.A., Raices, M., Panowski, S.H., and Hetzer, M.W. (2009). Age-dependent deterioration of nuclear pore complexes causes a loss of nuclear integrity in postmitotic cells. Cell *136*, 284–295.

Daigle, N., Beaudouin, J., Hartnell, L., Imreh, G., Hallberg, E., Lippincott-Schwartz, J., and Ellenberg, J. (2001). Nuclear pore complexes form immobile networks and have a very low turnover in live mammalian cells. J. Cell Biol. *154*, 71–84.

Damelin, M., and Silver, P.A. (2000). Mapping interactions between nuclear transport factors in living cells reveals pathways through the nuclear pore complex. Mol. Cell *5*, 133–140.

Debler, E.W., Ma, Y., Seo, H.-S., Hsia, K.-C., Noriega, T.R., Blobel, G., and Hoelz, A. (2008). A fence-like coat for the nuclear pore membrane. Mol. Cell *32*, 815–826.

Denning, D.P., and Rexach, M.F. (2007). Rapid evolution exposes the boundaries of domain structure and function in natively unfolded FG nucleoporins. Mol. Cell Proteomics *6*, 272–282.

Denning, D.P., Patel, S.S., Uversky, V., Fink, A.L., and Rexach, M. (2003). Disorder in the nuclear pore complex: the FG repeat regions of nucleoporins are natively unfolded. Proc. Natl. Acad. Sci. U.S.A. *100*, 2450–2455.

Devos, D., Dokudovskaya, S., Williams, R., Alber, F., Eswar, N., Chait, B.T., Rout, M.P., and Sali, A. (2006). Simple fold composition and modular architecture of the nuclear pore complex. Proc. Natl. Acad. Sci. U.S.A. *103*, 2172–2177.

Diepholz, M., Venzke, D., Prinz, S., Batisse, C., Flörchinger, B., Rössle, M., Svergun, D.I., Böttcher, B., and Féthière, J. (2008). A different conformation for EGC stator subcomplex in solution and in the assembled yeast V-ATPase: possible implications for regulatory disassembly. Structure *16*, 1789–1798.

Dingwall, C., and Laskey, R.A. (1991). Nuclear targeting sequences--a consensus? Trends Biochem. Sci. *16*, 478–481.

Dingwall, C., Sharnick, S.V., and Laskey, R.A. (1982). A polypeptide domain that specifies migration of nucleoplasmin into the nucleus. Cell *30*, 449–458.

Dong, X., Biswas, A., Süel, K.E., Jackson, L.K., Martinez, R., Gu, H., and Chook, Y.M.

(2009). Structural basis for leucine-rich nuclear export signal recognition by CRM1. Nature *458*, 1136–1141.

Doye, V., and Hurt, E. (1997). From nucleoporins to nuclear pore complexes. Curr. Opin. Cell Biol. *9*, 401–411.

Drin, G., Casella, J.-F., Gautier, R., Boehmer, T., Schwartz, T.U., and Antonny, B. (2007). A general amphipathic alpha-helical motif for sensing membrane curvature. Nat. Struct. Mol. Biol. *14*, 138–146.

Dupres, V., Dufrêne, Y.F., and Heinisch, J.J. (2010) Measuring cell wall thickness in living yeast cells using single molecular rulers. ACS Nano *4*, 5498-5504.

El-Husseini, A.E.-D., Craven, S.E., Brock, S.C., and Bredt, D.S. (2001). Polarized targeting of peripheral membrane proteins in neurons. J. Biol. Chem. *276*, 44984–44992.

Elad, N., Maimon, T., Frenkiel-Krispin, D., Lim, R.Y.H., and Medalia, O. (2009). Structural analysis of the nuclear pore complex by integrated approaches. Curr. Opin. Struct. Biol. *19*, 226–232.

Elsliger, M.A., Wachter, R.M., Hanson, G.T., Kallio, K., and Remington, S.J. (1999). Structural and spectral response of green fluorescent protein variants to changes in pH. Biochemistry *38*, 5296–5301.

Fahrenkrog, B., Hurt, E.C., Aebi, U., and Panté, N. (1998). Molecular architecture of the yeast nuclear pore complex: localization of Nsp1p subcomplexes. J. Cell Biol. *143*, 577–588.

Feldherr, C.M., and Akin, D. (1997). The location of the transport gate in the nuclear pore complex. J. Cell. Sci. *110 (Pt 24)*, 3065–3070.

Fernandez-Martinez, J., Phillips, J., Sekedat, M.D., Diaz-Avalos, R., Velazquez-Muriel, J., Franke, J.D., Williams, R., Stokes, D.L., Chait, B.T., Sali, A., et al. (2012). Structure-function mapping of a heptameric module in the nuclear pore complex. J. Cell Biol. *196*, 419-434.

Finlay, D.R., Newmeyer, D.D., Price, T.M., and Forbes, D.J. (1987). Inhibition of in vitro nuclear transport by a lectin that binds to nuclear pores. J. Cell Biol. *104*, 189–200.

Fischer, U., Huber, J., Boelens, W., and Mattajt, L. (1995). The HIV-1 Rev activation domain is a nuclear export signal that accesses an export pathway used by specific cellular RNAs. Cell *82*, 475-483.

Fontoura, B.M., Blobel, G., and Matunis, M.J. (1999). A conserved biogenesis pathway for nucleoporins: proteolytic processing of a 186-kilodalton precursor generates Nup98 and the novel nucleoporin, Nup96. J. Cell Biol. *144*, 1097–1112.

Fornerod, M., Ohno, M., Yoshida, M., and Mattaj, I.W. (1997). CRM1 is an export receptor for leucine-rich nuclear export signals. Cell *90*, 1051–1060.

Förster, T. (1948). Zwischenmolekulare energiewanderung und fluoreszenz. Annalen Der Physik *437*, 55-75.

Frey, S., and Görlich, D. (2007). A saturated FG-repeat hydrogel can reproduce the permeability properties of nuclear pore complexes. Cell *130*, 512–523.

Frey, S., and Görlich, D. (2009). FG/FxFG as well as GLFG repeats form a selective permeability barrier with self-healing properties. Embo J. *28*, 2554–2567.

Frey, S., Richter, R.P., and Görlich, D. (2006). FG-rich repeats of nuclear pore proteins form a three-dimensional meshwork with hydrogel-like properties. Science *314*, 815–817.

Gall, J.G. (1967). Octagonal nuclear pores. J. Cell Biol. *32*, 391–399.

Gautier, I., Tramier, M., Durieux, C., Coppey, J., Pansu, R.B., Nicolas, J.C., Kemnitz, K., and Coppey-Moisan, M. (2001). Homo-FRET microscopy in living cells to measure monomer-dimer transition of GFP-tagged proteins. Biophys. J. *80*, 3000–3008.

Goldfarb, D.S., Corbett, A.H., Mason, D.A., Harreman, M.T., and Adam, S.A. (2004). Importin alpha: a multipurpose nuclear-transport receptor. Trends Cell Biol. *14*, 505–514.

Gomez-Ospina, N., Morgan, G., Giddings, T.H., Kosova, B., Hurt, E., and Winey, M. (2000). Yeast nuclear pore complex assembly defects determined by nuclear envelope reconstruction. J. Struct. Biol. *132*, 1–5.

Görlich, D., Kostka, S., Kraft, R., Dingwall, C., Laskey, R.A., Hartmann, E., and Prehn,

S. (1995). Two different subunits of importin cooperate to recognize nuclear localization signals and bind them to the nuclear envelope. Curr. Biol. *5*, 383–392.

Görlich, D., Prehn, S., Laskey, R.A., and Hartmann, E. (1994). Isolation of a protein that is essential for the first step of nuclear protein import. Cell *79*, 767–778.

Grandi, P., Dang, T., Pané, N., Shevchenko, A., Mann, M., Forbes, D., and Hurt, E. (1997). Nup93, a vertebrate homologue of yeast Nic96p, forms a complex with a novel 205-kDa protein and is required for correct nuclear pore assembly. Mol. Biol. Cell *8*, 2017–2038.

Grandi, P., Doye, V., and Hurt, E.C. (1993). Purification of NSP1 reveals complex formation with "GLFG" nucleoporins and a novel nuclear pore protein NIC96. Embo J. *12*, 3061–3071.

Griffis, E.R., Altan, N., Lippincott-Schwartz, J., and Powers, M.A. (2002). Nup98 is a mobile nucleoporin with transcription-dependent dynamics. Mol. Biol. Cell *13*, 1282–1297.

Grüter, P., Tabernero, C., Kobbe, von, C., Schmitt, C., Saavedra, C., Bachi, A., Wilm, M., Felber, B.K., and Izaurralde, E. (1998). TAP, the human homolog of Mex67p, mediates CTE-dependent RNA export from the nucleus. Mol. Cell *1*, 649–659.

Guan, T., Müller, S., Klier, G., Panté, N., Blevitt, J.M., Häner, M., Paschal, B., Aebi, U., and Gerace, L. (1995). Structural analysis of the p62 complex, an assembly of O-linked glycoproteins that localizes near the central gated channel of the nuclear pore complex. Mol. Biol. Cell *6*, 1591–1603.

Harel, A., Orjalo, A.V., Vincent, T., Lachish-Zalait, A., Vasu, S., Shah, S., Zimmerman, E., Elbaum, M., and Forbes, D.J. (2003). Removal of a single pore subcomplex results in vertebrate nuclei devoid of nuclear pores. Mol. Cell *11*, 853–864.

Hellen, E.H., and Axelrod, D. (1987) Fluorescence emission at dielectric and metal-film interfaces. J. Opt. Soc. Am. B *4*, 337-350.

Herskowitz, I. (1988). Life cycle of the budding yeast Saccharomyces cerevisiae. Microbiol. Rev. *52*, 536–553.

Hinshaw, J.E., and Milligan, R.A. (2003). Nuclear pore complexes exceeding eightfold

rotational symmetry. J. Struct. Biol. *141*, 259–268.

Ho, A.K., Shen, T.X., Ryan, K.J., Kiseleva, E., Levy, M.A., Allen, T.D., and Wente, S.R. (2000). Assembly and preferential localization of Nup116p on the cytoplasmic face of the nuclear pore complex by interaction with Nup82p. Mol. Cell. Biol. *20*, 5736–5748.

Hodel, A.E., Hodel, M.R., Griffis, E.R., Hennig, K.A., Ratner, G.A., Xu, S., and Powers, M.A. (2002). The three-dimensional structure of the autoproteolytic, nuclear pore-targeting domain of the human nucleoporin Nup98. Mol. Cell *10*, 347–358.

Hoelz, A., Debler, E.W., and Blobel, G. (2011). The structure of the nuclear pore complex. Annu. Rev. Biochem. *80*, 613–643.

Holt, G.D., Snow, C.M., Senior, A., Haltiwanger, R.S., Gerace, L., and Hart, G.W. (1987). Nuclear pore complex glycoproteins contain cytoplasmically disposed O-linked N-acetylglucosamine. J. Cell Biol. *104*, 1157–1164.

Hood, J.K., and Silver, P.A. (1998). Cse1p is required for export of Srp1p/importin-alpha from the nucleus in Saccharomyces cerevisiae. J. Biol. Chem. *273*, 35142–35146.

Hsia, K.-C., Stavropoulos, P., Blobel, G., and Hoelz, A. (2007). Architecture of a coat for the nuclear pore membrane. Cell *131*, 1313–1326.

Hu, T., Guan, T., and Gerace, L. (1996). Molecular and functional characterization of the p62 complex, an assembly of nuclear pore complex glycoproteins. J. Cell Biol. *134*, 589–601.

Inoué, S., Shimomura, O., Goda, M., Shribak, M., and Tran, P.T. (2002). Fluorescence polarization of green fluorescence protein. Proc. Natl. Acad. Sci. U.S.A. *99*, 4272–4277.

Izaurralde, E., Kutay, U., Kobbe, von, C., Mattaj, I.W., and Görlich, D. (1997). The asymmetric distribution of the constituents of the Ran system is essential for transport into and out of the nucleus. Embo J. *16*, 6535–6547.

Jäkel, S., and Görlich, D. (1998). Importin beta, transportin, RanBP5 and RanBP7 mediate nuclear import of ribosomal proteins in mammalian cells. Embo J. *17*, 4491–4502.

Jeudy, S., and Schwartz, T.U. (2007). Crystal structure of nucleoporin Nic96 reveals a novel, intricate helical domain architecture. J. Biol. Chem. *282*, 34904–34912.

Jovanovic-Talisman, T., Tetenbaum-Novatt, J., McKenney, A.S., Zilman, A., Peters, R., Rout, M.P., and Chait, B.T. (2009). Artificial nanopores that mimic the transport selectivity of the nuclear pore complex. Nature *457*, 1023–1027.

Kadowaki, T., Hitomi, M., Chen, S., and Tartakoff, A.M. (1994). Nuclear mRNA accumulation causes nucleolar fragmentation in yeast mtr2 mutant. Mol. Biol. Cell *5*, 1253–1263.

Kalderon, D., Richardson, W.D., Markham, A.F., and Smith, A.E. (1984). Sequence requirements for nuclear location of simian virus 40 large-T antigen. Nature *311*, 33–38.

Kampmann, M., and Blobel, G. (2009). Three-dimensional structure and flexibility of a membrane-coating module of the nuclear pore complex. Nat. Struct. Mol. Biol. *16*, 782–788.

Kampmann, M (2009). Biophysical Characterization of Structure and Dynamics of Nuclear Pore Complex Components. Ph.D thesis, The Rockefeller University: U.S.A.

Kang, Y., and Cullen, B.R. (1999). The human Tap protein is a nuclear mRNA export factor that contains novel RNA-binding and nucleocytoplasmic transport sequences. Genes Dev. *13*, 1126–1139.

Katahira, J., Strässer, K., Podtelejnikov, A., Mann, M., Jung, J.U., and Hurt, E. (1999). The Mex67p-mediated nuclear mRNA export pathway is conserved from yeast to human. Embo J. *18*, 2593–2609.

Klebe, C., Bischoff, F.R., Ponstingl, H., and Wittinghofer, A. (1995). Interaction of the nuclear GTP-binding protein Ran with its regulatory proteins RCC1 and RanGAP1. Biochemistry *34*, 639–647.

Kraemer, D., Wozniak, R.W., Blobel, G., and Radu, A. (1994). The human CAN protein, a putative oncogene product associated with myeloid leukemogenesis, is a nuclear pore complex protein that faces the cytoplasm. Proc. Natl. Acad. Sci. U.SA. *91*, 1519–1523.

Kraemer, D.M., Strambio-de-Castillia, C., Blobel, G., and Rout, M.P. (1995). The essential yeast nucleoporin NUP159 is located on the cytoplasmic side of the nuclear

pore complex and serves in karyopherin-mediated binding of transport substrate. J. Biol. Chem. *270*, 19017–19021.

Kutay, U., Bischoff, F.R., Kostka, S., Kraft, R., and Görlich, D. (1997). Export of importin alpha from the nucleus is mediated by a specific nuclear transport factor. Cell *90*, 1061–1071.

Lange, A., Mills, R.E., Lange, C.J., Stewart, M., Devine, S.E., and Corbett, A.H. (2007). Classical nuclear localization signals: definition, function, and interaction with importin alpha. J. Biol. Chem. *282*, 5101–5105.

Langhorst, M.F., Genisyuerek, S., and Stuermer, C.A.O. (2006). Accumulation of FlAsH/Lumio Green in active mitochondria can be reversed by beta-mercaptoethanol for specific staining of tetracysteine-tagged proteins. Histochem. Cell Biol. *125*, 743–747.

Leksa, N.C., Brohawn, S.G., and Schwartz, T.U. (2009). The structure of the scaffold nucleoporin Nup120 reveals a new and unexpected domain architecture. Structure *17*, 1082–1091.

Liashkovich, I., Meyring, A., Kramer, A., and Shahin, V. (2011). Exceptional structural and mechanical flexibility of the nuclear pore complex. J. Cell. Physiol. *226*, 675–682.

Lim, R.Y.H., Fahrenkrog, B., Köser, J., Schwarz-Herion, K., Deng, J., and Aebi, U. (2007a). Nanomechanical basis of selective gating by the nuclear pore complex. Science *318*, 640–643.

Lim, R.Y.H., Huang, N.-P., Köser, J., Deng, J., Lau, K.H.A., Schwarz-Herion, K., Fahrenkrog, B., and Aebi, U. (2006). Flexible phenylalanine-glycine nucleoporins as entropic barriers to nucleocytoplasmic transport. Proc. Natl. Acad. Sci. U.S.A. *103*, 9512–9517.

Lim, R.Y.H., Köser, J., Huang, N.-P., Schwarz-Herion, K., and Aebi, U. (2007b). Nanomechanical interactions of phenylalanine-glycine nucleoporins studied by single molecule force-volume spectroscopy. J. Struct. Biol. *159*, 277–289.

Lowe, A.R., Siegel, J.J., Kalab, P., Siu, M., Weis, K., and Liphardt, J.T. (2010). Selectivity mechanism of the nuclear pore complex characterized by single cargo tracking. Nature *467*, 600–603.

Lubas, W.A., Smith, M., Starr, C.M., and Hanover, J.A. (1995). Analysis of nuclear pore protein p62 glycosylation. Biochemistry *34*, 1686–1694.

Lund, M.K., and Guthrie, C. (2005). The DEAD-box protein Dbp5p is required to dissociate Mex67p from exported mRNPs at the nuclear rim. Mol. Cell *20*, 645–651.

Lutzmann, M., Kunze, R., Buerer, A., Aebi, U., and Hurt, E. (2002). Modular self-assembly of a Y-shaped multiprotein complex from seven nucleoporins. Embo J. *21*, 387–397.

Madrid, A.S., Mancuso, J., Cande, W.Z., and Weis, K. (2006). The role of the integral membrane nucleoporins Ndc1p and Pom152p in nuclear pore complex assembly and function. J. Cell Biol. *173*, 361–371.

Maegawa, Y., Morita, H., Iyaguchi, D., Yao, M., Watanabe, N., and Tanaka, I. (2006). Structure of the catalytic nucleotide-binding subunit A of A-type ATP synthase from Pyrococcus horikoshii reveals a novel domain related to the peripheral stalk. Acta Crystallogr. D Biol. Crystallogr. *62*, 483–488.

Mattheyses, A.L., Hoppe, A.D., and Axelrod, D. (2004). Polarized fluorescence resonance energy transfer microscopy. Biophys. J. *87*, 2787–2797.

Melchior, F., Paschal, B., Evans, J., and Gerace, L. (1993). Inhibition of nuclear protein import by nonhydrolyzable analogues of GTP and identification of the small GTPase Ran/TC4 as an essential transport factor. J. Cell Biol. *123*, 1649–1659.

Melchior, F., Sweet, D.J., and Gerace, L. (1995). Analysis of Ran/TC4 function in nuclear protein import. Meth. Enzymol. *257*, 279–291.

Melčák, I., Hoelz, A., and Blobel, G. (2007). Structure of Nup58/45 suggests flexible nuclear pore diameter by intermolecular sliding. Science *315*, 1729–1732.

Miao, M., Ryan, K.J., and Wente, S.R. (2006). The integral membrane protein Pom34p functionally links nucleoporin subcomplexes. Genetics *172*, 1441–1457.

Mincer, J.S., and Simon, S.M. (2011). Simulations of nuclear pore transport yield mechanistic insights and quantitative predictions. Proc. Natl. Acad. Sci. U.S.A. *108*, E351–8.

Moeller, von, H., and Basquin, C. (2009). The mRNA export protein DBP5 binds RNA and the cytoplasmic nucleoporin NUP214 in a mutually exclusive manner. Nat. Struct. Mol. Biol. *16*, 247-254.

Moore, M.S., and Blobel, G. (1992). The two steps of nuclear import, targeting to the nuclear envelope and translocation through the nuclear pore, require different cytosolic factors. Cell *69*, 939–950.

Moore, M.S., and Blobel, G. (1993). The GTP-binding protein Ran/TC4 is required for protein import into the nucleus. Nature *365*, 661–663.

Moore, M.S., and Blobel, G. (1994). Purification of a Ran-interacting protein that is required for protein import into the nucleus. Proc. Natl. Acad. Sci. U.S.A. *91*, 10212–10216.

Moreno, H., Simos, G., and Segref, A. (1998). Nuclear mRNA Export Requires Complex Formation between Mex67p and Mtr2p at the Nuclear Pores. Mol. Cell. Biol. *18*, 6826-6838

Moroianu, J., and Blobel, G. (1995). Protein export from the nucleus requires the GTPase Ran and GTP hydrolysis. Proc. Natl. Acad. Sci. U.S.A. *92*, 4318–4322.

Moroianu, J., Blobel, G., and Radu, A. (1996). Nuclear protein import: Ran-GTP dissociates the karyopherin alphabeta heterodimer by displacing alpha from an overlapping binding site on beta. Proc. Natl. Acad. Sci. U.S.A. *93*, 7059–7062.

Nachury, M.V., and Weis, K. (1999). The direction of transport through the nuclear pore can be inverted. Proc. Natl. Acad. Sci. U.S.A. *96*, 9622–9627.

Nagy, V., Hsia, K.-C., Debler, E.W., Kampmann, M., Davenport, A.M., Blobel, G., and Hoelz, A. (2009). Structure of a trimeric nucleoporin complex reveals alternate oligomerization states. Proc. Natl. Acad. Sci. U.S.A. *106*, 17693–17698.

Napetschnig, J., Blobel, G., and Hoelz, A. (2007). Crystal structure of the N-terminal domain of the human protooncogene Nup214/CAN. Proc. Natl. Acad. Sci. U.S.A. *104*, 1783–1788.

Napetschnig, J., Kassube, S.A., Debler, E.W., Wong, R.W., Blobel, G., and Hoelz, A. (2009). Structural and functional analysis of the interaction between the nucleoporin

Nup214 and the DEAD-box helicase Ddx19. Proc. Natl. Acad. Sci. U.S.A. *106*, 3089–3094.

Nehrbass, U., Rout, M.P., Maguire, S., Blobel, G., and Wozniak, R.W. (1996). The yeast nucleoporin Nup188p interacts genetically and physically with the core structures of the nuclear pore complex. J. Cell Biol. *133*, 1153–1162.

Newmeyer, D. (1988). Nuclear import can be separated into distinct steps in vitro: nuclear pore binding and translocation. Cell *52*, 641-653

Ohtsubo, M., Okazaki, H., and Nishimoto, T. (1989). The RCC1 protein, a regulator for the onset of chromosome condensation locates in the nucleus and binds to DNA. J. Cell Biol. *109*, 1389–1397.

Oskolkov, N.N., Linse, P., Potemkin, I.I., and Khokhlov, A.R. (2011). Nematic ordering of polymers in confined geometry applied to DNA packaging in viral capsids. J Phys Chem B *115*, 422–432.

Panté, N., and Kann, M. (2002). Nuclear pore complex is able to transport macromolecules with diameters of about 39 nm. Mol. Biol. Cell *13*, 425–434.

Panté, N., Bastos, R., McMorrow, I., Burke, B., and Aebi, U. (1994). Interactions and three-dimensional localization of a group of nuclear pore complex proteins. J. Cell Biol. *126*, 603–617.

Patel, S.S., Belmont, B.J., Sante, J.M., and Rexach, M.F. (2007). Natively unfolded nucleoporins gate protein diffusion across the nuclear pore complex. Cell *129*, 83–96.

Paulillo, S.M., Phillips, E.M., Köser, J., Sauder, U., Ullman, K.S., Powers, M.A., and Fahrenkrog, B. (2005). Nucleoporin domain topology is linked to the transport status of the nuclear pore complex. J. Mol. Biol. *351*, 784–798.

Peters, R. (2005). Translocation through the nuclear pore complex: selectivity and speed by reduction-of-dimensionality. Traffic *6*, 421–427.

Peters, R. (2009). Translocation through the nuclear pore: Kaps pave the way. Bioessays *31*, 466–477.

Pollard, V.W., Michael, W.M., Nakielny, S., Siomi, M.C., Wang, F., and Dreyfuss, G. (1996). A novel receptor-mediated nuclear protein import pathway. Cell *86*, 985–994.

Pyhtila, B., and Rexach, M. (2003). A gradient of affinity for the karyopherin kap95p along the yeast nuclear pore complex. J. Biol. Chem. *278*, 42699-42708.

Rabut, G., Doye, V., and Ellenberg, J. (2004). Mapping the dynamic organization of the nuclear pore complex inside single living cells. Nat. Cell Biol. *6,* 1114–1121.

Radu, A., Blobel, G., and Moore, M.S. (1995a). Identification of a protein complex that is required for nuclear protein import and mediates docking of import substrate to distinct nucleoporins. Proc. Natl. Acad. Sci. U.S.A. *92*, 1769–1773.

Radu, A., Moore, M.S., and Blobel, G. (1995b). The peptide repeat domain of nucleoporin Nup98 functions as a docking site in transport across the nuclear pore complex. Cell *81,* 215–222.

Reid, R.J.D., Lisby, M., and Rothstein, R. (2002). Cloning-free genome alterations in Saccharomyces cerevisiae using adaptamer-mediated PCR. Meth. Enzymol. *350*, 258–277.

Rexach, M., and Blobel, G. (1995). Protein import into nuclei: association and dissociation reactions involving transport substrate, transport factors, and nucleoporins. Cell *83*, 683–692.

Ribbeck, K., and Görlich, D. (2001). Kinetic analysis of translocation through nuclear pore complexes. EMBO J. *20*, 1320-1330.

Richardson, W.D., Mills, A.D., Dilworth, S.M., Laskey, R.A., and Dingwall, C. (1988). Nuclear protein migration involves two steps: rapid binding at the nuclear envelope followed by slower translocation through nuclear pores. Cell *52*, 655–664.

Robbins, J., Dilworth, S.M., Laskey, R.A., and Dingwall, C. (1991). Two interdependent basic domains in nucleoplasmin nuclear targeting sequence: identification of a class of bipartite nuclear targeting sequence. Cell *64*, 615–623.

Rocheleau, J.V., Edidin, M., and Piston, D.W. (2003). Intrasequence GFP in class I MHC molecules, a rigid probe for fluorescence anisotropy measurements of the membrane environment. Biophys. J. *84*, 4078–4086.

Rosell, F.I., and Boxer, S.G. (2003). Polarized absorption spectra of green fluorescent protein single crystals: transition dipole moment directions. Biochemistry *42*, 177–183.

Rosenblum, J.S., and Blobel, G. (1999). Autoproteolysis in nucleoporin biogenesis. Proc. Natl. Acad. Sci. U.S.A. *96*, 11370–11375.

Rout, M.P., Aitchison, J.D., Magnasco, M.O., and Chait, B.T. (2003). Virtual gating and nuclear transport: the hole picture. Trends Cell Biol. *13*, 622–628.

Rout, M.P., Aitchison, J.D., Suprapto, A., Hjertaas, K., Zhao, Y., and Chait, B.T. (2000). The yeast nuclear pore complex: composition, architecture, and transport mechanism. J. Cell Biol. *148*, 635–651.

Ryan, K.J., and Wente, S.R. (2000). The nuclear pore complex: a protein machine bridging the nucleus and cytoplasm. Curr. Opin. Cell Biol. *12*, 361–371.

Schlaich, N.L., Häner, M., Lustig, A., Aebi, U., and Hurt, E.C. (1997). In vitro reconstitution of a heterotrimeric nucleoporin complex consisting of recombinant Nsp1p, Nup49p, and Nup57p. Mol. Biol. Cell *8*, 33–46.

Schmitt, C., Kobbe, von, C., Bachi, A., Panté, N., Rodrigues, J.P., Boscheron, C., Rigaut, G., Wilm, M., Séraphin, B., Carmo-Fonseca, M., et al. (1999). Dbp5, a DEAD-box protein required for mRNA export, is recruited to the cytoplasmic fibrils of nuclear pore complex via a conserved interaction with CAN/Nup159p. Embo J. *18*, 4332–4347.

Schrader, N., Koerner, C., Koessmeier, K., Bangert, J.-A., Wittinghofer, A., Stoll, R., and Vetter, I.R. (2008a). The crystal structure of the Ran-Nup153ZnF2 complex: a general Ran docking site at the nuclear pore complex. Structure *16*, 1116–1125.

Schrader, N., Stelter, P., Flemming, D., Kunze, R., Hurt, E., and Vetter, I.R. (2008b). Structural basis of the nic96 subcomplex organization in the nuclear pore channel. Mol. Cell *29*, 46–55.

Schwarz-Herion, K., Maco, B., Sauder, U., and Fahrenkrog, B. (2007). Domain topology of the p62 complex within the 3-D architecture of the nuclear pore complex. J. Mol. Biol. *370*, 796–806.

Schwoebel, E.D., Ho, T.H., and Moore, M.S. (2002). The mechanism of inhibition of Ran-dependent nuclear transport by cellular ATP depletion. J. Cell Biol. *157*, 963–974.

Schwoebel, E.D., Talcott, B., Cushman, I., and Moore, M.S. (1998). Ran-dependent signal-mediated nuclear import does not require GTP hydrolysis by Ran. J. Biol. Chem. *273*, 35170–35175.

Segref, A., Sharma, K., Doye, V., Hellwig, A., Huber, J., Lührmann, R., and Hurt, E. (1997). Mex67p, a novel factor for nuclear mRNA export, binds to both poly(A)+ RNA and nuclear pores. Embo J. *16*, 3256–3271.

Sheff, M.A., and Thorn, K.S. (2004). Optimized cassettes for fluorescent protein tagging in Saccharomyces cerevisiae. Yeast *21*, 661–670.

Shi, J., Blundell, T.L., and Mizuguchi, K. (2001). FUGUE: sequence-structure homology recognition using environment-specific substitution tables and structure-dependent gap penalties. J. Mol. Biol. *310*, 243–257.

Shulga, N., Roberts, P., Gu, Z., Spitz, L., Tabb, M.M., Nomura, M., and Goldfarb, D.S. (1996). In vivo nuclear transport kinetics in Saccharomyces cerevisiae: a role for heat shock protein 70 during targeting and translocation. J. Cell Biol. *135*, 329–339.

Siniossoglou, S., Lutzmann, M., Santos-Rosa, H., Leonard, K., Mueller, S., Aebi, U., and Hurt, E. (2000). Structure and assembly of the Nup84p complex. J. Cell Biol. *149*, 41–54.

Snay-Hodge, C.A., Colot, H.V., Goldstein, A.L., and Cole, C.N. (1998). Dbp5p/Rat8p is a yeast nuclear pore-associated DEAD-box protein essential for RNA export. Embo J. *17*, 2663–2676.

Snow, C.M., Senior, A., and Gerace, L. (1987). Monoclonal antibodies identify a group of nuclear pore complex glycoproteins. J. Cell Biol. *104*, 1143–1156.

Solmaz, S.R., Chauhan, R., Blobel, G., and Melčák, I. (2011). Molecular architecture of the transport channel of the nuclear pore complex. Cell *147*, 590–602.

Stade, K., Ford, C.S., Guthrie, C., and Weis, K. (1997). Exportin 1 (Crm1p) is an essential nuclear export factor. Cell *90*, 1041–1050.

Stavru, F., Hülsmann, B.B., Spang, A., Hartmann, E., Cordes, V.C., and Görlich, D. (2006). NDC1: a crucial membrane-integral nucleoporin of metazoan nuclear pore complexes. J. Cell Biol. *173*, 509–519.

Stewart, M. (2007). Ratcheting mRNA out of the nucleus. Mol. Cell *25*, 327–330.

Stoffler, D., Feja, B., Fahrenkrog, B., Walz, J., Typke, D., and Aebi, U. (2003). Cryo-electron tomography provides novel insights into nuclear pore architecture: implications for nucleocytoplasmic transport. J. Mol. Biol. *328*, 119–130.

Stoffler, D., Goldie, K.N., Feja, B., and Aebi, U. (1999). Calcium-mediated structural changes of native nuclear pore complexes monitored by time-lapse atomic force microscopy. J. Mol. Biol. *287*, 741–752.

Strawn, L.A., Shen, T., Shulga, N., Goldfarb, D.S., and Wente, S.R. (2004). Minimal nuclear pore complexes define FG repeat domains essential for transport. Nat. Cell Biol. *6*, 197–206.

Sukegawa, J., and Blobel, G. (1993). A nuclear pore complex protein that contains zinc finger motifs, binds DNA, and faces the nucleoplasm. Cell *72*, 29–38.

Sund, S.E., Swanson, J.A., and Axelrod, D. (1999). Cell membrane orientation visualized by polarized total internal reflection fluorescence. Biophys. J. *77*, 2266–2283.

Swaminathan, R., Hoang, C.P., and Verkman, A.S. (1997). Photobleaching recovery and anisotropy decay of green fluorescent protein GFP-S65T in solution and cells: cytoplasmic viscosity probed by green fluorescent protein translational and rotational diffusion. Biophys. J. *72*, 1900–1907.

Terry, L.J., and Wente, S.R. (2007). Nuclear mRNA export requires specific FG nucleoporins for translocation through the nuclear pore complex. J. Cell Biol. *178*, 1121–1132.

Terry, L.J., and Wente, S.R. (2009). Flexible gates: dynamic topologies and functions for FG nucleoporins in nucleocytoplasmic transport. Eukaryotic Cell *8*, 1814–1827.

Tetenbaum-Novatt, J., Hough, L.E., Mironska, R.,McKenney, A.S., and Rout, M.P. (2012) Nucleocytoplasmic transport: a role for non-specific competition in karyopherin-nucleoporin interactions. Mol.Cell. Proteomics (Epub ahead of print).

Theerthagiri, G., Eisenhardt, N., Schwarz, H., and Antonin, W. (2010). The nucleoporin Nup188 controls passage of membrane proteins across the nuclear pore complex. J. Cell Biol. *189*, 1129–1142.

Thompson, R.B., Gryczynski, I., and Malicka, J. (2002). Fluorescence polarization standards for high-throughput screening and imaging. BioTechniques *32*, 34, 37–8, 40, 42.

Timney, B.L., Tetenbaum-Novatt, J., Agate, D.S., Williams, R., Zhang, W., Chait, B.T., and Rout, M.P. (2006). Simple kinetic relationships and nonspecific competition govern nuclear import rates in vivo. J. Cell Biol. *175*, 579–593.

Tseng, S.S., Weaver, P.L., Liu, Y., Hitomi, M., Tartakoff, A.M., and Chang, T.H. (1998). Dbp5p, a cytosolic RNA helicase, is required for poly(A)+ RNA export. Embo J. *17*, 2651–2662.

Ullman, K.S., Shah, S., Powers, M.A., and Forbes, D.J. (1999). The nucleoporin nup153 plays a critical role in multiple types of nuclear export. Mol. Biol. Cell *10*, 649–664.

Velez, M., and Axelrod, D. (1988). Polarized fluorescence photobleaching recovery for measuring rotational diffusion in solutions and membranes. Biophys. J. *53*, 575–591.

Volkmer, A., Subramaniam, V., Birch, D.J., and Jovin, T.M. (2000). One- and two-photon excited fluorescence lifetimes and anisotropy decays of green fluorescent proteins. Biophys. J. *78*, 1589–1598.

Vrabioiu, A.M., and Mitchison, T.J. (2006). Structural insights into yeast septin organization from polarized fluorescence microscopy. Nature *443*, 466–469.

Vrabioiu, A.M., and Mitchison, T.J. (2007). Symmetry of septin hourglass and ring structures. J. Mol. Biol. *372*, 37–49.

Walther, T.C., Alves, A., Pickersgill, H., Loïodice, I., Hetzer, M., Galy, V., Hülsmann, B.B., Köcher, T., Wilm, M., Allen, T., et al. (2003). The conserved Nup107-160 complex is critical for nuclear pore complex assembly. Cell *113*, 195–206.

Walther, T.C., Fornerod, M., Pickersgill, H., Goldberg, M., Allen, T.D., and Mattaj, I.W. (2001). The nucleoporin Nup153 is required for nuclear pore basket formation, nuclear pore complex anchoring and import of a subset of nuclear proteins. Embo J. *20*, 5703–5714.

Walther, T.C., Pickersgill, H.S., Cordes, V.C., Goldberg, M.W., Allen, T.D., Mattaj, I.W., and Fornerod, M. (2002). The cytoplasmic filaments of the nuclear pore complex

are dispensable for selective nuclear protein import. J. Cell Biol. *158*, 63–77.

Wang, H., and Clapham, D.E. (1999). Conformational changes of the in situ nuclear pore complex. Biophys. J. *77*, 241–247.

Wente, S.R., and Blobel, G. (1993). A temperature-sensitive NUP116 null mutant forms a nuclear envelope seal over the yeast nuclear pore complex thereby blocking nucleocytoplasmic traffic. J. Cell Biol. *123*, 275–284.

Wente, S.R., Rout, M.P., and Blobel, G. (1992). A new family of yeast nuclear pore complex proteins. J. Cell Biol. *119*, 705–723.

Whittle, J.R.R., and Schwartz, T.U. (2009). Architectural nucleoporins Nup157/170 and Nup133 are structurally related and descend from a second ancestral element. J. Biol. Chem. *284*, 28442–28452.

Wu, X., Kasper, L.H., Mantcheva, R.T., Mantchev, G.T., Springett, M.J., and van Deursen, J.M. (2001). Disruption of the FG nucleoporin NUP98 causes selective changes in nuclear pore complex stoichiometry and function. Proc. Natl. Acad. Sci. U.S.A. *98*, 3191–3196.

Yamada, J., Phillips, J.L., Patel, S., Goldfien, G., Calestagne-Morelli, A., Huang, H., Reza, R., Acheson, J., Krishnan, V.V., Newsam, S., et al. (2010). A bimodal distribution of two distinct categories of intrinsically disordered structures with separate functions in FG nucleoporins. Mol. Cell Proteomics *9*, 2205–2224.

Yang, Q., Rout, M.P., and Akey, C.W. (1998). Three-dimensional architecture of the isolated yeast nuclear pore complex: functional and evolutionary implications. Mol. Cell *1*, 223–234.

Yuan, Y., and Axelrod, D. (1995). Subnanosecond polarized fluorescence photobleaching: rotational diffusion of acetylcholine receptors on developing muscle cells. Biophys. J. *69*, 690–700.

Zabel, U., Doye, V., Tekotte, H., Wepf, R., Grandi, P., and Hurt, E.C. (1996). Nic96p is required for nuclear pore formation and functionally interacts with a novel nucleoporin, Nup188p. J. Cell Biol. *133*, 1141–1152.

Zeitler, B., and Weis, K. (2004). The FG-repeat asymmetry of the nuclear pore complex

is dispensable for bulk nucleocytoplasmic transport in vivo. J. Cell Biol. *167*, 583–590.

Zemp, I., and Kutay, U. (2007). Nuclear export and cytoplasmic maturation of ribosomal subunits. FEBS Lett. *581*, 2783-2793.

Zilman, A., Di Talia, S., Chait, B.T., Rout, M.P., and Magnasco, M.O. (2007). Efficiency, selectivity, and robustness of nucleocytoplasmic transport. PLoS Comput. Biol. *3*, e125.

Zilman, A., Di Talia, S., Jovanovic-Talisman, T., Chait, B.T., Rout, M.P., and Magnasco, M.O. (2010). Enhancement of transport selectivity through nano-channels by non-specific competition. PLoS Comput. Biol. *6*, e1000804.